



HAL
open science

Aerodynamic Drag Reduction of a Square-Back Car Model Using Linear Genetic Programming and Physic-Based Control

Ruiying Li

► **To cite this version:**

Ruiying Li. Aerodynamic Drag Reduction of a Square-Back Car Model Using Linear Genetic Programming and Physic-Based Control. Other. ISAE-ENSMA Ecole Nationale Supérieure de Mécanique et d'Aérotechnique - Poitiers, 2017. English. NNT : 2017ESMA0014 . tel-01685306

HAL Id: tel-01685306

<https://theses.hal.science/tel-01685306v1>

Submitted on 16 Jan 2018

HAL is a multi-disciplinary open access archive for the deposit and dissemination of scientific research documents, whether they are published or not. The documents may come from teaching and research institutions in France or abroad, or from public or private research centers.

L'archive ouverte pluridisciplinaire **HAL**, est destinée au dépôt et à la diffusion de documents scientifiques de niveau recherche, publiés ou non, émanant des établissements d'enseignement et de recherche français ou étrangers, des laboratoires publics ou privés.

THÈSE

Pour l'obtention du grade de

DOCTEUR DE L'ÉCOLE NATIONALE SUPÉRIEURE DE MÉCANIQUE ET D'AÉROTECHNIQUE

(Diplôme National - Arrêté du 25 mai 2016)

École Doctorale :

Sciences et Ingénierie en Mécanique, Matériaux, Energétique et Aéronautique

Secteur de Recherche : MÉCANIQUE DES MILIEUX FLUIDES

Présentée par

Ruiying LI

Aerodynamic drag reduction of a square-back car model using linear genetic programming and physics-based control

Directeur de thèse : **M. Bernd R. Noack**

Co-directeur de thèse : **M. Jacques Borée**

Co-encadrant : **M. Laurent Cordier**

Soutenue le 13 December 2017 devant la Commission d'Examen

JURY

Rapporteurs:

L. Cattafesta

Professor, Florida State University, USA

L. Keirsbulck

Professor, University of Valenciennes, France

Membres du jury:

A. Morgans

Professor, Imperial College London, UK

C. N. Nayeri

Associate Professor, TU Berlin, Germany

F. Harambat

Ingénieur-Docteur, PSA Peugeot Citroën, France

B. R. Noack

Directeur de Recherche CNRS, LIMSI, France

L. Cordier

Chargé de Recherche CNRS, Institut Pprime, France

J. Borée

Professeur, Institut Pprime, France

工欲善其事，必先利其器。

《论语·卫灵公》

Good tools make good work.

Analects of Confucius

Acknowledgements

I would like to express my sincere gratitude to my advisors B. Noack, J. Borée and L. Cordier for their continuous support of my PhD study and related research, for their patience, motivation, and immense knowledge. I appreciate all their contributions of time and ideas to make my PhD experience productive and stimulating. The joy and enthusiasm they have for the research were contagious and motivational for me. Their guidance helped me in all the time of my research and writing of the papers and this thesis. I could not have imagined having better advisors and mentors for my PhD study. Without them, the present work would not have been possible.

Besides my advisors, I would like to thank the rest of my thesis committee: Prof. L. Cattafesta, Prof. L. Keirsbulck, Prof. A. Morgans and Dr. C.N. Nayeri, for their insightful comments and encouragement, but also for the hard questions which incited me to widen my research from various perspectives.

I would like to thank specially J.M. Breux with whom I have performed all my experiments. He has been always serious and patient with every single setup. The experimental results would not have been possible without his hard work. I am also grateful to F. Paillé for his very important work on the force balances and his close attention to our experiments. I sincerely thank R. Bellanger and P. Braud for the implementation of laser techniques as well as their friendliness.

I acknowledge F. Harambat for his enthusiastic guidance in PSA-Peugeot Citroën group and for the fruitful collaboration in the context of the OpenLab Fluidics. I would like to thank D. Barros and A. Spohn for their deep and insightful discussions. The colleagues around me have contributed immensely to my personal and professional time at ENSMA. The group has been a source of friendships as well as good advice and collaboration.

I highly appreciate valuable stimulating discussions during my PhD study with: S. Brunton, C. Chovet, Y. Haffner, E. Kaiser, S. Krajnović, R. Martinuzzi, V. Parezanović, R. Radespiel, P. Scholz, R. Semaan, M. Wahde and Y. Wang.

Last but not the least, I would like to thank my parents and my sister for supporting me spiritually throughout the past three years and Y. Cao for all the love.

Résumé étendu

La réduction de la traînée aérodynamique des véhicules terrestres est devenue un défi majeur en raison des contraintes de plus en plus fortes sur les émissions de CO₂ résultant de la consommation de carburant. Pour les véhicules de formes non profilées, la région de basse pression à l'arrière est responsable d'une partie importante de la traînée aérodynamique. A titre indicatif, plus de 50% de la résistance à l'avancement sur une autoroute a pour origine la traînée aérodynamique. Au cours de ces dernières années, le développement rapide du contrôle actif des écoulements a ouvert une nouvelle voie vers la réduction de traînée. Dans ce cadre, la manipulation du sillage par des dispositifs actifs est l'un des sujets les plus traités.

Le but de cette thèse est de développer des stratégies de contrôle efficaces pour la réduction de traînée aérodynamique des véhicules terrestres. Pour atteindre cet objectif, nous examinons expérimentalement les effets d'un forçage fluide sur le sillage d'un modèle de véhicule simplifié à culot droit. Le forçage est effectué par des jets pulsés placés aux arêtes du culot. Seize capteurs de pression répartis sur la surface arrière permettent d'estimer la traînée instantanée. Dans ce manuscrit composé de six chapitres, des stratégies de contrôle, basées sur des méthodes d'apprentissage ou sur la compréhension physique des phénomènes, sont mises en œuvre. Afin d'améliorer la compréhension, les résultats ainsi obtenus sont analysés physiquement.

Chapitre 1

Dans ce chapitre, nous introduisons le contexte industriel et sociétal de notre étude en considérant la réduction indispensable de la consommation et de l'émission de gaz à effet de serre. Nous présentons les mécanismes de base par lesquels la traînée est générée sur les véhicules terrestres. Nous nous intéressons principalement aux véhicules ayant un culot droit. Le décollement de l'écoulement dans le sillage des véhicules joue un rôle majeur dans la traînée. La compréhension fine des dynamiques intervenant dans le sillage aide à mieux contrôler l'écoulement de sillage. Une revue de la littérature est réalisée. Nous récapitulons les caractéristiques principales des instabilités dans la dynamique du sillage induit par le détachement des couches limites : instabilité convective pour le développement des couches cisillées turbulentes et instabilité absolue provoquant l'émission des tourbillons alternés de Von-Kàrmàn. Ces instabilités possèdent une large gamme d'échelles de temps et de longueur, et sont associées à la diminution de la pression derrière le véhicule. La dynamique de la bulle de recirculation conduit à un sillage moyen comprenant deux structures contrarotatives. Nous rappelons aussi des concepts démontrant les liens entre la forme de la bulle moyenne et la pression moyenne au culot dans les études de Roshko (1993 a, b) portant sur des sillages bidimensionnels. Ces concepts aident à

comprendre les effets du contrôle et enrichissent la conception des stratégies de contrôle.

Les dynamiques présentes dans le sillage turbulent sont une conséquence des interactions fortement non-linéaires entre les tourbillons à différentes échelles. La nature instable de l'écoulement rend le sillage très sensible aux excitations externes qui peuvent ainsi être adaptées pour répondre à des objectifs de contrôle spécifiques. Une revue des stratégies de contrôle pour la réduction de traînée est ensuite abordée dans le cas particulier des corps simplifiés de véhicule à culot droit. Le contrôle passif impose une légère modification de la configuration d'origine via des dispositifs additionnels comme des volets. Bien que les dispositifs passifs soient efficaces pour la réduction de traînée, leurs applications industrielles sont encore limitées car des surfaces additionnelles ne sont pas pratiques à utiliser. Par ailleurs, un autre inconvénient du contrôle passif est qu'il ne peut pas être désactivé lorsqu'il n'est pas nécessaire. Face à ces contraintes, des études sur le contrôle actif ont rapidement émergé au cours de ces dernières décennies. Le contrôle actif introduit de l'énergie dans le système et peut imiter les effets du contrôle passif. En outre, le contrôle peut alors être activé ou désactivé selon les besoins. Un des dispositifs actifs les plus utilisés pour manipuler des écoulements de sillage est le jet synthétique ou jet pulsé périodique. Ce type de forçage fluide instationnaire peut être appliqué d'une manière prédéterminée en boucle ouverte. Le forçage périodique en est un exemple particulier. Dans ce cas, la commande de contrôle ne dépend pas de l'état de l'écoulement. Le contrôle en boucle fermée, pour lequel l'actionnement est déterminé via des capteurs enregistrant l'état de l'écoulement, offre un potentiel supplémentaire pour améliorer l'efficacité du contrôle en adaptant la commande aux modifications de l'écoulement. Le contrôle en boucle fermée peut être basé sur un modèle. Cependant, les dynamiques fortement non linéaires présentes dans l'écoulement posent un défi immense pour construire un modèle dynamique forcé qui puisse traduire précisément les interactions des tourbillons aux différentes échelles.

Dans cette thèse, nous contournons ces difficultés de modélisation en développant une stratégie de contrôle sans modèle : le contrôle via la programmation génétique linéaire (LGPC). Cette méthode, entièrement basée sur les données, optimise les lois de contrôle via une technique d'apprentissage automatique qui imite le processus de l'évolution dans la nature. Basé sur un principe d'évolution génétique, le contrôle par LGPC explore et exploite la dynamique fortement non linéaire du sillage d'une manière non supervisée avec pas ou peu de connaissances antérieures sur le système. Ainsi, le problème revient à trouver une loi de contrôle qui optimise une fonction de coût donnée. Cette optimisation est réalisée par programmation génétique linéaire qui permet de faire évoluer un ensemble de lois de contrôle dans un espace de recherche de grande dimension. En particulier, notre étude généralise les études antérieures sur le contrôle par programmation génétique en incluant dans l'espace de recherche de contrôle le forçage multi-fréquences, le signal des capteurs, l'historique

des informations temporelles et leurs combinaisons. De cette manière, il est possible de construire tout type de loi de contrôle.

Chapitre 2

Dans ce chapitre, nous commençons par présenter la méthode LGPC. Par la suite, nous démontrons son efficacité pour stabiliser un système dynamique constitué de trois oscillateurs couplés non linéairement. Ces oscillateurs sont couplés via les taux de croissance et possèdent trois fréquences incommensurables. Ce système possède les mêmes caractéristiques dynamiques que celles rencontrées dans le contrôle des écoulements turbulents. Dans l'état non forcé, les premier et deuxième oscillateurs sont linéairement instables (amplitudes limitées), alors que le troisième est stable. L'objectif du contrôle est de stabiliser le premier oscillateur, en appliquant le forçage sur le deuxième et troisième oscillateur. Cet objectif peut être atteint en atténuant en boucle fermée le deuxième oscillateur ou en excitant en boucle ouverte le troisième. LGPC est utilisé pour explorer automatiquement ces mécanismes. Trois catégories de LGPC sont développées :

- LGPC-1 : $\mathbf{b} = K(\mathbf{h})$, contrôle multi-fréquences ;
- LGPC-2 : $\mathbf{b} = K(\mathbf{s})$, contrôle en boucle fermée basé sur les signaux des capteurs ;
- LGPC-3 : $\mathbf{b} = K(\mathbf{s}, \mathbf{h})$, contrôle généralisé.

La dernière catégorie comprend à la fois les capteurs \mathbf{s} et les fonctions périodiques \mathbf{h} , permettant que l'algorithme d'apprentissage choisisse automatiquement entre un contrôle en boucle ouverte, un contrôle en boucle fermée basé sur les capteurs ou une combinaison des deux en fonction de leur performance respective. LGPC-1 détermine automatiquement la fréquence optimale du forçage périodique et cela en utilisant moins de temps qu'un balayage exhaustif des paramètres. Les lois de contrôle obtenues avec LGPC-2 et -3 excitent toutes les deux le troisième oscillateur via un forçage à haute amplitude s'accompagnant d'une transition rapide. Quant à lui, le second oscillateur est maintenu à un faible niveau de fluctuation. Après la transition rapide, le premier et deuxième oscillateur entrent dans un état quasi-stable à des niveaux de fluctuation presque nuls. Le système n'a alors plus besoin d'être forcé et l'amplitude de la commande de contrôle s'atténue. Ainsi, le système complet est stabilisé en injectant de l'énergie uniquement au début de la fenêtre de contrôle. Les contrôleurs basés sur le retour des états du système surpassent le forçage périodique optimal parce qu'ils induisent un niveau de fluctuation plus faible et consomment une énergie d'actionnement inférieure. Les mécanismes d'actionnement qui ont été explorés démontrent que l'interaction entre des fréquences différentes peut constituer le seul mécanisme permettant de stabiliser un système, ce qui est typique pour le contrôle d'un écoulement turbulent.

Chapitre 3

Suite au succès rencontré sur le système dynamique traité au chapitre 2, LGPC est appliqué à des expériences réalisées sur un véhicule simplifié à culot droit pour réduire la traînée. La vitesse à l'infini amont est fixée à 15m/s, ce qui correspond à un nombre de Reynolds égal à $Re_H = 3 \times 10^5$ basé sur la hauteur H du modèle. A ce régime, le sillage présente une asymétrie selon la direction normale au sol et une symétrie selon la direction latérale. Des jets pulsés sont positionnés sur des fentes le long des quatre arêtes du culot. La direction de l'axe des jets est parallèle aux couches limites en amont du décollement. Les jets sont pilotés par des électrovannes réparties d'une manière homogène autour du périmètre des arêtes. Le système complet assure un jet quasi-bidimensionnel le long de chaque arête. Pour ce chapitre, les quatre fentes d'actionnement sont couplées à des déflecteurs de surface de type Coanda afin de bénéficier de l'effet Coanda. Un réservoir d'air comprimé de 3 litres est installé à l'intérieur de la maquette et connecté aux électrovannes. En changeant la pression dans le réservoir, l'amplitude du jet peut être réglée. Dans ce chapitre, la pression initiale du réservoir est fixée à $P_o^i = 4$ bar. Les paramètres à optimiser sont la fréquence et le rapport cyclique. Selon Barros et al. (2016b), le forçage périodique optimal sur cette configuration correspond à une fréquence élevée et à un rapport cyclique faible, associé à une réduction de traînée de 19%. Dans notre étude, LGPC-1 identifie rapidement un forçage bi-fréquence qui pilote simultanément les quatre fentes d'actionnement. Ce forçage, obtenu en testant seulement 200 individus et cela en moins d'une heure, correspond à une réduction de traînée de 22%, surpassant la valeur de référence obtenue avec le forçage périodique optimisé. L'énergie consommée par le forçage ne représente que 30% de l'énergie aérodynamique récupérée (seule l'énergie dissipée dans les jets instationnaires est comptabilisée ici). Les deux fréquences impliquées dans la meilleure loi de contrôle se trouvent être encore des fréquences élevées, soit $20St_H^{vs}$ et $40St_H^{vs}$ respectivement, St_H^{vs} étant la fréquence du détachement tourbillonnaire de Von-Kàrmàn. Ce forçage à haute fréquence conduit à une suppression du contenu énergétique à très basses fréquences des signaux de pression au culot et à une atténuation globale de l'énergie cinétique moyenne et turbulente dans le sillage, aboutissant à un sillage plus stabilisé. De manière concomitante, la géométrie moyenne du sillage est modifiée de sorte que les couches de cisaillement sont déviées vers l'intérieur du sillage, ce qui donne une bulle de recirculation plus courte, plus étroite et plus profilée. Le couplage de ces effets est responsable de la réduction de traînée. Par ailleurs, la loi de contrôle obtenue par LGPC-2, qui est basée sur les signaux des capteurs, reproduit le forçage à haute fréquence avec une réduction de traînée comparable au forçage périodique optimal. Dans la meilleure loi de contrôle, LGPC-2 sélectionne un seul capteur parmi les douze disponibles dans le culot. Nous montrons que ce capteur est capable, d'une part, de capturer une dynamique suffisamment forte de l'écoulement non forcé pour déclencher le cycle d'actionnement, et d'autre part, de donner un bon rapport signal

sur bruit afin de créer un forçage périodique à haute fréquence dans l'écoulement forcé. Par conséquent, LGPC-2 fournit non seulement l'optimisation des lois de contrôle mais également une optimisation de la sélection des capteurs. Le résultat de LGPC-3 est similaire à celui de LGPC-1. Les résultats des Chapitres 2 et 3 soulignent le potentiel de LGPC dans la découverte et l'exploitation de mécanismes de contrôle non linéaires efficaces.

Chapitre 4

Dans ce chapitre, nous étudions le cas d'un sillage intermittent présentant un comportement bimodal à dérapage nul. Ce sillage est caractérisé par une brisure de symétrie de la zone de recirculation qui bascule aléatoirement entre deux états asymétriques selon la direction latérale. L'écoulement naturel présenté dans le Chapitre 3 n'a pas montré ce comportement bimodal. D'après les études de Barros et al. (2017), le sillage bimodal peut être provoqué par un cylindre collé au sous-bassement du corps selon la direction latérale. La vitesse à l'infini amont est fixée à 30m/s, ce qui correspond à un nombre de Reynolds égal à $Re_H = 6 \times 10^5$. Nous observons qu'au moment du basculement entre les deux états, la pression au culot augmente, ce qui montre l'intérêt de symétriser le sillage en terme de réduction de traînée. Des essais de forçage périodique sur une seule arête montrent que le sillage est toujours bloqué dans un des deux états asymétriques et présente une région de pression plus basse proche de l'arête forcée. Finalement, nous en déduisons une stratégie de contrôle en boucle fermée permettant de symétriser le sillage. Cette stratégie repose sur du contrôle en opposition. Pour cela, nous utilisons le gradient latéral de pression au culot comme retour d'information en temps réel. Lorsqu'une région de pression plus basse est détectée le long d'une arête, le forçage est appliqué sur l'arête opposée afin de générer une inversion de la recirculation. La performance de la symétrisation du sillage dépend notamment de la fréquence de forçage. Le sillage le plus symétrique est obtenu pour $St_H = 0,8$. Barros et al. (2016b) ont montré que cette valeur de fréquence amplifie le plus les instabilités de la couche cisailée et induit l'augmentation la plus élevée de fluide entraînée dans la région de recirculation. Ces caractéristiques de l'actionnement permettent à $St_H = 0,8$ de modifier efficacement la recirculation de l'écoulement et de supprimer les ruptures de symétrie. Cependant, l'augmentation de pression au culot est limitée à 3%. En effet, bien que les états symétriques du sillage augmentent la pression au culot, les effets d'actionnement associés à $St_H = 0,8$ (augmentation du mélange de la couche de cisaillement et amplification du détachement tourbillonnaire de Von-Kàrmàn), sont préjudiciables à l'augmentation de la pression au culot. Par conséquent, cette stratégie de contrôle doit encore être améliorée pour atténuer l'effet néfaste de l'actionnement. Un moyen possible est de déterminer l'énergie minimale nécessaire pour déclencher le basculement d'un état vers l'autre.

Chapitre 5

Ce chapitre traite du sillage asymétrique avec un angle de dérapage modéré égal à 5 degrés. Cette valeur de l'angle est choisie car elle est représentative des valeurs de dérapage rencontrées fréquemment par un véhicule. La vitesse à l'infini amont est fixée à 25m/s, ce qui correspond à un nombre de Reynolds égal à $Re_H = 5 \times 10^5$. Pour l'écoulement non forcé, le sillage moyenné en temps présente une recirculation plus large proche du côté sous le vent. En appliquant un forçage périodique sur une seule arête, nous observons que le forçage sur l'arête sous le vent augmente la traînée alors que celui sur l'arête au vent entraîne une réduction de traînée. Dans ce dernier cas, la réduction de traînée la plus élevée (environ 6%) est obtenue pour deux fréquences ayant une différence d'un ordre de grandeur : (i) l'actionnement à basse fréquence ($St_H = 0,48$) augmente particulièrement la turbulence de la couche de cisaillement, et ainsi modifie la recirculation à grande échelle en réduisant la traînée par symétrisation du sillage ; (ii) l'actionnement à haute fréquence ($St_H = 6$) agit comme un volet fluidique et réduit la traînée par un effet de vectorisation de la couche cisailée. Ces résultats de forçage périodique au vent nous inspirent la construction d'un contrôle bi-fréquence afin de réduire davantage la traînée en combinant la symétrisation du sillage avec l'effet de volet fluidique. Toutefois, en combinant les deux fréquences $St_H = 0,48$ et $St_H = 6$, c'est-à-dire en considérant un forçage du type $St_H^{bf} = 0,48 \otimes 6$, il y a une inversion de l'asymétrie du sillage par rapport à l'écoulement non forcé, et une diminution de la réduction de traînée par rapport au cas de la fréquence unique $St_H = 0,48$. Cette découverte indique que $St_H^{bf} = 0,48 \otimes 6$ n'est pas adapté pour symétriser le sillage. En faisant varier dans ce forçage bi-fréquence la valeur de la basse fréquence, nous avons trouvé que la configuration optimale est $St_H^{bf} = 0,24 \otimes 6$. Ce forçage donne une réduction de traînée de 7% qui surpasse le forçage optimal à la fréquence unique. Le sillage correspondant est simultanément symétrisé et vectorisé. Nous pouvons ainsi considérer ce contrôle bi-fréquence comme un forçage « ajusté » à basse fréquence en « ajoutant » un volet fluidique. Ces mécanismes d'actionnement qui combinent les deux effets de la symétrisation et de la vectorisation ne peuvent pas être explorés par un forçage à fréquence unique. En outre, en appliquant LGPC-3 sur l'arête au vent dans l'objectif de minimiser la traînée, nous retrouvons de manière automatique la même combinaison de fréquences, soit $St_H = 0,24$ et $St_H = 6$. Ce résultat démontre à nouveau l'efficacité de LGPC pour déterminer une loi de contrôle optimale avec peu de connaissances préalables du système. Finalement, l'effet engendré en ajoutant des surfaces Coanda au voisinage des fentes d'actuation est étudié. Le couplage de la surface Coanda et de l'actuation bi-fréquence au vent amplifie encore la vectorisation et la turbulence de la couche de cisaillement, aboutissant à une asymétrie de sillage inversée pour toute la gamme de basse fréquence étudiée.

Chapitre 6

Ce chapitre résume les résultats présentés dans ce manuscrit de thèse. Nous montrons que les stratégies de contrôle développées dans cette étude sont efficaces pour contrôler différents types de sillages derrière un modèle simplifié de véhicule. Les analyses physiques des résultats clarifient des facteurs importants pour modifier la traînée du modèle, comme la vectorisation de la couche de cisaillement et la symétrisation du sillage. Des perspectives sont aussi discutées. Nous pouvons étendre la recherche actuelle à des conditions plus complexes de vitesse amont variable ou de rafale. Pour cela, nous pouvons chercher avec LGPC un contrôleur robuste en incluant la vitesse amont comme un capteur supplémentaire ou en évaluant la fonction de coût dans différentes conditions de fonctionnement. Par ailleurs, LGPC peut être appliqué sur le sillage bimodal afin d'explorer de nouveaux mécanismes d'actionnement autres que le contrôle par opposition. Nous pouvons également imaginer aborder des problèmes avec un angle important de dérapage pour chercher de manière couplée à réduire la consommation et à améliorer la sécurité de conduite. Pour cela, nous pouvons développer une version multi-objectif de LGPC afin de déterminer l'actionnement optimisé correspondant au pilotage indépendant des quatre fentes d'actionnement.

Table of contents

Chapter 1	Introduction	1
1.1	Industrial context	1
1.2	Bluff body wakes	2
1.2.1	Origin of drag	2
1.2.2	Wake dynamics	4
1.2.3	Simplified square-back car model	6
1.3	Flow control	7
1.4	Objectives and outline of the thesis	12
Part I	Linear genetic programming control	15
Chapter 2	Design of linear genetic programming control	17
2.1	Linear genetic programming control	17
2.1.1	Control problem	18
2.1.2	Ansatz for the control law	18
2.1.3	Linear genetic programming control	19
2.1.4	Visualization of control laws	23
2.2	Application on a three-oscillator model	24
2.2.1	Problem formulation	24
2.2.2	Open-loop periodic forcing	26
2.2.3	Results of LGPC	27
2.2.4	Control landscape for LGPC-3	33
2.3	Summary	34
Chapter 3	Drag reduction of a car model by LGPC	35
3.1	Control problem	36
3.2	Experimental setup	36
3.2.1	Flow configuration and wind tunnel	36
3.2.2	Actuator system	38
3.2.3	Pressure sensors and measurements	39
3.2.4	Real-time system	42
3.2.5	Experimental implementation of LGPC	42
3.3	Unforced flow	44
3.4	LGPC-1: multi-frequency forcing	45
3.4.1	LGPC-1 results	46
3.4.2	Analysis of the optimal control law	50
3.4.3	Analysis of the near wake	53
3.5	LGPC-2: Feedback control	54
3.5.1	LGPC-2 results	55
3.5.2	Visualization of control laws	57
3.5.3	Analysis of the optimal control law	59
3.5.4	Morlet filtering of sensor signals	62
3.6	LGPC-3 and multiple-input control	64
3.7	Summary	64

Part II	Physics-based control	67
Chapter 4	Feedback control of bi-modal wake dynamics	69
4.1	Bi-modal wake features and manipulations	69
4.2	Experimental setup	70
4.3	Unforced bi-modal flow	72
4.4	Single edge open-loop forcing	75
4.5	Feedback control	80
4.5.1	Control design and performance	80
4.5.2	Effects on the base pressure and near wake	83
Chapter 5	Drag reduction of the car model at yaw	87
5.1	Crosswind effects	87
5.2	Experimental setup	89
5.3	Unforced flow	92
5.4	Leeward forcing	96
5.4.1	Global effects of actuation	96
5.4.2	Effects on the base pressure and near wake	98
5.5	Windward forcing	103
5.5.1	Global effects of actuation	103
5.5.2	Effects on the base pressure and near wake	105
5.6	Windward bi-frequency forcing	112
5.6.1	Global effects of bi-frequency actuation	112
5.6.2	Effects on the base pressure and near wake	117
5.6.3	Analysis of the phase-averaged velocity statistics	121
5.6.4	On the drag reduction using LGPC	125
5.7	Unsteady Coanda blowing effect	127
Chapter 6	Conclusions and perspectives	135
6.1	General synthesis	135
6.2	Perspectives	138
Appendix A	Classical multidimensional scaling (CMDS)	151

Chapter 1

Introduction

Focus of the present thesis is drag reduction of road vehicles which is of crucial importance for the sustainable development of natural resources. In these introductory paragraphs, we briefly review the origin of drag for road vehicles, identify the importance of wake flow in the drag and address the main wake dynamics with a particular attention on the simplified square-back car models. The development of flow control strategies smooths the path for achieving drag reduction. We provide an overview of the current wake control strategies, highlighted by successful experimental practices. Finally, we outline the topics covered in the manuscript.

Contents

1.1	Industrial context	1
1.2	Bluff body wakes	2
1.2.1	Origin of drag	2
1.2.2	Wake dynamics	4
1.2.3	Simplified square-back car model	6
1.3	Flow control	7
1.4	Objectives and outline of the thesis	12

1.1 Industrial context

Over the past 50 years, sales of automobiles undergo a tremendous growth ascribed to the continuous innovations in horsepower, safety, and rider amenities. The number of vehicles in operation worldwide, including cars, trucks and buses, surpassed the 1 billion-unit mark in 2010 for the first time ever (Sousanis, 2011). This number is expected to double worldwide in the next two decades. The billion vehicles pose a severe challenge for the planet to sustain, as they are emitting extraordinary quantities of greenhouse gases as carbon-dioxide CO_2 into the atmosphere, are draining the world's conventional petroleum supplies, are inciting political skirmishes over oil, and are overwhelming city roads (Sperling & Gordon, 2008). In particular, European union legislation has set standards for new passenger cars regarding their CO_2 emissions. The current limit is set as 130 grams of CO_2 per kilometer, and the new limit imposes a reduction of 30% (95 grams of CO_2/km) by the year 2021 (EU, 2017). Car manufacturers have to pay an excess emissions premium for the exceeded emissions.

The limited fuel resources and the CO_2 regulation have forced the car manufacturers to adapt novel technologies faster than anticipated. The improvements of the technology in engines, transmissions, materials and aerodynamics are mainly pursued. The focus of the present study is to improve the aerodynamic performance of road vehicles aiming at drag reduction.

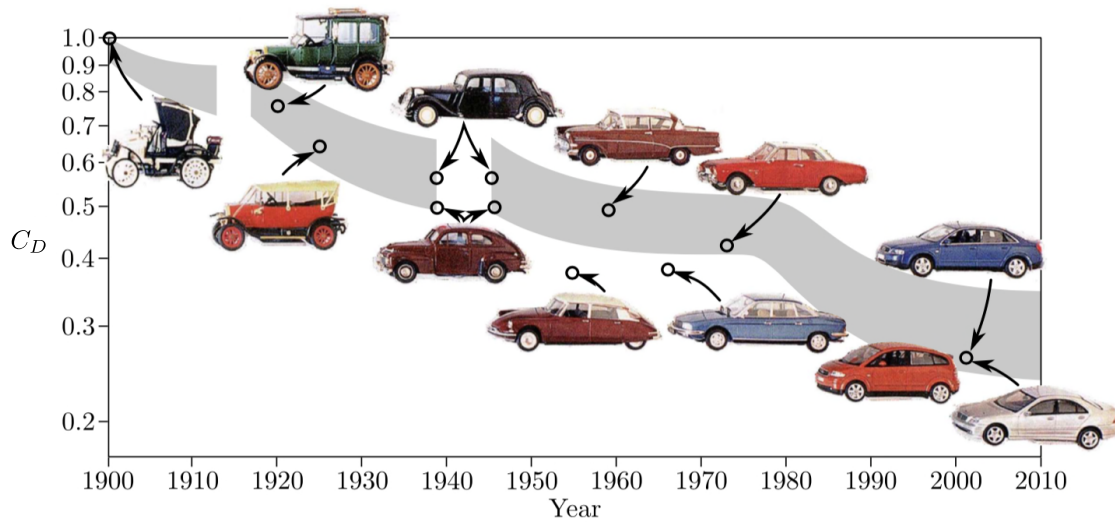


Figure 1.1: History of the drag for road vehicles (Hucho, 1998; Grandemange, 2013). C_D is the normalized drag coefficient.

In fact, when road vehicles move in a fluid, they have to resist a force acting opposite to their motion. This force is known as the *drag*. When the fluid is a gas like air, it is specifically called aerodynamic drag, which is the concern of our study. The power consumed to resist the drag constitutes an important portion of the total power expense. At a speed of 50 km/h the aerodynamic drag accounts for 50% of the total drag reaching 80% at 130 km/h (Brunton & Noack, 2015). This explains why the car manufacturers are interested in improving the aerodynamic performance of road vehicles, as highlighted in Fig. 1.1 for the history of the drag evolution since 1900 (Hucho, 1998). These improvements of drag reduction were mainly achieved by the optimization of the vehicle shape. Nowadays, the shapes of vehicles are very alike (Rossitto, 2016) because all the manufacturers are pursuing the shape optimization for drag reduction and tend to follow one unique optimal shape under the similar constraints from functional, economic and aesthetic aspects. This leaves little room to reduce further the drag from the geometry of vehicles. Therefore, alternative technologies without the geometry modification should be flourished to provide more design liberties.

Flow control can help to fulfill these requirements and is the topic of the present study. Flow control is a rapidly progressing research field existing in a multitude of applications including drag reduction of road vehicles, ships and submarines, lift increase of airplanes and efficiency improvement of renewable energies (Brunton & Noack, 2015). Here, we are particularly interested in its application on the drag reduction of road vehicles. Our aim is to develop effective control strategies to minimize the drag thus to reduce the fuel consumption and CO₂ emissions. In the following, we give an introduction about the basic flow features surrounding road vehicles. Numerous flow control strategies for drag reduction will be reviewed and the challenges confronted to the flow control will be highlighted.

1.2 Bluff body wakes

1.2.1 Origin of drag

In this section we present the basic mechanisms by which drag is generated on road vehicles. Figure 1.2(a) shows a sketch of the flow around a car model. In a relative reference, we consider that the car is at rest and the flow moves from the left to right. The oncoming flow impinges on

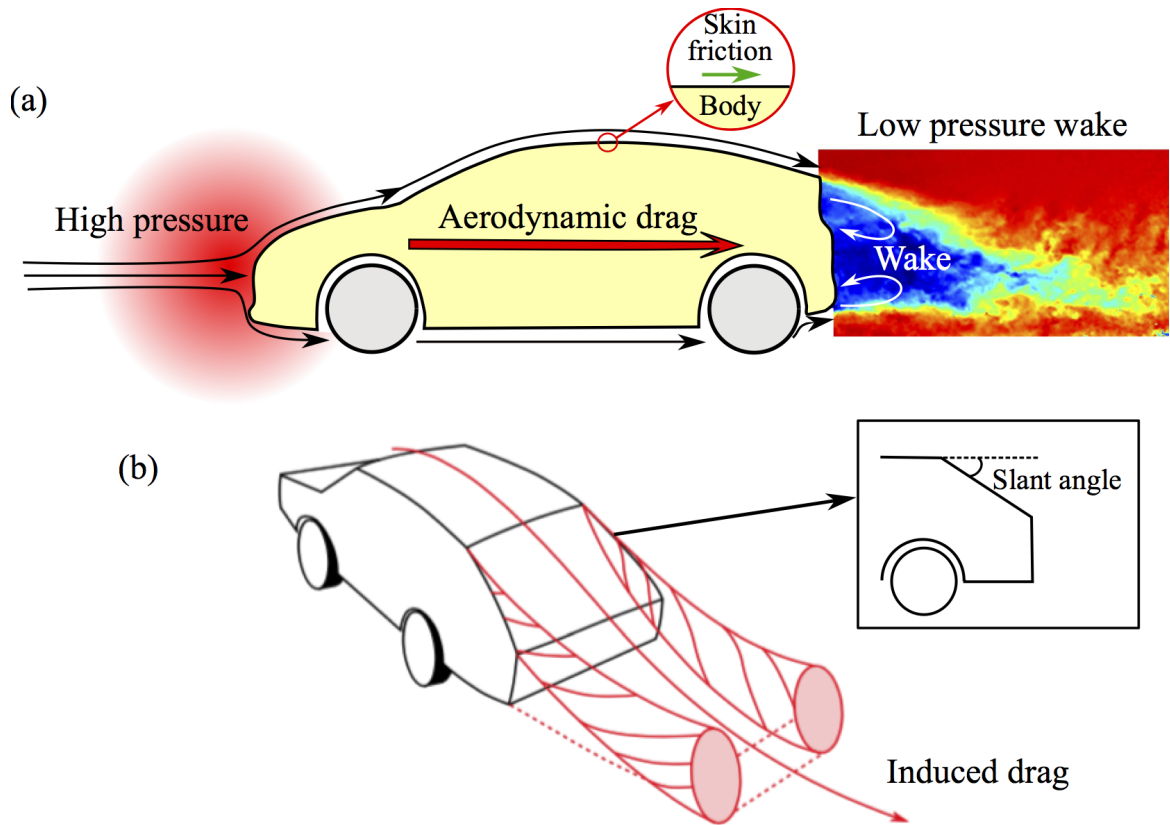


Figure 1.2: Sketch illustrating the drag origin for road vehicles: (a) aerodynamic drag, skin friction; (b) induced drag if existed (Hucho, 1998). The color in the wake flow of (a) indicates the intensity of the streamwise velocity (blue: low velocity; red: high velocity).

the front part of the car model and comes to a complete stop, creating a high pressure region. Whereas at the rear part, due to the abrupt change of the car geometry, the flow is forced to separate from the model trailing edges and forms a recirculation region behind the model associated with a low pressure inside. This separated flow is denominated *wake*. The pressure difference between the front and rear part of the model creates an important resistance to the motion of the car which is called the *pressure drag*.

On the other hand, along the surfaces of the car, the flow creates a shear force parallel to the surface which corresponds to the so-called *friction drag*. The nature of friction drag is due to *viscosity* of the fluid. For the geometries like cars, the main contribution of the drag comes from the pressure drag, and the bodies having this feature is referred to as *bluff bodies*. In contrast, aircrafts and ships suffer primarily from friction drag, and the geometries alike are called *streamlined bodies*, which are not the concern of the present work.

Additionally, for certain models having a moderate slant angle (often between 10° to 30°) at the rear part, see Fig. 1.2(b) for a fastback car model (Hucho, 1998), a pair of intense counter-rotating longitudinal vortices develops in the wake due to the pressure difference between the car's roof and side surface. The portion of drag related to these vortices is called *induced drag*, which is commonly studied in aeronautics. The control of induced drag is often the interest for sedan or fastback cars. For square-back blunt-edged cars, this is of less concern as the wake is governed by the massive recirculation flow behind the base where no intense streamwise vortices are observed. However, high asymmetry in such wakes may change the organization of the recirculation flow which is likely to result in a pair of counter-rotating vortices in the far wake (Grandemange *et al.*, 2015). Nevertheless, the influence of such vortices on the drag remains unclear.

The illustration above highlights the importance of wake to drag. Hence, wake manipulation has been the subjects of intense research (Choi *et al.*, 2008). The aim is often to increase the pressure over the vehicle base surface, in this way the pressure difference decreases and the drag reduces.

1.2.2 Wake dynamics

After showing the importance of wake, now we describe the fundamental characteristics of bluff body wakes to understand the involved dynamics.

The investigated wake flow is highly turbulent at a Reynolds number of the order 10^5 since we are interested in the conventional speed of cars for industrial applications. Figure 1.3 shows a sketch of the wake flow on the vertical symmetric plane of a square-back car in a two-dimensional point of view for clarity. However, we note that the real flow is highly three-dimensional with more complexities.

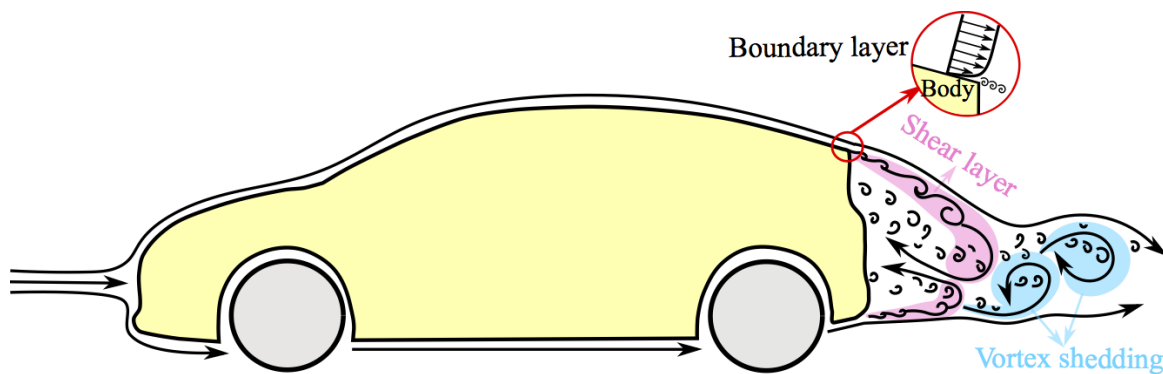


Figure 1.3: A sketch illustrating the fundamental wake features behind a square-back car. The separation of the boundary layer imposed by the sharp edge conditions the roll-up of the free shear layers whose interaction yields the periodic vortex shedding and the reversed flow in the wake region.

In general, the wake is characterized by a broadband spectrum of vortex length and time scales interacting strongly among them. The *boundary layer* develops along the car surface and is forced to separate at the blunt trailing edges due to the abrupt change of geometry. For cars having a curved trailing edge or a slant window, the flow separates due to an adverse pressure gradient and the separation point is not fixed. The boundary layer detachment sheds concentrated *vorticity* into the wake and conditions the roll-up of the free *shear layers* originating from the trailing edges. From the stability point of view, shear layer or, equivalently, mixing layer, is convectively unstable (Huerre & Monkewitz, 1990). Its streamwise evolution is a noise amplifier of upstream perturbations. This feature is also known as the Kelvin-Helmholtz instability (Drazin & Reid, 2004). As illustrated in Fig. 1.4 for a canonical mixing layer, the small-scale vortices near the origin of the mixing layer roll up gradually into larger and larger *coherent* structures, manifesting the high-dimensional multi-scale vortex dynamics involved in this type of flow.

The shear layers originating from opposite edges carry vorticity of opposite sign. When the vortex in one shear layer grows large and strong enough, it is capable to interact with its facing shear layer. Gerrard (1966) introduced an interesting scenario to interpret this interaction in the wake of a two-dimensional cylinder, as illustrated in Fig. 1.5(a). Fluid on the lower side is drawn across the wake by the action of the growing vortex I on the upper side. Part (1) and (2) are entrained by the upper shear layer while part (3) induces a reversed flow and creates a vortex II close to the base carrying an opposite sign to the entraining vortex I, but the

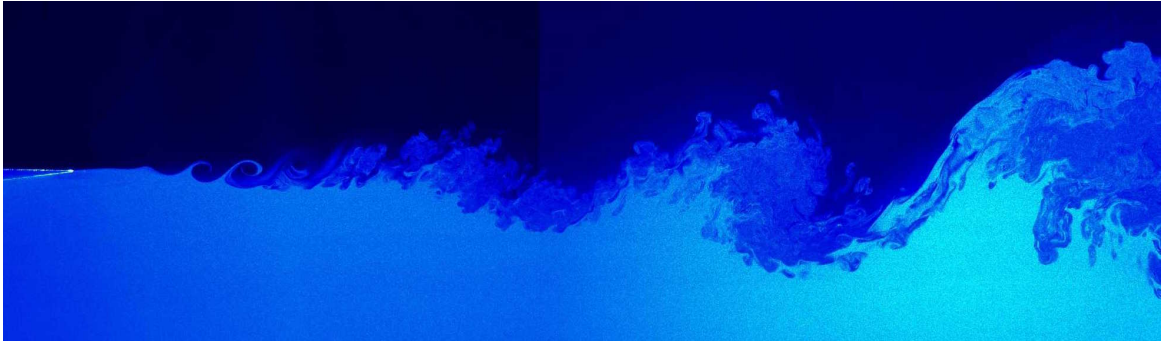


Figure 1.4: Illustration of the streamwise evolution of a canonical mixing layer (courtesy from V. Parezanović).

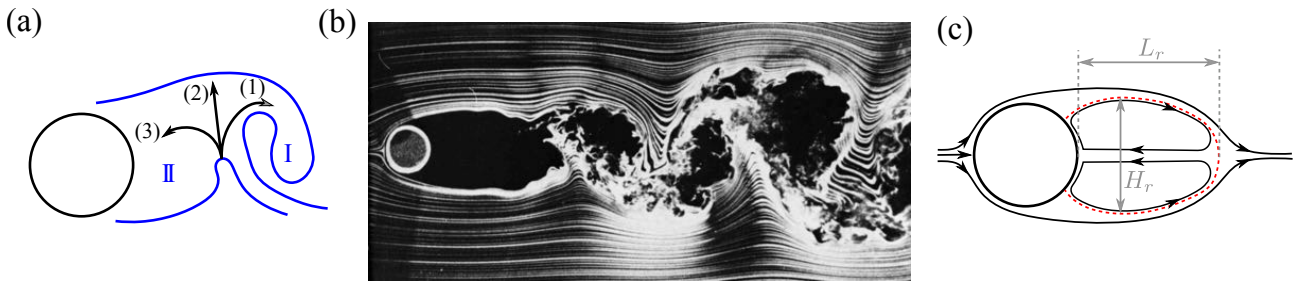


Figure 1.5: (a) Illustration of the interaction of opposing shear layers in a two-dimensional cylinder wake (Gerrard, 1966). (b) Vortex shedding in the flow past a cylinder at $Re = 10^4$ (figure from Van Dyke 1982). (c) Sketch of the mean cylinder wake (adapted from Grandemange 2013). The red dashed line indicates the recirculation bubble boundary. L_r and H_r are the bubble length and width respectively. For square-back bluff bodies, H_r is the height H of the model.

intensity of vortex II is considerably less than that of vortex I. The approach of oppositely-signed vorticity in sufficient concentration cuts off the connection of the upper shear layer to vortex I. Thus vortex I ceases to increase in strength and is shed from the body, and now the lower shear layer takes the role to draw the fluid from the upper side across the wake. This scenario occurs periodically and leads to the famous *vortex shedding* dynamic, as exemplified in Fig. 1.5(b). In time average, see Fig. 1.5(c), this periodic process leads to a *recirculation bubble* zone with two trapped recirculating structures inside. As introduced in § 1.2.1, the low pressure inside this zone accounts for an important part of the total drag. Analyses on the relation between the base pressure and the bubble size have been performed by Roshko (1993a,b). The bubble size is determined by the streamlines enclosing the recirculation region. They modeled the base pressure by working with the balance of pressure and stress forces on the mean wake (Sychev, 1982) and concluded that the base pressure decreases with the increasing wake bluffness (Roshko, 1955). A higher bluffness corresponds to a shorter and wider bubble and a low aspect ratio L_r/H_r , where L_r and H_r are the bubble length and width respectively. Indeed, according to Gerrard (1966), the vortex II in Fig. 1.5(a) tends to be weaker the greater the entrained flow in (1) and (2) is. As a consequence, the formation of vortex II is closer to the base resulting in a shorter bubble length L_r and a decrease of pressure inside the recirculating region and also near the base.

The scenario above is mainly associated with two-dimensional flows in which cases the vortex shedding dynamic is prominent. For the three-dimensional wake of a car, the interaction of shear layers comes from all four edges resulting in a more complex wake dynamic. However, the vortex shedding mode is still discernible in the symmetry planes of the model but has a much lower energy than that of the two-dimensional flows. In stability theory, vortex shedding is characterized as an absolute instability exhibiting an oscillatory behavior (Huerre & Monkewitz,

1990). In summary, the turbulent wake dynamics are a consequence of the strongly nonlinear interactions of high-dimensional multi-scale vortices. The intrinsically unstable nature makes the wake flow highly sensitive to external excitations which can be tailored to meet specific control goals (to be commented in § 1.3).

1.2.3 Simplified square-back car model

In vehicle aerodynamics, numerous studies have been conducted with the simplified model of road vehicles as they can reproduce the important flow structures around realistic road vehicles and favor the comparison between different experimental and numerical studies. One of the most investigated models is the *Ahmed body*, proposed originally by S. R. Ahmed in 1984 (Ahmed *et al.*, 1984). Figure 1.6 shows two variants of the Ahmed body. They both have a rounded front part, but one has a slanted rear surface permitting to study the effect of a variable slant angle, while the other has a square-back base surface. Through the work of Ahmed *et al.* (1984), the comprehension of the flow around different shapes of road vehicles has been significantly improved. Since then, Ahmed body has been the model of intensive research in both numerical simulations (Krajnović & Davidson, 2005*a,b*; Minguez *et al.*, 2008; Guilmineau, 2008; Aljure *et al.*, 2014; Östh *et al.*, 2014) and experiments (Bayraktar *et al.*, 2001; Lienhart & Becker, 2003; Grandemange *et al.*, 2013*b*; Zhang *et al.*, 2015; Barros *et al.*, 2016*a,b*). The present study focuses particularly on the square-back variant of the Ahmed body.

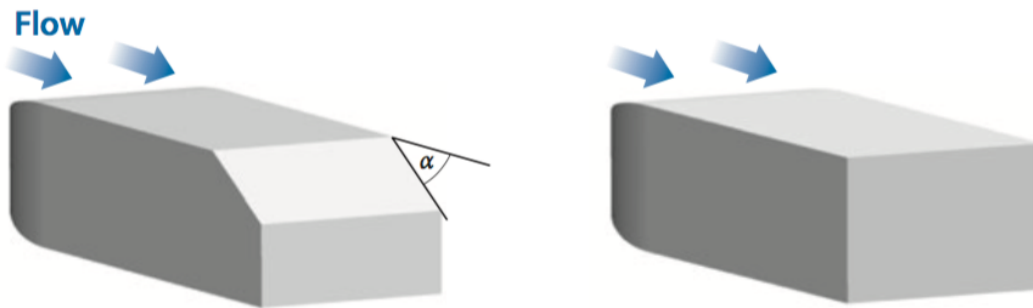


Figure 1.6: Ahmed body for a slanted (left) and square-back (right) rear surfaces (adapted from Choi *et al.* 2014).

The dynamics in the near wake region described in § 1.2.2 have been observed in multiple studies of the simplified square-back car models. A typical non-dimensional parameter for characterizing different wake dynamics is the *Strouhal number* $St = fl/U_\infty$, also called the dimensionless frequency, where f is the characteristic frequency of the motion, l the characteristic length of the model and U_∞ the oncoming velocity. In the following, we list some typical frequencies reported in the literature.

- Shear layer dynamics: Duell & George (1999) measured at the start of the top shear layer a dimensionless frequency of $St_H = 1.157$ based on the model height H and associated it with the vortical structures being rolled-up by the shear layer close to the blunt trailing edge. As these vortices are convected along the shear layer, vortex pairing occurs which halves the characteristic frequency. Similar observations have been made by Barros (2015): the most amplified frequency at several streamwise locations inside the shear layer decreases with the increasing streamwise distance. This scenario agrees well with that observed in a canonical mixing layer flow (Ho & Huerre, 1984).
- Vortex shedding: this mode has been observed in multiple studies (Grandemange *et al.*, 2013*b*; Lahaye *et al.*, 2014; Volpe *et al.*, 2015; Barros *et al.*, 2016*a,b*) and they all identified

a frequency around $St \sim 0.2$ which is the value typically found in the two-dimensional flows (Roshko, 1955; Gerrard, 1966; Bearman, 1965). In particular, the peak of the associated energy is more clear when the measurement is taken in the plane of symmetry. Moreover, the vortex shedding frequency is one order of magnitude lower than the dynamics in shear layers.

- Bubble pumping: some studies also observed a very low frequency around $St \sim 0.08$ from the base pressure signals or velocity fluctuations inside the recirculation bubble (Duell & George, 1999; Khalighi *et al.*, 2001; Lahaye *et al.*, 2014; Volpe *et al.*, 2015). The origin of this frequency can be traced back to the study of Berger *et al.* (1990) on the wake past a disk. The authors revealed an axial oscillation of the rear stagnation point of the recirculation bubble from the flow visualization experiments and termed this phenomenon as the bubble pumping.

Although similar dynamics are found in the aforementioned literature, the recirculating flow orientation in the mean wake differs among them and is demonstrated to be very sensitive to perturbations of the experimental setup, slight variation of the cross-sectional geometry and ground clearance (the distance between the model undersurface and ground). Grandemange *et al.* (2013a) systemically studied the impacts of the ground clearance and various aspect ratios H/W (H and W are the model height and width respectively) on the wakes past the blunt-edged models. The main results are highlighted in Fig. 1.7 where the wake symmetry and asymmetry are represented by the probability distributions of the pressure gradients along the spanwise (y) and wall-normal directions (z). The organization of the recirculating flow inside the wake is sketched in the inserted figures. For the case of $H/W = 0.74$ (Ahmed body geometry), increasing the ground clearance breaks the initial symmetric distribution of the lateral wake. Instead, a bi-modal wake appears which is characterized by two preferable asymmetric states switching between them in a stochastic way (Grandemange *et al.*, 2013b) and is associated with the bifurcations in the laminar regime (Grandemange *et al.*, 2012; Rigas *et al.*, 2014). Besides, a residual yaw angle is very likely to trap the wake in one asymmetric state. Concomitantly, the vertical wake is also modified pointing to a close link between the lateral and vertical wake organization. Conversely, at $H/W = 1.34$, the lateral wake remains symmetric with the increasing ground clearance, whereas the bi-modal behavior appears in the wall-normal direction beyond a certain value.

Recently, Barros *et al.* (2017) investigated the effects of the underflow perturbations on the recirculating flow orientation for a square-back car model with $H/W = 0.85$ at a given ground clearance. The perturbations are imposed with passive devices located between the model and the ground. By changing the size of the passive devices, the wall-normal wake transitions from the initially asymmetric topology to a symmetric distribution. Concomitantly, the initially symmetric lateral wake changes to the intermittent bi-modal wake, indicating a competition between the spanwise and wall-normal wake balance. The flow states identified in Grandemange *et al.* (2013b) and Barros *et al.* (2017) prove the high sensitivity of the square-back body wakes and unify the distinct wake topologies observed in the aforementioned literature.

Understanding the wake dynamics and the mean wake topologies is important because on the one hand it inspires the conception of flow control strategies for drag reduction, on the other hand, it constitutes a base for the physical understanding of the control effects throughout the manuscript.

1.3 Flow control

In this section, we give a review on the flow control strategies applied on the bluff body wakes for drag reduction purpose. The focus is placed on the direct wake control of the blunt-edged

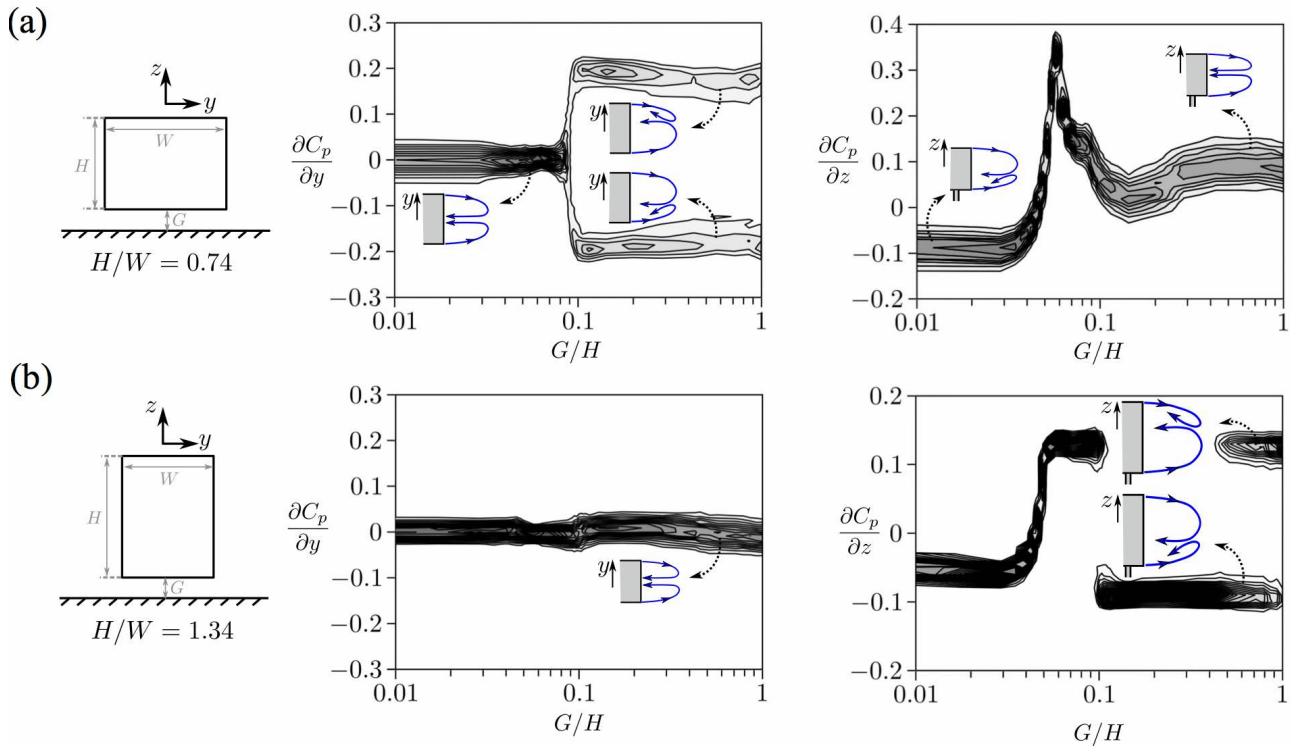


Figure 1.7: Impacts of the ground clearance and cross-sectional geometry on the organization of the mean recirculating flow in the wake (adapted from Grandemange *et al.* 2013a). Figures show the probability density function of the base pressure gradients $\partial C_p/\partial y$ and $\partial C_p/\partial z$ in the spanwise/lateral direction (y) and wall-normal direction (z) respectively as a function of the ground clearance G/H , where C_p is the normalized base pressure, H is the model height, W the width and G the ground clearance. The inserted sketches illustrate the recirculation structures in the wake.

bluff bodies having a fixed separation point.

Flow control can be classified into three groups: passive, active open-loop and active closed-loop controls. Passive control uses actuators without power input to improve the desired performance by imposing a small change of the original configuration. The use of base cavities and boat tails is considered to be one of the most effective and practical passive devices for drag reduction (Choi *et al.*, 2014). Figure 1.8 shows a sketch of the base cavity and boat tail. A base cavity is formed by four downstream extension plates placed around the base perimeter and parallel to the model side surfaces. Successful applications of the base cavity can be found in Duell & George (1993, 1999), Khalighi *et al.* (2001, 2012) and Evrard *et al.* (2016). They reported an increase of the base pressure with a more uniform distribution and a reduction of the wake unsteadiness and turbulence intensities. The recirculation bubble is narrower in Khalighi *et al.* (2001, 2012) and longer in Evrard *et al.* (2016). Ventilated cavities are studied by Howell *et al.* (2012) and García de la Cruz *et al.* (2017b) with a similar observation of the base pressure increase. A boat tail resembles the cavity but the extension plates are tilted inward rendering a slant angle with the model side surfaces. The slanted plates deviate the flow at the trailing edges and lead to a narrower bubble (Khalighi *et al.*, 2012). The base pressure is concomitantly increased. It is shown that the length and slant angle of the boat tail strongly affect the drag-reduction performance (Han *et al.*, 1992; Yi, 2007). Fourrié *et al.* (2011) applied a deflector on the upper edge of a slanted Ahmed body and achieved 9% drag reduction with a deflection angle of about 4° . Although passive devices are effective for drag reduction, their industrial applications are still limited as the extended surfaces are impractical and cannot be ‘turned off’ when not needed.

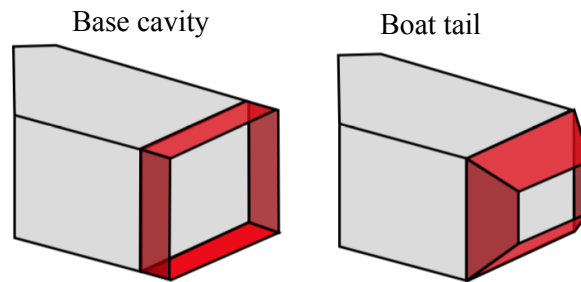


Figure 1.8: Passive control devices: base cavity and boat tail (figure from Barros 2015).

Facing the constraints of passive control devices, studies on active flow control (AFC) using actuators with power input have rapidly emerged in recent decades. AFC can imitate the effects of passive control. In addition, AFC may be turned on or off depending on the requirement. Cattafesta & Shelpak (2011) give an extensive overview of possible actuation mechanisms, whereas Choi *et al.* (2008) present the most common AFC approaches on bluff bodies. AFC can be performed in a predetermined open-loop manner regardless of the flow state. Vehicle models with steady jet blowing at the trailing edges have been investigated by Rouméas *et al.* (2009); Wassen *et al.* (2010) and Littlewood & Passmore (2012). By varying the angle of the jets with respect to the free-stream flow, they concluded that a jet angled into the wake at 45° creates a turning of the flow and leads to a better base pressure recovery than the other investigated angles. The effect is similar to that created by a boat tail, hence such blowing can be considered as a *fluidic boat tail*. Further drag reduction was achieved by coupling the jet with a Coanda surface to create a Coanda effect (Geropp & Odenthal, 2000; Englar, 2001, 2004; Pfeiffer & King, 2012; Khalighi *et al.*, 2012) which deviates the free-stream flow towards the center of the wake region, increasing the pressure on the model base. A main issue of the steady blowing is its high energy investment. Only a few cases in the literature above deliver a positive balance between the gain in drag reduction and the energy spent in driving the jets.

To improve the actuation efficiency, the use of unsteady periodic synthetic or pulsed jets becomes a promising alternative strategy. Actually, their application in flow control gains a satisfactory achievement in recent years (Glezer *et al.*, 2005; Krentel *et al.*, 2010; Park *et al.*, 2013; Joseph *et al.*, 2013; Oxlade *et al.*, 2015; Seifert *et al.*, 2015; Barros *et al.*, 2016*b*). Beyond the benefits in actuation efficiency, the interaction of the unsteady jets at distinct frequencies with the unstable wake dynamics constitutes a key enabler for flow control. As discussed in § 1.2, the convectively unstable shear layers have characteristics of nonlinear amplifiers, thus being sensitive to external forcing at distinct frequencies. This sensitivity can be highlighted by the excited mixing layer submitted to different forcing frequencies (Parezanović *et al.*, 2015), as demonstrated in Fig. 1.9. Excitation at the low frequency $f = 10$ Hz provokes an earlier creation of large-scale structures and increases the layer growth rate, resulting in an enhanced mixing. On the contrary, the high frequency $f = 400$ Hz prevents the formation of the large-scale structures and reduces the growth rate of the mixing layer, leading to a stabilization of the flow. In fact, the forcing at a given frequency is able to govern the growth of the instability wave, therefore the shear layer submitted to different excitations behaves quite distinctly (Fiedler, 1998). Due to the changes in shear layer dynamics, their interactions and the resulting vortex shedding are accordingly modified, so do the mean wake and the related drag. The low-frequency wake control has been demonstrated to either enhance the flow instability manifested by the amplified oscillation of vortex shedding (Glezer *et al.*, 2005; Barros *et al.*, 2016*a*; Gao *et al.*, 2016) or attenuate the instability by destroying the formation of shedding (Pastoor *et al.*, 2008). Conversely, the high frequency forcing is able to stabilize the turbulent wake (Glezer

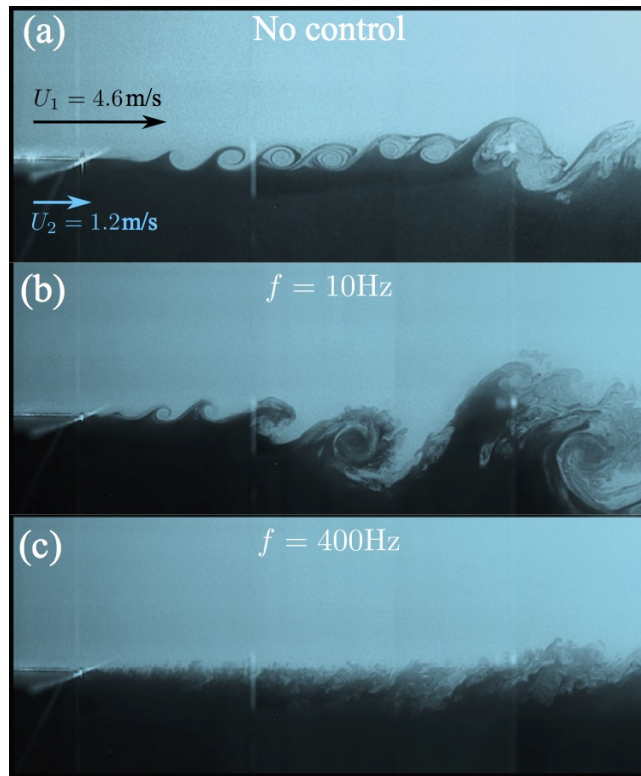


Figure 1.9: Smoke visualization of the effect of pulsed jets on a transient mixing layer (figure reproduced from Parezanović *et al.* 2015). (a) Unforced flow. (b) Excitation at $f = 10 \text{ Hz}$. (c) Excitation at $f = 400 \text{ Hz}$.

et al., 2005; Qubain, 2009; Morrison & Qubain, 2009; Vukasinovic *et al.*, 2010; Oxlade *et al.*, 2015; Barros *et al.*, 2016b). The control enabler is the frequency-crosstalk effect relying on the nonlinear interactions of low-frequency, high-frequency and the dominant modes of the flow. Moreover, similar to the Coanda steady blowing, the combination of passive devices and unsteady actuation has been also developed by numerous studies, such as Chaligné *et al.* (2013); Nayeri *et al.* (2009); Schmidt *et al.* (2015); Barros *et al.* (2016b) and Seifert *et al.* (2016). The main idea is to further increase the performance of the unsteady forcing by coupling it to the Coanda and boat-tailing effects.

Closed-loop control, for which the actuation is determined by the sensors recording the flow state, offers further potential to improve the actuation efficiency by adapting the control to changing flow conditions. An extensive overview of the recent developments of closed-loop turbulence control is given in Brunton & Noack (2015). Depending on the operating timescale of controllers and the required design effort, most literature on closed-loop control falls in one of the four categories presented in Fig. 1.10. There exists a well established framework for the stabilization of laminar flows with in-time model-based control. ‘In-time’ means that the controller operates on the timescale of the physical processes (Brunton & Noack, 2015). The control may be based on a local linearization of the Navier-Stokes equation. Various configurations have been studied, such as boundary layer flow (Liepmann & Nosenchuck, 1982; Bagheri *et al.*, 2009), circular cylinder wake (Roussopoulos, 1993) and open cavity flow (Rowley *et al.*, 2006; Samimy *et al.*, 2007). However, turbulent flow is characterized by broadband frequency dynamics with complex frequency crosstalk: actuation at one frequency may change the whole spectrum of frequencies and thus ultimately affects the mean flow. In this case, a physics-based model-based control logic should be able to distill the complex physical mechanism and its relation to control. This implies that, for many cases, frequency crosstalk needs to be incorporated

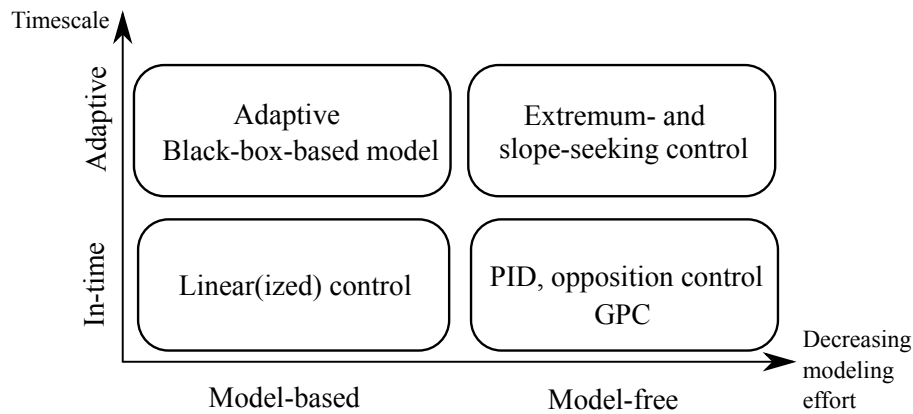


Figure 1.10: Schematic illustrating popular choices for control design (GPC: Genetic Programming Control).

in the model which indeed constitutes a big challenge. Simple examples of such control-oriented models can be found in Luchtenburg *et al.* (2009) and Sipp (2012) which describe an actuation at lower or higher frequency for stabilizing the dominant vortex shedding oscillation. In general, incorporating multiple frequency crosstalks in a model-based control strategy constitutes a significant challenge, both, from a robust modeling and from a control design perspective, due to the difficulties in the mathematical modelling of the nonlinearities and limited knowledge of flow. Nevertheless, model-based feedback control has enjoyed many success stories for weakly and moderately nonlinear dynamics with only a few dominant frequencies. A large portion of the controllers in this case are derived from a reduced-order model, such as Galerkin (Gerhard *et al.*, 2003) or vortex models (Protas, 2004), or simple experimentally obtained input-output black-box models (Becker *et al.*, 2005; Henning & King, 2005, 2007; Dahan *et al.*, 2012). For the latter category, adaptive concepts are quite promising to maintain performance goals under uncertainties (Garwon & King, 2005). ‘Adaptive’ means that the controller operates on a timescale much larger than the physical processes. The response to adaptive control may be adequately modeled by linear or weakly nonlinear dynamics (Pfeiffer & King, 2012) by averaging over many strongly nonlinear frequency crosstalk mechanisms.

Alternatively, closed-loop control has been designed in a model-free manner, where no underlying model is required. Adaptive approaches can be used to find automatically the optimal actuation parameters by a slow feedback of a working open-loop control. Extremum and slope-seeking control are the most widely used adaptive controllers. The former often optimizes the actuation frequency by identifying the extremum with respect to a given cost function, while the latter assures a minimum actuation amplitude to achieve the desired performance. Drag reduction of a bluff body targeting the lowest cost of global energy consumption has been achieved by Beaudoin *et al.* (2006) and Pastoor *et al.* (2008). Although this approach is not in-time, the slow feedback has benefits to maintain the performance despite slowly changing environmental conditions. In-time model-free control may be performed by first specifying a given parameterized control structure, such as PID (Proportional-Integral-Derivative) controller (Zhang *et al.*, 2004), and then employing tuning methodologies to improve performance. Other methods are the physics-based opposition and phase control. This kind of controller often requires a previous understanding of the actuation effects. Examples include the skin-friction reduction in a wall-bounded turbulent flow (Choi *et al.*, 1994) and the stabilization of the wake past a D-shaped body (Pastoor *et al.*, 2008). In more complex configurations with multiple actuators and sensors, no generic simple recipes for the control law can be offered. The challenge of the problem lies on the appropriate selection of actuators, sensors and optimization of control laws under a given specific objective.

Yet, when looking at the flight maneuvers of birds, it is clear that nature has found impressive flow control solutions without apparent knowledge of the flow governing equations or reduced-order modeling. An eagle, for instance, can land gently under gusty wind conditions and in rain by moving its wings and feathers to manipulate fluid forces. This suggests us an alternative way to perform flow control through optimization process emulating nature's evolution. Machine learning, and in particular evolutionary algorithms, can help us to achieve the control goal by mimicking the learning process of nature. The development of evolutionary computation starts from the fundamental work of Holland (1962); Rechenberg (1965); Schwefel (1968) over 50 years ago. With the current advancement of big data and progress of powerful computer techniques, machine learning gets a fertile ground to grow and has been applied in myriad applications of control, modeling and prediction (Dracopoulos & Kent, 1997; Fleming & Purshouse, 2002; Duriez *et al.*, 2016). Genetic algorithms (Holland, 1962) and genetic programming (Koza, 1992) are the two most applied evolutionary algorithms. They can learn and refine an effective control only based on the control performance (cost function) as measured on the control system. Genetic algorithms are employed for the parameter identification of controllers with a given structure like PID controller (Benard *et al.*, 2015). Genetic programming achieves both structure and parameter identification, thus it enables to identify arbitrary nonlinear control laws. In this case, neither a model, nor the control law structure needs to be known. The methodology of solving optimal control problems with methods of genetic programming is referred to as Genetic Programming Control (GPC). This recent topic enables control on challenging nonlinear high-dimensional systems before we are fully able to understand the mechanisms. Successful applications of GPC include the separation control (Gautier *et al.*, 2015; Debien *et al.*, 2016) and mixing layer control (Parezanović *et al.*, 2016). In particular, Duriez *et al.* (2016) have highlighted the merit of GPC by showing the limitations of a linear system identification for the strongly nonlinear mixing layer. They identified a linear input-output model from actuations to sensors data and concluded that the linear model fails to capture the stochastic fluctuations and coherent nonlinear phenomena of the flow.

1.4 Objectives and outline of the thesis

In this study, we aim to develop effective active flow control strategies for drag reduction of a simplified square-back car model in experiments. The actuation is performed by pulsed jets at the trailing edges and the flow is monitored with 16 pressure sensors distributed at the rear side. We address the challenges of nonlinear turbulence control—which is often beyond the capabilities of model-oriented approach—by developing a simple yet powerful model-free control strategy: the data-driven linear genetic programming control (LGPC). LGPC advances the previous GPC by employing linear genetic programming (LGP) as a simpler algorithm for the control of multiple-input multiple-output systems. The control problem is formulated as an optimization problem: find a control logic which optimizes a given cost function as the drag reduction. This optimization is performed by LGP which enables to explore and evolve control laws in a high-dimensional control search space by learning from the training data of experiments. No or little prior knowledge about the controller is required for LGPC. The innovation in this work is a very general ansatz for the control search space which includes multi-frequency forcing, sensor-based feedback including also time-history information feedback and combinations thereof, thus any perceivable control logic can be constructed.

We apply LGPC on the drag control experiments of the square-back car model. The investigated wake presents a lateral symmetry and a wall-normal asymmetry due to the ground effect. This wake was studied previously by Barros *et al.* (2016b) using periodic forcing. The aim of this study is to explore further drag reduction by searching control laws in a control space

more general than periodic forcing. On the other hand, we also investigate the turbulent wakes having a lateral asymmetry: an intermittent bi-modal wake at zero yaw and an asymmetric wake at a moderate yaw angle of 5 degrees. Periodic forcing is first performed on these flows to be compared with other control strategies. From the flow responses to the periodic forcing tests, we infer a physics-based controller with a given structure for each asymmetric wake. A parametric study with respect to the actuation frequency is performed to identify the optimal parameter in the inferred control law. In particular, for the yawed configuration, LGPC is also applied targeting drag reduction and the results are compared with those obtained with the physics-based approach.

The outline of the thesis is as follows. The manuscript is separated into two parts with respect to the two control strategies mentioned above. Part I introduces the design of LGPC and demonstrates its application on the stabilization of a forced nonlinearly coupled three-oscillator model (Chapter 2) and on the drag control experiments (Chapter 3). The three-oscillator model illustrates that frequency crosstalk between actuation and dynamics can be the only enabling mechanism for stabilization — as typical in turbulence control. Moreover, the system comprises open- and closed-loop stabilization mechanisms, foreshadowing another feature of the studied experiment. Chapter 3 pursues the drag reduction of the square-back car model using LGPC in experiments. The additional challenges compared to the dynamical system comprise the high-dimensional dynamics, time delays, high-frequency noise, low-frequency drifts and implementation of the algorithm in the experimental hardware. These factors have been automatically exploited by LGPC. Additionally, we justify the optimization of LGPC by studying in-depth the actuation mechanisms associated with the optimal control law.

Part II applies the physics-based control building on the prior knowledge derived from the periodic forcing tests. In Chapter 4, an opposition feedback control is proposed to suppress the bi-modal behavior of the wake. We give a detailed analysis of the base pressure recovery mechanisms from which the pros and cons of the control are learned. Chapter 5 extends the drag reduction problem to the small yaw angle configuration. We come up with a bi-frequency forcing strategy which outperforms the single-frequency forcing and explores the actuation mechanisms that can not be achieved by the latter. In addition, a comparison between LGPC and the bi-frequency forcing is addressed.

Finally, we summarize in Chapter 6 the main results and provide an outlook of future works to improve and generalize the present approach.

PART I

Linear genetic programming control

Chapter 2

Design of linear genetic programming control

Most of the following contents are presented in Li et al. (2017b).

In this chapter we discuss the central topic of this part: the use of linear genetic programming control (LGPC) for the optimization of control laws in a high-dimensional search space. We present the concept of LGPC, its implementation details on complex systems with multiple actuators and sensors, and a visualization method to draw a landscape of the discovered control laws for further investigations. In addition, we apply LGPC on an illustrative example—a forced nonlinearly coupled three-oscillator model—to demonstrate the performance of LGPC and to foreshadow the complex frequency crosstalk in turbulent flows.

Contents

2.1	Linear genetic programming control	17
2.1.1	Control problem	18
2.1.2	Ansatz for the control law	18
2.1.3	Linear genetic programming control	19
2.1.4	Visualization of control laws	23
2.2	Application on a three-oscillator model	24
2.2.1	Problem formulation	24
2.2.2	Open-loop periodic forcing	26
2.2.3	Results of LGPC	27
2.2.4	Control landscape for LGPC-3	33
2.3	Summary	34

2.1 Linear genetic programming control

Following Duriez *et al.* (2016), the control design is formulated as a regression problem: find the control law which optimizes a given cost function. We employ linear genetic programming as a powerful and general regression method for nonlinear functions and for potential multiple extrema of the cost function. In § 2.1.1, a general control problem is formulated. In § 2.1.2, we introduce a matrix as simple control law representation. This law will be evolved with linear genetic programming (LGP) described in § 2.1.3. This evolution is visualized with classical multidimensional scaling method as outlined in § 2.1.4.

2.1.1 Control problem

We consider a multiple-input multiple-output (MIMO) system with the state $\mathbf{a} \in \mathbb{R}^{N_a}$, an input vector $\mathbf{b} \in \mathbb{R}^{N_b}$ commanding actuation and an output vector $\mathbf{s} \in \mathbb{R}^{N_s}$ sensing the state. Here, N_a , N_b and N_s denote the dimension of the state, the number of actuators and sensors, respectively. The general form of the system reads

$$\frac{d\mathbf{a}}{dt} = \mathbf{F}(\mathbf{a}, \mathbf{b}) \quad (2.1a)$$

$$\mathbf{s} = \mathbf{G}(\mathbf{a}) \quad (2.1b)$$

$$\mathbf{b} = \mathbf{K}(\mathbf{s}). \quad (2.1c)$$

The control \mathbf{b} directly affects the state \mathbf{a} through a general nonlinear propagator \mathbf{F} . \mathbf{G} is a measurement function comprising the sensor signals \mathbf{s} as function of the state \mathbf{a} . The control objective is to construct a MIMO controller $\mathbf{b} = \mathbf{K}(\mathbf{s})$ so that the system has a desirable behaviour. Most control objectives can be formulated in a cost function $J(\mathbf{a}, \mathbf{b})$. The definition of J depends on the control goal. For instance, in a drag reduction problem, we define J as the drag power penalized by the actuation power.

The aim is to find the control law $\mathbf{b} = \mathbf{K}(\mathbf{s})$ which optimizes a given cost function J . The cost only depends on the control law, or, symbolically $J(\mathbf{K}(\mathbf{s}))$ for a well-defined initial value problem or statistically stationary actuation response. Summarizing, the control task is transformed to an optimization problem via cost minimization and is equivalent to finding \mathbf{K}^{opt} such that

$$\mathbf{K}^{\text{opt}}(\mathbf{s}) = \underset{\mathbf{K}}{\operatorname{argmin}} J(\mathbf{K}(\mathbf{s})). \quad (2.2)$$

2.1.2 Ansatz for the control law

A control law maps N_s sensor signals into N_b actuation commands. For simplicity, we assume a single-input plant, i.e. $N_b = 1$. Following linear genetic programming (Brameier & Banzhaf, 2007), we assume this control law can be represented by a given maximum number of *instructions*. These instructions change the content of N_r *registers*, r_1, \dots, r_{N_r} . The registers may be variables or constants. As concrete example, we assume that the first N_s registers are initialized with the sensor signals, the next $N_b = 1$ register represents the actuation command, initially zero, and the next registers contain N_c constants. These constants are the same for all considered control laws in one optimization.

An instruction includes an *operation* on one or two registers and assigns the result of the operation to a *destination register*, e.g., the instruction $r_1 := r_2 + r_3$ includes two operands, the registers r_2 and r_3 , and assigns the result to r_1 . One instruction with two operands can be coded as an array of four integers referring to the two operands, the operator and the destination register, respectively. Note that for the instruction with one operand only an array of three integers is required. However, to maintain a unified representation, a fourth integer is equally assigned but ignored. Consequently, the set of N_i instructions can be coded as a matrix \mathcal{M} with dimension $N_i \times 4$. An example with $N_i = 5$ is presented in Fig. 2.1. Constant registers are write-protected. This means that the constants cannot be destination registers and their values are initialized at the beginning of a run from a user-defined range. One or more variable registers are defined as output register(s). The remaining variable registers are referred to as input registers. For the decoding, the input registers are initialized by the sensor values and the output register(s) by zero. The destination registers are updated after each instruction. After executing all the instructions, the final expression of the output register yields the control law K . This matrix representation can interpret the instructions efficiently by casting the integer

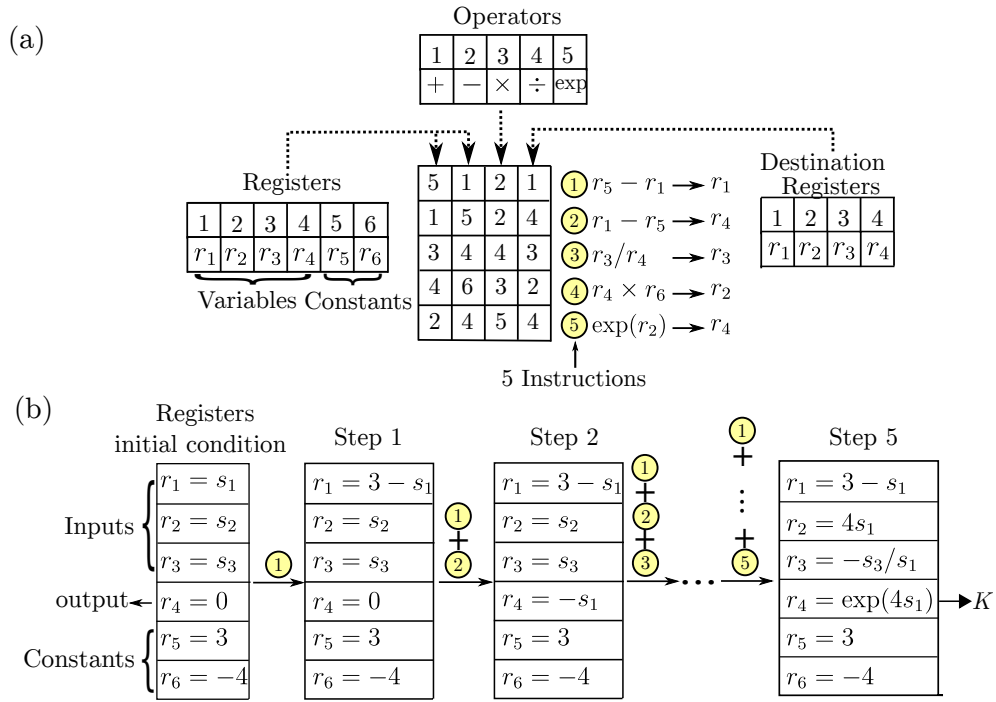


Figure 2.1: (a) An example of matrix \mathcal{M} comprising five instructions ($N_i = 5$). The matrix is displayed in the centre of the figure. The five instructions are shown on the right side of the matrix. Let $\mathcal{R} = \{r_1, r_2, r_3, r_4, r_5, r_6\}$ denotes the set of registers, indexed by the integer numbers $\{1, \dots, 6\}$. The first four registers are variables, i.e. they can be assigned a new value. The last two registers are constants and therefore write-protected. The operand(s) of instructions are coded in the first two columns of the matrix. They can assume any value from $\{1, \dots, 6\}$. The operator set $\mathcal{O} = \{+, -, \times, \div, \exp\}$ is indexed by an integer number $\{1, \dots, 5\}$ and coded in the third column of the matrix. The last column encodes the destination registers, which can be one of the variables from $\{r_1, \dots, r_4\}$. (b) Interpretation of the matrix \mathcal{M} . In this example, we have three input registers $\{r_1, r_2, r_3\}$ and one output register r_4 . Input registers are initialized by the sensors and output register by zero. Step 1 shows the updated registers after implementing the first instruction. Based on this result, we implement the second instruction and obtain the updated result in step 2, etc. The final expressions are obtained after implementing all five instructions. The expression of output register r_4 is the targeted function K .

values.

There is only a finite number of control laws for a given number of registers N_r , of operations N_o and of constants N_c :

$$[N_r \times N_r \times N_o \times (N_r - N_c)]^{N_i}.$$

This number is, however, astronomical, even accounting for different matrices leading to the same control law. Already the simple matrix of Fig. 2.1 has over 1.9×10^{14} different realizations. Despite the discrete nature of possible control laws, almost any reasonably smooth control law can be approximated by such a set of instructions with suitable number of instructions.

Evidently, an exhausting search of control laws and testing in an experiment is not an option. Instead, we optimize the control laws by employing linear genetic programming (LGP) as powerful evolutionary search algorithm. The optimization process of LGP is provided in the following section.

2.1.3 Linear genetic programming control

The employed control optimization has many similarities with GPC (Duriez *et al.*, 2016) using the classical tree-based genetic programming (TGP) by Koza (1992). In this work, we advance

GPC with simpler LGP as regression method. TGP and LGP are equivalent in the sense that any LGP-law can be expressed in TGP and vice versa. The difference is the linear versus recursive coding of LGP and TGP, respectively. The function in TGP is represented as a recursive tree, as shown in Fig. 2.2. The root holds the output variable, each branching node is an elementary operator, such as $+$, $-$, \times , \div , and leaves hold the sensor inputs and constants. The control law b is obtained by expressing the tree in a recursive way. Instead, LGP represents

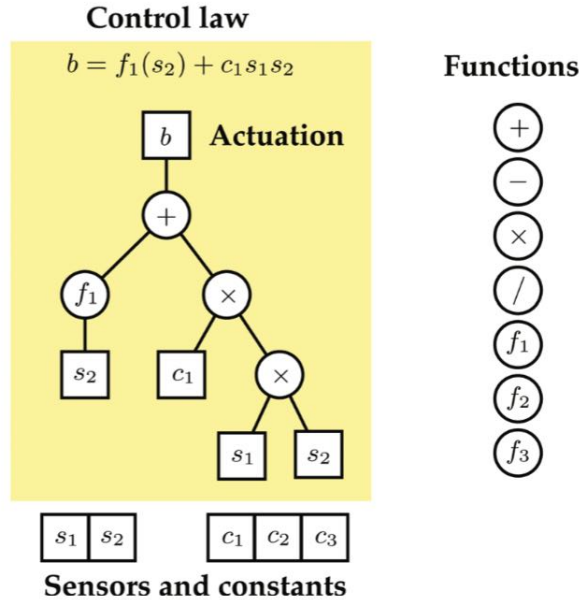


Figure 2.2: Illustration of function tree representation used in TGP. Figure from Brunton & Noack (2015).

a function with a sequence of instructions (see Fig. 2.1). The term *linear* in LGP refers to the linear sequence of instructions, and not to superposition principle like in differential equations. We select LGP over TGP based on two reasons. First, multiple usage of register contents results into a graph-based data flow which permits a more compact solution than the tree-based structure. In addition, by simply changing the number of input and output registers, LGP is applicable to systems with multiple actuators and multiple sensors. The linear instructions are much easier to code and implement in this case than the tree-based counterpart. Second, in LGP, special noneffective and effective codes coexist. The noneffective code refers to the instructions not having an impact on the program output, e.g. the third instruction $r_3 := r_3/r_4$ in Fig. 2.1(a). The omission of this instruction will not modify the final output $r_4 = \exp(4s_1)$. The noneffective code is considered to be beneficial. It protects the effective code from bad variation effects of genetic operations and allows the variations to remain neutral in terms of performance. Given these attributes, we choose LGP over TGP to perform this study. As presented before, we refer to this method as *linear genetic programming control* (LGPC).

The implementation of LGPC for closed-loop control is sketched in Fig. 2.3. The real-time control process occurs in the inner loop with a control law proposed by LGPC. The control law is evaluated in the dynamical system during an evaluation time T . Then, a cost J is attributed to it quantifying the performance of the control law. The cost value J for each control law is sent to LGPC through a slow outer loop where LGPC can learn from them and evolve these laws.

The learning process is detailed in the lower part of Fig. 2.3. An initial population of control law candidates, called *individuals*, is generated randomly like in a Monte-Carlo method, corresponding to the first exploration of the search space. Each individual is evaluated in

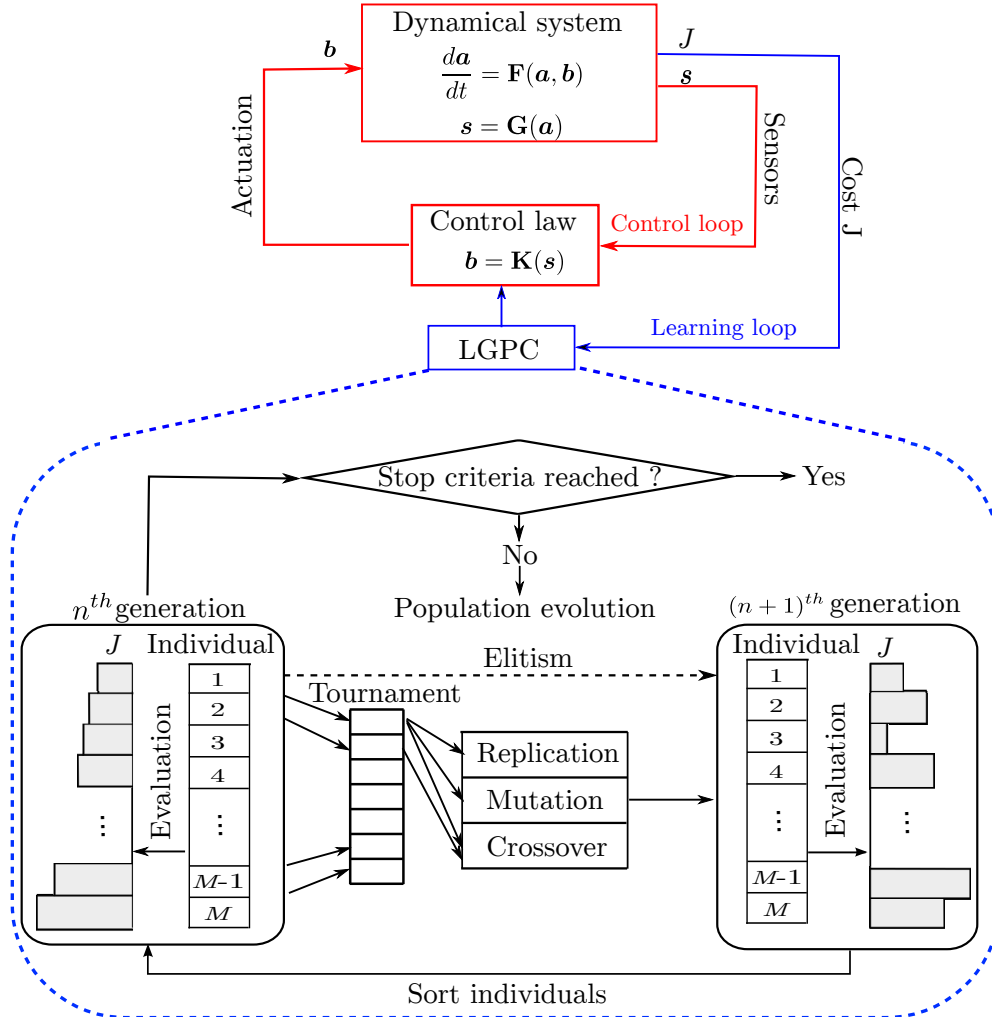


Figure 2.3: LGPC implementation. The real-time closed-loop control is performed in the inner loop (red lines). The control plant feeds back the sensor output \mathbf{s} to the control law. This control law proposed by LGPC computes the actuation command based on \mathbf{s} and sends it to the plant. A cost J is attributed to the control law after its evaluation during the time T . In the outer learning loop, LGPC uses these costs J to evolve the new population of control laws. The LGPC learning process is depicted in the lower part. On the leftmost side, an evaluated generation with M individuals is sorted in ascending order based on J . If the stopping criterion is met, the learning process is terminated. If not, the next generation (on the rightmost side) is evolved by genetic operators (elitism, replication, mutation, and crossover). After being evaluated, this generation is sorted as indicated by the arrow at the bottom. We repeat the process from left to right until the stopping criterion is met.

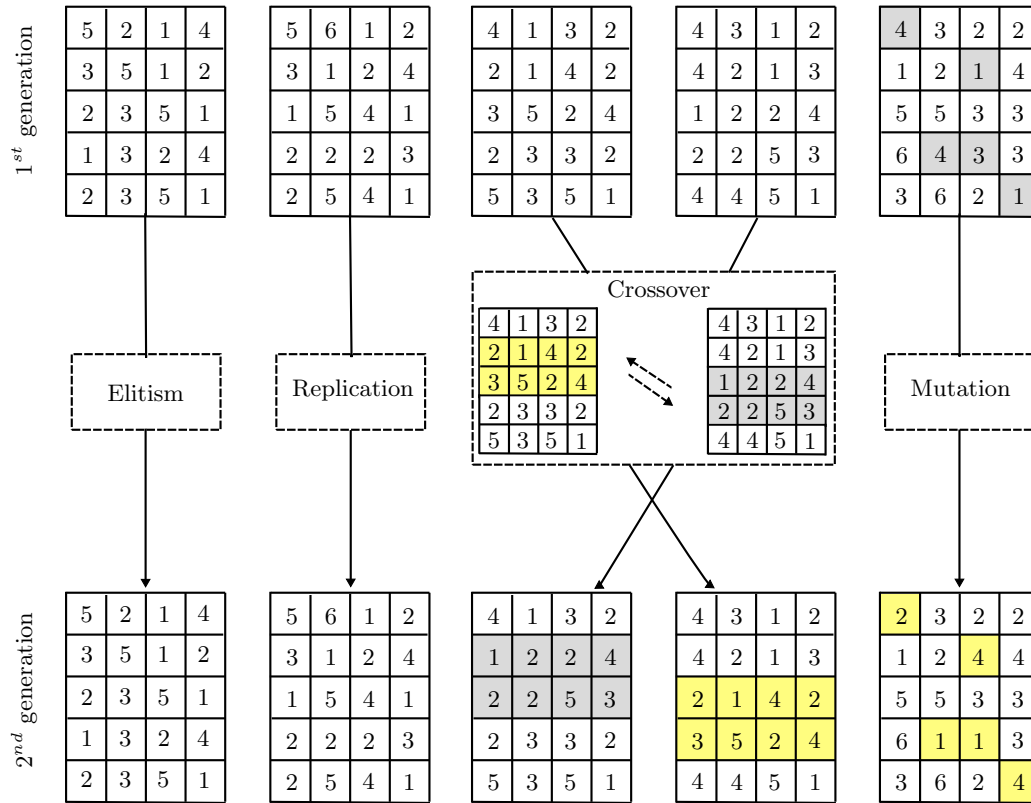


Figure 2.4: A simple example showing the realization of genetic operations on the individuals for a fixed number of instructions.

the inner loop and a cost J is attributed to them. After the whole generation is evaluated, its individuals are sorted in ascending order based on J . The next generation of individuals is then evolved from the previously evaluated one by genetic operators (elitism, replication, crossover, and mutation). Elitism is a deterministic process which copies a given number of top-ranking individuals directly to the next generation. This ensures that the next generation will not perform worse than the previous one. The remaining genetic operations are stochastic in nature and have specified selection probabilities. The individual(s) used in these genetic operators is (are) selected by a tournament process: N_t randomly chosen individuals compete in a tournament and the winner (based on J) is selected. Replication copies a statistically selected number of individuals to the next generation. Thus better performing individuals are memorized. Crossover involves two statistically selected individuals and generates a new pair of individuals by exchanging randomly their instructions. This operation contributes to breeding better individuals by searching the space around well-performing individuals. In the mutation operation, random elements in the instructions of a statistically selected individual are modified. Mutation serves to explore potentially new and better minima of J . These genetic operations are directly applied to the matrices as depicted in Fig. 2.4. After the new generation is filled, the evaluation of this generation can be pursued in the plant. This learning process will continue until some stopping criterion is met. There is no mathematically assured convergence for LGPC. Different stopping criteria are used. Ideally, the process is stopped when a known global minimum is obtained (which is unlikely in an experiment). Alternatively, the evolution terminates upon too slow improvement from one generation to the next or when a predefined maximum number of generations is reached. By definition, the targeted optimal control law is the best individual of the last generation.

LGPC can also be used to explore open-loop control by including time-periodic functions \mathbf{h}

in the inputs of control law, i.e. $b = K(\mathbf{h})$. This method permits to search a much more general multi-frequency control which is hardly accessible to a parametric study of single frequency. Furthermore, the range of LGPC can be extended by comprising both the sensors \mathbf{s} and time-periodic functions \mathbf{h} into the inputs of K . This results in a non-autonomous control law $b = K(\mathbf{s}, \mathbf{h})$. This generalization permits to select between open-loop actuation $b = K(\mathbf{h})$, sensor-based feedback $b = K(\mathbf{s})$ or combinations thereof $b = K(\mathbf{s}, \mathbf{h})$ depending on which performs better. In the following, we term the approach optimizing open-loop frequency combinations $b = K(\mathbf{h})$ as LGPC-1. The approach to optimize autonomous controllers $b = K(\mathbf{s})$ is referred to as LGPC-2. The generalized non-autonomous control design $b = K(\mathbf{s}, \mathbf{h})$ is denoted as LGPC-3.

2.1.4 Visualization of control laws

LGPC systematically explores the control law space by generating and evaluating a large number of control laws from one generation to the next. An assessment of the similarity of control laws gives additional insights into their diversity and convergence to optimal control laws, i.e. into the explorative and exploitative nature of LGPC. For that purpose, we rely on Multidimensional Scaling (MDS) (Mardia *et al.*, 1979), a method classically used to visualize abstract data in a low-dimensional space. The main purpose of MDS is to visualize the (dis)similarity of objects or observations. MDS comprises a collection of algorithms to detect a meaningful low-dimensional embedding given a dissimilarity matrix. Here, we employ Classical Multidimensional Scaling (CMDS) which originated from the works of Schoenberg (1935) and Young & Householder (1938).

Let us define N_K as the number of objects to visualize, and $\mathbf{D} = (D_{ij})_{1 \leq i, j \leq N_K}$ as a given distance matrix of the original high-dimensional data. The aim of CMDS is to find a centred representation of points $\mathbf{\Gamma} = [\gamma_1 \ \gamma_2 \ \dots \ \gamma_{N_K}]$ with $\gamma_1, \dots, \gamma_{N_K} \in \mathbb{R}^r$, where r is typically chosen to be 2 or 3 for visualization purposes, such that the pairwise distances of the points approximate the true distances, i.e. $\|\gamma_i - \gamma_j\|_2 \approx D_{ij}$. The details of the implementation are given in Appendix A.

We choose to visualize all control laws in a two-dimensional space $r = 2$. Thus, the number of objects is $N_K = M \times N$, where M is the number of individuals in a generation, and N is the total number of generations. The distance between two control laws b_i and b_j , $i, j \in \{1, \dots, N_K\}$ shall measure their ‘effective difference’. Let us consider the non-autonomous feedback $b_i = b_i(\mathbf{s}_i, \mathbf{h}_i)$. Here, $\mathbf{s}_i(t)$ denotes the sensor reading and $\mathbf{h}_i(t)$ the harmonic control input on the corresponding b_i -forced system. The squared difference between b_i and b_j is defined as

$$D_{ij}^2 = \frac{1}{2} \left(\overline{|b_i(\mathbf{s}_i(t), \mathbf{h}_i(t)) - b_j(\mathbf{s}_i(t), \mathbf{h}_i(t))|^2 + |b_i(\mathbf{s}_j(t), \mathbf{h}_j(t)) - b_j(\mathbf{s}_j(t), \mathbf{h}_j(t))|^2} \right) + \alpha |J_i - J_j|. \quad (2.3)$$

The time average of the first term in Eq. (2.3), represented by the overbar, is taken over the sensor reading \mathbf{s}_i and harmonic input \mathbf{h}_i of the control law b_i , and \mathbf{s}_j and \mathbf{h}_j of the control law b_j in the evaluation time interval. The permutation of control laws b_i and b_j with its arguments guarantees that the distance matrix is symmetric. More importantly, this ensures that the control laws are compared in the relevant sensor space with an equal probability of both forced systems.

The second term in Eq. (2.3) penalizes the difference of their achieved costs J with coefficient α . The penalization coefficient α is chosen as the ratio between the maximum difference of two control laws (first term of D_{ij}^2) and the maximum difference of the cost function (second term of D_{ij}^2). Thus, the dissimilarities between control laws and between the cost functions have

comparable weights in the distance matrix D_{ij} . This penalization evidently smoothes the control landscape.

A problem may arise for the comparison of two pure open-loop forcings b_i and b_j . We expect, for instance, that $b_i = \cos(t)$ and $b_j = \sin(t)$ give rise to the same actuation response modulo a time shift $\tau = \pi/2$ and would consider these control laws as equivalent. Even for sensor-based feedback enriched by harmonic input, we expect the actuation response to be 'in phase' or synchronized with the harmonic input. This expectation is taken into account by minimizing the difference between two control commands modulo a time shift:

$$D_{ij}^2 = \min_{\tau} \left(\frac{1}{2} \left(|b_i(\mathbf{s}_i(t), \mathbf{h}_i(t)) - b_j(\mathbf{s}_i(t-\tau), \mathbf{h}_i(t-\tau))|^2 + |b_i(\mathbf{s}_j(t), \mathbf{h}_j(t)) - b_j(\mathbf{s}_j(t-\tau), \mathbf{h}_j(t-\tau))|^2 \right) + \alpha |J_i - J_j| \right) \quad (2.4)$$

Evidently, Eq. (2.3) and Eq. (2.4) coincide at $\tau = 0$.

Summarizing, the square of the distance matrix $\mathbf{D}^2 = (D_{ij}^2)$ is defined as follows:

- (1) If both control laws have non-trivial harmonic input (are non-autonomous), Eq. (2.4) defines the distance.
- (2) Otherwise, Eq. (2.3) is employed.

Applying CMDS to the distance matrix \mathbf{D} , each control law b_i is associated with a point $\boldsymbol{\gamma}_i = (\gamma_{i,1}, \gamma_{i,2})$ such that the distance between different $\boldsymbol{\gamma}_i$ emulates the distance between control laws defined by Eq. (2.3) and Eq. (2.4). More generally, $\boldsymbol{\gamma}_i$ are feature vectors, the coefficients of which represent those features that contribute most on average to the discrimination of different control laws.

2.2 Application on a three-oscillator model

Before implementing LGPC in experiments, we first apply it on a well-defined dynamical system to illustrate its performance in resolving complex problems. The aim is to stabilize a forced dynamical system with three nonlinearly coupled oscillators at three incommensurable frequencies extending the generalized mean-field model (Luchtenburg *et al.*, 2009) (see Chapter 5 of Duriez *et al.* 2016). Figure 2.5 gives a sketch illustrating the dynamics of the three-oscillator model. The goal is to stabilize the first unstable, amplitude-limited oscillator, while the forcing is performed on the second and third oscillator. The second oscillator has also unstable, amplitude-limited dynamics and destabilizes the first oscillator. The third oscillator has linear stable dynamics and has a stabilizing effect on the first. The stabilization of the first oscillator can be performed by closed-loop suppression of the second oscillator or open-loop excitation of the third one. In the following, we formulate the control problem mathematically (§ 2.2.1), parametrically explore the effect of periodic forcing like in many turbulence control experiments (§ 2.2.2), and apply LGPC (§ 2.2.3).

2.2.1 Problem formulation

The system has three oscillators at frequency $\omega_1 = 1$, $\omega_2 = \pi$ and $\omega_3 = \pi^2$, the coordinates of which being (a_1, a_2) , (a_3, a_4) and (a_5, a_6) , respectively. The evolution equation of the state

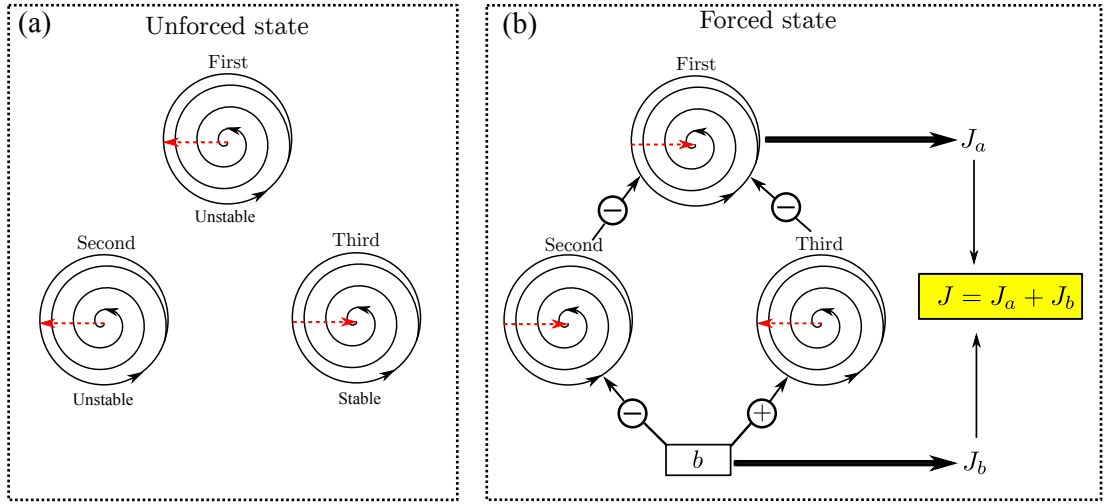


Figure 2.5: Illustration of the three-oscillator model: (a) unforced state and (b) forced state. The red dashed arrows indicate the trend of the oscillator amplitudes at unforced and forced states respectively. The sign ‘-’ and ‘+’ in (b) represent the suppression and excitation of oscillators, respectively.

$\mathbf{a} = (a_1, a_2, \dots, a_6)$ reads:

$$\begin{aligned}
 \frac{da_1}{dt} &= \sigma_1 a_1 - \omega_1 a_2 & \frac{da_3}{dt} &= \sigma_2 a_3 - \omega_2 a_4 & \frac{da_5}{dt} &= \sigma_3 a_5 - \omega_3 a_6 \\
 \frac{da_2}{dt} &= \sigma_1 a_2 + \omega_1 a_1 & \frac{da_4}{dt} &= \sigma_2 a_4 + \omega_2 a_3 + b & \frac{da_6}{dt} &= \sigma_3 a_6 + \omega_3 a_5 + b \\
 \sigma_1 &= -r_1^2 + r_2^2 - r_3^2 & \sigma_2 &= 0.1 - r_2^2 & \sigma_3 &= -0.1 \\
 \omega_1 &= 1 & \omega_2 &= \pi & \omega_3 &= \pi^2,
 \end{aligned} \tag{2.5}$$

where $r_1^2 = a_1^2 + a_2^2$, $r_2^2 = a_3^2 + a_4^2$ and $r_3^2 = a_5^2 + a_6^2$ denote the fluctuation level of the three oscillators, respectively. The growth rate for each oscillator is denoted by $\sigma_i, i = 1, \dots, 3$. The frequency for each oscillator is denoted by $\omega_i, i = 1, \dots, 3$. Without forcing $b \equiv 0$, the first and second system are linearly unstable with asymptotic amplitudes $r_1^u = r_2^u = \sqrt{0.1}$. Here, and in the following, the superscript ‘ u ’ refers to asymptotic values for unforced dynamics. The third system is linear and stable, i.e. converges to the vanishing amplitude $r_3^u = 0$. The forcing b is only applied on the second and third oscillators. A linearization of Eqs. (2.5) around the fixed point $\mathbf{a} = \mathbf{0}$ yields three uncoupled oscillators thus makes the first oscillator uncontrollable.

The effect of the forcing on the first oscillator can be inferred from the growth rate formula for σ_1 (see first column in Eqs. (2.5)). The fluctuation level r_2 of the second system destabilizes the first oscillator, while the third system stabilizes it with increasing fluctuation level r_3 . Hence, stabilization of the first oscillator may be achieved by exploiting one of two frequency crosstalk mechanisms: stabilizing the second system or exciting the third one. The stabilization of the second system requires feedback $b = K(\mathbf{a})$ while excitation of the stable oscillator can be performed with periodic forcing $b(t) = B \sin(\pi^2 t)$ at the resonance frequency and sufficiently large amplitude B .

The cost function to be minimized is the averaged energy of the unstable oscillator $J_a = \overline{a_1^2 + a_2^2}$ penalized by the actuation cost $J_b = \overline{b^2}$. Here, the temporal averaging is indicated by the overbar. Without forcing, $J_a^u = (r_1^u)^2$ and $J_b \equiv 0$. We normalize the total cost by the unforced value J_a^u of the first oscillator to characterize the relative benefit of actuation:

$$J = \frac{J_a + J_b}{J_a^u}. \tag{2.6}$$

By definition, $J = 1$ for the unforced system.

The numerical evaluation of J is based on the integration of the dynamical system Eq. (2.5) with the initial condition $\mathbf{a}(0) = (0.1, 0, 0.1, 0, 0.1, 0)$ at $t = 0$. In the first 10 periods of the target oscillator, i.e. for $t \in [0, t_0]$ with $t_0 = 10 \frac{2\pi}{\omega_1} = 20\pi$, no forcing is applied and the system converges to unforced quasi-periodic dynamics $(r_1^u)^2 = 0.1$, $(r_2^u)^2 = 0.1$, $r_3^u = 0$. The cost functional is evaluated in the next 500 periods, $t \in [20\pi, 1020\pi]$. This time interval contains an actuated transient but is dominated by the post-transient dynamics, thus sufficient for statistical averaging.

2.2.2 Open-loop periodic forcing

First, open-loop periodic forcing is studied, following a practice of many turbulence control experiments. The goal is to minimize the cost function Eq. (2.6) with periodic forcing $b(t) = B \sin(\omega t)$ employing a parametric variation of the amplitude B and frequency ω in the range of $[0, 1]$ and $[0, 4\pi]$, respectively. The performance (Eq. (2.6)) at amplitude B and frequency ω is scanned with increments 0.01 and 0.01π , respectively. The corresponding colormap of J is shown in Fig. 2.6. This figure displays a local minimum of $J^\circ = 0.031$. The corresponding parameters are denoted by the superscript ‘ \circ ’ in the following. The low value indicates a stabilization by over one order of magnitude in the fluctuation level, accounting for the actuation expense. The minimum J is reached at the eigenfrequency of the third oscillator $\omega^\circ = \pi^2$, as $\sigma_1 < 0$ for $r_3^2 > 0.1$, numerically observing that the second oscillator is hardly affected by the forcing at a non-resonant frequency, $r_2^\circ \approx r_2^u = \sqrt{0.1}$. The optimal amplitude $B^\circ = 0.07$ is numerically determined as the best trade-off between the achieved stabilization and actuation cost. This amplitude leads to $r_3^2 \approx 0.12$ and $\sigma_1 \approx -0.02$. For a larger time evaluation horizon, the current results suggest a better performance at lower actuation $B \approx 0.05$ leading to $r_3^2 \approx 0.1$ which just neutrally stabilizes the first oscillator $\sigma_1 \approx 0$, exploiting that the second oscillator is unaffected by forcing. The corresponding analytical approximations are described in Chapter 5 of Duriez *et al.* (2016).

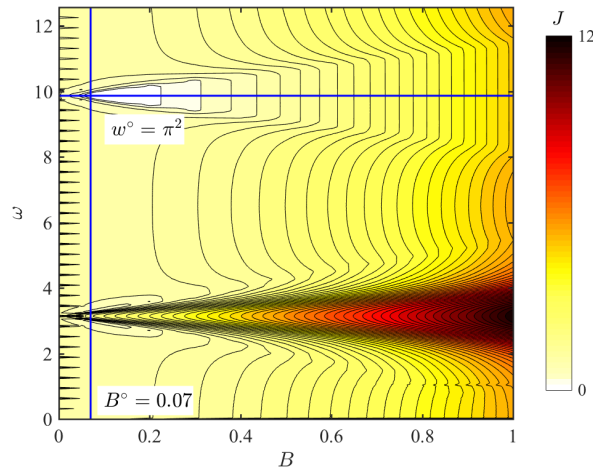


Figure 2.6: Colormap of cost value J under the periodic forcing $b(t) = B \sin(\omega t)$.

On the other hand, the maximal J value is associated with the forcing at the eigenfrequency of the second oscillator $\omega_2 = \pi$, as the excitation of r_2 leads to $\sigma_1 > 0$, resulting in an increase of r_1 . These results show that the enabler of open-loop control is the third oscillator rather than the second.

The unforced transient and actuated dynamics of the system are illustrated in Fig. 2.7 under the optimal periodic forcing $b^\circ(t) = 0.07 \sin(\pi^2 t)$. The unforced state during the time window

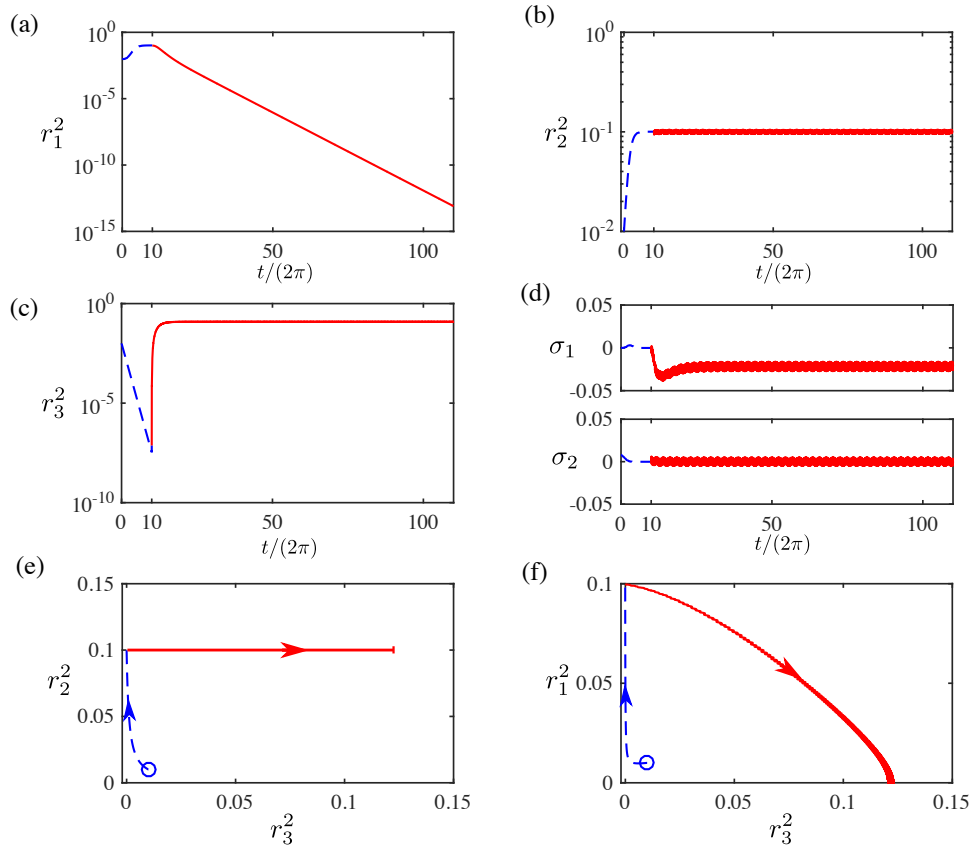


Figure 2.7: Dynamics of the model system Eq. (2.5) with the optimal periodic forcing $b^\circ(t) = 0.07 \sin(\pi^2 t)$ applied at $t/(2\pi) \geq 10$. Unforced state: blue dashed line; forced state: red line. (a-d) Time evolution of r_1^2 , r_2^2 , r_3^2 , σ_1 and σ_2 . Only the first 110 periods are shown here for clarity. (e) Phase portrait of r_2^2 against r_3^2 and (f) r_1^2 against r_3^2 . The circle indicates the initial point and the arrows the time direction.

$t \in [0, 20\pi]$ is depicted by a blue dashed line and the forced one at $t > 20\pi$ by a red curve. For clarity, only the first 110 periods are shown in Fig. 2.7 (a-d). Figure 2.7 (e,f) cover the whole time interval $t \in [0, 1020\pi]$. When unforced, the unstable oscillators self-amplify towards the limit cycle $(r_1^u)^2 = (r_2^u)^2 = 0.1$, whilst the stable oscillator vanishes to $(r_3^u)^2 = 0$. Convergence is implied by $\sigma_1 = 0$ and $\sigma_2 = 0$. Once b starts at $t_0 = 20\pi$, r_3 is rapidly excited to an energy level of $r_3^2 = 0.12$, while r_2 keeps its original fluctuation level $r_2^2 = 0.1$. The resulting system yields $\sigma_1 < 0$ which leads consequently to the stabilization of (a_1, a_2) , i.e. $r_1^2 \approx 0$. The phase portraits in Fig. 2.7(e) and (f) illustrate the interactions between different oscillators. The circle indicates the initial point and the arrows the time direction. The forced trajectories represent low-pass filtered data, i.e. do not resolve cycle-to-cycle variation. In particular, Fig. 2.7(f) shows clearly that r_1^2 decreases with the increase of r_3^2 , corroborating that a high-frequency forcing stabilizes a low-frequency unstable oscillator via frequency crosstalk.

2.2.3 Results of LGPC

LGPC is applied to solve the control problem of § 2.2.1. For all LGPC tests, up to $N = 50$ generations with $M = 500$ individuals in each are evaluated. Hereafter, we denote the cost value of the m th individual in the n th generation by J_m^n ($m = 1, \dots, M; n = 1, \dots, N$). After generating the individuals, each is pre-evaluated based on the state \mathbf{a} of the unforced system. The resulting actuation command is an indicator for their feedback control performance. If

Parameters	Value
Population size	$M = 500$
Total generation	$N = 50$
Tournament size	$N_t = 7$
Elitism	$N_e = 1$
Replication	$P_r = 10\%$
Crossover	$P_c = 60\%$
Mutation	$P_m = 30\%$
Min. instruction number	2
Max. instruction number	30
Operations	$+, -, \times, \div, \sin, \cos, \tanh, \ln$
Number of constants	$N_c = 6$
Constant range	$[-10, 10]$

Table 2.1: LGPC parameters for the three-oscillator model.

no actuation ($b = 0, \forall t$) is obtained in the pre-evaluation, this individual cannot change the unforced state. As a consequence, the individual is not subjected to a testing and is assigned a high cost value. This pre-evaluation step saves numerical testing time. Additionally, the actuation command is limited to the range $[-1, 1]$ to emulate an experimental amplitude-bounded actuator.

The parameters of LGPC are similar to those of most GPC studies (see, e.g. the textbook Duriez *et al.* 2016) and listed in table 2.1. Elitism is set to $N_e = 1$, i.e. the best individual of a generation is copied to the next one. The probabilities for replication, crossover and mutation are 10%, 60% and 30%, respectively. The individuals on which these genetic operations are performed are determined from a tournament selection of size $N_t = 7$. The instruction number in the initial generation is selected between 2 to 30 with a Gaussian distribution to ensure the population diversity. Moreover, duplicate individuals are rejected and replaced by new explored individuals. In the following generations, the instruction number in one individual can be changed by the genetic operators. The maximum instruction number for each individual is capped by 100. Elementary operations comprise $+, -, \times, \div, \sin, \cos, \tanh$ and \ln . The operation ‘ \div ’ and ‘ \ln ’ are protected, i.e. the absolute value of the denominator of \div is set to 10^{-2} when $|x| < 10^{-2}$. Similarly, $\ln(x)$ is modified to $\ln(|x|)$ where $|x|$ is set to 10^{-2} when $|x| < 10^{-2}$. In addition, we choose six random constants in the range $[-10, 10]$ with uniform probability distribution.

In the following, we introduce successively the results of open-loop multi-frequency forcing LGPC-1, full-state feedback control LGPC-2 and non-autonomous control LGPC-3.

LGPC-1

First we search for generalizing the open-loop control by including the best periodic forcing at all eigenfrequencies, i.e. $b = K(\mathbf{h})$ where $\mathbf{h} = (h_1, h_2, h_3) = (\sin(t), \sin(\pi t), \sin(\pi^2 t))$. This approach, called LGPC-1, contains the best periodic forcing frequency $\omega^\circ = \pi^2$, thus it should be at least as good than the optimal periodic forcing b° . Figure 2.8 displays the ‘spectrogram’ of the cost values for the whole collection of control laws. Each generation n is seen to consist of a large range of cost values. The decreasing J values towards the right bottom with increasing generation evidences the learning of increasingly better control laws. The best cost value of each generation is highlighted by a red line. The best individual ($m = 1$) in the last generation ($n = 50$) reads

$$b^\circ(t) = -0.37 \sin(-0.18 \sin(\pi^2 t)). \quad (2.7)$$

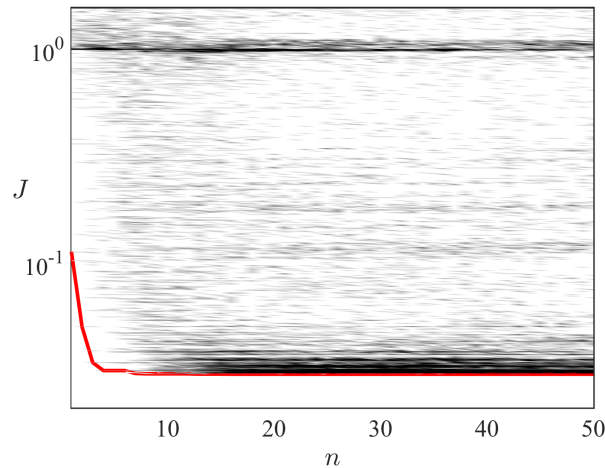


Figure 2.8: Spectrogram of all computed J_m^n ($m = 1, \dots, M; n = 1, \dots, N$) for LGPC-1. For each generation n , J_m^n is ordered with respect to their cost $J_1^n \leq J_2^n \leq \dots \leq J_M^n$. The color shows the distribution of cost values. Darker color indicates larger proportion. The red line highlights the best cost value of each generation J_1^n .

Here, and in the following, the superscript ‘ \circ ’ refers to LGPC-1. When applying a first order approximation on b° , we get $b^\circ(t) \approx 0.067 \sin(\pi^2 t)$. This expression resembles that of the optimal periodic forcing $b^\circ(t) = 0.07 \sin(\pi^2 t)$, and leads to a slightly better cost $J^\circ = 0.03$ as a better amplitude with a higher precision is explored by LGPC-1. The dynamics of the system with b° are similar to Fig. 2.7 and are not shown here for brevity.

If we increase the precision of B to 0.001 in the parameter scan of the periodic forcing in § 2.2.2, we should find the same result. However, the number of evaluations raises to $N_B \times N_\omega = 1001 \times 401 = 401000$ (N_B and N_ω being the number of the amplitudes and frequencies to be tested, respectively) which is 16 times that of LGPC-1 which equals $M \times N = 500 \times 50 = 25000$. In summary, LGPC-1 identifies automatically the optimal frequency $\omega^\circ = \pi^2$ and the optimal amplitude $B^\circ = 0.067$ by employing less time than that for the periodic forcing with an exhaustive parameter sweep.

LGPC-2

Next, an autonomous full-state feedback law (LGPC-2) is optimized,

$$b = K(\mathbf{a}) = K(a_1, a_2, a_3, a_4, a_5, a_6).$$

The ‘spectrogram’ of the cost values is shown in Fig. 2.9. The successive jumps of the best cost value for each generation (red line) reflect the evolution process to better individuals. The targeted LGPC-2 feedback law, i.e. the best individual in the last generation, reads as follows:

$$b^\blacksquare = \tanh \left(\sin \left(\tanh \left(\tanh \left(\tanh \left(\left(\ln(a_4) + \frac{5.8}{1-a_6} a_4 \right) a_4 \right) \right) \right) \right) \right). \quad (2.8)$$

Here, and in the following, the superscript ‘ \blacksquare ’ refers to LGPC-2. The corresponding cost $J^\blacksquare = 0.0038$ is more than seven times better than the value achieved with the optimal open-loop control b° . Closed-loop control b^\blacksquare leads to both, a smaller fluctuation level J_a and a lower actuation energy J_b . The corresponding dynamics are depicted in Fig. 2.10. Instead of the regular excitation of periodic forcing, Fig. 2.10(a) shows that b^\blacksquare gives a strong initial ‘kick’ on the system by exciting the third oscillator to a high energy level of $r_3^2 = 0.5$ (see Fig. 2.10(d),

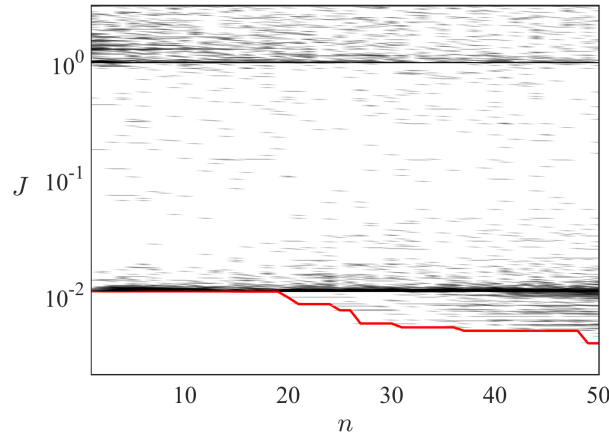


Figure 2.9: Same as Fig. 2.8, but for LGPC-2.

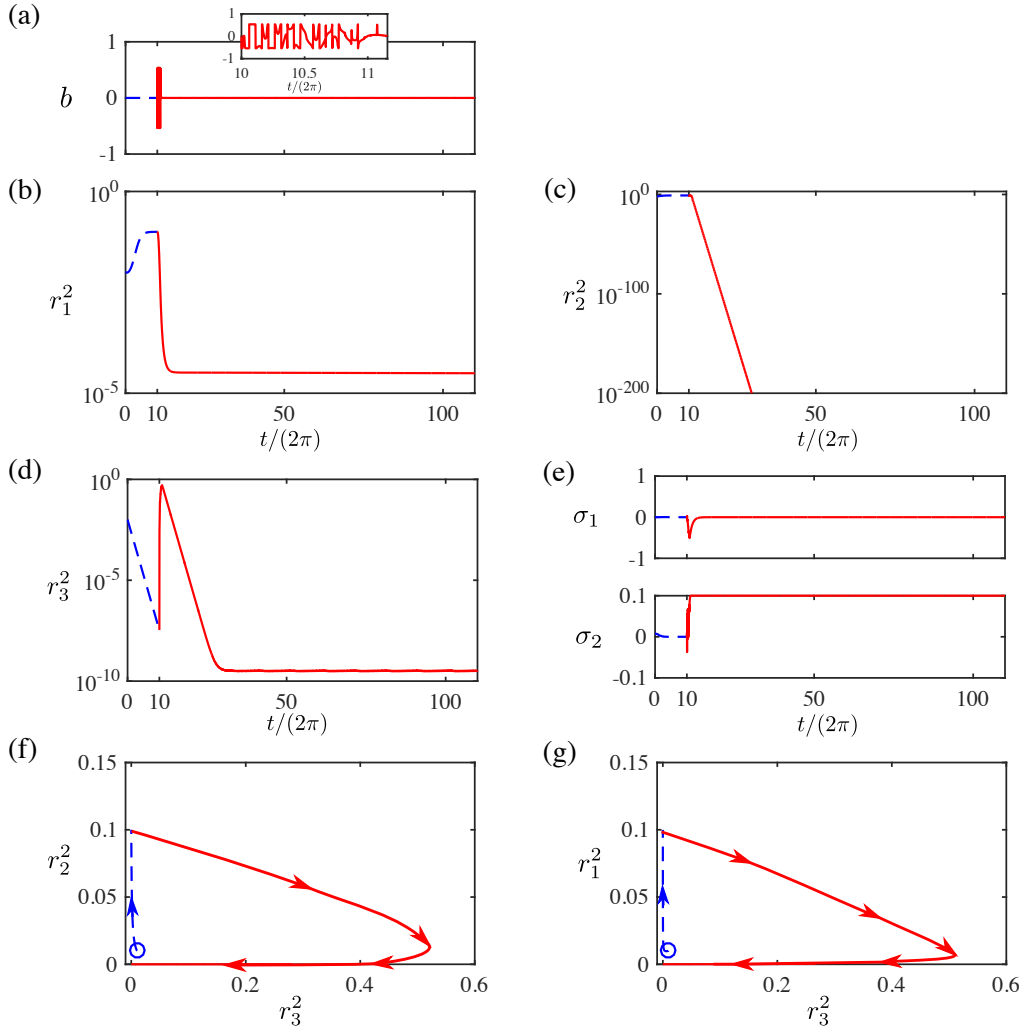


Figure 2.10: Dynamics of the dynamical system Eq. (2.5) with the LGPC-2 control b^\blacksquare applied at $t/(2\pi) \geq 10$. Unforced state: blue dashed line; forced state: red line. (a-e) Time evolution of b , r_1^2 , r_2^2 , r_3^2 , σ_1 and σ_2 . Only the first 110 periods are shown here for clarity. (f) Phase portrait of r_2^2 against r_3^2 and (g) r_1^2 against r_3^2 . The circle indicates the initial point and the arrows the time direction.

(f) and (g)), while simultaneously stabilizing the second oscillator, $r_2^2 \approx 0$ (see Fig. 2.10(c) and (f)). The first oscillator exhibits consequently a fast decay as σ_1 has decreased to $\sigma_1 = -0.5$ due to the change in r_2^2 and r_3^2 (see Fig. 2.10(b), (e) and (g)). This fast transient takes about one period $\Delta t = 2\pi$, see the close view of forcing b in Fig. 2.10(a). It should be emphasized

that LGPC-2 discovers and exploits both frequency crosstalk mechanisms: the excitation of the third oscillator for a quick transient and the suppression of the second oscillator to sustain the low fluctuation level of the target dynamics.

Following this fast transient, the first and second oscillators enter into a quasi-stable state at nearly vanishing fluctuation levels. Subsequently, the control command vanishes as full-state feedback shows no need to actuate after the energy is defeated. With vanishing b , the third oscillator decays exponentially fast. This transient process converges to the fixed point as depicted in Fig. 2.10(f) and (g). Now, the first oscillator has a stabilizing growth rate $\sigma_1 \approx -r_1^2$. LGPC-2 shows an example of the performance of feedback control better than the open-loop control. With only a tiny investment of actuation energy at the very beginning of the control, the whole system remains stabilized without actuation even after thousands of periods.

It should be noted that closed-loop control is not necessarily better than open-loop actuation. Suppose the growth-rate of the first oscillator reads

$$\sigma_1 = 0.1 - r_1^2 + r_2^2/100 - r_3^2. \quad (2.9)$$

In this case, exciting the third oscillator is the only effective stabilizing mechanism and this excitation can already be done with open-loop forcing.

LGPC-3

Finally, we explore a more general class of control laws which combines full-state feedback \mathbf{a} and the best periodic forcing at all eigenfrequencies $\mathbf{h} = (\sin(t), \sin(\pi t), \sin(\pi^2 t))$, as discussed in § 2.1. Then, the generalized LGPC-3 control law $b = K(\mathbf{a}, \mathbf{h})$ includes the pure full-state feedback and the best periodic forcing frequency ω° . Hence, it should be at least as good than LGPC-2. The learning process is similar to Fig. 2.9, thus we do not show the convergence of cost values here for brevity. The optimal control law from LGPC-3 reads

$$b^\bullet(t) = \tanh \left(\sin \left(\tanh \left((3a_2 \sin(t) \sin(\pi^2 t) - a_4) \right) \right) \right). \quad (2.10)$$

Here, and in the following, the superscript ‘ \bullet ’ refers to LGPC-3 results. This control law achieves a better cost value $J^\bullet = 0.0025$ compared to LGPC-2 with similar dynamics. Hence, the results are not detailed here to avoid redundancies. It is worth to note that Eq. (2.10) can also be expressed as $b^\bullet = K_1(3a_2 h_1 h_3 - a_4)$ where K_1 represents the operator ‘ $\tanh(\sin(\tanh(\cdot)))$ ’. To shed light on the contribution of each term to b^\bullet , Fig. 2.11 displays the temporal evolution of the actuation command b^\bullet and the relevant input from the states and from the harmonic functions. It shows that the harmonic component $h_1 h_3$ destabilizes the stable oscillator by a quasi-periodic forcing while the states a_2 and a_4 act as an amplitude regulator.

To summarize, optimal periodic forcing (PF), open-loop multi-frequency forcing (LGPC-1), full-state feedback (LGPC-2), and generalized feedback (LGPC-3) are compared. The contributions to the cost function are depicted in Fig. 2.12, showing that the generalized feedback outperforms the optimal periodic forcing and full-state feedback. The stabilizing mechanisms are schematically depicted in Fig. 2.13.

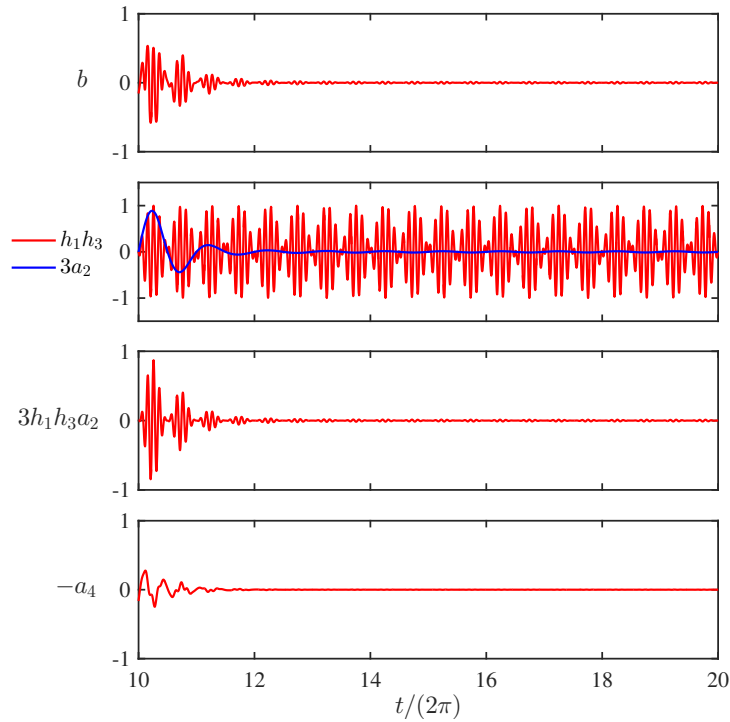
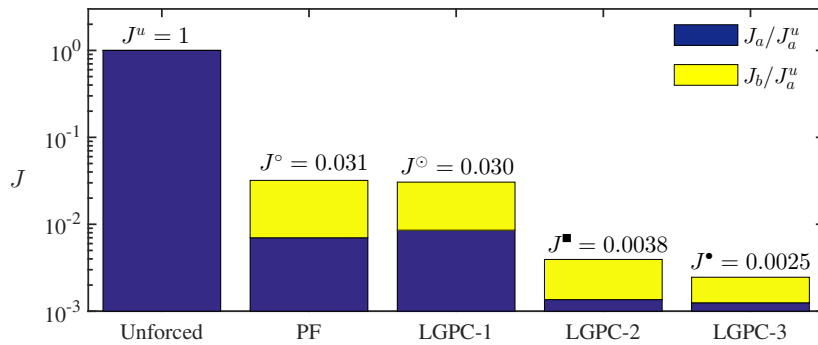
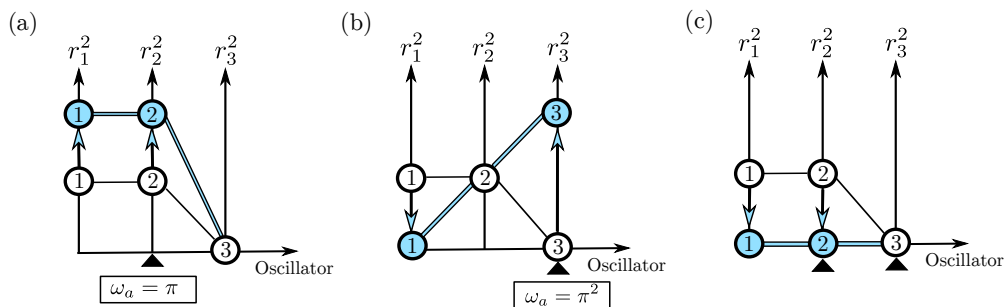
Figure 2.11: Time evolution of b^\bullet , h_1h_3 , a_3 and a_4 .Figure 2.12: Synthesis of J for different controls.

Figure 2.13: Synthesis of system dynamics under the forcing. The energy level of each oscillator is qualitatively indicated by circles. Unforced state: white circles connected by black lines; forced state: colored circles connected by colored lines. (a) Open-loop forcing at actuation frequency $\omega_a = \pi$. (b) Open-loop forcing at actuation frequency $\omega_a = \pi^2$. (c) Feedback control. The triangles indicate the oscillator(s) contributing to alter the first oscillator. The arrows show the transition state when control is applied.

2.2.4 Control landscape for LGPC-3

In this section, we illustrate the control laws and cost function values by an easily interpretable ‘topological landscape’ using the visualisation technique described in § 2.1.4. Figure 2.14 visualizes the control laws determined by LGPC-3 following Eq. (2.4) for the three-oscillator model. Due to the huge number of control laws ($N_K = 500 \times 50 = 25000$), we present every 10th individual in every 10th generation for clarity. Each symbol represents a control law which is color-coded with respect to its performance ranking, for instance the dark color represents the best 10% of the presented control laws. The control laws in the first generation cover a significant portion of the control space, like in a Monte-Carlo search. When the value of n increases, we observe a global movement of control laws towards the region close to $(\gamma_1, \gamma_2) \approx (0, 0)$ where better performance is obtained (darker color), suggesting the convergence towards better controllers. Moreover, the distances between control laws of different generations are also decreased resulting in a dense distribution, pointing to an increased similarity between control laws. In particular, at the last generation $n = 50$, the control laws only occupy a small region of the control space. The inserted figure gives a close view of the control laws near the origin point, where the best control law(s) are found at $(\gamma_1, \gamma_2) \approx (-0.18, 0.02)$. These observations show that LGPC has effectively explored the control space and identified the extrema in this space. The control laws become more and more similar with increasing generation.

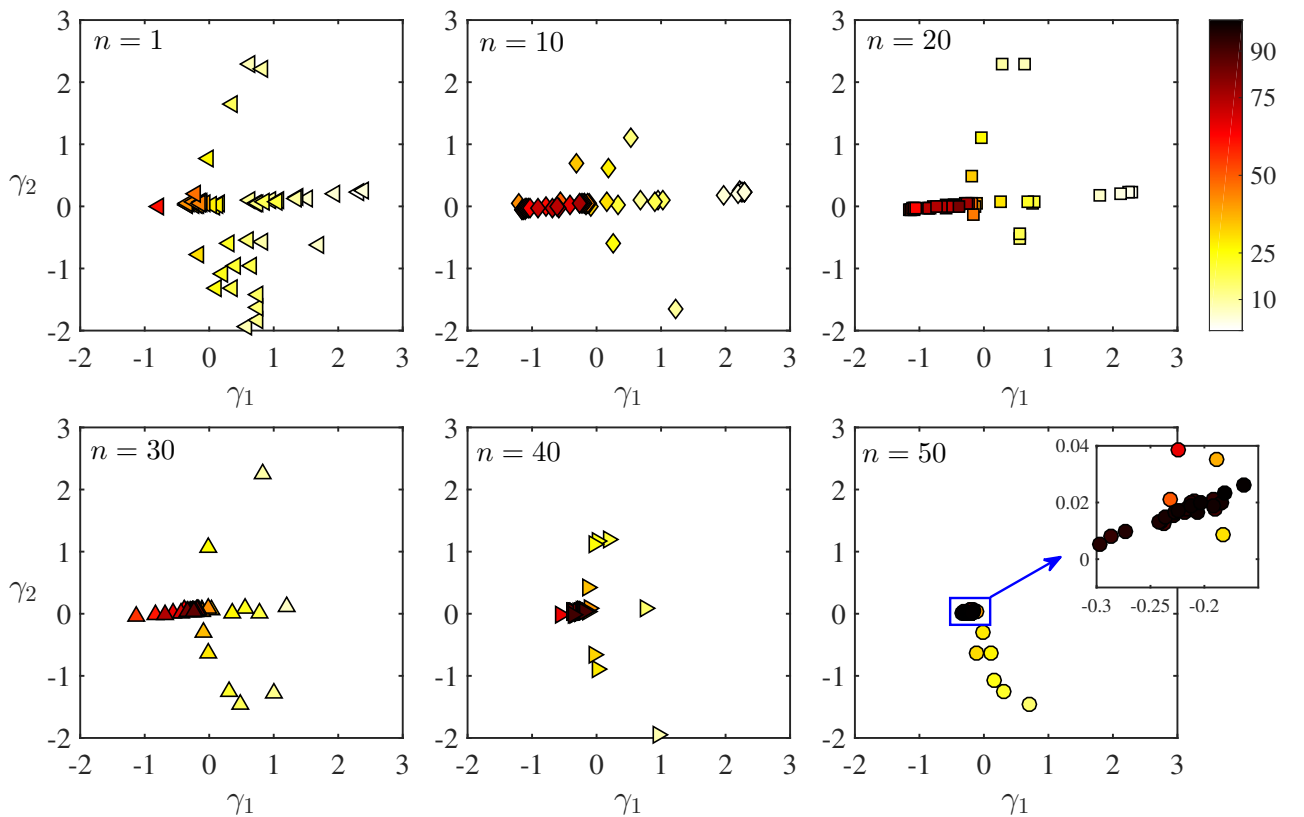


Figure 2.14: Visualization of the control laws obtained for the three-oscillator model by LGPC-3. n represents the generation number. The color scheme corresponds to the percentile rank of the control laws with respect to their performance J . Darker color presents better performance. Control law b_i is presented by the point $\gamma = (\gamma_1, \gamma_2)$. The distance between two control laws, i.e. two points, approximates their respective dissimilarity.

2.3 Summary

Three categories of LGPC are investigated in this work: an open-loop multi-frequency control $b = K(\mathbf{h})$, named LGPC-1, an autonomous sensor-based feedback control $b = K(\mathbf{s})$, termed LGPC-2, and a generalized non-autonomous control $b = K(\mathbf{s}, \mathbf{h})$ comprising the sensors \mathbf{s} and time-periodic functions \mathbf{h} , called LGPC-3. All of them are successfully applied to the stabilization of a forced nonlinearly coupled three-oscillator model. The obtained control laws stabilize the first unstable oscillator by exploiting two frequency crosstalk mechanisms: (1) the excitation of the third oscillator by a hard 'kick' for a quick transient and (2) the suppression of the second oscillator to sustain the low fluctuation level of the target dynamics. Following the quick transient, the first and second oscillators enter into a quasi-stable state at nearly vanishing fluctuation levels. Hence, the full-state feedback hardly needs to actuate and the control command starts to vanish. The whole system is stabilized with only a small investment of the actuation energy at the very beginning of the control. Thus, LGPC laws show a performance over the optimal open-loop control as both a lower fluctuation level and a lower actuation energy are obtained. The explored control demonstrate the vital importance of frequency crosstalk for control design.

The visualization landscape of control laws provides not only a simple and revealing picture of the exploration and exploitation characteristics of the control approach, but also inspires further improvement of the methodology. The example given in Fig. 2.14 indicates clearly the search space topology and distills the local extrema in this feature space. This feature space has been shown to estimate the cost function of an untested control law (Kaiser *et al.*, 2017) and may be used to avoid the redundant testing of control laws in unpromising terrain. Thus, testing time can be reduced. The visualization is becoming an important component of LGPC for on-line decisions during a control experiment.

Chapter 3

Drag reduction of a car model by LGPC

Most of the following results are published in Li et al. (2017a).

In this chapter we apply LGPC on the turbulence control experiments of a square-back car model. The objective is to find an effective control law minimizing the drag and to understand the associated actuation mechanisms. The three categories of LGPC introduced in the previous chapter are all investigated. For each category, we justify the optimization of LGPC by analyzing the instantaneous flow responses corresponding to the optimal control law and the mean wake modifications.

Contents

3.1	Control problem	36
3.2	Experimental setup	36
3.2.1	Flow configuration and wind tunnel	36
3.2.2	Actuator system	38
3.2.3	Pressure sensors and measurements	39
3.2.4	Real-time system	42
3.2.5	Experimental implementation of LGPC	42
3.3	Unforced flow	44
3.4	LGPC-1: multi-frequency forcing	45
3.4.1	LGPC-1 results	46
3.4.2	Analysis of the optimal control law	50
3.4.3	Analysis of the near wake	53
3.5	LGPC-2: Feedback control	54
3.5.1	LGPC-2 results	55
3.5.2	Visualization of control laws	57
3.5.3	Analysis of the optimal control law	59
3.5.4	Morlet filtering of sensor signals	62
3.6	LGPC-3 and multiple-input control	64
3.7	Summary	64

3.1 Control problem

The control objective is a net energy saving from drag reduction accounting for the actuation expenditure. Both, the drag reduction and the actuation energy are determined for the best presented control laws. However, for the rapid testing of many control laws, we employ two results of an open-loop study in the same experiment by Barros *et al.* (2016b). First, the drag is in good approximation a monotonous function of base-pressure coefficient for all actuation frequencies. Second, the invested actuation power was found to be a small fraction of the drag-related power saving. In summary, the base-pressure coefficient can be expected to be a good surrogate for control goal. The resulting cost function J is defined in terms of the pressure sensors over the rear side:

$$J = \frac{\langle \overline{C_p} \rangle_a}{\langle \overline{C_p} \rangle_u}. \quad (3.1)$$

Here, $C_p = (p - p_o)/q$ is the pressure coefficient, where p is the local static pressure, p_o is the free-stream static pressure and $q = 0.5\rho U_\infty^2$ is the dynamic pressure corresponding to a free-stream velocity of U_∞ . $\langle C_p \rangle$ and $\overline{C_p}$ represent the area-averaged and time-averaged pressure coefficient, respectively (see the following section § 3.2.3 for the pressure sensor distribution). The subscript ‘a’ indicates the value for the actuated flow, whereas the subscript ‘u’ corresponds to the unforced flow. Thus, the cost function J represents the relative change of the area- and time-averaged base pressure by actuation with respect to the unforced flow.

The performance of the control law is quantified by J . C_p is negative at the rear side due to the decreased pressure in the wake. By definition, $J = 1$ for the unforced flow. $J < 1$ quantifies the increase of base pressure, corresponding to a reduction of the drag. Inversely, $J > 1$ stands for a drag increase. As outlined in the previous chapter, the control task is to minimize the cost function. The three categories of LGPC introduced in Chapter 2 are all investigated: the open-loop multi-frequency forcing $b = K(\mathbf{h})$ (LGPC-1), feedback control $b = K(\mathbf{s})$ (LGPC-2) and the non-autonomous control $b = K(\mathbf{s}, \mathbf{h})$ (LGPC-3). In this study, the actuation b is performed with pulsed jets located at the four trailing edges. The time-periodic functions \mathbf{h} contain different frequencies of the pulsed jets. For sensor feedback, \mathbf{s} is composed of the pressure sensors distributed over the rear surface. The details of the actuators and sensors will be described in the following section.

3.2 Experimental setup

In this section, the experimental facility is described, following an input-output framework appropriate to flow control. In § 3.2.1, the wind tunnel is outlined. The actuator system and measurements (pressure sensors, drag and velocity) are then detailed in § 3.2.2 and § 3.2.3, respectively. Section 3.2.4 presents the real-time system, followed by the experimental implementation details of LGPC in § 3.2.5.

3.2.1 Flow configuration and wind tunnel

Experiments are conducted in a closed-loop wind tunnel (S620, ENSMA, Poitiers, France). A schematic of the entire wind tunnel facility is shown in Fig. 3.1 which depicts the position of the test section, the fan system and the flow conditioning grids. The convergence ratio between the grid section and the rectangular test section is 7:1. The test section measures 2.4 m wide, 2.6 m high and 6 m long. The maximum free-stream velocity is about 60 m s^{-1} with a turbulence intensity of approximately 0.5%. The flow stability in the tunnel is ensured for velocities greater than 5 m s^{-1} .

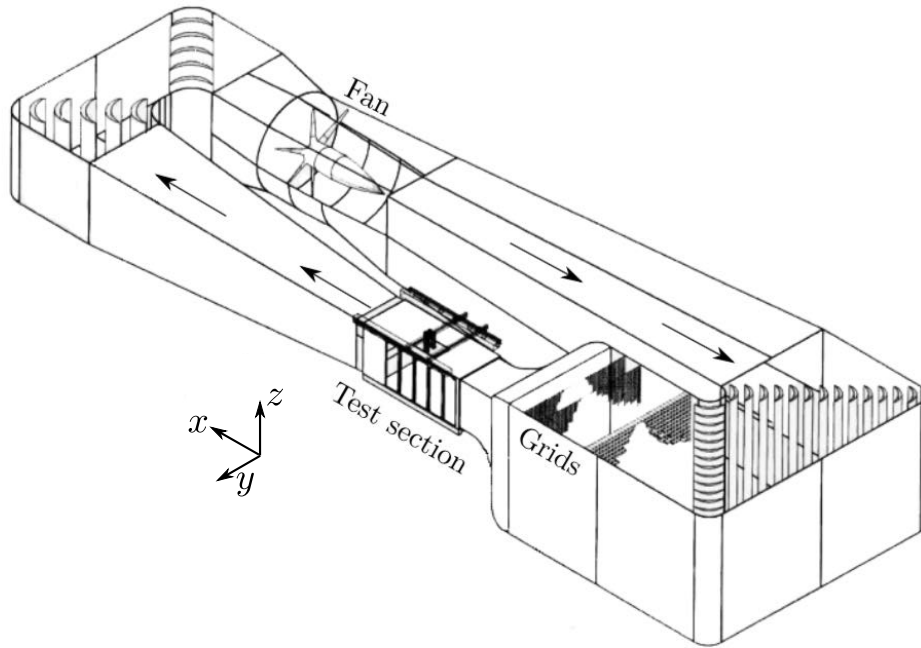


Figure 3.1: Schematic of wind tunnel facility. The arrows inside the tunnel indicate the direction of the generated flow.

A sketch of the model in the test section is presented in Fig. 3.2(a). The blunt-edged bluff body is a simplified car model similar to the square-back Ahmed body (Ahmed *et al.*, 1984). It has the following dimensions: height $H = 0.297$ m, width $W = 0.350$ m and length $L = 0.893$ m. $S = HW$ is the frontal area of the bluff body. The front edges are rounded with a radius of 0.085 m. The model is mounted over a raised floor with an elliptical leading-edge to control the boundary layer thickness. An adjustable trailing edge flap at the end of the raised floor is used to control the incident angle on the leading edge. Without the model, the zero incident angle is obtained at $\alpha_{\text{Flap}} = 5.7^\circ$. After this adjustment, the model is installed with a ground clearance of $G = 0.05$ m, as in Ahmed *et al.* (1984). The blockage ratio considering the upper area above the raised floor is 2.2%.

The flow is described in a Cartesian coordinate system with x, y, z representing streamwise, spanwise (or lateral) and transverse (or wall-normal) directions, respectively. The origin O is placed on the raised floor at the streamwise position of the rear surface.

A Pitot tube mounted on the roof measures the static pressure p_o and the upstream velocity U_∞ in the wind tunnel. Besides, a temperature probe installed close to the Pitot permits to obtain the wind tunnel temperature T_o . T_o together with the static pressure p_o allow us to calculate the flow density ρ . Given these quantities, we are able to calculate the Reynolds number based on the height of the model $Re_H = \rho H U_\infty / \mu$ where μ is the dynamic viscosity of the air. The results in this chapter are obtained with a constant free-stream velocity $U_\infty = 15 \text{ m s}^{-1}$, corresponding to $Re_H \approx 3 \times 10^5$. The turbulent boundary layer thickness at this velocity is measured at $x = -L = -3H$ with a micro-Pitot tube and without the model installed in the wind tunnel. The boundary layer thickness based on 99% of the free-stream velocity is $\delta_{0.99} = 0.26G$. The corresponding shape factor is $H_{\text{shape}} = 1.4$ suggesting a turbulent boundary layer. In the study of Barros (2015), the author compared the boundary layer characteristics at $x = -3.4H$ with and without the model at a similar upstream velocity, and the results show that the presence of model does not change importantly $\delta_{0.99}$ but leads to a lower H_{shape} .

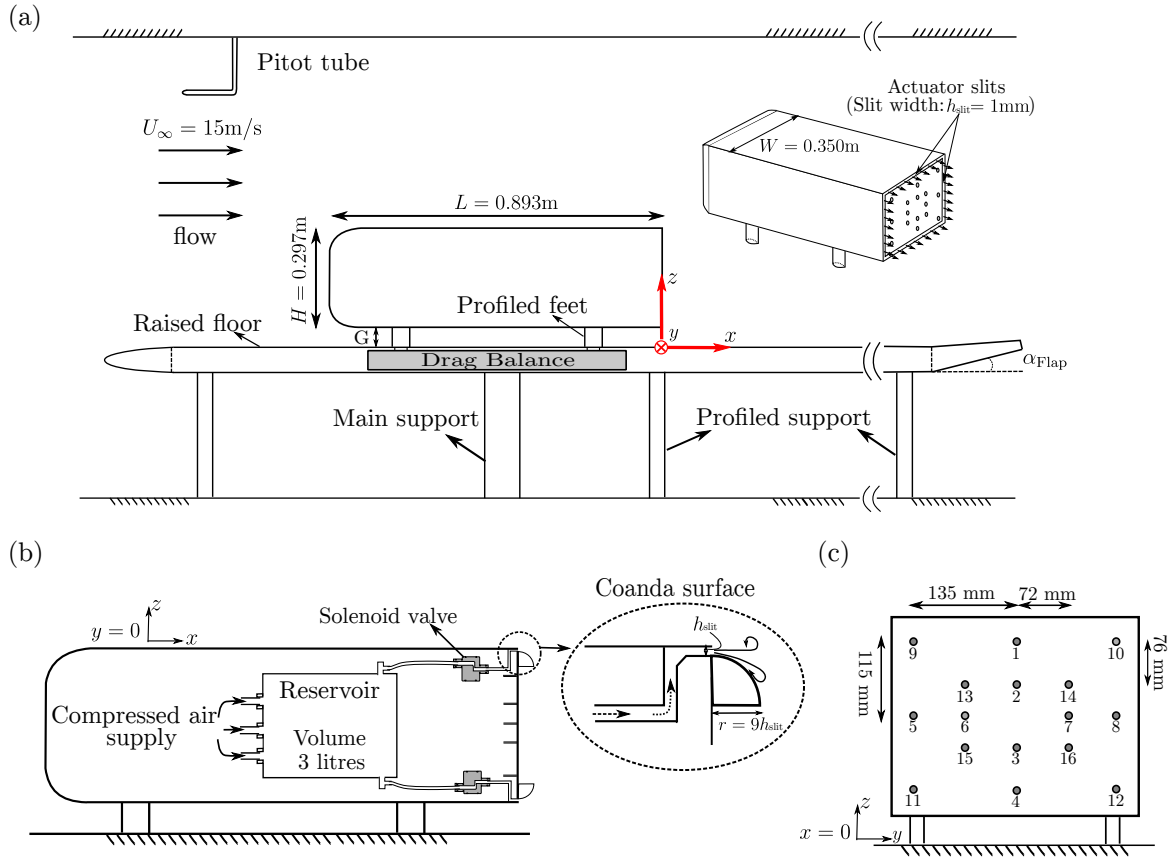


Figure 3.2: Experimental setup. (a) Wind tunnel and model geometries. Inserted figure shows actuators and sensors on the model. (b) Side view of actuation system. (c) Locations of pressure sensors.

3.2.2 Actuator system

The model is equipped with actuator slits at all four trailing edges, as illustrated in Fig. 3.2(a). The slit width is $h_{\text{slit}} = 1 \text{ mm}$. The pressured air, which is supplied by a compressed air reservoir, are blown tangentially to the free-stream velocity through these slits. The reservoir with volume 3 litres is positioned inside the model and connected to the laboratory compressed air network through three 10 mm diameter tubes. The internal pressure of the reservoir is referred to as P_0 .

The pulsed blowing is driven by 32 solenoid valves (Matrix[®] OX 821.100C2KK) which are installed between the reservoir and the actuator slits, as depicted in Fig. 3.2(b). These valves are distributed homogeneously along the trailing edges. The zone between the outlet of the valves and the slit exit is specifically designed so that the exiting flow is continuous along the periphery of four edges, as detailed in Barros *et al.* (2016b). The solenoid valve generates the pulsed jet in ON/OFF mode within the frequency range $[0, 500] \text{ Hz}$. The system enables to control the frequency at the four edges simultaneously or independently. In the present study, we control only the ON/OFF of the solenoid valves. Note that the actuator system has a mechanical time delay between the control command and the induced fluctuation at the outlet of the slit. This time delay of about 1 ms is identified by measuring simultaneously the voltage of the valve and the velocity fluctuation at the outlet of the slit. In addition, a rounded surface of radius $9h_{\text{slit}}$ adjacent to each slit exit is installed as an additional passive device in a manner similar to Barros *et al.* (2016b). Figure 3.2(b) shows a close-up view of the Coanda surface at the exit zone.

The actuation amplitude can be characterized by the momentum coefficient:

$$C_\mu = \frac{S_{\text{Jet}} \overline{V_{\text{Jet}}^2}}{S U_\infty^2} \quad (3.2)$$

where S_{Jet} is the slit cross-sectional area and V_{Jet} the jet velocity. The overbar denotes the time average. The jet velocity is measured at 1 mm downstream of the centreline of the slit exit by the use of a single hot-wire probe in still-air without the Coanda surface. V_{Jet} depends on the actuation frequency f , duty cycle DC and supply pressure P_0 . For open-loop control, f and DC are predetermined while for closed-loop control, they are unknown before implementing the control law. In this study, we choose to maintain a constant initial supply pressure at $P_0^i = 4$ bar before actuation. When actuation starts, the pressure in the reservoir decreases to about $P_0 = 1.4$ bar with a continuous blowing. With a pulsed blowing, P_0 depends on the actuation frequency f and duty cycle DC . We exemplify in Fig. 3.3 the time series of jet velocity for two frequencies having one order of magnitude difference with the initial pressure $P_0^i = 4$ bar. At the low frequency $f = 20$ Hz, the velocity signal exhibits a rectangular waveform with an overshoot at the beginning of each stroke phase. While at the high frequency $f = 400$ Hz, the signal presents an irregularly triangle waveform. The initial pressure level $P_0^i = 4$ bar is used throughout the experiments. The actuation amplitude C_μ is finally obtained by *a posteriori* measurement of V_{Jet} using the registered open- and closed-loop actuation signals.

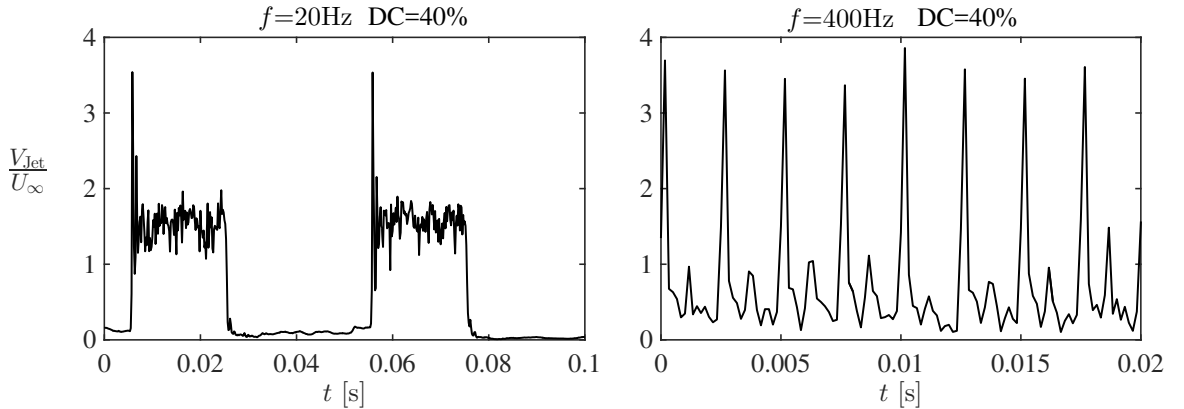


Figure 3.3: Time series of jet velocity measured at 1 mm downstream of the centreline of the actuation slit.

3.2.3 Pressure sensors and measurements

Pressure sensors

Drag reduction is highly correlated with the base pressure from which the control performance can be quantified. We have 16 pressure taps distributed at the rear surface, as illustrated in Fig. 3.2(a) with a perspective view. These pressure taps are numbered as presented in Fig. 3.2(c). The pressure is obtained by differential sensors *Sensortech*[®] HCLA02X5DB with the following characteristics: operating pressure range ± 250 Pa, response delay 0.5 ms and uncertainty due to non-linearity and hysteresis less than 0.25% of full-scale span. These sensors are connected to the pressure taps through a 0.04 m long metallic tube and a 0.9 m long vinyl tube as indicated in Fig. 3.4(a). A 2 m long tube is added as a branch of the vinyl tube before it reaches the pressure sensor. This long tube is designed to damp pressure oscillators inside

the tube ducts. Besides, all the sensors are connected in common to the static pressure p_o of the wind tunnel through a 10m long vinyl tube connected with the Pitot tube on the roof.

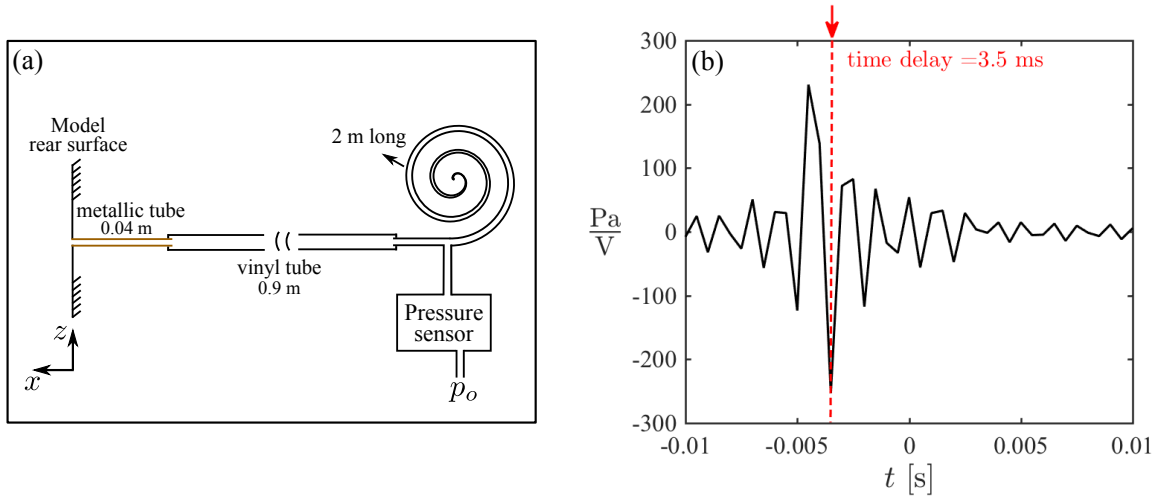


Figure 3.4: Pressure sensor properties. (a) Sketch of the connection between the pressure tap and the differential sensor (figure from Barros 2015). p_o is the static pressure in the wind tunnel. (b) Impulse response of one sensor.

The tube mounting between the pressure taps and sensors results in distortions between the recorded signals and the pressure values at the taps location. The recorded signals can be corrected by rebuilding the signals at the taps location. A specially designed coupler having a reference microphone B&K is applied to obtain a transfer function for each sensor. An intrinsic impulse response is then derived for each sensor from this transfer function. We present in Fig. 3.4(b) an example of this impulse response. The corrected signal is obtained by convolving the impulse response with the measured signal. The methodology has been successfully applied in the literature (Ruiz *et al.*, 2009, 2010; Beaudet, 2014). The distortion of recorded signals is inferred from the spectrum of the transfer function. It presents a low-pass filter behaviour with a linear phase. The linear phase leads to a time delay of about 3.5 ms (involving the response delay 0.5 ms of the sensor) between the fluctuations at the pressure taps and the recorded signals, as shown in its impulse response in Fig. 3.4(b). The passband of the low-pass filter, calculated at -3dB in amplitude, is $f \in [0, 100]$ Hz corresponding to a Strouhal number range of $St_H = fH/U_\infty \in [0, 2]$. This interval covers $St_H = 0.2$ which is the typical vortex shedding frequency found in the bluff body wakes (Roshko, 1955). When the flow is forced at frequencies higher than 100 Hz, the pulsation strongly affects the sensing. Indeed, the forcing frequency is so energetic that the sensor spectrum still manifests a high energy level at the forcing frequency despite the energy attenuation by the tube mounting. Based on this fact, the recorded signals can be used reasonably. This correction can only be performed *a posteriori* but not on-line. Unless the information at the location of pressure taps is needed (the analysis in § 3.4.2), all the results are obtained directly from the recorded signals without correction.

The pressure measurements are sampled at a rate of $F_s = 2$ kHz. The time-history pressure signals will be used as sensor signals in the closed-loop control (see details in § 3.2.4) to determine in real-time the actuation. The dimensionless pressure coefficient is defined for each pressure tap i as:

$$C_{p_i} = \frac{p_i - p_o}{q}, \quad i = 1, \dots, 16 \quad (3.3)$$

where p_i is the measured pressure.

Drag measurements

To quantify the effects of actuation on the drag, the aerodynamic force is measured using an in-house unidirectional balance mounted inside the raised floor, as depicted in Fig. 3.2(a). The principle of the balance is to measure the displacement of two metal plates by the use of a 9217A Kistler piezoelectric high sensitive sensor. The upper plate is connected to the model through four profiled support feet. The lower plate is fixed to the main support as well as the raised floor. The aerodynamic force on the model creates a downstream displacement of the upper plate against the lower one resulting in an expansion of the sensor. We can then derive the drag force F_D from this deformation. This concept idea of balance is described in the study of Winkelmann & Gonzalez (1990). The calibration of the system is performed by the use of standard masses up to 2 kg using a pulley system connected to the rear surface of the mounted model (Barros, 2015).

The data acquisition is performed at the same sampling rate of pressure measurements $F_s = 2$ kHz. A low-pass filter at 1 Hz is used to get the time-averaged drag F_D . The corresponding time-averaged drag coefficient C_D is defined according to:

$$C_D = \frac{F_D}{qS}. \quad (3.4)$$

Note that the pulsed jets could create a thrust on the model. For accurate estimation of the drag, this thrust is measured in quiescent air using the registered open- and closed-loop actuation signals and subtracted from the measured drag at full speed. For the rapid testing of a large amount of control laws, we select the base pressure recovery as the cost function due to the reasons described in § 3.1. Drag measurements are only performed for the top performing control laws.

Velocity measurements

For analyzing the wake dynamics, velocity fields are obtained using a two-component Particle Image Velocimetry (PIV) system. The measurements are taken in the symmetry plane located at $y = 0$. Two field dimensions are investigated, as indicated in Fig. 3.5. The first field measures $1.4H \times 2H$ and spans the whole wake containing entirely the recirculation flow region. The second field focuses on the shear layer dynamics in a region downstream of the top trailing edge and has a small size of $0.5H \times 0.34H$. For both fields, the measured regions are illuminated by a laser sheet generated by a Nd:YAG laser. The images are captured by a LaVision Imager LX 16M camera with resolution of 4920×3280 pixels. For the larger field, image pairs are captured at a frequency of 3 Hz. The time between a pair of images yielding one velocity field is $90 \mu\text{s}$. While for the smaller field, random and phase-locked PIV are both performed. They have the same time interval $10 \mu\text{s}$. The random PIV is recorded with a frequency of 3 Hz. The phase-locked PIV is triggered by an external clock at a frequency of 4 Hz. Velocity vectors for both fields are processed with an interrogation window of 32×32 pixels with a 50% overlap,

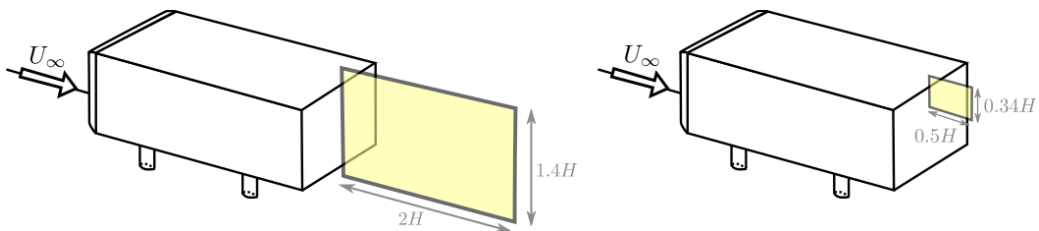


Figure 3.5: PIV fields of view.

giving a spatial resolution of 2.3 mm and 0.54 mm corresponding to $0.008H$ and $0.0018H$ for the large and small field respectively. The velocity statistics are computed with 1000 independent images.

Hot-wire is used to measure the jet velocity as mentioned in § 3.2.2. The measurements are obtained by a StreamlinePro Anemometer System using a single wire probe (55P11) which is fixed to a profiled displacement system installed on the roof of the wind tunnel.

3.2.4 Real-time system

For closed-loop control, real-time processing is performed by a Labview Real-Time module, which is implemented on a *National Instrument* PXIe-8820 Real-Time controller running at a sampling rate of $F_{RT} = 2$ kHz, where the subscript RT indicates Real-Time. Sensor data acquisition for open- and closed-loop control is performed at the same sampling rate by a *National Instrument* PXIe-6363 DAQ card. Four digital outputs are used to operate the four actuator slits in ON/OFF mode. Since the solenoid valve cannot respond in less than 1 ms, the ON/OFF command needs to have at least 1 ms. Under the present sampling rate F_{RT} , this value corresponds to two sampling points. For the effective working of the actuator, a verification is performed before sending the command to the actuators to ensure that the ON/OFF command lasts at least 1 ms.

The reachable periodic frequencies f consistent with F_{RT} can be derived from $f = F_{RT}/N_{sp}$, where N_{sp} is the number of sampling points in one time period of f . The working frequency range of actuators ($[0, 500]$ Hz) imposes a minimum value for N_{sp} , being $N_{sp} \geq 4$. For a given f , the possible duty cycles DC can be deduced from $DC = i/N_{sp}$, $i = 2, \dots, N_{sp} - 2$. The value of i starts from 2 and ends at $N_{sp} - 2$ to ensure a response time of 1 ms (2 sampling points) for an effective working of the actuators. Thus, the number of possible duty cycles N_{DC} for a given f is $N_{DC} = N_{sp} - 3 = F_{RT}/f - 3$, which increases with N_{sp} and decreases with f . Figure 3.6 represents with blue dots the ensemble of periodic forcing frequencies f and duty cycles DC calculated in the way described above. The Strouhal number St_H is also shown. It is clear that the number of possible duty cycles reduces as the frequency increases due to the limited sampling points in one period. The red filled circles highlight the selected periodic forcing cases considered in the following. Hereafter, all the frequencies are given in terms of St_H .

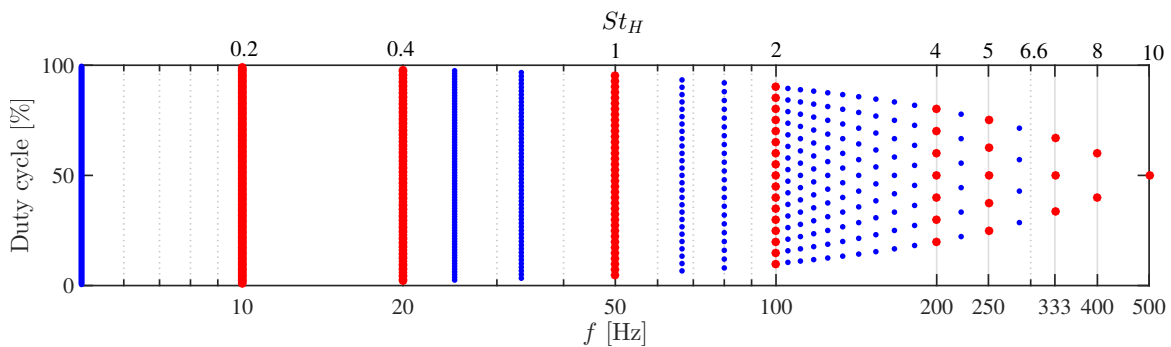


Figure 3.6: Ensemble of open-loop frequencies f and duty cycles DC derived from $F_{RT} = 2$ kHz. Blue dots represent a subset of the combinations of f and DC consistent with F_{RT} . Red dots highlight the cases considered in this study.

3.2.5 Experimental implementation of LGPC

The LGPC architecture is shown schematically in Fig. 3.7. In experiments, LGPC is executed in the same way as for the dynamical system plant in Chapter 2:

1. LGPC provides a generation of control laws to be evaluated by the experimental plant.
2. The plant evaluates and grades the individuals in terms of the given cost function.
3. LGPC evolves the next generation.
4. The process from 1 to 3 iterates until a pre-determined criterion is met.
5. After this learning phase, the best control law is determined.

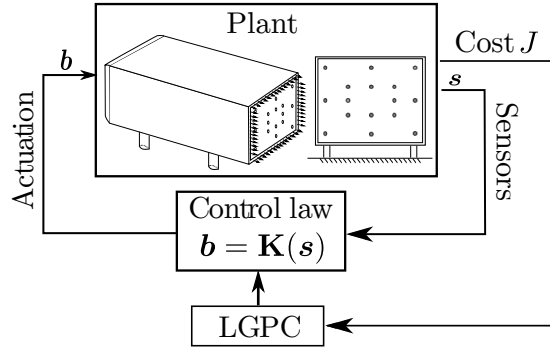


Figure 3.7: Schematic of LGPC architecture in experiments.

LGPC encompasses new features to adapt to experimental applications. As the solenoid valve works in ON/OFF mode, the output of the control laws is passed through the Heaviside function to transform the continuous output to a binary ON/OFF signal, i.e. $H(K(\mathbf{s}))$, where $K(\mathbf{s})$ gives a continuous output and H represents the Heaviside function. In the following, we assume that K is the binarized control law, i.e. $b = 1$ and $b = 0$ correspond to actuation ON and OFF, respectively. This binary operation eliminates the amplitude information in the control laws. Therefore, the same actuation signal b can be obtained from different control law expressions. The uncertainty in the actuation mechanism may change J in different evaluations for the same individual. If an individual appears multiple times in several generations, it is evaluated each time and its cost is the averaged value of all its past evaluations. A predetermined number of best individuals in each generation are re-evaluated several times to ensure good and robust performance.

The LGPC parameters for this study are displayed in table 3.1. Each generation is composed of $M = 50$ individuals. An optional pre-evaluation of individuals is performed for all the generations. After generating the individuals, each is pre-evaluated based on the pressure signal of the unforced flow. The resulting actuation command is an indicator for their feedback control performance. If no actuation ($b = 0, \forall t$) or continuous blowing ($b = 1, \forall t$) is obtained in the pre-evaluation, this individual may be considered a prospectively bad performer and is discarded for evaluation by assigning a high cost value to it. This pre-evaluation step saves experimental testing time.

Elitism is set to $N_e = 1$, i.e. the best individual of a generation is copied to the next. The replication, crossover and mutation probability are 10%, 50% and 40%, respectively. The individuals on which these genetic operations are performed come from a tournament selection of size $N_t = 7$. The instruction number varies between 5 to 30 (except where noted otherwise) with a Gaussian distribution. Elementary operations comprise $+$, $-$, \times , \div , \sin , \cos , \tanh and \log_{10} . The operation \log_{10} is protected, i.e. $\log_{10}(x)$ is modified to $\log_{10}(|x|)$ where x is the variable. If the actuation command at time t_k is not a number (NaN) or infinity (Inf) due to the sensitive operator \div , it is modified to take the command one step before, i.e. $b(t_k) = b(t_{k-1})$. In addition, we choose six random constants in the range $[-1, 1]$.

Parameters	Value
Population size	$M = 50$
Tournament size	$N_t = 7$
Elitism	$N_e = 1$
Replication	$P_r = 10\%$
Crossover	$P_c = 50\%$
Mutation	$P_m = 40\%$
Min. instruction number	5
Max. instruction number	30
Operations	$+, -, \times, \div, \sin, \cos, \tanh, \log_{10}$
Number of constants	$N_c = 6$
Constant range	$[-1, 1]$

Table 3.1: LGPC parameters in the experiments.

The evaluation of every individual takes $T = 10$ s. This value corresponds to 500 convective time units defined by $t_c = H/U_\infty$. For the unforced flow, the convergence time determined by

$$T_{\text{conv}} = \operatorname{argmin}_t \left| \frac{\langle C_p(t) \rangle - \langle \overline{C_p} \rangle}{\langle \overline{C_p} \rangle} \right| < 0.5\%$$

is about $300t_c$. To give an idea about this convergence time for the forced flow, we investigate open-loop forcing signals at $f = 5$ Hz and $f = 500$ Hz, representing large and small actuation time scales respectively. The convergence time is around $450t_c$ for $f = 5$ Hz and $200t_c$ for $f = 500$ Hz. These results indicate that $T = 10$ s $\approx 500t_c$ is sufficient for an approximately accurate average value. It should be noted that LGPC requires only an accurate ordering of the costs associated with the considered individuals. Hence, we refrain from using, say, 100 s to obtain slightly more accurate values. There is a time gap of about 6 s between two individuals for data recording, reservoir refilling and communication between LGPC and the control module. The best five individuals of each generation are re-evaluated five times. Overall, approximately five generations each consisting of 50 individuals are evaluated in less than two hours.

3.3 Unforced flow

We first give a brief review of the unforced flow to establish a basic understanding of the wake. Throughout this manuscript, all physical quantities are normalized by U_∞ and H . Figure 3.8(a) shows in the symmetry plane $y=0$ the contour maps of the time-averaged streamwise velocity \bar{u} combined with the streamlines. We remark that the streamlines give only a qualitative 2D picture of the wake as the flow is fully three-dimensional. As outlined in Chapter 1, the shear layer emerging from the four trailing edges develops and rolls up into large-scale structures. This amplification of the shear layer dynamics is crucial to entrain the free-stream fluid into the wake region, leading to the formation of a recirculation bubble. The negative values of \bar{u} (blue zone) point out clearly the momentum loss in the wake which is closely related to the drag. Streamlines in Fig. 3.8(a) show that two counter-rotating structures coexist in the mean wake, where the upper structure rotating in the clockwise direction is bigger and closer to the rear surface than the lower one. The vertical wake asymmetry is not surprising as the presence of the ground acts as a perturbation, leading to flow features that differ from above and under the model. The distribution of the 2D-approximated turbulent kinetic energy $k = 0.5(\overline{u'^2} + \overline{w'^2})$ is shown in Fig. 3.8(b), where $u' = u - \bar{u}$ and $w' = w - \bar{w}$ represent the velocity fluctuations. It

highlights the concentration of k in the shear layer region resulting from the important velocity fluctuations. The evolution of the shear layer leads to an increase of k along the streamwise direction. Moreover, the fluctuations are more important in the lower shear layer due to the ground effect.

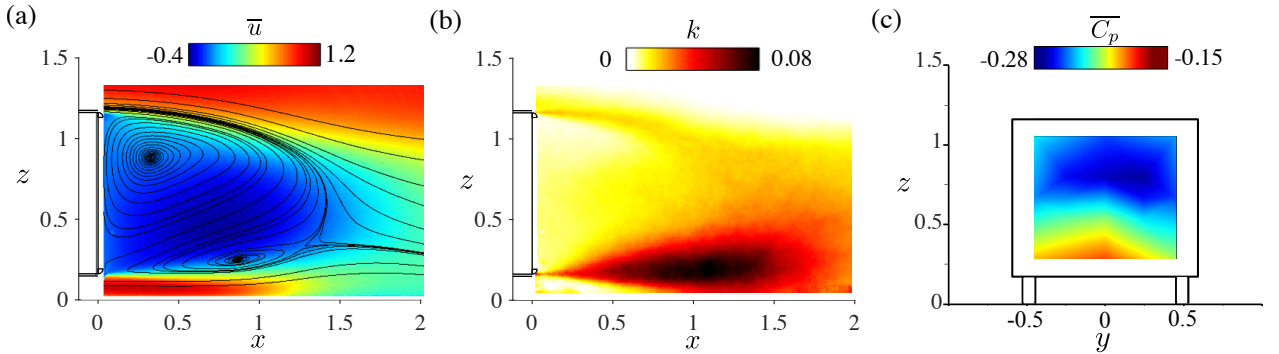


Figure 3.8: Time-averaged wake for the unforced flow in the vertical symmetry plane $y = 0$. From left to right: (a) the contour maps of the time-averaged streamwise velocity \bar{u} overlapped with the streamlines; (b) the turbulent kinetic energy k and (c) the time-averaged base pressure.

The time-averaged base pressure distribution, measured during 1 min, is shown in Fig. 3.8(c). The top-down asymmetry along z is in agreement with the wake topology in Fig. 3.8(a). A low pressure zone is obtained near the upper edge, which is associated with the upper large clockwise vortex. The pressure distribution is nearly symmetric along y implying a symmetric wake in the spanwise direction. Its slight asymmetry may be related to the imperfections of the model and wind tunnel.

At the working condition $U_\infty = 15 \text{ m s}^{-1}$, the area- and time-averaged base pressure coefficient is $\langle \overline{C_p} \rangle = -0.235$. The corresponding time-averaged drag coefficient is $C_D = 0.306$, which was measured with the Coanda surface. In table 3.2, we summarize these quantities for various Reynolds numbers corresponding to $U_\infty = 10, 15$ and 20 m s^{-1} , respectively. With increasing Re_H , $\langle \overline{C_p} \rangle$ increases and C_D decreases. These observations are the same as stated in Barros *et al.* (2016b), and are assumed to be related to the flow detachment on the model's front curved edges. In fact, these separations may impact the separating boundary layer at the trailing edges and the wake, leading to modifications in C_D .

$Re_H = HU_\infty/\nu$	$\langle \overline{C_p} \rangle$	C_D
2×10^5	-0.236	0.343
3×10^5	-0.235	0.306
4×10^5	-0.232	0.286

Table 3.2: Unforced flows: averaged base pressure and drag coefficients for various Reynolds number.

3.4 LGPC-1: multi-frequency forcing

We refer input and output to the experimental plant, i.e., input indicates actuation and output implies sensor. Except stated otherwise, the same actuation is maintained along all edges. This simultaneous actuation is referred to as single-input. A preliminary periodic forcing is performed as benchmark for the results of LGPC. The tested frequencies and duty cycles (DC) are the subset of the harmonics derived from $F_{RT} = 2 \text{ kHz}$, see the red dots in Fig. 3.6. The optimal periodic forcing is found at $St_H^\circ = 6.6$ and $DC^\circ = 33\%$, resulting in $J = 0.67$ which

corresponds to 33% base pressure recovery associated with 22% drag reduction. Hereafter, this optimal solution, denoted by b° and named as SIPF for single-input periodic forcing, will be used as reference.

In the turbulent wake, the frequency dynamics are broadband suggesting that the periodic forcing space may be not sufficient to search for the optimal control law. In this section, we extend the search space of open-loop control by exploring the multi-frequency forcing using LGPC-1. The results of LGPC-1 are given in § 3.4.1. The corresponding optimal control is analyzed in detail in § 3.4.2 and the mean wake modifications associated with the optimal control is presented in § 3.4.3.

3.4.1 LGPC-1 results

The introduction of multiple frequencies in the actuation should expand the search space of control laws. Multi-frequency forcing has already reported benefits in other flow configurations, for instance pressure recovery in a diffuser (Narayanan *et al.*, 2002). So far, this was not explored for the drag reduction problem. LGPC-1 is particularly appropriate for constructing multi-frequency signals and determining the optimal actuation. In the case with simultaneous actuation along four edges, this control category can be also labeled as SIMFF for single-input multi-frequency forcing.

In the LGPC-1 framework, the open-loop control laws are written as $b(t) = K(\mathbf{h}(t))$. We define $\mathbf{h} = \{h_1, \dots, h_9\}$ where $h_i(t) = \sin(2\pi f_i t)$ represents the harmonic function at the frequency f_i . The values of f_i considered in this study and the corresponding Strouhal number $St_{H_i} = f_i H / U_\infty$ are presented in table 3.3. The goal is to find an optimal function K^h , where the superscript ‘h’ indicates harmonic, such that $b^h(t) = K^h(\mathbf{h}(t))$ minimizes the cost function J .

Controller input	h_1	h_2	h_3	h_4	h_5	h_6	h_7	h_8	h_9
f_i (Hz)	10	20	50	100	200	250	333	400	500
St_{H_i}	0.2	0.4	1	2	4	5	6.6	8	10

Table 3.3: Description of the harmonic functions $h_i(t) = \sin(2\pi f_i t)$ used as inputs of LGPC-1 for multi-frequency forcing.

Four generations with 50 individuals in each generation are evaluated. The generation number is small because after four generations half of the individuals have similar J values near the optimal one as shown in Fig. 3.9(a). When the number of generation n increases, we observe a global trend to obtain lower values of J , but the evolution of the top-performing individuals is insignificant. To clarify this behavior, the cost J_1^n of the optimal individual ($m = 1$) in each generation n is shown in Fig. 3.9(b). The dots correspond to the averaged J values and the error bars show the standard deviation of repeating evaluations of the optimal control law. For the two first generations ($n = 1, 2$), the optimal individual exhibits the same frequency ($St_H^\circ = 6.6$) and duty cycle ($DC^\circ = 33\%$) as the optimal SIPF solution b° . In the third generation, a new individual evolves leading to a gain of 1% in reduction of J compared to the previous generations. This individual is confirmed to be the optimal one at the fourth generation. Due to the experimental uncertainties, there is a slight difference in the averaged J values for the identical actuations, like the optimal individual at $n = 3$ and $n = 4$.

We focus on the converged generation. Due to the binary ON/OFF command, and the necessity to apply an Heaviside function to the control law (see § 3.2.5), it is possible to have different control laws which give the same actuation b . For instance, the first five individuals of the last generation may have only three different kinds of actuations with respect to the

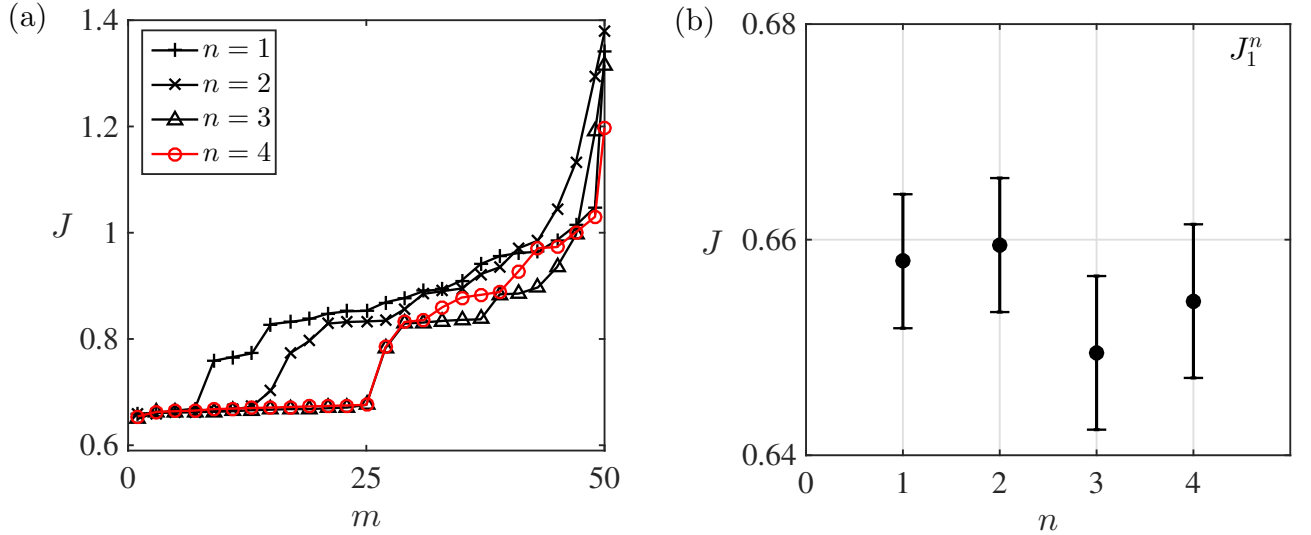


Figure 3.9: Results of LGPC-1 for single-input multi-frequency forcing. (a) Evolution of the cost function J versus the individuals m for four generations $n = 1, \dots, 4$. (b) Cost of the optimal individual J_1^n in the four generations $n = 1, \dots, 4$. The dots correspond to the averaged J values and the error bars show the standard deviation of repeating evaluations of the optimal control laws.

spectral behavior. In the following, we name the first three distinct actuations in the top-ranking individuals of the last generation as b_1^h, b_2^h and b_3^h , respectively. The actuation power spectral densities S_b for b_m^h ($m = 1, \dots, 3$) are displayed in Fig. 3.10(a) in the range $St_H \in [0, 10]$ with a vertical shift for clarity. One period of the actuation b_m^h and its corresponding duty cycle are presented in Fig. 3.10(b). The solution b_3^h contains a single-frequency corresponding to the optimal SIPF b° . b_1^h and b_2^h exhibit a multi-frequency dynamics with the dominant frequency $St_H = 8$ and $St_H = 6.6$, respectively, and their subharmonics ($St_H = 4$ and $St_H = 3.3$).

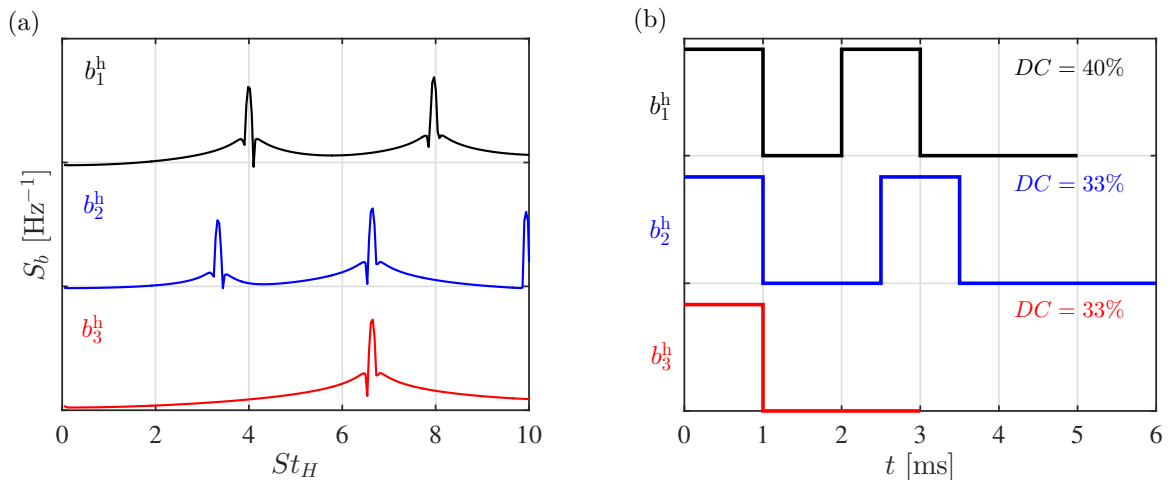


Figure 3.10: Actuation properties of the three top performing individuals in the last generation of LGPC-1. (a) Power spectral densities S_b for the control laws b_1^h, b_2^h and b_3^h . (b) One period of the actuation b_m^h ($m = 1, \dots, 3$). Values on the vertical axis are shifted for clarity.

To discuss the energetic efficiency of the control, we define an actuation efficiency coefficient A_e and a relative power savings coefficient P_s as follows:

$$A_e = \frac{|\Delta C_D| SU_\infty^3}{S_{\text{Jet}} \overline{V_{\text{Jet}}^3}} \quad \text{and} \quad P_s = \frac{\frac{1}{2} |\Delta C_D| SU_\infty^3 - \frac{1}{2} S_{\text{Jet}} \overline{V_{\text{Jet}}^3}}{\frac{1}{2} \overline{C_{D_u}} SU_\infty^3}, \quad (3.5)$$

with $\Delta C_D = \overline{C_{D_u}} - \overline{C_{D_a}}$ where the subscripts ‘u’ and ‘a’ indicate the unforced and actuated flows, respectively. The actuation efficiency A_e represents the ratio between the mechanical power gained by the drag reduction and the mechanical power consumed by the pulsed jets. The relative power saving P_s represents the net power saving related to the control normalized by the power consumed by the aerodynamic drag in the unforced flow. The expressions of the control laws b_m^h , $m = 1, \dots, 3$ are reported in table 3.4 with the corresponding values of the cost J , the actuation amplitude C_μ , the actuation efficiency A_e and the power saving P_s . All the actuation efficiencies A_e are greater than 1 and all the relative power saving coefficients P_s are greater than 0 indicating that the net energy balance is positive. The optimal actuation b_1^h results in about 34.6% of base pressure recovery. The returned gain of the invested actuation power is approximately three. The power consumed by the aerodynamic drag has been saved by 15.6%.

Control law	J	$C_\mu (\times 10^{-3})$	A_e	P_s
$b_1^h = H(h_5/h_8 - 0.622)$	0.654	9.834	2.958	0.156
$b_2^h = H((h_9 - h_7) - 0.2)$	0.661	10.927	2.317	0.131
$b_3^h = H((-0.479h_7 - 0.2))$	0.664	9.609	2.841	0.146

Table 3.4: Performance of the three top performing individuals in the last generation of LGPC-1. H represents the Heaviside function. By definition, $H(x) = 0$ if $x \leq 0$ and $H(x) = 1$ otherwise.

In the following, we study the convergence of LGPC-1 towards the optimal control law by analyzing how the different harmonic functions h_i are selected over the generations. The percentage P_{h_i} of having h_i involved in the individuals is displayed in Fig. 3.11(a) for all the generations. In the first generation, all the harmonic functions are loosely equivalent to be chosen. Note that if the population was larger, we would have a uniform distribution of h_i . At the second generation, the percentage of presence of h_7 raises abruptly for becoming largely dominant. At the third generation, P_{h_8} grows and now becomes dominant. At convergence, h_7 and h_8 are the two harmonic functions most commonly found in all the individuals. This result demonstrates the ability of LGPC-1 to select automatically the optimal harmonic forcing parameters. The spectrum of J -values of individuals which include h_i in the expression of the individuals is shown for all the generations in Fig. 3.11(b). More precisely, we plot for each individual the cost J (in ordinate) against the harmonic functions h_i (in abscissa) occurring in it. Over the generations, the data points move progressively from a relatively sparse distribution to a concentrated distribution in the bottom right region, proving that the best individuals are obtained for high frequencies.

In addition, multiple-input multi-frequency forcing (MIMFF) has also been performed by driving the top, down, left and right actuators independently. The search space is much more larger than that of the single-input control. The optimal single-input control law (SIMFF) was inserted in the first generation to accelerate convergence. The results show that LGPC-1 with multiple inputs did not improve the performance for the best single-input law.

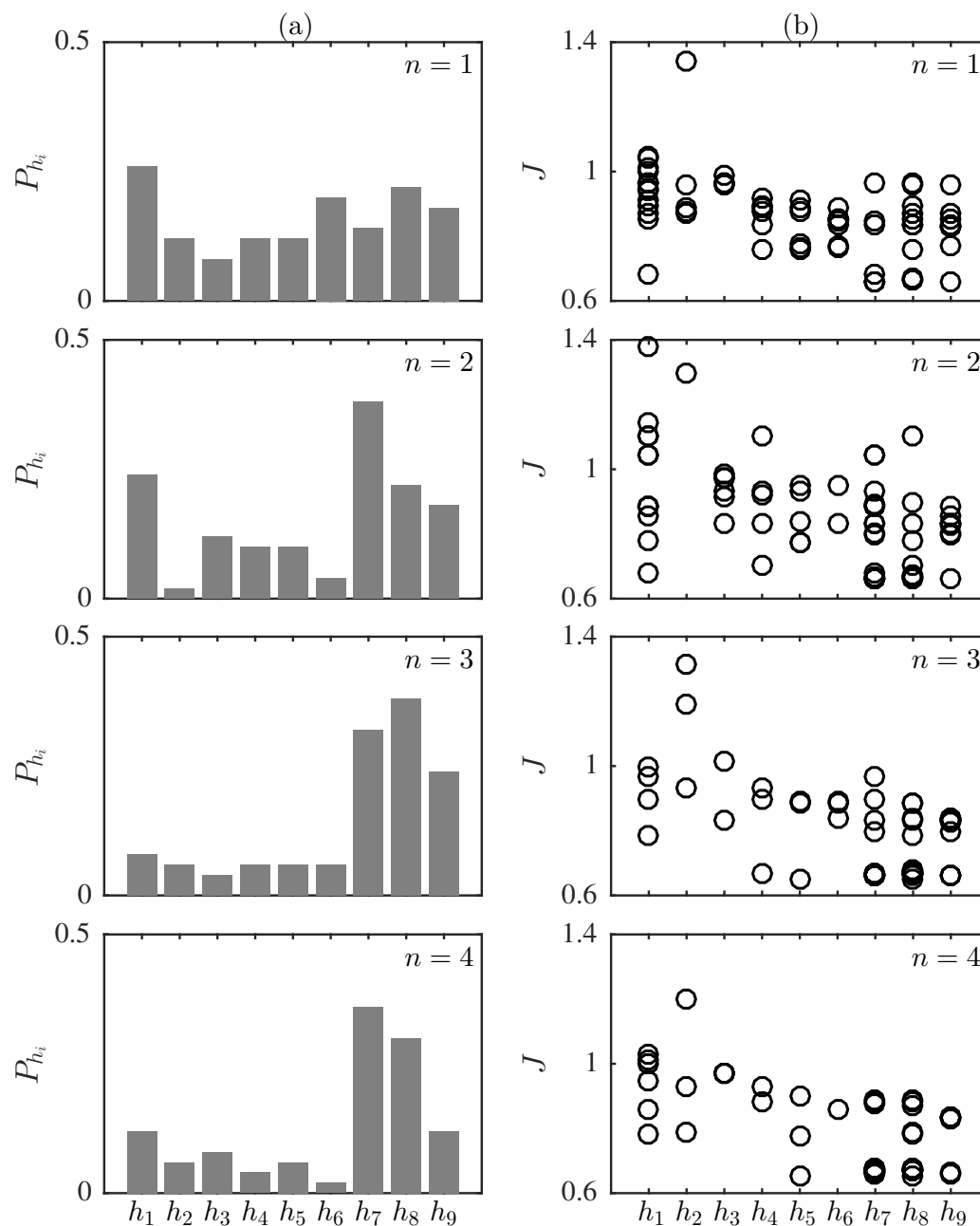


Figure 3.11: Convergence of LGPC-1 for single-input multi-frequency forcing. For each generation $n = 1, \dots, 4$, we represent: (a) the percentage P_{h_i} of having h_i in the expression of the individuals, (b) the spectrum of J -value of individuals which include h_i in their expression.

3.4.2 Analysis of the optimal control law

Now we focus on how the optimal single-input LGPC-1 law $b^\odot = b_1^h = H(h_5/h_8 - 0.622)$ influences the base pressure. We first investigate the instantaneous impact of actuation on the base pressure. Figure 3.12(a) represents the time evolution of the bottom-middle pressure coefficient C_{p_4} under several periods of the actuation b^\odot . C_{p_4} is corrected in amplitude and phase based on the approach described in § 3.2.3. In addition, b^\odot is shifted 1 ms downward in time to take into account the actuator delay (see § 3.2.2). The corrected signals are used here because we are interested in the pressure response at the base surface to the actuation. We notice in Fig. 3.12(a) that the apparent frequency in pressure fluctuation is tightly related to that of the actuation. This correlation can be further inferred from the spectral coherence $\Psi_{b, C_{p_i}}$ which is defined at each frequency f as follows:

$$\Psi_{b, C_{p_i}}(f) = \frac{G_{b, C_{p_i}}(f)}{\sqrt{G_b(f) G_{C_{p_i}}(f)}}, \quad i = 1, \dots, 16 \quad (3.6)$$

where $G_{b, C_{p_i}}$ is the cross-spectral density between the actuation b^\odot and the i th pressure coefficient C_{p_i} , and G_b and $G_{C_{p_i}}$ are the auto-spectral density of b^\odot and C_{p_i} , respectively. Figure 3.12(b) displays the amplitude of the spectral coherence $\Psi_{b, C_{p_i}}$. We observe a level of coherence of about 100% at $St_H = 4$ and $St_H = 8$ which are indeed the forcing frequencies shown in Fig. 3.10(a). These high values of coherence at the forcing frequencies have been equally observed for the other pressure signals implying that all sensors over the base are correlated to the actuation regardless of their locations. From these observations a question arises: do the sensors respond to the actuation at the same time? To address this question, the coherence $\Psi_{C_{p_i}, C_{p_j}}$ between the pressure signals C_{p_i} and C_{p_j} is studied. From $\phi_{i,j}$, the phase of $\Psi_{C_{p_i}, C_{p_j}}$, we have determined the time shift at frequency f between the pressure signals C_{p_i} and C_{p_j} as $\phi_{i,j}/(2\pi f)$. This value is of the order of 0.2 ms for all sensors which may be related to the distance between pressure taps and to the slight length difference of tube mounting of two sensors. We can then conclude that all the pressure signals respond to the actuation at the same time.

The results above have important implications for the understanding of actuation effects. As described in Barros *et al.* (2016b), the combination of pulsed jets and Coanda surface creates

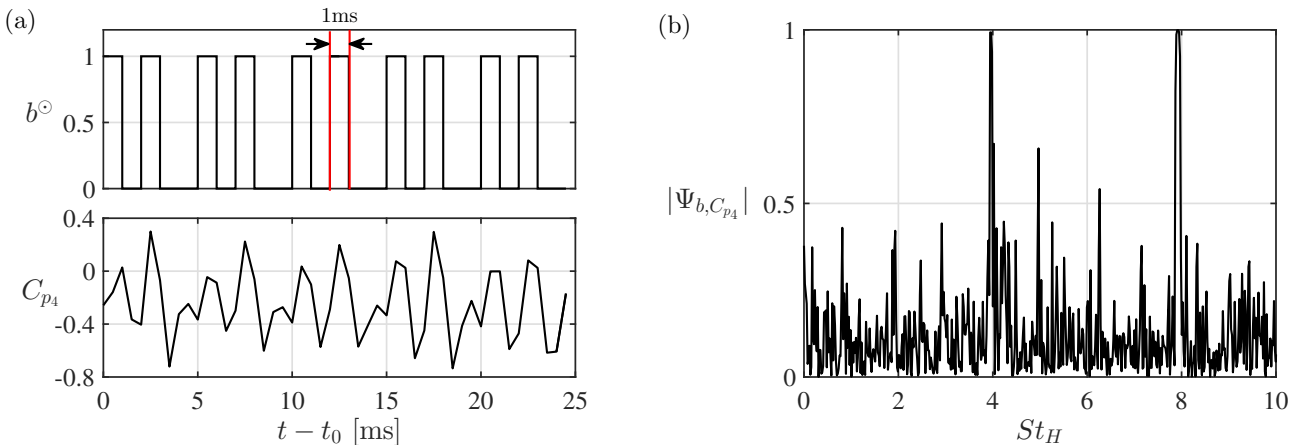


Figure 3.12: Impact of the optimal LGPC-1 law b^\odot on the pressure coefficients. (a) Instantaneous response of C_{p_4} to the actuation b^\odot . The time is shifted by a randomly chosen value t_0 . (b) Amplitude of the spectral coherence between the actuation b^\odot and pressure coefficient C_{p_4} .

a *boat-tailing effect* resulting in an inward shear layer deviation close to the separating edges, and thus yields a time-averaged base pressure increase. Here we want to elucidate the existence of an instantaneous boat-tailing effect by analysing the temporary response of the pressure to the actuation. The underlying dynamics can be derived from the time history of the area-averaged pressure $\langle C_p \rangle$ under the unsteady forcing. Figure 3.13 shows the phase average of the jet velocity, denoted by $\llbracket V_{\text{Jet}} \rrbracket$, and the phase average of the area-averaged base pressure, denoted by $\llbracket \langle C_p \rangle \rrbracket$, under a frequency $St_H = 2$ (a) and the optimal control b^\odot (b). The symbol $\llbracket \cdot \rrbracket$ stands for the phase average ¹. A moderate value of frequency is chosen in (a) to gain insights on the jet propagation over the surface due to its relatively long pulse duration. An overshoot of $\llbracket V_{\text{Jet}} \rrbracket$ is observed at the very beginning of the blowing in Fig. 3.13(a), which may be related to the specific functioning of the valve, i.e. the sudden pressure relief at the outlet of the just opened valve. This overshoot lasts about 1 ms and then the jet stabilizes and

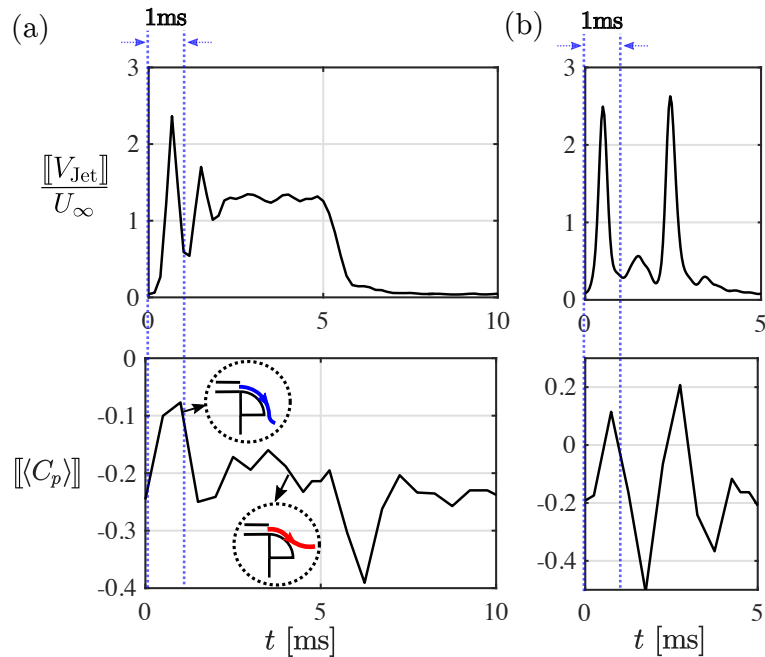


Figure 3.13: Phase-averaged jet velocity $\llbracket V_{\text{Jet}} \rrbracket / U_\infty$ and pressure coefficient $\llbracket \langle C_p \rangle \rrbracket$ with $\langle C_p \rangle$ the area-averaged base pressure. (a) Forced flow at $St_H = 2$ and $DC = 50\%$. (b) Optimal LGPC-1 law b^\odot . The phase average is performed with respect to the lower frequency i.e. $St_H = 4$. The vertical dashed line indicates the time duration for the unsteady overshoot. The inserted figures indicate the different interaction of the jet flow with the Coanda surface in the unsteady and quasi-steady state, respectively.

develops to a quasi-steady blowing. A similar duration of the overshoot has been observed in lower frequencies corroborating that this is probably a characteristic of the actuators. The pressure signal shows correspondingly a sudden and strong increase just at the same time of the overshoot. Following the stabilization of the blowing, the pressure also stabilizes and fluctuates around a particular value. We conjecture that the fluctuations at the different states, unsteady overshoot and quasi-steady blowing, are related to the movement of the separation point over the Coanda surface. We then propose a conceptual scenario attempting to explain the different mechanisms in the unsteady overshoot and quasi-steady state. During the unsteady overshoot, the jet travels over the rounded surface carrying a strong velocity inside the forefront of the jet while facing a relatively low-velocity flow on its outside. As a first-order approximation, this process is too short to give the opportunity to the viscosity to affect the flow. Therefore, the

¹ $\llbracket g \rrbracket(t) = \frac{1}{N_{\text{period}}} \sum_{i=0}^{N_{\text{period}}} g(t + iT)$, where g is the quantity to calculate, N_{period} the number of periods included in the recording time and T the period.

instantaneous velocity acceleration is almost totally used to compensate the reversed pressure force over the rounded surface. We denote by t_{Prop} the propagation time of the jet from the slit exit to the end of the Coanda surface. This propagation time can be estimated as $t_{\text{Prop}} = \ell / \overline{V_{\text{Jet}}}$ where $\ell = \pi r/2$ is the arc length of the surface and $\overline{V_{\text{Jet}}}$ is the time-averaged jet velocity. If we approximate $\overline{V_{\text{Jet}}}$ by the oncoming velocity U_∞ , we obtain $t_{\text{Prop}} = 0.94$ ms. This value is surprisingly close to the duration of the unsteady overshoot. This means that the jet flow can completely attach on the surface within the unsteady state under the condition of $\overline{V_{\text{Jet}}} > U_\infty$. By intuition, the flow may be highly deviated as illustrated in the inserted figure for the overshoot state. Once entering into the steady state, the pressure fluctuation decreases. The reason is twofold: first, the jet velocity has significantly decreased compared with the overshoot resulting in a lower jet momentum flux; second, viscous effects have now the time to reduce the mean wall momentum and to induce an earlier flow separation and a less deviated flow, as shown in the inserted figure for the quasi-steady state. When the blowing is stopped, there is a significant decrease of pressure which remains unclear. It seems as if the jet closure somehow induces a strong detachment of the flow.

Given the important role played by this unsteady effect, one would expect that the actuation should take advantage of this unsteady overshoot to gain benefits in the base pressure. Figure 3.13(b) shows the phase-averaged jet velocity $[[V_{\text{Jet}}]]$ measured for the actuation b^\odot . This jet velocity exhibits two overshoots in one period. The base pressure is consequently excited to a high value. Our conjecture above concerning the relation between the pressure increase and the flow deviation is confirmed here by the phase-locked PIV measurements of the small field surrounding the Coanda surface, as presented in Fig. 3.14. The red circles in the figures of $[[\langle C_p \rangle]]$ indicate the phases of the velocity fields. In Fig. 3.14(a), the flow is attached until to the end of the Coanda surface, resulting in a significant flow deviation manifested by the streamline curvature. Correspondingly, we observe an increase of $[[\langle C_p \rangle]]$. Fig. 3.14(b) shows a less deviated streamline due to an earlier flow separation on the curved surface, hence the resulting $[[\langle C_p \rangle]]$ is much smaller than that in (a).

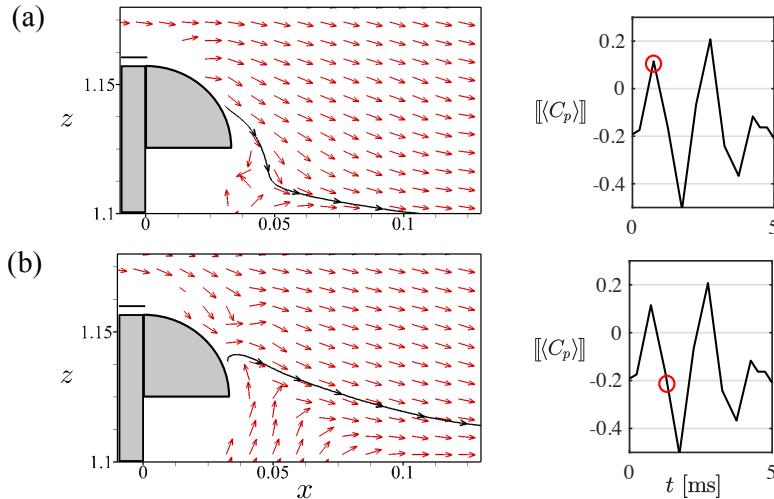


Figure 3.14: Phase-locked velocity vectors for the forced flow with the optimal LGPC-1 law b^\odot at (a) phase $t/T = 0.1$ and (b) phase $t/T = 0.2$. T is the period with respect to $St_H = 4$. The red circles in the figures of $[[\langle C_p \rangle]]$ indicate the phase of the velocity field on the left. The streamlines are drawn to highlight the change of its curvature.

The repeated unsteady flow deviation as presented in Fig. 3.14(a) leads ultimately to a time-averaged base pressure recovery. This explains why the high-frequency forcing yields a better performance. We define t_{Pulse} the pulse duration of one pulsed jet and t_{Int} the intermittent

time between two successive pulsed jets. It is expected that t_{Pulse} could be as small as possible to eliminate the quasi-steady blowing. In addition, $\llbracket V_{\text{Jet}} \rrbracket$ should be strong enough to drive the jet to the end of the Coanda surface in t_{Pulse} . Considering the actuator response time and the characteristic time for the overshoot, the smallest value for t_{Pulse} is determined to be 1 ms. Surprisingly, the top-ranking individuals in Fig. 3.10(b) are all in good agreement with our hypothesis. They have all $t_{\text{Pulse}} = 1$ ms but t_{Int} is different. The optimal control $b^\odot = b_1^h$ is the only actuation including $t_{\text{Int}} = 1$ ms, as shown in Fig. 3.12(a). We may conclude that b^\odot meets best the requirements for t_{Pulse} , t_{Int} and $\llbracket V_{\text{Jet}} \rrbracket$ ensuring a maximized repeat of the unsteady overshoot effect, and therefore is chosen as the optimal controller.

3.4.3 Analysis of the near wake

Now, we focus on the effects of the best LGPC-1 control b^\odot on the near wake dynamics identified from the PIV measurements. We remind that all presented quantities are normalized by U_∞ and H . Figure 3.15 shows the color map of the time-averaged velocity norm $\|\mathbf{u}\| = \sqrt{\bar{u}^2 + \bar{w}^2}$ overlapped with 2D streamlines (a, b) and 2D estimation of the turbulent kinetic energy $k = \frac{1}{2}(\overline{u'^2} + \overline{w'^2})$ (c-f) for the unforced (a,c,e) and controlled flow (b,d,f). \bar{u} and \bar{w} represent the time-averaged streamwise and cross-stream velocity, respectively. u' and w' are their corresponding velocity fluctuations.

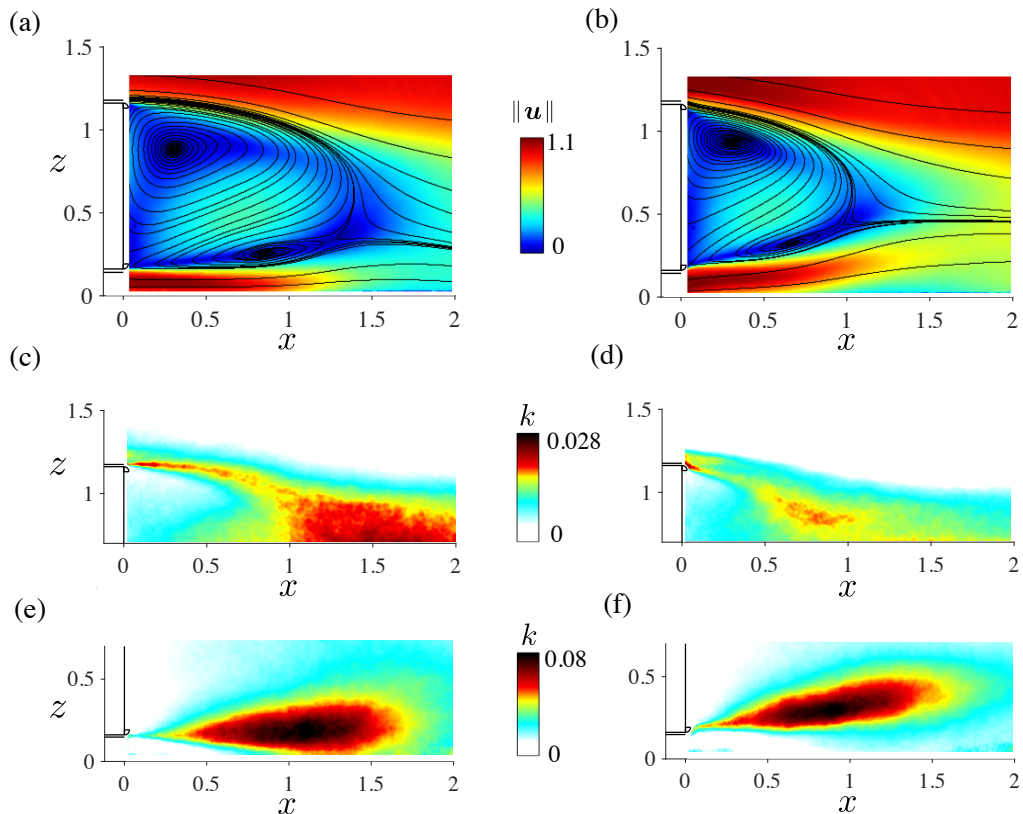


Figure 3.15: Near wake dynamics for the unforced baseline flow (a,c,e) and the forced flow with the optimal LGPC-1 control b^\odot (b,d,f). (a,b) Time-averaged velocity norm $\|\mathbf{u}\|$ and 2D streamlines; (c,d) 2D estimation of the turbulent kinetic energy k for the upper shear layer; (e,f) k for the lower shear layer.

The forcing induces significant changes in the wake. First, the shear layers are highly deviated towards the center of the wake, resulting in a thinner and shorter recirculation bubble.

The bubble length L_r is quantified by the maximum streamwise position of the contour line $\bar{u} = 0$, i.e.

$$L_r = \max_x(\bar{u}(x) = 0). \quad (3.7)$$

For the forced flow, $L_r \approx 1.06$, reduced by 25% compared with the baseline flow length $L_r \approx 1.42$. The vectorization of the shear layer is highlighted in Fig. 3.16(a) by the velocity angle $\theta = \arctan(\bar{w}/\bar{u})$ of the streamline emerging from the point $(x, z) = (0.033, 1.198)$ located close to the top separating edge. The angle variation immediately downstream of the trailing edge ($x < 0.1$) indicates that there is a reversal in the sign of the streamline curvature. This modification of curvature results in a local rise in base pressure. Second, the vectorization of shear layers is accompanied by an overall reduction of the turbulent kinetic energy k inside the recirculation bubble, which can be qualitatively observed in Fig. 3.15(d) and (f). Following the analyses in Barros *et al.* (2016b), we quantify the modification of the wake dynamics by evaluating the streamwise evolution of the integral of the turbulent kinetic energy $\mathcal{K}(x)$ and averaged kinetic energy $\mathcal{E}(x)$ inside the domain $\Omega_{(\bar{u}<0)}$ defined as follows:

$$\mathcal{K}(x) = \int_{\Omega_{(\bar{u}<0)}} k(x, y) dy, \quad (3.8)$$

$$\mathcal{E}(x) = \underbrace{\int_{\Omega_{(\bar{u}<0)}} \frac{\bar{u}^2(x, y)}{2} dy}_{\mathcal{U}(x)} + \underbrace{\int_{\Omega_{(\bar{u}<0)}} \frac{\bar{w}^2(x, y)}{2} dy}_{\mathcal{W}(x)}. \quad (3.9)$$

The results are shown in Fig. 3.16 (b) and (c). We observe an overall reduction of \mathcal{K} in the forced flow from $x/L_r = 0.25$, indicating an attenuation of the velocity fluctuations in the wake. A decrease of \mathcal{E} is discernible very close to the base ($x/L_r < 0.08$) and further downstream $x/L_r > 0.33$. Between these two bounds, there is a slight increase of \mathcal{E} . To gain insights into this evolution, we present separately the contribution of streamwise velocity $\mathcal{U}(x)$ and cross-stream velocity $\mathcal{W}(x)$ to $\mathcal{E}(x)$. The decrease of \mathcal{E} in the range $x/L_r < 0.08$ is directly related to the reduction of \mathcal{W} near the base, indicating that the cross-stream flow adjacent to the base is less energetic in the forced flow. Further downstream, \mathcal{W} increases compared with the baseline flow. In fact, the prominent deviation of the shear layers pushes the flow towards the central region of the wake and thus increases the absolute value of cross-stream velocity. Correspondingly, we observe an increase of \mathcal{E} in the range $x/L_r \in [0.08, 0.33]$. Beyond $x/L_r = 0.33$, the decrease of \mathcal{U} is amenable to the diminution of \mathcal{E} . The overall attenuation of \mathcal{U} indicates that the streamwise motion of the reversed flow is reduced by the forcing.

These observations show that a base pressure recovery is associated with: (1) the vectorization of the shear layers which changes the streamline curvature and narrows and shortens the bubble; (2) the stabilization of the wake induced by the enhanced interaction of the small- and large-structures due to the high-frequency forcing. These mechanisms are consistent with the results in Barros *et al.* (2016b) except that they did not observe a shorter bubble. This difference is related to the actuation parameters. We actuate at a lower frequency and higher amplitude, yielding a higher angle deviation which is responsible for reducing the bubble length.

3.5 LGPC-2: Feedback control

In this section, we explore the opportunities of the sensor-based closed-loop control by employing LGPC-2. Similar to the previous section, all actuators are operated simultaneously by a single actuation command. The results of LGPC-2 are given in § 3.5.1. The resulting control

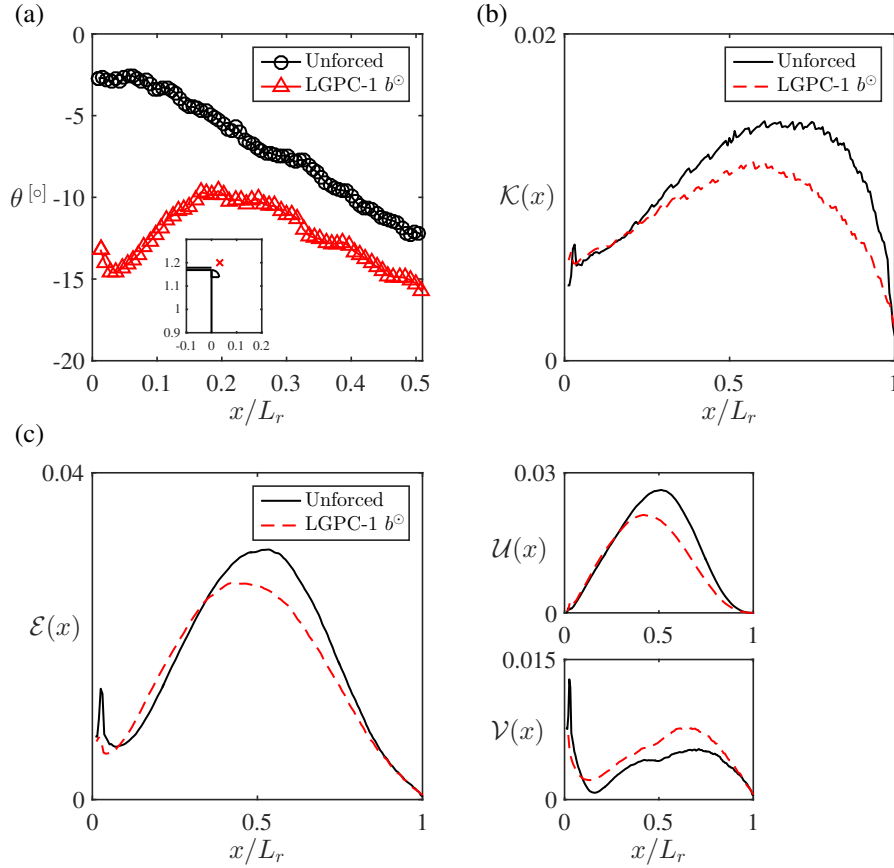


Figure 3.16: Effects of the optimal LGPC-1 control b^{\ominus} on the shear layer deviation and the velocities inside the recirculation bubble. (a) Evolution of the velocity angle θ along the streamline emerging from the point $(x, z) = (0.033, 1.198)$ (marked by ‘x’ in the inserted figure) close to the top trailing edge; (b,c) streamwise evolution of \mathcal{K} (see Eq. (3.8)) and \mathcal{E} (see Eq. (3.9)).

laws are visualized and interpreted in § 3.5.2. Section 3.5.3 presents a physical analysis of the optimal control law.

3.5.1 LGPC-2 results

The closed-loop control law is expressed as $b = K(\mathbf{s})$, where \mathbf{s} consists of the pressure sensors distributed over the rear surface. For the feedback, it was found that the first 12 sensors in Fig. 3.2(c) are sufficient for the performance of the controller, the sensors 13–16 providing redundant information. The cost J is evaluated based on all 16 sensors following Eq. (3.1). This control is referred to as single-input multiple-output (SIMO) as we have one actuation command and 12 sensor signals. From the sensors, only the fluctuation part is fed back to mitigate the effect of slow drifts. The fluctuation of i th sensor s'_i is defined as:

$$s'_i(t) = s_i(t) - \bar{s}_i(t) \quad (3.10)$$

where

$$\bar{s}_i(t) = \frac{1}{\tau_{\text{av}}} \int_{t-\tau_{\text{av}}}^t s_i(t) dt \quad (3.11)$$

is the moving average of the signal over a period $\tau_{\text{av}} = 0.1$ s. Summarizing, the control law has the form

$$b = K(\mathbf{s}') \quad \text{with} \quad \mathbf{s}' = \{s'_1, \dots, s'_{12}\}.$$

The results of the LGPC-2 experiment are presented in Fig. 3.17. We stop LGPC-2 after five generations because the cost J does not evolve anymore. Figure 3.17(a) shows the evolution of J versus the index of the individual m . Almost all the individuals improve their values of cost function compared to those of the first generation. We focus on the evolution of the optimal individual in each generation in Fig. 3.17(b). The optimal individual yielding $J \approx 0.72$ is found from the generation $n = 2$ and is further confirmed as the optimal one until $n = 5$. The error bar is determined from re-evaluations of mathematically equivalent control laws in all the generations. The spectrum of the optimal individual in the final generation $n = 5$, denoted by b^\bullet , is shown in Fig. 3.17(c). The spectrum of the optimal SIPF b° is also included for comparison. b^\bullet evidences a dominant frequency at $St_H = 6.9$ with a duty cycle of $DC = 34.7\%$. Both parameters are quite close to those of b° . However, b^\bullet has a more complex spectrum than b° . The components of this spectrum are more clear in Fig. 3.18 where the time evolution of frequency is shown using the continuous Morlet wavelet transform (Lewalle, 1995). After a short transient, the control self-sustains loosely around $St_H = 6.9$ with occasionally coexistent low-frequency components.

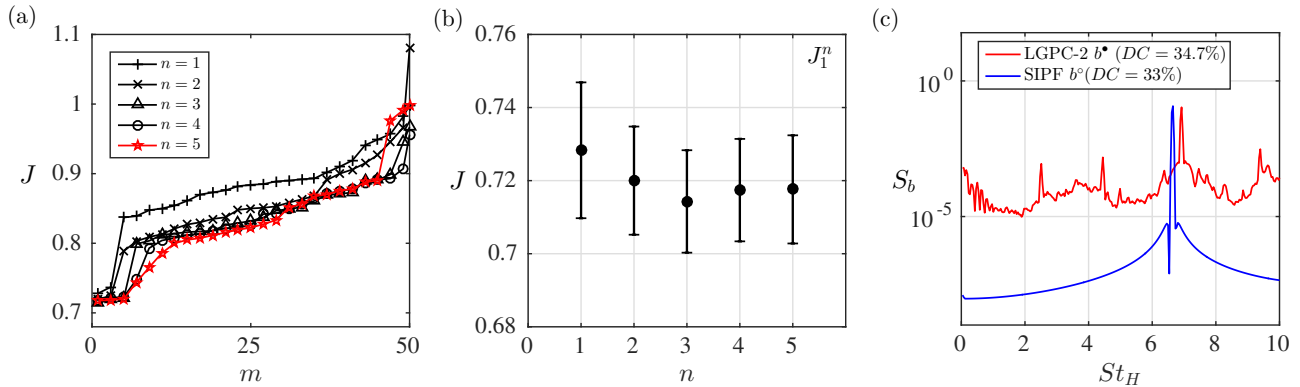


Figure 3.17: Results of LGPC-2 for sensor-based single-input multiple-output (SIMO) control. (a) Evolution of the cost function J versus the individuals m for five generations $n = 1, \dots, 5$. (b) Cost of the optimal individual J_1^n in each generation n . (c) Power spectral density S_b for the optimal LGPC-2 law b^\bullet and the optimal SIPF b° .

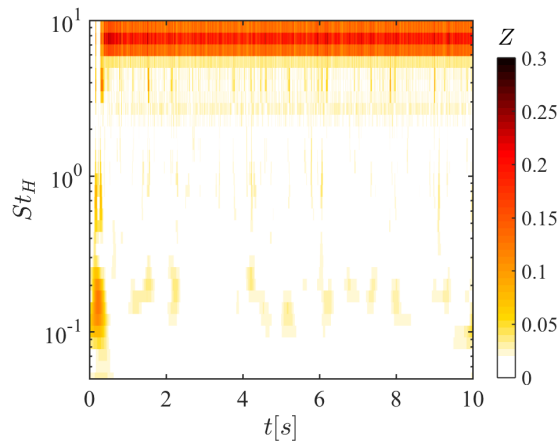


Figure 3.18: Time evolution of frequency for the optimal LGPC-2 control b^\bullet . Z is the norm of Morlet wavelet transform. Higher value indicates higher energy in the spectrum.

Table 3.5 compares the main characteristics of b^\bullet and b° . Closed-loop control has similar actuation features (dominant frequency and duty cycle) as b° . Yet, the performance of b^\bullet is

slightly worse. The presence of low-frequency components in b^\bullet may degrade the performance.

	St_H	DC	J	$C_\mu (\times 10^{-3})$	A_e	P_s
b^\bullet	6.9	34.7%	0.718	10.147	2.428	0.096
b°	6.6	33%	0.664	9.609	2.841	0.146

Table 3.5: Performance of the optimal LGPC-2 control b^\bullet compared with the optimal SIFP b° .

Intriguingly, the optimal control law reads

$$b^\bullet = H(\tanh(\tanh(s'_4)) - 0.1). \quad (3.12)$$

Over the 12 sensors, the optimal control law selects only s'_4 . We present in Fig. 3.19 how LGPC-2 progressively identifies s'_4 in the optimal control law. Figure 3.19(a) illustrates the percentage $P_{s'_i}$ of having s'_i involved in the individuals, and subfigure (b) represents the spectra of J -values of individuals which include s'_i in their expression. Like in Fig. 3.11, the first generation $n = 1$ chooses each sensor signal with comparable percentage. For a sufficiently large population, all the sensor signals would have nearly equal percentage. We observe a minimum J value at s'_4 in the first generation. The advantage of choosing s'_4 is already evident from the second generation. Half of the individuals in the following generations select s'_2, s'_3 and s'_4 . Correspondingly, the data points in Fig. 3.19(b) represent the progressing move of J from a uniform distribution over all the sensors to a concentrated distribution over s'_2, s'_3 and s'_4 . In particular, the highest probability is found at s'_4 . This observation indicates that LGPC-2 provides not only an optimal law but also a sensor selection when initially multiple sensors are provided to the controller. This optimal law will be physically interpreted in § 3.5.3.

3.5.2 Visualization of control laws

A two-dimensional visualization of control laws is obtained by applying the method described in § 2.1.4. This visualization contributes to get a better understanding of the evolution of control laws. The entire collection consisting of $N_K = M \times N = 50 \times 5 = 250$ individuals is considered here. The penalization coefficient in the distance matrix Eq. (2.3) is chosen to be $\alpha = 3.5$ according to the description in § 2.1.4. CMDS, as explained in § A, yields an ensemble of two-dimensional feature vectors $\{\gamma_i\}_{i=1}^{N_K}$, with $\gamma_i = (\gamma_{i1}, \gamma_{i2})^T$. For each individual i , the mutual distances between feature vectors quantify the dissimilarity between different control laws. For further analysis, the ensemble is then partitioned using the k-means clustering algorithm (Lloyd, 1956; Kaiser *et al.*, 2014). Mainly five clusters, denoted by $k_c \in \{1, \dots, 5\}$, can be distinguished. The resulting Voronoi diagram of the clusters is displayed in Fig. 3.20. Each control law is displayed as a circle which is color-coded by the ordering, here defined in terms of the percentile rank. For instance, an individual that performs equal or better than 90% of the ensemble of evaluated control laws is said to be at the 90th percentile rank.

The broad distribution of points over the space illustrates that LGPC-2 has successfully explored a diversity of control laws. The clusters are ordered according to the mean J -value in a cluster. Thus, it can be seen from the distribution of J that the control laws in the lower clusters $k_c = 1, 2, 3$ have better performance than the upper ones $k_c = 4, 5$. The top-ranking control laws are located in the cluster $k_c = 1$. A spectral analysis of the control laws in each cluster shows that this clustering partition discriminates their actuation frequency characteristics. The control laws in the cluster $k_c = 1$ exhibit a similar spectrum as that of the optimal actuation b^\bullet shown in Fig. 3.17(c). Their dominant frequency is around $St_H = 6.9$. The control laws in its neighbouring cluster $k_c = 4$ have the similar dominant frequency as the laws of

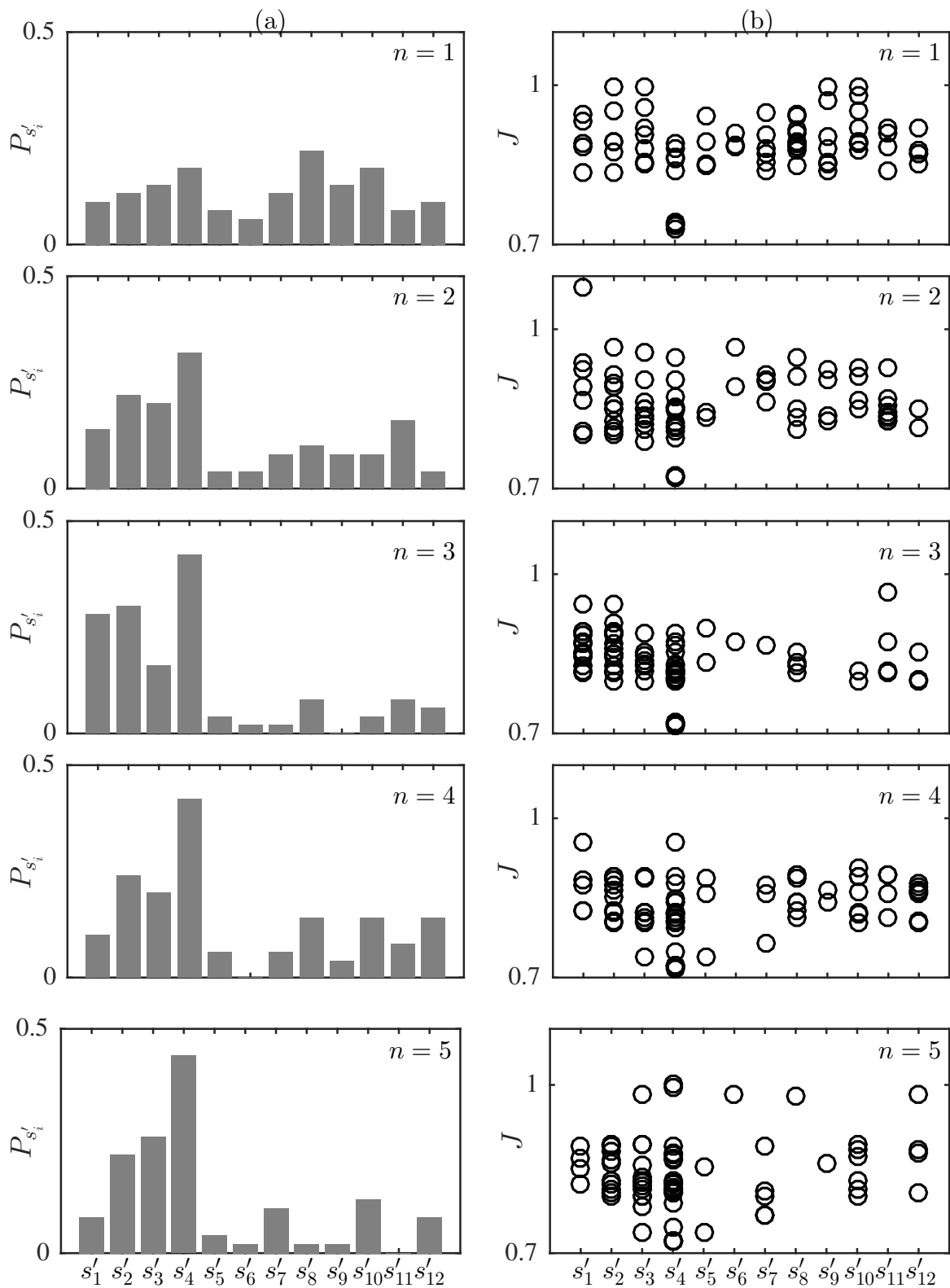


Figure 3.19: Convergence of LGPC-2 for single-input multiple-output (SIMO) control. For each generation $n = 1, \dots, 5$, we represent: (a) the percentage $P_{s'_i}$ of having s'_i in the expression of the individuals, (b) the spectrum of J -value of individuals which include s'_i in their expression.

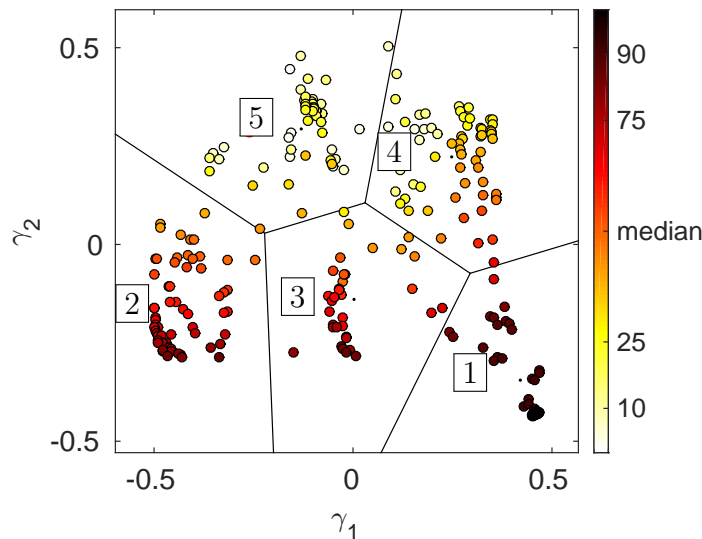


Figure 3.20: Visualization of (dis)similarity associated with the entire collection (250 individuals) of the sensor-based LGPC-2 control laws. Each circle represents an individual control law and the distance between two control laws approximates their respective dissimilarity. The color scheme corresponds to the percentile rank of the control laws with respect to their performance J . Darker color indicates better individuals with lower J values. The feature vectors $\{\gamma_i\}_{i=1}^{N_K}$ are further analyzed by applying a cluster algorithm. The best performing individuals belong to cluster 1.

$k_c = 1$. However, they have a larger duty cycle resulting in a different energy distribution in the actuation spectrum. The clusters $k_c = 3$ and 5 contain the control laws showing a white noise behaviour with no obvious dominant frequencies. The control laws in the upper cluster $k_c = 5$ have a larger duty cycle that those of the lower cluster $k_c = 3$. The control laws in the cluster $k_c = 2$ possess clearly a high dominant frequency around $St_H = 8.6$. It seems that the horizontal coordinate distinguishes the actuation frequencies, whilst the vertical coordinate differentiates the duty cycles. These observations are consistent with their performance distributions. By looking into the evolution of points as the generation increases, a global downward shifting can be observed which indicates their convergence to the top-performing individuals. The visualization provides a simple and revealing picture of the exploration and exploitation characteristics of the control approach, inspiring further improvement of the methodology.

3.5.3 Analysis of the optimal control law

In this section, we analyze the pressure dynamics with an aim of understanding why LGPC-2 has determined the optimal law b^\bullet (see Eq. (3.12)).

We have mentioned previously in § 3.4.2 that better performance is expected for a large jet velocity V_{Jet} under high-frequency forcing. As we binarize the ON/OFF control command with a Heaviside function, an oscillating movement around the threshold of the Heaviside function is responsible to trigger intermittently the actuation. Therefore, the selected sensors are expected to fulfil three properties. First, they should exhibit fluctuations of the unforced baseline to provoke the actuation at the very beginning. Second, they should highly correlate with the high-frequency forcing and yield corresponding fluctuations around the threshold. Third, the low-frequency drifts in the sensors originating from the motion of the separated bubble or the vortex shedding, should not interfere with the high-frequency feedback between actuation and sensing. These expected properties guide our analysis of the sensors for insights into the sensor selection.

First, we search for sensors with large fluctuation levels for the unforced flow. Figure 3.21(a)

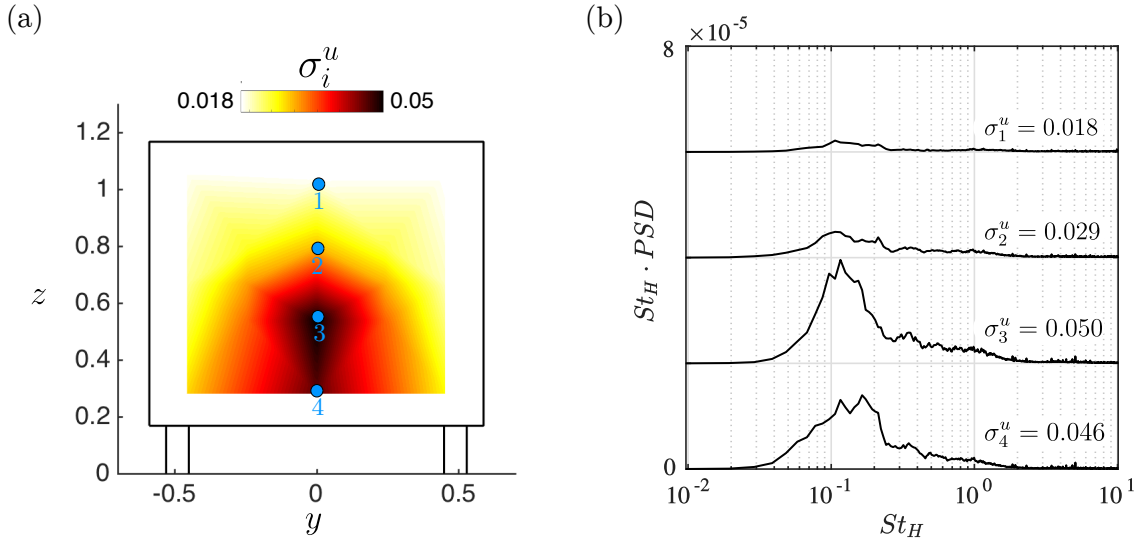


Figure 3.21: Characteristics of the sensor fluctuation in the unforced flow. (a) Color map of the standard deviation of the sensor signal σ_i^u , $i = 1, \dots, 16$. (b) The spectra of sensor signals s_i' located on the symmetry line $y = 0$. Values on the vertical axis are shifted for clarity. The levels of standard deviation σ_i^u of s_i' ($i = 1, \dots, 4$) are also given in the figure.

displays the color map of the standard deviation σ_i^u of the sensor signal s_i' ($i = 1, \dots, 16$) for the unforced flow. The largest fluctuation level can be observed in the vicinity of the lower edge, especially close to the symmetry line $y = 0$. The spectral analysis is carried out using the signals on this symmetry line. The resulting power spectral density (PSD) is shown in Fig. 3.21(b) with a vertical shift for clarity. Clearly, s_3' and s_4' feature a larger fluctuation level than the others. The vortex shedding mode around $St_H = 0.2$ can hardly be seen in this figure. The important energy content around $St_H = 0.1$ in each sensor indicates a global motion of the separation bubble, which is induced by an axial oscillation of the recirculation bubble (Berger *et al.*, 1990). The energy reaches its maximum in sensor s_3' . Based on this observation, we assume that s_3' and s_4' could be the desired candidate sensors in LGPC-2. The next analysis concerns the forced flow. Figure 3.22 shows the color map of the standard deviation of the sensor signal s_i' ($i = 1, \dots, 16$) and the spectra of the sensors on the symmetry line ($y = 0$) under the optimal sensor-based LGPC-2 control b^\bullet (a,c,e) and the optimal SIPF b° (b,d,f). The latter is presented for comparison. Note that the color bar range is different from that in Fig. 3.21. For both forced flows, the pressure fluctuation level is highly increased by the actuation compared to the unforced flow. Fluctuations in the LGPC-2 case are higher than those in the SIPF case. This is assumed to be related to higher actuation fluctuations introduced by the LGPC-2 control, as evidenced in Fig. 3.17(c). These fluctuations are reflected on the base pressure due to the high level of correlation between actuation and sensing at the frequency of actuation (see § 3.4.2). In addition, the region with high fluctuation level is shifted slightly towards the centre of the base for both cases. Characteristic features of high-frequency forcing are the large time delay ($\tau_d = 4.5$ ms) from actuation to sensing and the high correlation between actuation and sensing. The time delay roughly corresponds to two periods of the optimal periodic forcing $St_H^\circ = 6.6$. For closed-loop control, these features indicate that the actuation pulse will be felt by the sensors after time τ_d , and this oscillation in sensors will trigger in real-time another actuation pulse. In other words, an actuation pulse is triggered by the effect of previous pulses. Once some stochastic flow perturbations produce a high-frequency sensor oscillation around the right threshold, the system would self-sustain the high frequency forcing. This explains why the optimal feedback law yields such highly periodic dynamics. One can confirm this behavior from

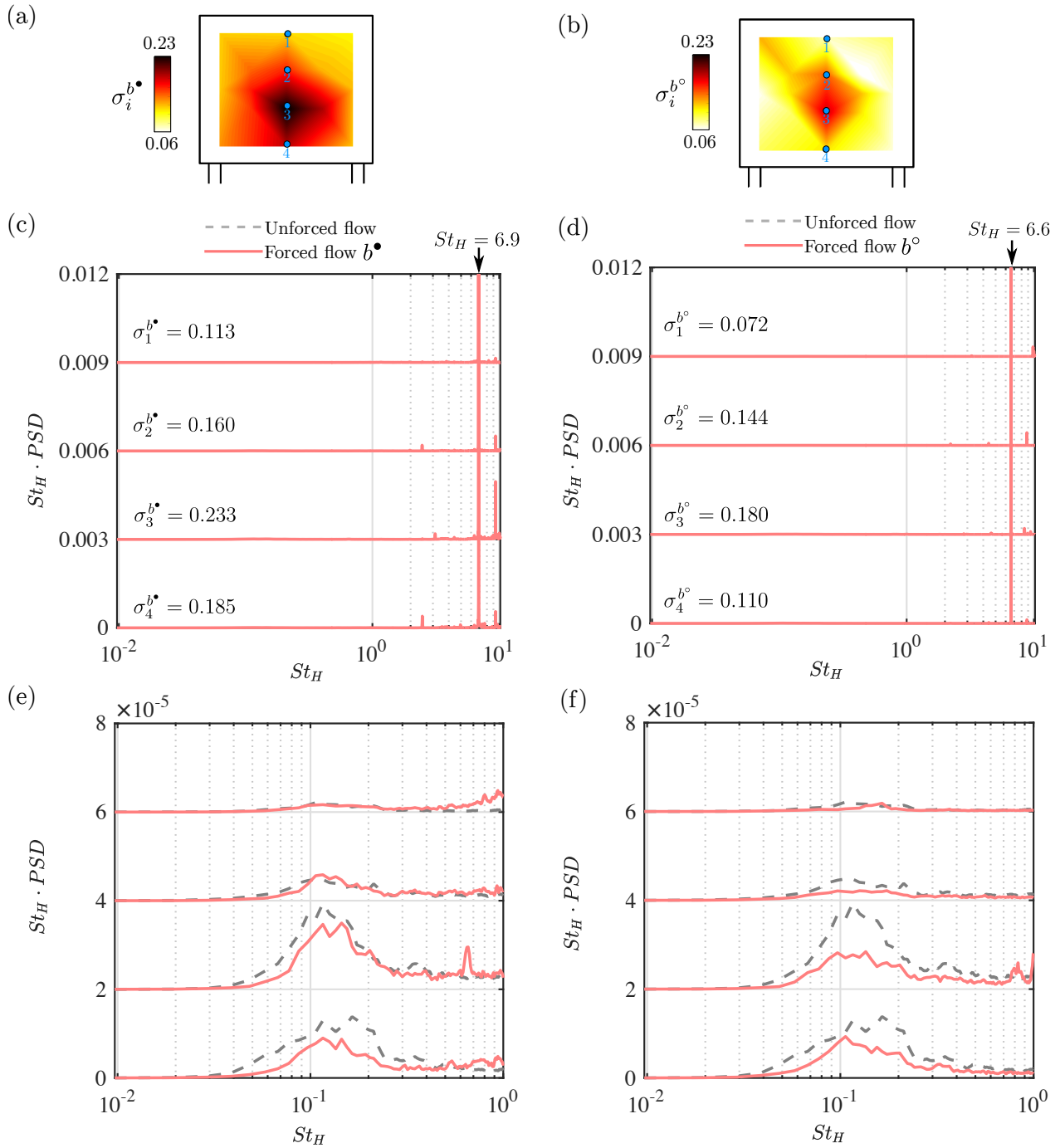


Figure 3.22: Characteristics of the sensor fluctuation in forced flows for (a,c,e) the optimal LGPC-2 control b^\bullet and (b,d,f) the optimal SIPF b° . (a,b) Color maps of the standard deviation of the sensor signals. (c,d) Spectra of sensor signals on the symmetry line $y = 0$ within the frequency range $St_H = [0, 10]$. The arrows indicate the dominant forcing frequency. (e,f) Spectra of above sensors with the low-frequency range $St_H = [0, 1]$. Values on the vertical axis are shifted for clarity. Spectrum of the unforced flow is repeated (in dashed grey line) for comparison.

the spectra in Fig. 3.22(c,d) where the forcing frequencies, indicated by the arrows, are felt by all sensors, being in agreement with the previous results in § 3.4.2. Based on these analyses, we assume that both s'_3 and s'_4 have the capability to capture and amplify the perturbation created by the actuation and feed it back to maintain the forcing.

We now focus on the low-frequency spectrum of the sensor signals under the forcing, which is highlighted in Fig. 3.22(e,f). The spectra of the unforced flow is also presented for reference. An important observation is that the prominent low-frequency dynamics (around $St_H = 0.1$) in the unforced flow is damped by the high-frequency forcing. This damping is even more evidenced by comparing the spectrum of the area-averaged base pressure $\langle C_p \rangle$, as depicted in Fig. 3.23. This may be related with the enhanced interactions between small- and large-scale motions introduced by the forcing, which consequently increases the dissipation in the shear layer and inhibit the entrainment of fluid in the recirculating flow (Oxlade *et al.*, 2015; Barros *et al.*, 2016b). Moreover, the damping effect is more prominent for the optimal SIPF b° , the drag reduction of which is better than that of the optimal LGPC-2 b^\bullet . Thus, we conjecture that the damping in the natural instabilities (bubble pumping or vortex shedding) may be a constituent part for the drag reduction. Figure 3.22(e,f) also presents that for both forced flows, the maximum energy at low frequencies is reproducibly found for s'_3 . This property is, however, a disadvantage for selecting s'_3 as feedback sensor, due to the third postulated sensor property. All these considerations lead naturally to the selection of s'_4 for feedback.

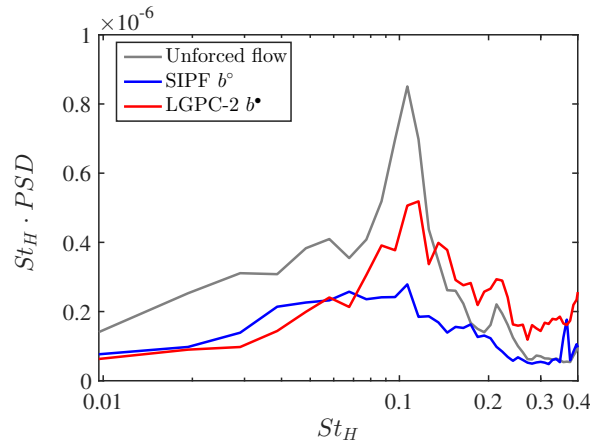


Figure 3.23: Spectrum of the area-averaged base pressure $\langle C_p \rangle$ for the unforced flow (black line), the optimal LGPC-2 b^\bullet (red line) and the optimal SIPF b° (blue line) within the low frequency range $St_H = [0, 0.5]$.

In summary, s'_4 captures, on the one hand, strong enough dynamics in the unforced flow to trigger the feedback cycle and, on the other hand, small enough low-frequency dynamics in the forced flow to maintain the fluctuations around the trigger threshold. Given these conditions, s'_4 is capable to create a nearly periodic high-frequency forcing and it self-adapts to converge to the optimal periodic forcing. Due to the complex dynamics in the flow, closed-loop control has a much noisier spectrum than open-loop control. In time domain, this indicates that there exist a variety of pulse durations t_{Pulse} and intermittent quiet times t_{Int} in the actuation command. In light of the analysis of § 3.4.2, this variety may influence the instantaneous curvature of the shear layer and degrade globally the control performance.

3.5.4 Morlet filtering of sensor signals

In this section, we explore the potential benefits of extracting frequencies of interest in the sensor signals by applying a specific filter. A Morlet wavelet Filter (MF) is particularly suited

to this task. In time domain, the Morlet wavelet ψ is a cosine function modulated by a Gaussian envelope. It is then defined for a frequency f_c as:

$$\psi(t) = \frac{1}{\sqrt{2\pi\sigma}} \exp\left(-\frac{t^2}{2\sigma^2}\right) \cos(2\pi f_c t). \quad (3.13)$$

In frequency domain, MF is a band-pass filter which attenuates the undesired frequencies outside the range $[f_c - \lambda/2, f_c + \lambda/2]$, where λ represents the bandwidth which is governed by the parameter σ . In our applications, only the fourth sensor s_4 identified for the optimal LGPC-2 control is chosen as the output of the plant, resulting in SISO (single-input single-output) system. To avoid the confusion, we denote the fourth sensor s_4 as s and its fluctuation s'_4 as s' . The sensor \mathbf{s} in the feedback control law $b = K(\mathbf{s})$ is defined as $\mathbf{s} = [\hat{s}, \dots, \hat{s}_5, \bar{s}, s']$, where

$$\begin{aligned} \hat{s}_i(t) &= \int_0^{\tau_P} \psi_i(\tilde{t}) s'(t + \tilde{t} - \tau_P) d\tilde{t}, \quad i = \{1, \dots, 5\} \\ \bar{s}(t) &= \frac{1}{\tau_P} \int_{t-\tau_P}^t s(t) dt \\ s'(t) &= s - \bar{s}(t). \end{aligned} \quad (3.14)$$

ψ_i represents the i th Morlet wavelet and \bar{s} is the moving average of the signal over a period of $\tau_P = 0.1$ s. For $i = \{1, \dots, 5\}$, we set $f_{c_i} = \{100, 200, 250, 320, 400\}$ Hz. The corresponding Strouhal numbers are $St_{H_{c_i}} = f_{c_i} H / U_\infty = \{2, 4, 5, 6.5, 8\}$. Figure 3.24 represents the five wavelets in the time and frequency domains. One may notice that the center frequencies in the frequency domain are slightly different to the values of f_{c_i} . This is related to the frequency resolution of the MF which is determined by the wavelet length τ_P considered in Eq. (3.14). In the present study, the wavelet includes 200 points for a time window of $\tau_P = 0.1$ s within the frequency $f_{RT} = 2$ kHz. This leads to a frequency resolution of about $\Delta f = 10$ Hz ($\Delta St_H = 0.2$). The spectra can then be shifted within $\Delta St_H = 0.2$ with respect to the set ones.

The optimal control law $b^\bullet = H(\tanh(\hat{s}_4) - 0.13)$ is obtained after four generations. \hat{s}_4 denotes the filtered signal of s through the wavelet ψ_4 with the centred frequency at $St_{H_c} = 6.5$.

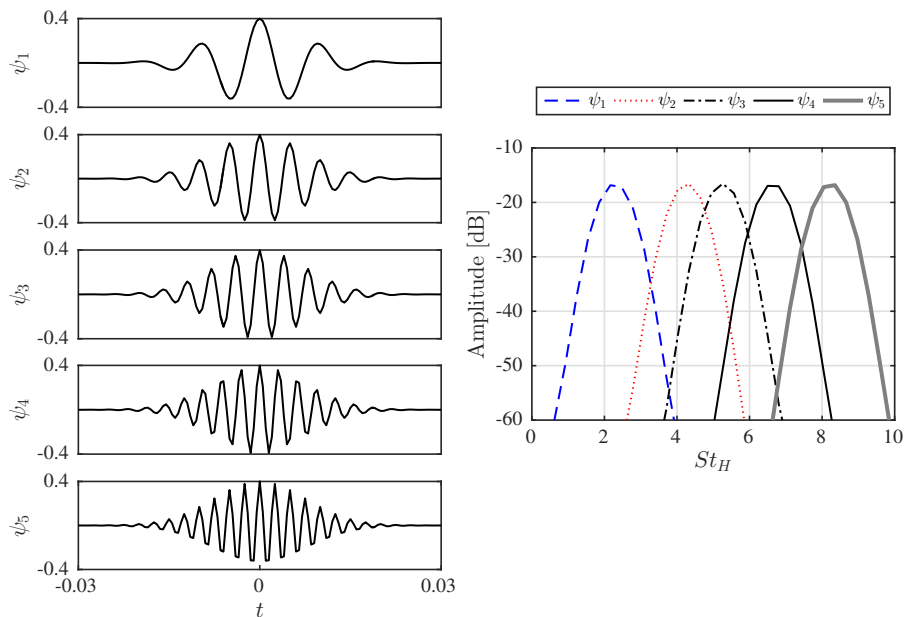


Figure 3.24: Morlet wavelets in time domain (left) and frequency domain (right).

This frequency is closest to that of the optimal periodic forcing $St^\circ = 6.6$ among the provided filtering frequencies. The spectra of the b^\bullet , b° and b° are shown in Fig. 3.25. b° shows a single peak at $St_H = 6.6$, indicating that the noisy fluctuations in b° are filtered out by the MF. As a result, b° leads to approximately a single-frequency forcing which is the same as the optimal SIPF b° , and yields $J = 0.67$ as well.

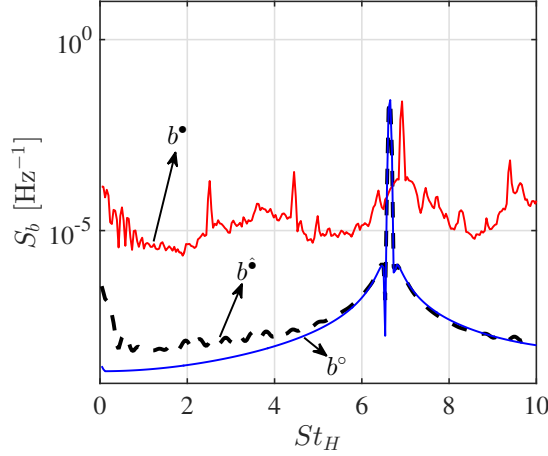


Figure 3.25: Power spectral density S_b of the optimal SISO control law (category LGPC-2) b^\bullet . The spectra of the optimal SIPF b° and the optimal SIMO control law b^\bullet (category LGPC-2) are also given for comparison.

3.6 LGPC-3 and multiple-input control

Finally, a test of the generalized non-autonomous control LGPC-3 is performed by combining the optimal harmonic forcing $h^\circ = \sin(2\pi f^\circ t)$ and the sensors \mathbf{s}' of LGPC-2 of § 3.5.1, i.e. $b = H(K(\mathbf{s}', h^\circ))$. LGPC-3 converges quickly to the optimal periodic forcing b° . The finding is in agreement with the results of LGPC-2 where the optimal control emulates the optimal periodic forcing but is slightly worse. LGPC-3 prefers to select the optimal periodic forcing to the sensor feedback. Upon these results, we do not pursue LGPC-3 with $b = H(K(\mathbf{s}', \mathbf{h}))$ by including multiple frequencies in this experiment. We assume the result will be the same with LGPC-1.

In addition, tests by operating separately the four actuation slits were also performed with the sensor feedback, constituting a multiple-input multiple-output forcing (MIMO). The optimal control laws quickly converge to single-input simultaneous actuation at all four sides, suggesting no performance benefit from operating the four actuators independently in this study. This may be related to the underlying physics for minimizing the drag reduction. It is required to have four edges forced simultaneously to achieve maximized deviation of the flow curvature. However, in the cases where distinct actuators yields different effects, e.g. actuators at different chord position of an airfoil, MIMO control may be a promising control method.

3.7 Summary

The performance in terms of the cost value J is synthesized in Fig. 3.26. In all considered classes of control laws, LGPC-1 identifies a bi-frequency forcing as the most effective control which induces 34% base pressure recovery associated with 22% drag reduction. It beats the past benchmark 19% obtained from periodic forcing with the same configuration (Barros *et al.*,

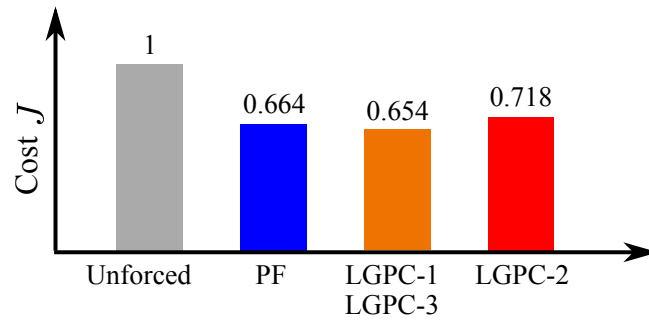


Figure 3.26: Synthesis of the cost value J for different controls. PF: periodic forcing.

2016b). The consumed actuation energy accounts for only 30% of the aerodynamic power saving. It is noteworthy that this control law has been identified by testing only 200 individuals in less than 1 hour. The testing time is less than employed for finding the best frequency and duty cycle for the periodic reference with an exhausting parameter sweep. The two frequencies included in the optimal control law are both one order of magnitude larger than the natural vortex shedding frequency, indicating that the drag reduction is achieved at high frequencies. The associated instantaneous flow response shows that this actuation takes the full advantage of the unsteady shear layer deviation resulted from the interaction of the high-frequency pulsed jets with the Coanda surface. The mean wake geometry is modified such that the shear layers close to the trailing edges are deviated towards the wake center, resulting in a shorter, narrower, more stream-lined shaped bubble. The change of the mean wake geometry is accompanied with a reduction of the velocity fluctuations inside the recirculating bubble. The drag reduction is ultimately achieved by the combined effect of the wake shaping and the damping of velocity fluctuations.

In particular, the feedback control LGPC-2 reproducibly selects only one sensor near the center of the bottom edge in the optimal control law. The corresponding actuation shows a highly periodic behavior whose dominant frequency is close to the optimal periodic forcing frequency. It was further shown that the selected sensor listens to the high-frequency flow components with good signal to noise ratio, thus capable of creating a nearly periodic high-frequency forcing and it self-adapts to converge to the optimal periodic forcing. This finding suggests that LGPC provides not only an optimal actuation but also a sensor optimization for a general class of control laws. Moreover, LGPC-2 finds a SISO control as the optimal control law in a SIMO framework. This observation guided us to explore SISO control with the optimal sensor and its time history information. The resulting SISO control law outperforms the optimal SIMO control and yields a similar actuation as the optimal periodic forcing.

PART II

Physics-based control

Chapter 4

Feedback control of bi-modal wake dynamics

Part of the following contents are published in Li et al. (2016).

In this chapter, we apply a physics-based feedback control to manipulate an intermittent bi-modal wake flow targeting wake symmetrization. Fluidic actuation is applied on lateral edges. The physics-based controller is inferred from preliminary single edge open-loop tests and is demonstrated to successfully suppress the bi-modality. The results show a slightly base pressure recovery concomitant with the wake symmetrization. By analyzing the associated pressure gradient and near wake features, we identify that this pressure recovery is due to a net balance between the favorable effect of wake symmetrization and adverse effect of shear-layer mixing and vortex shedding amplification.

Contents

4.1	Bi-modal wake features and manipulations	69
4.2	Experimental setup	70
4.3	Unforced bi-modal flow	72
4.4	Single edge open-loop forcing	75
4.5	Feedback control	80
4.5.1	Control design and performance	80
4.5.2	Effects on the base pressure and near wake	83

4.1 Bi-modal wake features and manipulations

The turbulent wake of the square-back car model presented in Chapter 3 presents a spanwise symmetry and a top-bottom asymmetry due to the ground effect. However, the wake of such square-back bluff bodies is very sensitive to perturbations, such as the ground clearance and the support setup between the model and the ground. Recently, Grandemange *et al.* (2013b) has identified a reflectional symmetry breaking behavior in the turbulent wake of a similar square-back body under a well aligned condition. The relative wake is denoted by bi-modal wake, also known as bi-stable wake. The feature of a bi-modal wake consists of two mirror asymmetric flow states which switch between them in a stochastic way. Such symmetry breaking behavior of turbulent wakes have been equally observed in very distinctive geometries, such as the flow over a three-dimensional double backward-facing step (Herry *et al.*, 2011), a notch-back vehicle shape model (Lawson *et al.*, 2007) and the wake of an axisymmetric bluff body

(Rigas *et al.*, 2014). However, the asymmetry is not observed in the mean wake obtained over long-time averages when two asymmetric states are equiprobable. Recent studies link this feature of bi-modality or multi-modality (for the axisymmetric wake in Rigas *et al.* 2014) to the symmetry breaking seen at low Reynolds numbers and attribute the feature to a supercritical pitchfork bifurcation observed both numerically (Fabre *et al.*, 2008; Meliga *et al.*, 2009) and experimentally (Grandemange *et al.*, 2012; Rigas *et al.*, 2014) with increasing Reynolds number.

Several techniques have been applied to manipulate such instantaneous symmetry breaking wakes targeting the attenuation of the bi-modal behavior. Most of the studies use passive devices. Grandemange *et al.* (2014) and Cadot *et al.* (2015) perturbed the wake of the square-back Ahmed body with a vertical control cylinder, showing that if adequately located the bi-modal behavior could be suppressed, associating with a drag reduction. Recent experiments of Evrard *et al.* (2016) show that the bi-modal wake has been symmetrized using base cavities, leading to a drag reduction around 10%. The asymmetric flow states and its inherent vortex topology are fully stabilized increasing the base pressure. Similar results have been achieved for the axisymmetric body using a perimetric slit located at the base edge communicating an internal cavity with the external flow (García de la Cruz *et al.*, 2017b). The results above suggest the importance of symmetrization of such wakes for drag reduction. Although these passive controls are effective, the suppression of the bi-modal behavior remains unclear due to the geometric modifications. This gives us the motivation to investigate geometry-free active control techniques and especially to develop feedback control approaches in order to adapt in real time to the flow states (Brunton & Noack, 2015).

Only few studies address the feedback control of bi-modal wakes. Evstafyeva *et al.* (2017) numerically simulated the actuation effects of unsteady synthetic jets on the low-Reynolds-number wake of the square-back Ahmed body by applying a linear feedback control strategy with the aim to attenuate the base pressure fluctuations. The results show a reduction in drag and re-symmetrization of the wake. Brackston *et al.* (2016) performed the experimental feedback control for high-Reynolds-number wake of the Ahmed body. The wake bi-modality is modeled by a nonlinear Langevin equation using the statistical modeling approach proposed in Rigas *et al.* (2015). Based on this model, they designed a feedback controller to suppress the symmetry-breaking modes using oscillating lateral flaps. The controller achieves a successful suppression of the bi-modality of the wake and concomitantly reduces the drag by 2%.

In this study, we present the first feedback control of bi-modal wake using unsteady pulsed-jets. The control authority of the unsteady jets for drag manipulation has been shown in Chapter 3, Oxlade *et al.* (2015) and Barros *et al.* (2016a,b). Here, we explore its capability in the bi-modal turbulent wake control. A physics-based opposition control strategy is proposed to mitigate wake asymmetries. Successful applications of opposition control range from wall-bounded flows to yaw moment and vortex shedding control (Choi *et al.*, 1994; Pastoor *et al.*, 2008; Pfeiffer & King, 2012). Our goal is twofold: first we show that feedback control using pulsed jets can be used to manipulate asymmetric bi-modal dynamics of a turbulent wake flow; then we quantify the pressure recovery resulted from the wake symmetrization by comparing the feedback performance with open-loop strategies. To achieve this control, the wake is forced by two lateral jets located at the rear edges of the model and monitored with base pressure sensors.

4.2 Experimental setup

The experimental facility and the model are identical to the ones used in Chapter 3. This section only details the essentials and differences with the setup presented in § 3.2.

Grandemange *et al.* (2013a) showed that the symmetry-breaking mode depends upon the cross-sectional aspect ratio of the car model and ground effect. Given the model used in this study and the ground clearance $G = 0.05\text{ m}$, no bi-modal behavior is observed in the wake as presented in Chapter 3. However, following the sensitivity analysis of Barros *et al.* (2017) and Barros (2015), we disturb the underflow with a spanwise cylinder of diameter 8 mm (see Fig. 4.1(a)) to obtain a balanced wake along z and bi-modal dynamics along y , as the case in Grandemange *et al.* (2013b). The position of the cylinder (here at $x = -0.05H$) was carefully chosen in order to have two equiprobable asymmetric states in a relatively long time (about 5 min). The control results throughout this chapter (and of only this chapter) were obtained with this wake configuration. All measurements were conducted with a constant free-stream velocity $U_\infty = 30\text{ m s}^{-1}$ corresponding to a Reynolds number $Re_H = U_\infty H / \nu = 6 \times 10^5$.

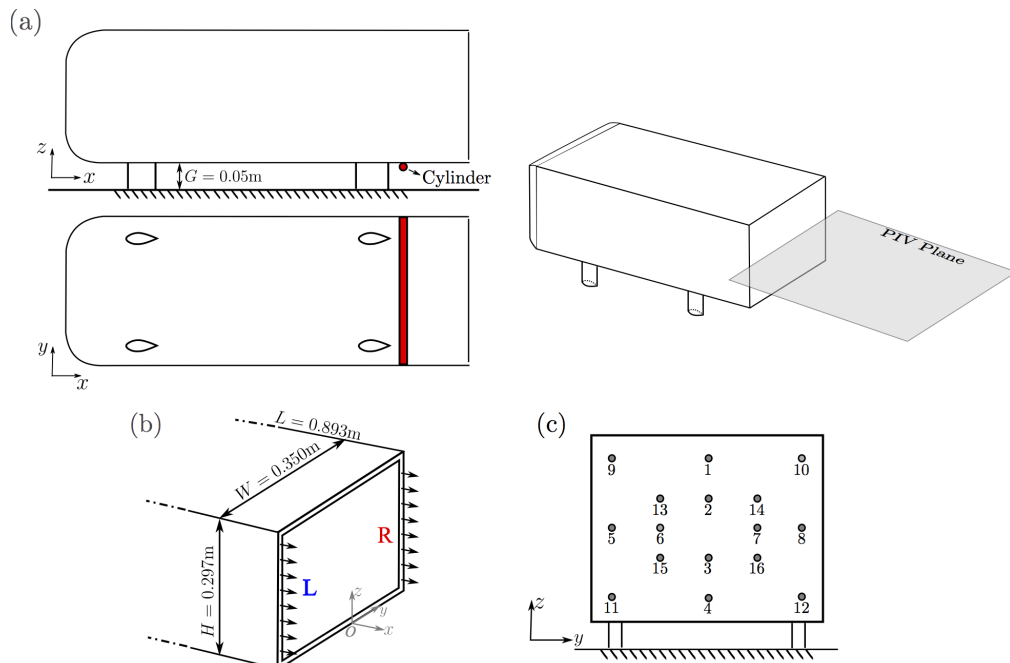


Figure 4.1: Experimental setup. (a) Sketch of the model showing the position of the perturbing cylinder and PIV plane. (b) Lateral actuation slits. (c) Distribution of the pressure sensors over the rear surface.

The actuator system utilizes only two lateral slits: right (R, $y > 0$) and left (L, $y < 0$) as indicated in Fig. 4.1(b). Same as the previous chapter, we denote by V_{Jet} the exit jet velocity, and by $V_{\text{eff}} = (\overline{V_{\text{Jet}}^2})^{\frac{1}{2}}$ the effective jet velocity where the overline represents a time average. The forcing amplitude is defined by the momentum coefficient C_μ (see Eq. (3.2)). This forcing amplitude can be regulated by setting the initial input pressure P_0^i of the compressed air reservoir inside the model. Figure 4.1(c) reminds the readers the 16 unsteady pressure locations over the base surface. Their measurements are used to quantify the forcing effects on the base pressure and to provide sensing for the real-time feedback control.

Wake velocity measurements are carried out using a two-dimensional PIV system in the mid-height plane $z = 0.67$ (see Fig. 4.1(a)) to analyze the bi-modal dynamics and control effects. The whole wake is captured by two LaVision Imager Pro X 4M cameras with a resolution of 2048×2048 pixels. The field of view covers a region of approximately $2.3 H \times 1.6 H$. Velocity vectors are processed with an interrogation window of 32×32 pixels and a 50% overlap, resulting in a spatial resolution of 3.9 mm corresponding to $0.013H$. The time between one pair of images is $65\ \mu\text{s}$ and the image pairs are recorded at a sampling rate of 3.5 Hz. For the unforced flow, due to the long time-scale of the asymmetric states, we recorded 7500 images in order to

cover as many as possible the switching events and to approach an equiprobable distribution of asymmetric states. For forced flows, 2000 images were taken.

Closed-loop actuation and data acquisition are controlled using the same instruments as presented in § 3.2.4: a National Instrument[®] PXIe-8820 Real-Time system coupled to a PXIe-6363 DAQ card, both running with a sampling frequency of 2 kHz.

4.3 Unforced bi-modal flow

In this section, we describe the fundamental features of the unforced flow in order to compare with the forced flows in the following sections.

Wake asymmetries can be quantified by estimating the base pressure gradients $\partial C_p/\partial y$ and $\partial C_p/\partial z$ which are defined as follows:

$$\begin{aligned}\frac{\partial C_p}{\partial y} &= \frac{1}{2} \frac{C_{p8} - C_{p5}}{y_8 - y_5} + \frac{1}{2} \frac{C_{p7} - C_{p6}}{y_7 - y_6}, \\ \frac{\partial C_p}{\partial z} &= \frac{1}{2} \frac{C_{p1} - C_{p4}}{z_1 - z_4} + \frac{1}{2} \frac{C_{p2} - C_{p3}}{z_2 - z_3}.\end{aligned}\tag{4.1}$$

These estimations use the pressure sensors in the symmetric ($y = 0$) and horizontal ($z = 0.67$, mid-height of the body) planes, respectively. Time series of these gradients in the unforced flow and their probability density functions (PDF) are presented in Fig. 4.2(a). We denote by $t^* = t/t_c = t/(H/U_\infty)$ the dimensionless time. Pressure was acquired during 5 minutes, corresponding to flow statistics over $t^* = 3 \times 10^4$. The PDF of $\partial C_p/\partial y$ reports clearly the lateral bi-modal reversals and shows the two most probable asymmetric gradients at $(\partial C_p/\partial y)_{\text{peak}} \simeq \pm 0.15$. The time scale of being in one state is about $10^3 H/U_\infty$. Along the wall-normal axis z , the PDF of $\partial C_p/\partial z$ is centered around zero, indicating a statistically symmetric pressure field along z . This feature is similar to what has been observed in Grandemange *et al.* (2013b).

Although the time taken to switch between two states is negligible with respect to the long time scale of each state, it is still interesting to look at this quantity for better understanding of the switching process. We estimate this switching time T_{sw} by the transition time of $\partial C_p/\partial y$ between two peaks of the PDF. We apply a first-order low-pass filter with a cut-off frequency of $St_{H_c} = 0.03$ on $\partial C_p/\partial y$ to better distinguish the switching moment. This cutoff frequency corresponds to a time scale of $30t_c$. An ensemble of 150 flipping events are investigated. The distribution of T_{sw} for these switches is shown in Fig. 4.2(b). It presents a large range of time scales varying from $18t_c$ to $115t_c$. This distribution leads to a mean value of $\overline{T_{sw}}/t_c \approx 43$ and a standard deviation of $\sigma/t_c = 18$. In particular, $\overline{T_{sw}}$ is about 7 times larger than the vortex shedding period ($T_{vs}/t_c = 6.25$ when $St_H^* = 0.16$ (Barros, 2015), which means that a slow reorganization of the near wake flow is involved in this process.

Figure 4.3(a) shows the time-averaged base pressure and velocity field in the mid-height plane. The pressure map shows a uniform lower pressure region surrounded by a higher pressure along the lateral edges. Symmetry distribution is seen both along y and z . The base pressure for this baseline flow is $\langle \overline{C_p} \rangle_u = -0.235$. In the velocity map, the 2D streamlines show clearly two balanced counter-rotating structures in the recirculating region, corroborating a symmetric topology over long time averages. The fluctuation intensity is demonstrated by the mean turbulent kinetic energy k . It is concentrated along the lateral shear layers with a comparable intensity in each side. From these mean distributions, we can hardly distinguish the asymmetric states related to the PDF peaks in Fig. 4.2(a).

In order to better understand the pressure and wake dynamics, we isolate the two reflectional asymmetric states and the low probable symmetric state by a conditional average with respect

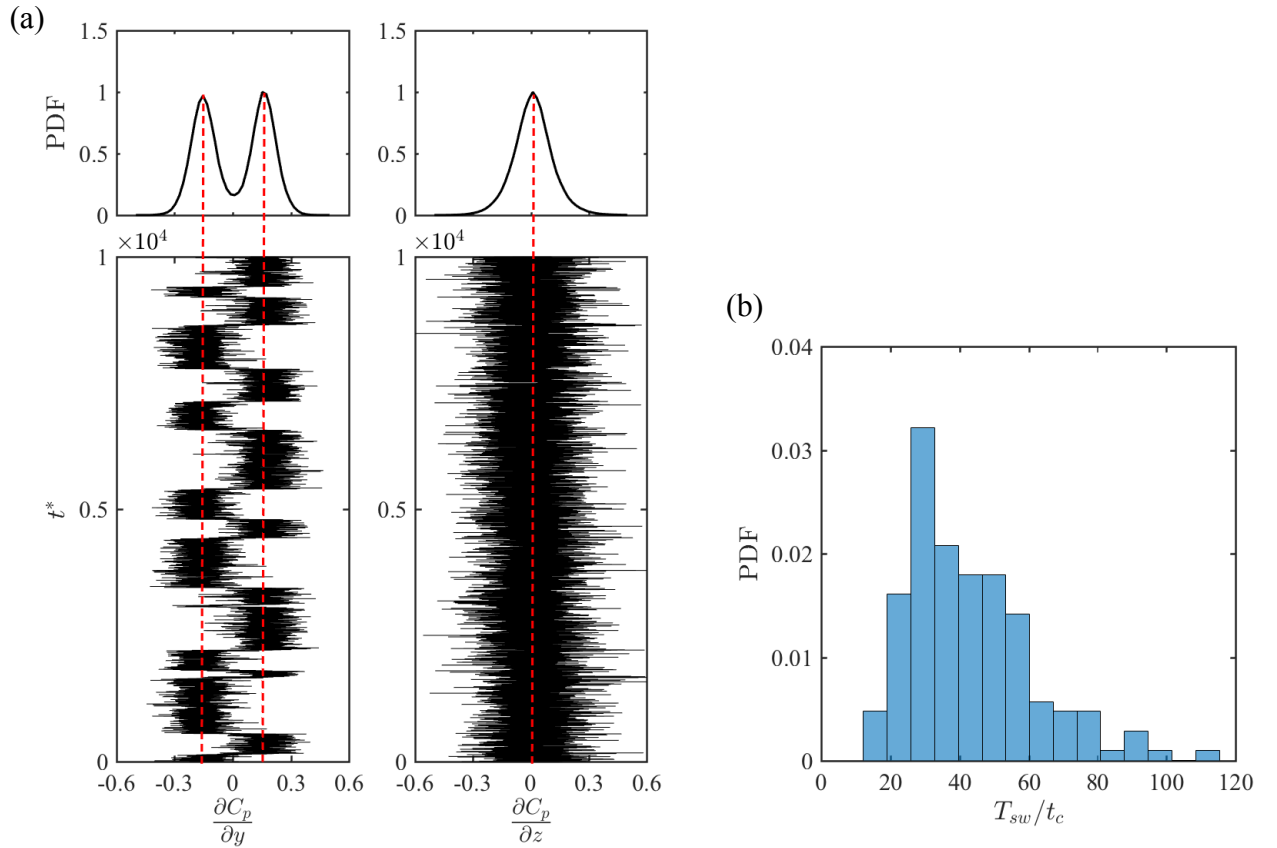


Figure 4.2: Unforced bi-modal flow. (a) Time series of pressure gradients and probability density function (PDF) along the y and z directions. PDFs are normalized by their maximum values. $t^* = t/t_c$ is the dimensionless time. The dashed lines represent the most probable values. For clarity, only part of the recording signals are presented in the lower figures. (b) Distribution of the switching time scale T_{sw} between the transition of two states.

to the value of $\partial C_p/\partial y$. We apply again the low-pass filter presented before (cut-off frequency $St_{H_c} = 0.03$) on $\partial C_p/\partial y$ to better distinguish each state. The filtered gradient is denoted by $\widehat{\partial C_p/\partial y}$. By selecting a threshold at $\widehat{\partial C_p/\partial y} = \pm 0.06$, which corresponds to 40% of the most probable gradient $(\partial C_p/\partial y)_{\text{peak}}$, we define three states: state #N_u for negative values in $\widehat{\partial C_p/\partial y} < -0.06$, state #P_u for positive values in $\widehat{\partial C_p/\partial y} > 0.06$ and state #S_u for values in $-0.06 < \widehat{\partial C_p/\partial y} < 0.06$. The subscript ‘u’ stands for the unforced flow. The simultaneous measurement of the velocity and base pressure allow us to identify the state of each captured velocity field and then to correlate the conditionally averaged velocity to that of the base pressure. Although 7500 images were taken, only around 500 images locate at state #S_u due to its small characteristic time scale in comparison with those of the asymmetric states #N_u and #P_u.

Figure 4.3(b), (c) and (d) display the conditionally averaged base pressure and velocity field for the states #P_u, #N_u and #S_u, respectively. For the state #P_u, a low pressure region is seen near the left edge ($y < 0$), corresponding to the large counter-clockwise rotating structure at the same side. The high pressure region near the right edge results from the impingement of the recirculating flow on the model base. The relevant kinetic turbulent energy exhibits a higher intensity along the right shear layer ($y > 0$). The state #N_u flips the observations above regarding the state #P_u to their opposite side. For the low probable state #S_u, the pressure map is symmetric and more uniform than the other two states. It presents a high pressure region along the central line $y = 0$. This distribution agrees with the corresponding

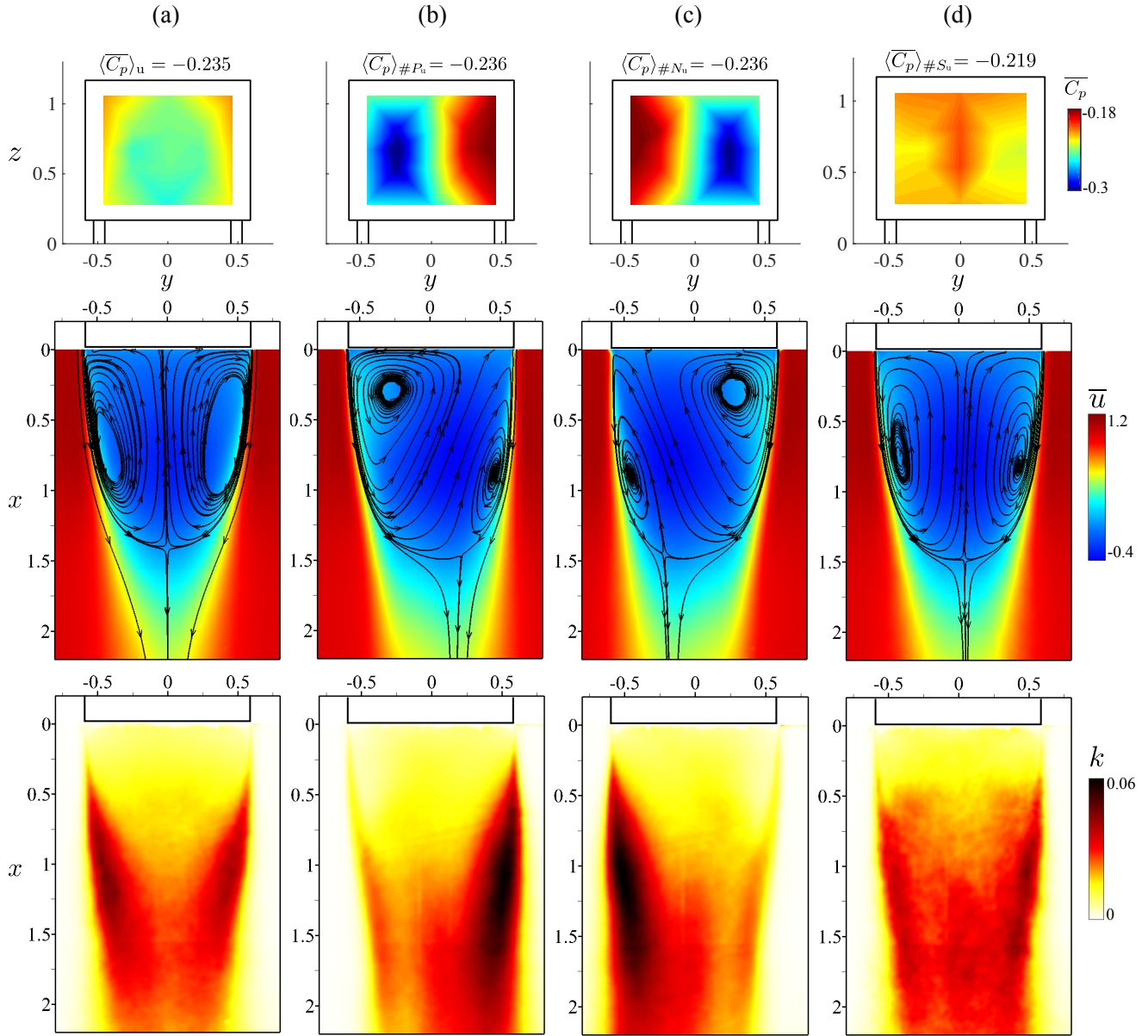


Figure 4.3: Time-averaged results for the unforced bi-modal flow. From top to bottom: distribution of time-averaged base pressure $\overline{C_p}$, streamwise velocity \overline{u} overlaid with streamlines and turbulent kinetic energy k . From left to right: (a) total time-averaged results; conditional averaged results for state (b) $\#P_u$, (c) $\#N_u$ and (d) $\#S_u$.

velocity field where the recirculating flow impinges normally on the central base. Besides, the mean streamline topology is very similar to that presented in Fig. 4.3(a) for the total mean field but presents a 6% longer bubble length. The k distribution of the state $\#S_u$ is also symmetric, but is noisy due to the limited number of images which do not provide a good convergence for the second order statistics. Another interesting point is the comparison of the conditionally averaged base pressure of each state with the total mean value $\langle \overline{C_p} \rangle_u = -0.235$. The two asymmetric states lead to the same value: $\langle \overline{C_p} \rangle_{\#P_u} = \langle \overline{C_p} \rangle_{\#N_u} = -0.236$ which is 0.4% lower than $\langle \overline{C_p} \rangle_u$. While the symmetric state $\#S_u$ yields $\langle \overline{C_p} \rangle_{\#S_u} = -0.219$, being 7% greater than $\langle \overline{C_p} \rangle_u$. The variation of the base pressure for the three states can be also seen from the diagram of the time series of the area-averaged base pressure $\langle C_p \rangle$ versus $\partial C_p / \partial y$, as shown in Fig. 4.4. The distribution is colored by the PDF of $\partial C_p / \partial y$. The unstable symmetric mode $\#S_u$, observed when two stable asymmetric modes switch, clearly shows a higher base

pressure (about 7%), corroborating the need for the symmetrizing control in order to achieve the drag reduction. The conditionally averaged results here agree qualitatively with those in Grandemange *et al.* (2013b); Volpe *et al.* (2015); Perry *et al.* (2016).

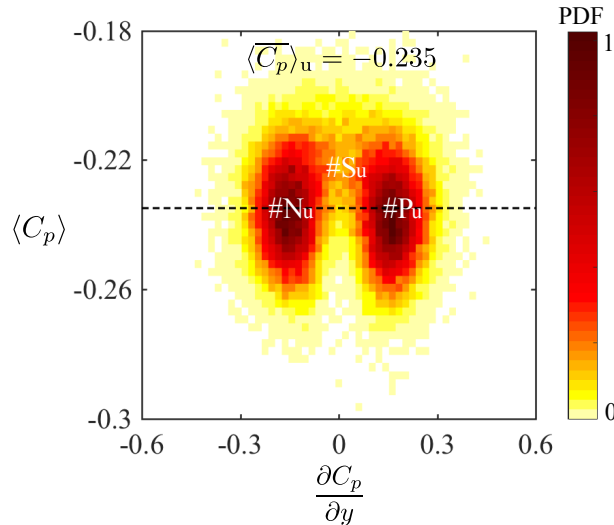


Figure 4.4: Diagram of the time series of the area-averaged base pressure $\langle C_p \rangle$ versus $\frac{\partial C_p}{\partial y}$ colored by the PDF of $\frac{\partial C_p}{\partial y}$. The PDF are normalized by their maximum value. The dashed line indicates the time- and area-averaged base pressure value $\langle C_p \rangle_u$. The regions corresponding to the three states $\#N_u$, $\#S_u$ and $\#P_u$ are also marked in the figure.

4.4 Single edge open-loop forcing

Before performing the feedback control, single edge open-loop forcing is applied to get insights on the wake response to actuation.

A parametric study is performed with frequencies within $St_H \in [0.1, 2]$ under a constant initial supply pressure $P_0^i = 1.5$ bar. The duty cycle is fixed at $DC=50\%$. The resulting effective jet velocity is about $V_{\text{eff}} = 0.2U_\infty$ for all the frequencies, leading to $C_\mu \approx 5 \times 10^{-4}$. The actuation is applied either along right (R) or left (L) edge for a duration of 2 min, amounting to $12000t_c$. Figure 4.5(a) exemplifies the variation of PDF of $\frac{\partial C_p}{\partial y}$ and the corresponding color map of base pressure for $St_H = \{0.2, 0.8, 2\}$ applied on R and L respectively. When the control is applied on R, all PDFs of $\frac{\partial C_p}{\partial y}$ are concentrated at a negative value, presenting only one asymmetric state of type $\#N$. Correspondingly, the base pressure distributions show a lower pressure close to the forced edge R. Similarly, forcing on L results in the asymmetric state of type $\#P$, featuring a lower pressure close to the edge L and a PDF concentrated at a positive $\frac{\partial C_p}{\partial y}$. These features are observed for the whole range of the tested frequencies mentioned above and are in agreement with the single slit actuation results in Barros (2015) where no bi-modal behavior was measured. We note that the wake remains statistically symmetric along z for all open-loop tests (not shown here).

The pressure response when actuation suddenly starts is reported in Fig. 4.5(b) for the case of $St_H = 0.8$. Once actuation is turned on, the wake quickly selects the relevant asymmetric state. We further check the time T_{sw} taken to switch from one mode to the other submitted to the actuation. The mean value $\overline{T_{sw}}$ obtained from 8 independent experiments at $St_H = 0.8$ is $\overline{T_{sw}}/t_c = 38$, which is of the same order of magnitude as $\overline{T_{sw}}/t_c = 40$ of the unforced bi-modal flow (Fig. 4.2(b)). Moreover, when compared to $\langle C_p \rangle_u$, the base pressure of the forced flow in Fig. 4.5(a) is reduced by 4%, 9% and 6% for $St_H = 0.2, 0.8$ and 2, respectively. The results have

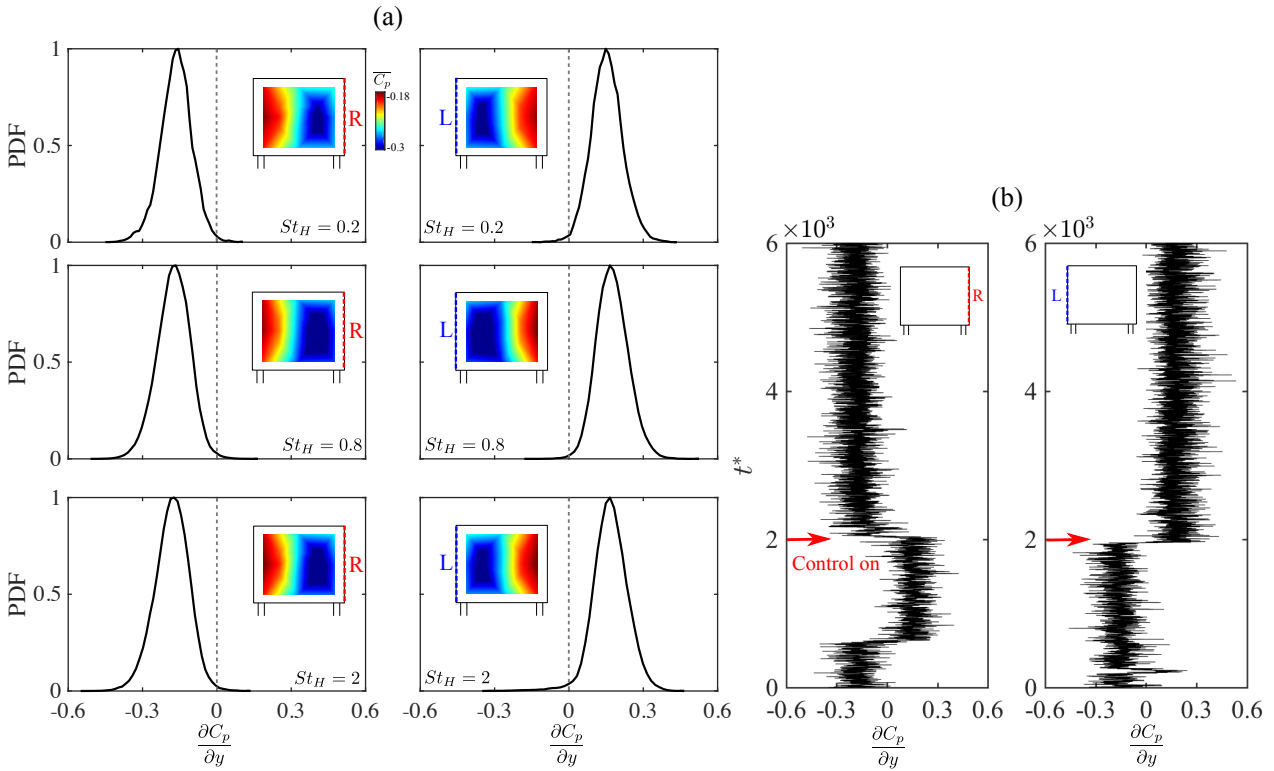


Figure 4.5: Results of single edge, open-loop forcing. (a) PDF of $\partial C_p / \partial y$ for controls applied on the right (R) and left (L) edge respectively with $St_H \in \{0.2, 0.8, 2\}$; the forced edge is highlighted by a dashed line. (b) Time evolution of pressure gradients for the forcing at $St_H = 0.8$ along R and L; the arrows indicate the onset of actuation.

no dependence on which edge the actuation is applied. In particular, the pressure is even lower than the asymmetric state of the unforced flow (Fig. 4.3(b) and (c)). This finding indicates that single-edge forcing modifies the wake dynamics by local excitation of one shear-layer which results in a drag increase.

In the following, we investigate specifically the forced wake dynamics at $St_H = 0.8$ which leads to the highest drag increase. Only the results of the right edge forcing are presented. We assume that the mechanisms are the same for the left edge forcing. As the forced flow presents only the state $\#N$, it is interesting to compare it with the state $\#N_u$ of the unforced flow. Figure 4.6(a) depicts the wake topologies by 2D streamlines obtained from the unforced flow state $\#N_u$ and the forced flow. Both present a large clockwise-rotating structure at the side $y > 0$, in agreement with the location of the low pressure region. Although they feature a similar pattern of flow organization, the bubble length of the forced flow is reduced by 5%. The position of the saddle point (indicated by ‘Sa’ in the figures) is also modified. The streamwise position is decreased by 10% from $x_s = 1.45$ (unforced flow) to $x_s = 1.3$ (forced flow), whereas the off-axis distance $|y|_s$ is significantly increased by 50%, moving from $y_s = -0.22$ (unforced flow) to $y_s = -0.33$ (forced flow). These results suggest that the forced wake is more oriented towards the left side and leads to a higher degree of asymmetry. This observation is also confirmed by the pressure distribution along the mid-height line (Fig. 4.6(b)) and the mean pressure gradient value: with actuation $(\overline{\partial C_p / \partial y})_a = -0.18$, being 20% greater than the negative peak value $(\overline{\partial C_p / \partial y})_{\text{peak}} = -0.15$. The pressure decrease induced by the forcing is more pronounced near the forced edge R and thus yields a more important gradient.

The observations above show a close link between the decrease of base pressure and the shorter and more asymmetric wake. The shorter wake associated with a lower base pressure

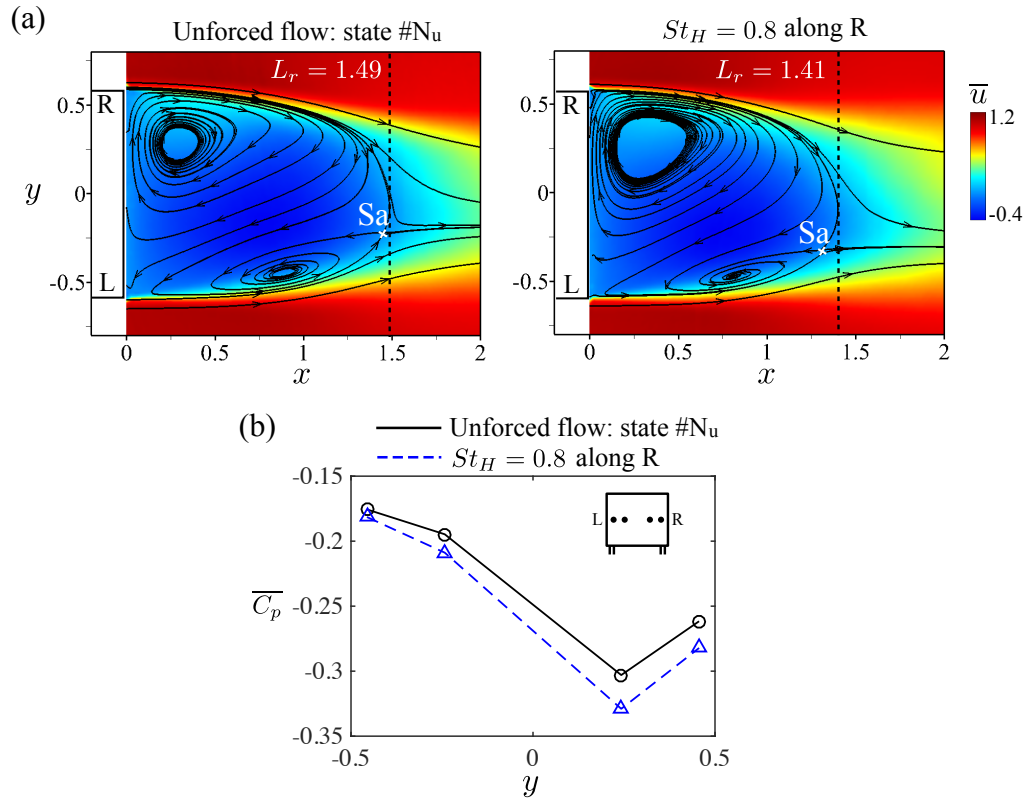


Figure 4.6: Results of the right edge forcing at $St_H = 0.8$. (a) 2D streamlines for the unforced flow state #Nu_u (left) and the forced flow (right) overlaid on the contour maps of the mean streamwise velocity \bar{u} . L_r (see Eq. (3.7)) indicates the bubble length and is highlighted by the dashed line. The letters R and L indicate the right and left side respectively. (b) Pressure distribution along the mid-height line of the model.

has been already investigated in Barros *et al.* (2016b) with a top-edge forcing around the same frequency $St_H = 0.8$. They found that the velocity fluctuations along the forced shear layer are most amplified at frequencies close to $St_H = 0.8$. Here, we observe similarly a noticeable increase of velocity fluctuations along the forced right shear layer, as demonstrated in Fig. 4.7(a-c) for the Reynolds stresses $\overline{u'u'}$, $\overline{u'v'}$ and $\overline{v'v'}$, respectively. Moreover, the left shear layer shows also a minor increase of velocity fluctuations, indicative of the interactions between two facing shear layers. The modifications of velocity fluctuations along the shear layers are directly related to the local pressure gradient along the boundary of the recirculation bubble as demonstrated in the following equation (Bradshaw, 1973):

$$\frac{1}{\rho} \frac{\partial \bar{p}}{\partial n} = \frac{\bar{u}_s^2}{R_s} - \frac{\partial \overline{v'_n v'_n}}{\partial n}, \quad (4.2)$$

where \bar{u}_s is the velocity along a curved streamline, R_s the radius of the local streamline curvature, \mathbf{n} the vector normal to the streamline and v'_n the velocity fluctuation along \mathbf{n} in the streamline coordinates. The terms negligible to \bar{u}_s are neglected. When integrated along \mathbf{n} , an increase of the velocity fluctuation $\overline{v'_n v'_n}$ leads directly to a decrease of pressure. On the other hand, the shortening of the bubble length with a conservation of the wake height decreases the aspect ratio L_r/H of the recirculation bubble which leads to a higher wake bluffness with a lower radius R_s of the bubble curvature, as observed in the 2D wakes (Roshko, 1955, 1993b). The reduction of R_s is detrimental for the drag as it increases $\partial p / \partial n$, resulting in a lower pressure along the recirculation boundary. According to Barros *et al.* (2016b), at first order approximation, the variation of pressure along the bubble boundary $(\delta C_p)_{\partial B} = (C_{p_a})_{\partial B} - (C_{p_u})_{\partial B}$

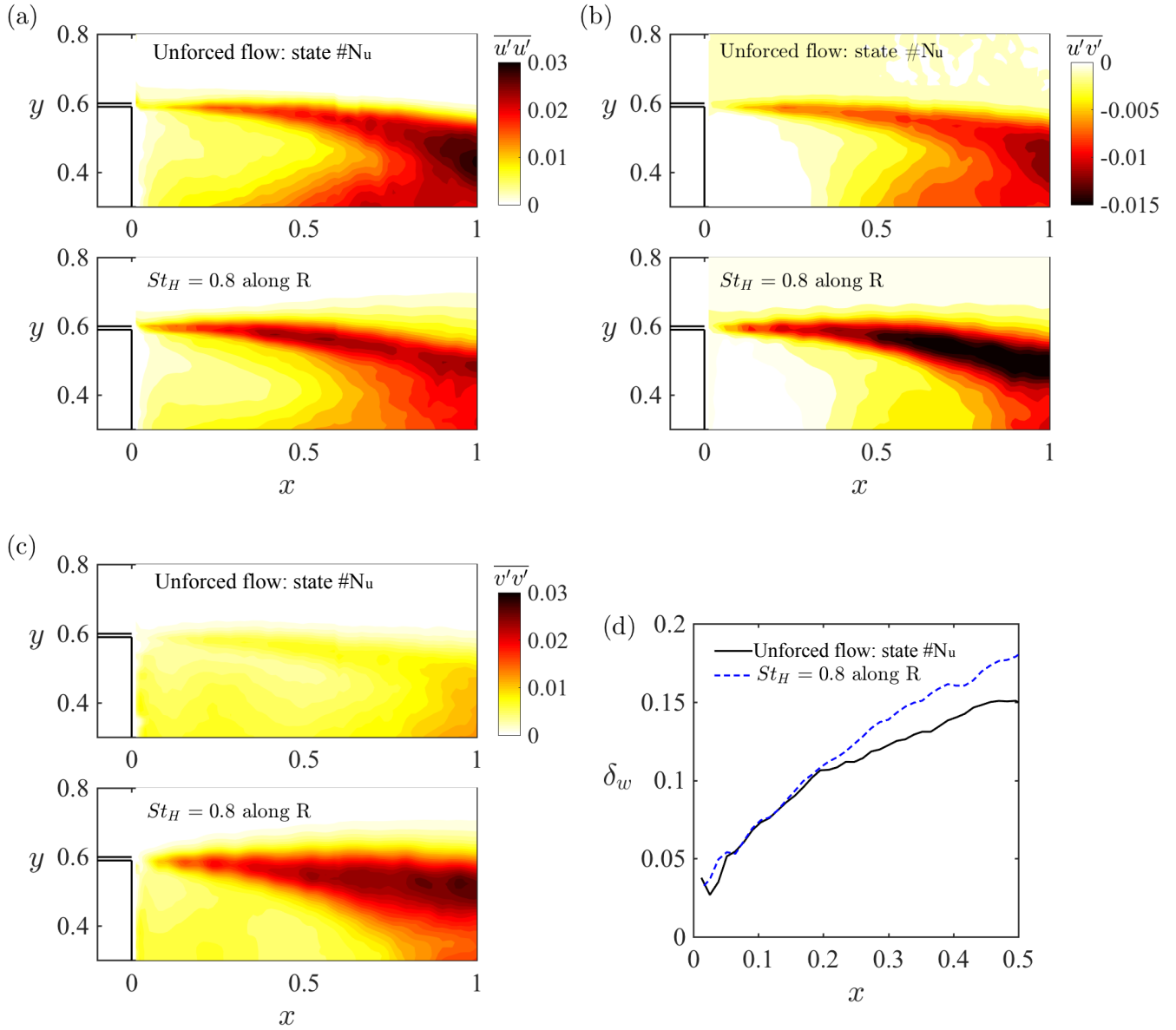


Figure 4.7: Effects on shear layer dynamics of the right edge forcing at $St_H = 0.8$. (a-c) Distribution of the Reynolds stresses $\overline{u'u'}$, $\overline{u'v'}$ and $\overline{v'v'}$ for the unforced flow state #N_u and the forced flow. (d) Streamwise evolution of the shear layer thickness δ_w .

determines that of the base pressure $(\delta C_p)_{\text{base}}$. This was quantified by the balance of streamwise forces acting on the contour of the mean recirculation region (Sychev, 1982; Roshko, 1993a,b). Hence, when $(\delta C_p)_{\partial B} < 0$, we get $(\delta C_p)_{\text{base}} < 0$, pointing to a decrease of base pressure.

Additionally, the enhancement of shear layer dynamics modifies its associated thickness and growth rate. To clarify these modifications, we quantify the shear layer thickness evolution by the vorticity thickness following Brown & Roshko (1974)

$$\delta_w = |\omega|_{\text{max}}^{-1} \int_{y_{\text{min}}}^{y_{\text{max}}} |\omega| dy \approx \frac{\bar{u}_{\text{max}} - \bar{u}_{\text{min}}}{\left| \frac{\partial \bar{u}}{\partial y} \right|_{\text{max}}}. \quad (4.3)$$

Here, we take $y_{\text{max}} = 0.8$ in the outer flow and $y_{\text{min}} = 0$ on the symmetric line. Only the initial development of the shear layer in the range $x \in [0, 0.5]$ is investigated. The streamwise evolution of δ_w for the forced shear layer is shown in Fig. 4.7(d). The increase of δ_w corresponds well to the evolution of Reynolds stresses in Fig. 4.7(a-c) where a larger region of high fluctuation

values is observed in the forced shear layer. Moreover, the increase of the derivative $d\delta_w/dx$ indicates a higher growth rate of the shear layer. As entrainment is the main process responsible for the shear layer growth, more fluid is expected to be entrained from the free stream into the wake region by actuation. We further quantify the entrained flow using the streamwise evolution of the integral of the spanwise velocity kinetic energy $\mathcal{V}(x)$ inside the domain $\Omega_{\bar{u}<0}$ defined as follows:

$$\mathcal{V}(x) = \int_{\Omega_{\bar{u}<0}} \frac{\bar{v}^2(x, y)}{2} dy. \quad (4.4)$$

The result is shown in Fig. 4.8. The overall increase of $\mathcal{V}(x)$ corroborates the expectation above and is in agreement with the result of Barros *et al.* (2016b). The increased degree of asymmetry observed in Fig. 4.6 is most likely related to the enhancement of entrained flow from the forced shear layer. Concomitantly, the higher growth rate brings an earlier interaction of the opposing shear layers which reduces the bubble length L_r . As discussed in the previous paragraph, the reduction of L_r is associated with a decrease of R_s , hence the change of the bubble curvature is an implicit consequence of the increase of shear layer turbulence.

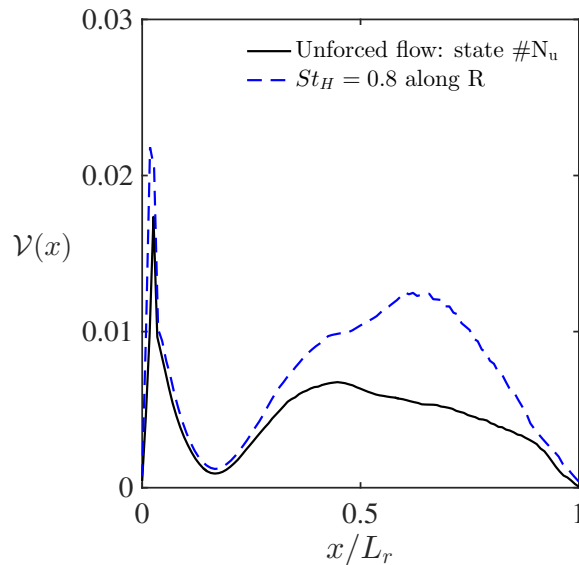


Figure 4.8: Streamwise evolution of \mathcal{V} , see Eq. (4.4), inside the recirculation bubble.

The higher degree of asymmetry may also have a detrimental effect on drag. It has been shown in Grandemange *et al.* (2013c, 2014) that an asymmetric wake is associated with an induced drag which is likely related to the square of the lateral force $\overline{C_y^2}$. With the presence of the bi-modality, the lateral force C_y was seen to switch between two equal and opposite extremes as the behavior of $\partial C_p / \partial y$ (Brackston *et al.*, 2016; Perry *et al.*, 2016). Once the state is locked, we assume that C_y is also locked around one extreme value. Higher degree of asymmetry would lead to a greater C_y and consequently a higher induced drag.

To summarize, the single edge open-loop forcing locks the wake into one asymmetric flow state and induces pressure decrease close to the forced edge. The reason of drag increase is twofold. First, in the near wake, the increase of velocity fluctuations along the forced shear layer decreases the base pressure leading to a higher drag. Second, the higher degree of asymmetry may lead to a higher induced drag due to the longitudinal vortices in the far wake. Further measurements on the iso- x planes would be required to confirm the second factor. The results are inspiring for the design of the feedback control described in the following section.

4.5 Feedback control

Single edge forcing results show the ability of control to force asymmetric states. Based on this fact, we propose an opposition control strategy to symmetrize the unforced bi-modal wake. In § 4.5.1, we present the design of the controller and the resulting performance. In § 4.5.2, we illustrate the impacts on the base pressure and near wake of the optimal controller obtained in § 4.5.1.

4.5.1 Control design and performance

The aim of the control is to symmetrize the wake. Single edge forcing induces a pressure drop close to the forced edge, thus by detecting the local pressure drop along one rear side, forcing can be applied on the opposite edge to generate an instantaneous and opposing flow reversal. The control law needs a real-time feedback of the flow asymmetry, which can be obtained by computing $\partial C_p / \partial y$. The low-pass filter used in § 4.3 to identify the states of the unforced flow is again applied on the gradient to distinguish the long-time bi-modal dynamics from the other time scales of the wake. We remind that the filtered value is denoted by $\widehat{\partial C_p / \partial y}$. The block control diagram is illustrated in Fig. 4.9(a). The controller can be expressed by:

$$\begin{aligned} b^R(t) &= \text{H}\left(\frac{\widehat{\partial C_p}}{\partial y} - \alpha\right) \text{H}(\sin(2\pi ft)) \\ b^L(t) &= \text{H}\left(-\frac{\widehat{\partial C_p}}{\partial y} - \alpha\right) \text{H}(\sin(2\pi ft)), \end{aligned} \quad (4.5)$$

where b^R and b^L represent the control along right (R) and left (L) edge, respectively. H denotes the Heaviside function which transforms the continuous output to a binary output ($\text{H}(x) = 0$, if $x \leq 0$; $\text{H}(x) = 1$, otherwise). The term involving $\widehat{\partial C_p / \partial y}$ determines when the control should be applied. A positive pressure gradient threshold α must be defined beforehand: for example, $\widehat{\partial C_p / \partial y} > \alpha$ implies right edge actuation while no actuation is applied when $|\widehat{\partial C_p / \partial y}| < \alpha$. The choice of α is a compromise between the control performance and the actuation cost. At this moment, we follow the procedure in § 4.3 for the identification of different states and set $\alpha = 0.06$ as the threshold. The influence of different values of α on the result will be detailed later.

This controller combines the closed-loop gradient feedback with an open-loop periodic forcing. When actuation is commanded, i.e. $\text{H}(\widehat{\partial C_p / \partial y} - \alpha) = 1$ or $\text{H}(-\widehat{\partial C_p / \partial y} - \alpha) = 1$, jets are pulsed with a frequency f and a given pressure supply P_0^i . The duty cycle within each periodic of pulse is fixed at 50%. A systematic study is conducted by varying the frequency f in the range of $St_H \in [0.1, 2]$ with a similar supply pressure $P_0^i = 1.5$ bar as in the previously described open-loop forcing case. The actuation is applied during 2 min, amounting to $12000t_c$. Figure 4.9(b) presents the resulting PDFs of $\partial C_p / \partial y$. The most probable values (dashed lines) show a convergent-divergent diagram with respect to $\partial C_p / \partial y = 0$ for increasing frequency. A remarkable damping of asymmetries is found within the frequency range $St_H \in [0.2, 1]$. The degree of asymmetry can be quantified by the root mean square of the pressure gradients, defined by $\text{RMS} = ((\partial C_p / \partial y)^2)^{\frac{1}{2}}$. Either the bi-modal symmetry breaking or locking in one of two asymmetric states will induce large RMS: smaller RMS values mean more symmetric wakes (Grandemange *et al.*, 2014). Thus RMS is used here as an indicator of control performances. The variation of RMS with respect to St_H are shown in Fig. 4.9(c). Compared to the unforced value $\text{RMS}_u = 0.167$, all frequencies lead to a smaller RMS, indicative of a lower

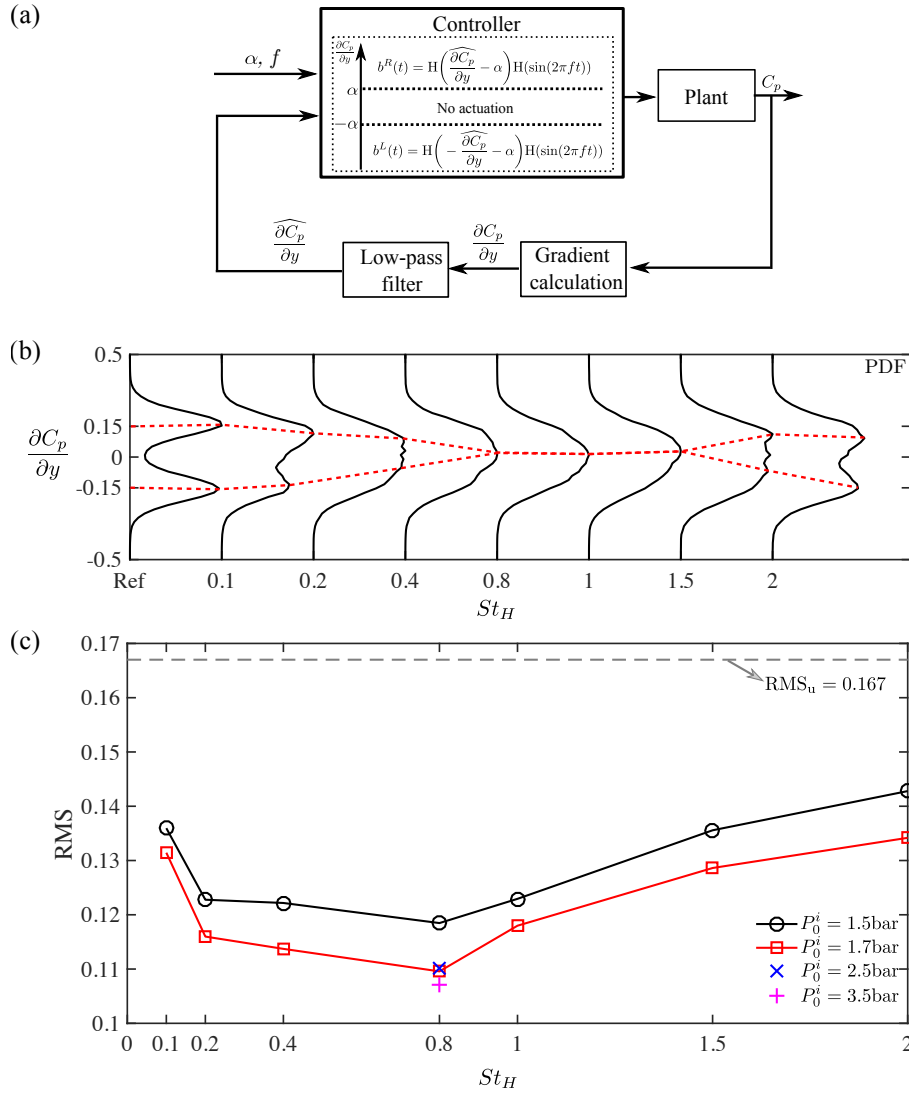


Figure 4.9: Feedback control results. (a) Block diagram of the closed-loop control. α is the threshold to trigger the control and f is the forcing frequency. (b) PDF of $\frac{\partial C_p}{\partial y}$ for the unforced flow (Ref) and the closed-loop forced flows at $P_0^i = 1.5$ bar versus St_H . The PDFs are shifted for clarity. The dashed lines indicate the most probable values. (c) RMS of $\frac{\partial C_p}{\partial y}$ versus St_H at different supply pressures P_0^i . The baseline yields $RMS_u = 0.167$.

degree of asymmetry. The optimal control leading to the most symmetric distribution with the minimum RMS is found at $St_H = 0.8$. We equally show in Fig. 4.9(c) the RMS values obtained with a higher supply pressure $P_0^i = 1.7$ bar to illustrate the influence of the jet amplitude. The curve remains the same trend of variation with increasing St_H but shifts overall towards lower values. The minimum RMS still locates at $St_H = 0.8$. We further investigate if the RMS at $St_H = 0.8$ can be more reduced if we continue to increase P_0^i . The results with $P_0^i = 2.5$ bar and 3.5 bar are provided in Fig. 4.9(c). No important improvement is noted, suggesting that the performance of the feedback control at $St_H = 0.8$ has converged from the supply pressure $P_0^i = 1.7$ bar.

According to the investigations in § 4.4 and in Barros *et al.* (2016b), the actuation at $St_H = 0.8$ particularly enhances shear layer mixing and induces higher entrainment responsible for altering the recirculating dynamics. The results of the feedback control corroborate the impact of actuation at this time-scale. At higher frequencies ($St_H = 1.5$ and 2), the PDFs exhibit a wide distribution with a higher RMS. In fact, shear layer mixing is less enhanced at these frequencies when compared to $St_H \in [0.2, 1]$ (Barros, 2015). The actuation is consequently

less effective to symmetrize the bi-modal wake.

In the following, we focus on the actuation responses of the flow to the forcing at $St_H = 0.8$ and $P_0^i = 1.5$ bar. Feedback control transients are presented in Fig. 4.10(a). The lateral asymmetries are notably damped when actuation is turned on, as demonstrated by the time series of $\widehat{\partial C_p / \partial y}$ and the centered PDF. A close view of the feedback evolution is presented in the time plot of Fig. 4.10(b). Edge activation always occurs once the gradient crosses the threshold and is represented by b^R (red) and b^L (blue) respectively for the right and left edges. In this particular feedback case, the mean duty cycle, i.e. the total opening time of the valves divided by the whole control time, is $DC = 30\%$, which is only 60% that of the open-loop control having $DC = 50\%$. The small duty cycle value indicates a low-energy consumption for this control strategy. The influence of the choice of α is investigated at $St_H = 0.8$. Figure 4.10(c) shows the PDFs obtained at $\alpha = \{0.02, 0.06, 0.1\}$, corresponding to 13%, 40% and 67% of $(\partial C_p / \partial y)_{\text{peak}}$ respectively. Their RMS values and mean duty cycles are also given in the figure. All three values of α lead to a zero-centralized distribution. $\alpha = 0.06$ is seen to be the optimal choice in terms of the performance of symmetrization as it presents a thinner distribution with

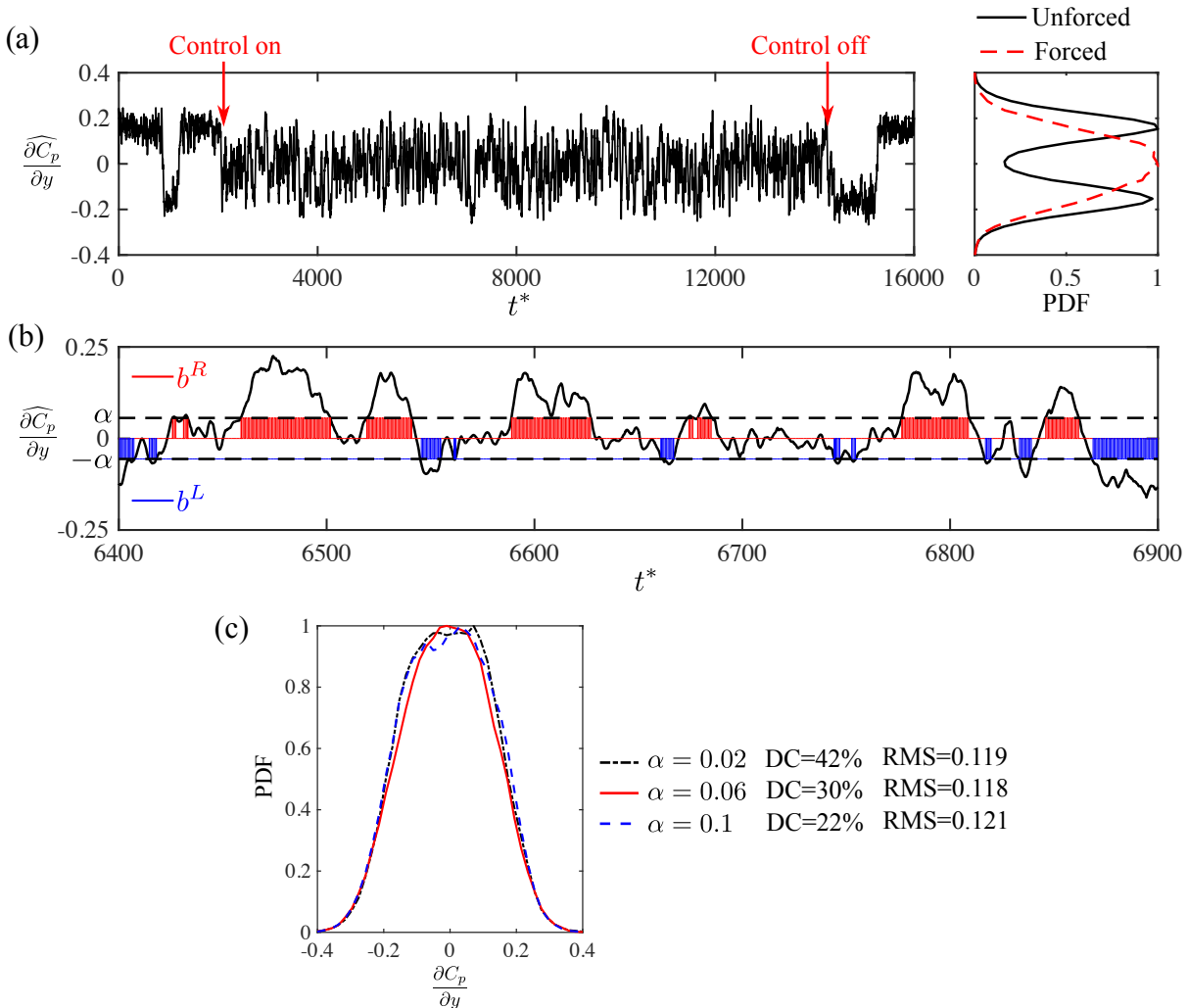


Figure 4.10: Feedback control results with $St_H = 0.8$ and $P_0^i = 1.5$ bar. (a) Time evolution of the filtered pressure gradient $\widehat{\partial C_p / \partial y}$ and the PDF of $\partial C_p / \partial y$. The arrows indicate the start and end of the control. (b) Zoom of the feedback control. The control commands b^L and b^R are scaled and shifted for figure clarity. (c) PDFs of $\partial C_p / \partial y$ for three threshold values: $\alpha = \{0.02, 0.06, 0.1\}$. Their corresponding duty cycle DC and RMS are also provided in the figure.

a lower RMS. The mean duty cycle DC decreases with increasing α . At $\alpha = 0.02$, the no-actuated interval $|\overline{\partial C_p / \partial y}| < 0.02$ is too narrow, therefore the actuation switches frequently between the right and left edge resulting in a high DC . As the actuation introduces the pressure fluctuation, we assume that the higher DC at $\alpha = 0.02$ is amenable to its slightly larger RMS when compared to the case of $\alpha = 0.06$. Reversely, at $\alpha = 0.1$, the no-actuated interval $|\overline{\partial C_p / \partial y}| < 0.1$ is too wide, therefore the gradient fluctuations are higher than that constrained by $|\overline{\partial C_p / \partial y}| < 0.06$ and lead to also a higher RMS. Hence we chose $\alpha = 0.06$ as the appropriate value as it presents a good compromise between the control performance and the energy investment.

4.5.2 Effects on the base pressure and near wake

Having discussed the effect of the feedback control on the wake asymmetry, it is worth assessing their impact on the mean base pressure. Although there is a clear variation of the RMS with St_H , the base pressure is increased by approximately 3% for all the investigated frequencies. The results point out the benefit of the feedback control to the drag reduction, but also show that there is not a linear dependence of the drag reduction on the degree of asymmetry (quantified by RMS). Wake symmetrization is not the only mechanism that changes drag. The concomitant actuation effect may also play an important role. To understand the coupled effects, we investigate the base pressure and mean wake resulted from the feedback control at $St_H = 0.8$ with $P_0^i = 1.5$ bar.

Figure 4.11(a) compares the base pressure and near wake for the bi-modal baseline flow, the conditionally averaged state $\#S_u$ of the unforced flow and the feedback controlled flow. The comparison of the forced flow with the unforced state $\#S_u$ is interesting as they both feature a symmetric distribution. The forced flow leads to a mean base pressure of $\langle \overline{C_p} \rangle_a^{CL} = -0.229$, being 3% larger than the mean unforced value $\langle \overline{C_p} \rangle_u$. However, $\langle \overline{C_p} \rangle_a^{CL}$ is 4% lower than the averaged pressure $\langle \overline{C_p} \rangle_{\#S_u}$ of the state $\#S_u$. For the velocity field, all three cases are symmetric with respect to $y = 0$, but show a discrepancy in the bubble length and the positions of the two centers of the recirculating zones. The bubble length follows an order of $(L_r)_u < (L_r)_a^{CL} < (L_r)_{\#S_u}$. Intriguingly, the base pressure obeys a similar order: $\langle \overline{C_p} \rangle_u < \langle \overline{C_p} \rangle_a^{CL} < \langle \overline{C_p} \rangle_{\#S_u}$. This finding agrees with the discussion in § 4.4 regarding the influence of the change of L_r on the radius R_s of the bubble curvature and the base pressure (Eq. (4.2)). Here, a longer bubble length L_r implies a larger R_s which is favorable to increase the base pressure. Besides, the centers of the recirculating zones in the forced flow are closer to the base than the other two cases, meaning that the roll-up process of the shear layer has been changed by actuation. In fact, forcing at $St_H = 0.8$ enhances the shear layer mixing and increases the entrainment of external momentum into the wake (see § 4.4). These features of excitation make it efficient to promote the switching of asymmetric states and thus leads to a more symmetric wake. On the other hand, the enhancement of shear layer mixing leads to high turbulent fluctuations and reduces the bubble length, both decreasing the base pressure according to Eq. (4.2) in § 4.4 which may explain why $\langle \overline{C_p} \rangle_a^{CL}$ is lower than $\langle \overline{C_p} \rangle_{\#S_u}$.

In Fig. 4.11(b), we analyze the power spectral density of $\partial C_p / \partial y$ to shed light on the lateral wake dynamics. The spectrum of the unforced bi-modal flow points to a high energy content in the low frequency band $St_H < 0.02$, corresponding to the long time scale between two switches. Nevertheless, the conditionally averaged state $\#S_u$ of the unforced flow shows a significant lower value in this frequency interval. Conversely, a broadband energy increases at smaller time scales of $St_H > 0.1$. In particular, we can recognize a peak at $St_H = 0.16$ which is the vortex shedding frequency measured in the unforced flow (Barros *et al.*, 2016a). Note that this peak is not discernible for the asymmetric states $\#N_u$ and $\#P_u$ (not shown here). The

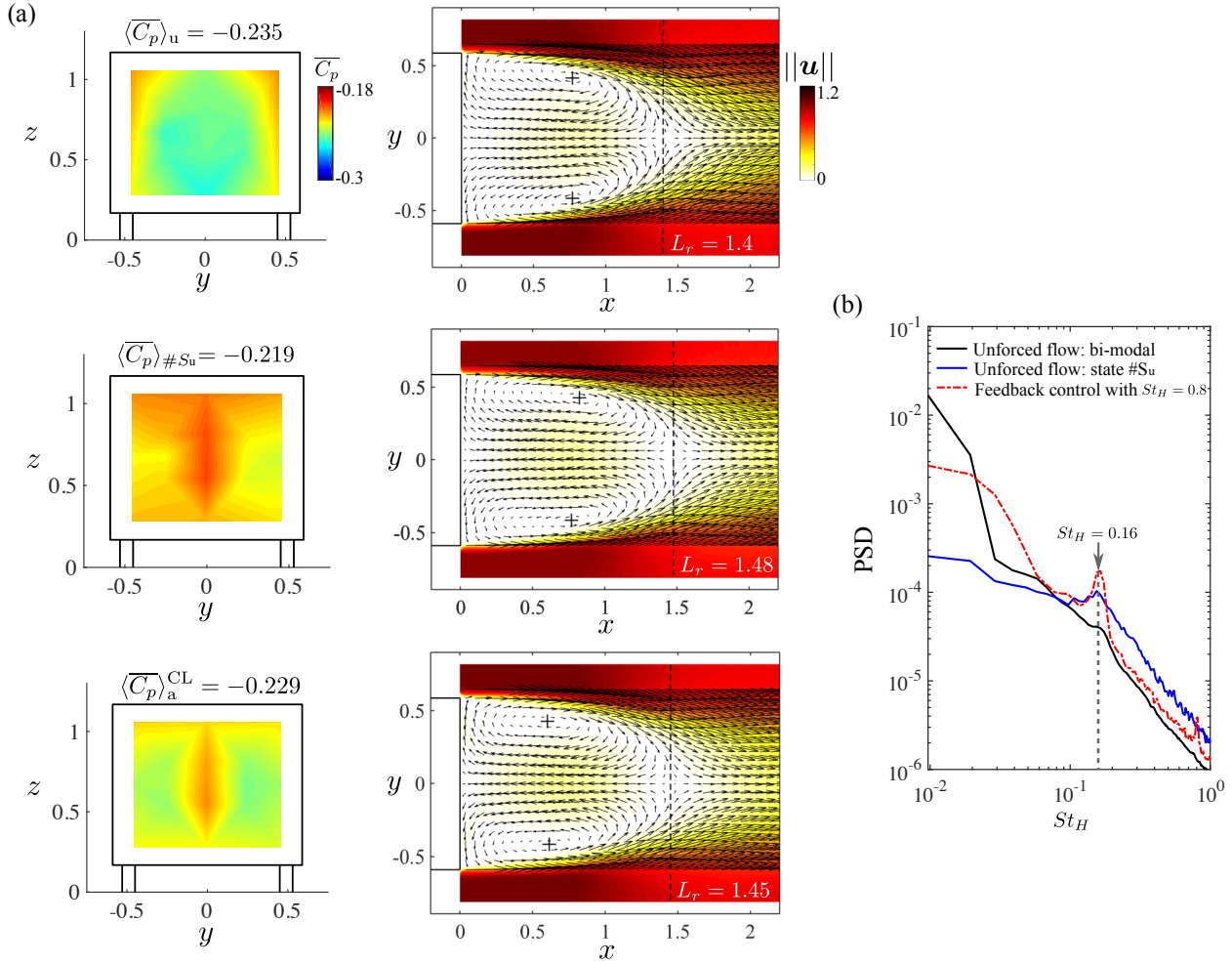


Figure 4.11: Effects of the feedback control at $St_H = 0.8$ with $P_0^i = 1.5$ bar on the base pressure, near wake and spectrum of the gradient $\partial C_p / \partial y$. (a) Color maps of the base pressure and velocity magnitude $\|\mathbf{u}\|$ for the unforced bi-modal flow (top), the conditionally averaged state #S_u (middle) and the feedback controlled flow (bottom). Velocity vectors are overlaid on the maps of $\|\mathbf{u}\|$. The bubble length is highlighted by a dashed line. The symbols '+' indicate the location of the centers of the recirculation zones. (b) Power spectral density (PSD) of the lateral pressure gradient $\partial C_p / \partial y$.

finding suggests that the shedding process is more prominent in a symmetric wake. For the feedback controlled flow, a damping of the energy at $St_H < 0.02$ is clear compared to the bi-modal flow, revealing the suppression of the bi-modality. The high energy content at $St_H < 0.1$ corresponds to the time taken to switch continuously from one state to the other submitted to the actuation. When compared to the state #S_u, the forced flow features a greater energy at $St_H < 0.1$, indicative of a more fluctuating movement at these time scales. Moreover, a discrete peak also appears at $St_H = 0.16$ and its intensity is much higher than that of the state #S_u. According to Barros *et al.* (2016a), the amplification of the antisymmetric vortex shedding leads to an increase of the drag. This constitutes another reason for the lower $\langle C_p \rangle_a^{CL}$ with respect to $\langle C_p \rangle_{\#S_u}$.

Figure 4.12 presents the diagrams of $\langle C_p \rangle$ versus $\partial C_p / \partial y$ for the three configurations above to compare the effects of the wake symmetrization and enhancement of shear layer mixing on the statistics of $\langle C_p \rangle$. The plot is colored by the PDF of $\partial C_p / \partial y$. In Fig. 4.12(a), one can clearly notice the benefit of the symmetric state #S_u which leads to a higher base pressure. In Fig. 4.12(b), the detrimental influence of the shear layer excitation can be recognized as the mean pressure value $\langle C_p \rangle_a^{OL}$ is 9% lower than $\langle C_p \rangle_u$. When applying the feedback control

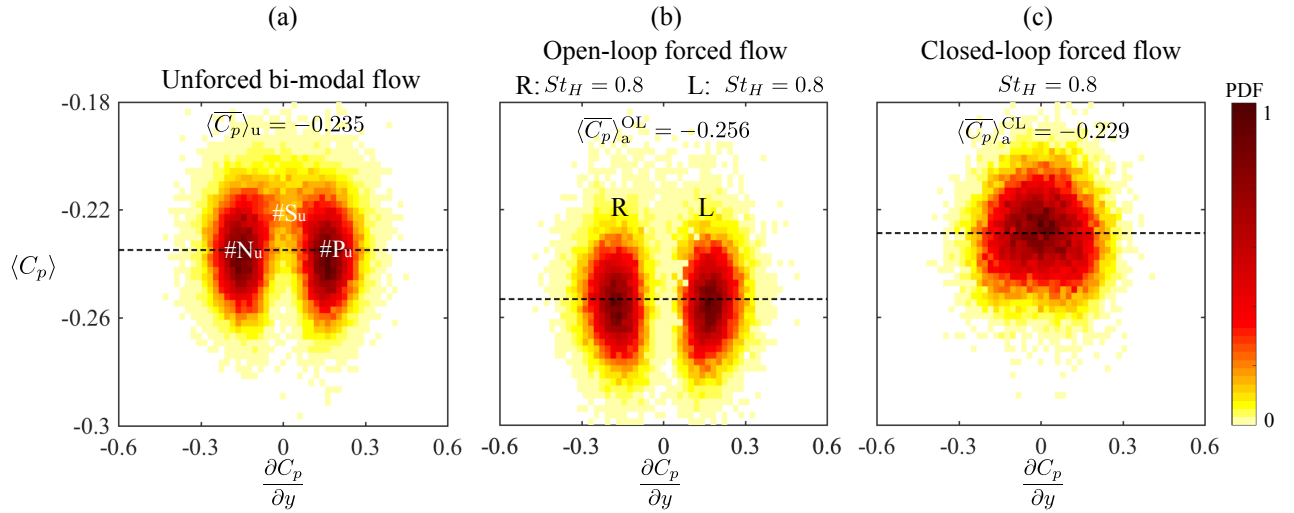


Figure 4.12: Diagrams of the time-varying area-averaged base pressure $\langle C_p \rangle$ versus $\partial C_p / \partial y$ colored by the PDF of the latter. (a) Unforced bi-modal flow. (b) Single edge open-loop control along R and L respectively with $St_H = 0.8$ and $P_0^i = 1.5$ bar. The results for R and L are superposed in this figure. (c) Closed-loop control with $St_H = 0.8$ and $P_0^i = 1.5$ bar. The dashed line indicates the corresponding time- and area-averaged base pressure value $\langle \overline{C_p} \rangle$.

with $St_H = 0.8$, as displayed in Fig. 4.12(c), the two effects shown in Fig. 4.12(a) and (b) are combined and yields ultimately a slight pressure recovery (3%) with a symmetrized distribution of $\partial C_p / \partial y$.

The findings above indicate that the base pressure recovery mechanism associated with the feedback control is a trade-off between the favorable effect of wake symmetrization and the adverse effect of shear layer mixing and vortex shedding amplification. At $St_H = 0.8$, although the degree of asymmetry is most reduced, it also leads to the most important mixing of shear layer and amplification of vortex shedding. For the other frequencies, the shear layer mixing is less enhanced and the vortex shedding is less amplified, however, the asymmetric states are also less suppressed. Hence, the resulting base pressure recovery for all the frequencies does not differ significantly from each other.

In conclusion, the physics-based feedback opposition control has been able to mitigate the bi-modal wake dynamics through the unsteady shear layer forcing. We find that by reducing the wake asymmetry, as measured by the root mean square of the lateral pressure gradient, the base pressure is increased by 3%, indicative of a slight drag reduction. The results align with the studies of Cadot *et al.* (2015); Evrard *et al.* (2016) and Brackston *et al.* (2016) which show that the suppression of the bi-modality can yield a drag reduction. Only a modest 3% base pressure recovery is achieved because the favorable effect of the wake symmetrization is counteracted by the increase of the shear layer dynamics. Yet, the amplified shear layer dynamics are indispensable for the wake symmetrization. In order to advance the control performance with the present setup, improvements of the control should be made to reduce the detrimental effect of periodic actuation phases. It would be particularly interesting to determine the minimal energy needed to trigger the mode switching. The study paves the way for the control of wake balance or reorientation which is of great importance in windy environment.

Chapter 5

Drag reduction of the car model at yaw

In this chapter, we pursue drag reduction of the car model at a slight yaw angle with the oncoming velocity. Fluidic actuation is applied on different lateral edges. We analyze the effects of forcing on drag and correlate these effects on the modifications of the base pressure and near wake to shed light on the underlying flow control mechanisms. Based on the flow responses to the periodic forcing, a physics-based bi-frequency actuation is proposed which outperforms the optimal periodic forcing. Moreover, the forcing effects by the addition of the Coanda surface are compared to those without this surface, demonstrating the sensitivity of the wake dynamics to different types of actuations.

Contents

5.1	Crosswind effects	87
5.2	Experimental setup	89
5.3	Unforced flow	92
5.4	Leeward forcing	96
5.4.1	Global effects of actuation	96
5.4.2	Effects on the base pressure and near wake	98
5.5	Windward forcing	103
5.5.1	Global effects of actuation	103
5.5.2	Effects on the base pressure and near wake	105
5.6	Windward bi-frequency forcing	112
5.6.1	Global effects of bi-frequency actuation	112
5.6.2	Effects on the base pressure and near wake	117
5.6.3	Analysis of the phase-averaged velocity statistics	121
5.6.4	On the drag reduction using LGPC	125
5.7	Unsteady Coanda blowing effect	127

5.1 Crosswind effects

Road vehicles are often exposed to side flows, for example when passing through a constant crosswind, wind gusts or unsteady wakes by other vehicles. The flow in the vehicle's reference system will be the vector combination of the side flow and the reciprocal of vehicle's forward velocity (Sims-Williams, 2011), as depicted in Fig. 5.1.

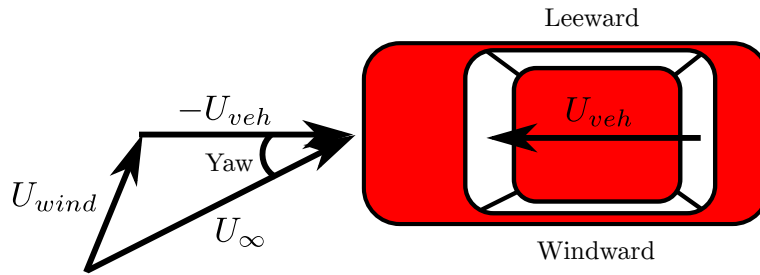


Figure 5.1: Vector combination of the vehicle velocity U_{veh} and side wind U_{wind} . U_{∞} : the resultant velocity vector seen by the vehicle. Adapted from Sims-Williams (2011).

The lateral side which is sheltered from the wind is called leeward, while the opposite flank facing the wind is denominated as windward. The side wind introduces the imbalance dynamics between the windward and leeward side, resulting in an asymmetric pressure distribution over the side surfaces of the vehicle. These asymmetric features raise mainly two concerns. First, they affect the driving comfort and safety, especially under unsteady crosswinds. The vehicle can be deviated from its trajectory by the combined action of the side force and yaw moment. In the cases of buses, trucks or trains, the vehicle can be even overturned by the effect of roll moment (Baker, 1986) due to their large lateral side area. The driving comfort and safety are mostly the concerns for large yaw angles of more than 20 degrees. Second, the drag increases under crosswind conditions as observed in previous studies (Gohlke *et al.*, 2007; Grandemange *et al.*, 2015; García de la Cruz *et al.*, 2017a; Rossitto *et al.*, 2017). Gohlke *et al.* (2007) and Rossitto *et al.* (2017) reported a quasi-linear drag increase with increasing yaw angles up to 15° . This increased drag is of major interest especially at small yaw angles as the yaw moment barely induces any risks in this case. In particular, small angles commonly appear in the real world situations. Figure 5.2, reported by D’Hooge *et al.* (2014), shows that the majority of possible yaw angles are within the range of 0° to 6° , which covers more than 88% of the probability distribution. It is not the intention of this study to assess the driving safety due to large yaw

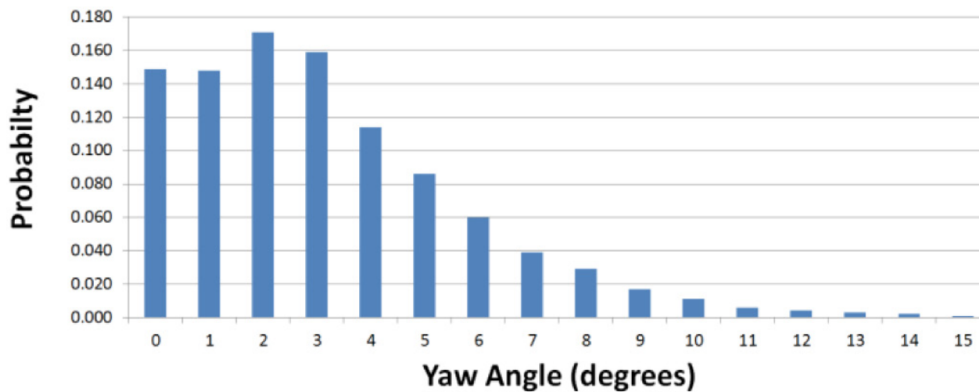


Figure 5.2: Probability distribution of the yaw angle for a ground vehicle traveling at 70 mile per hour (D’Hooge *et al.*, 2014).

angles or unsteady crosswinds but to explore the potential of drag reduction for vehicles at small yaw angles. The simplest measure is to determine the drag coefficient at a representative average yaw angle (Howell, 2015).

Flow control using passive or active devices for drag reduction of vehicles under yaw angles is challenging and remains relatively not well understood. García de la Cruz *et al.* (2017a) minimizes the drag force of a sub-scaled Ahmed body with two lateral rear flaps. They per-

formed a parametric study by varying different flap deflections, yaw angles and flap lengths. Optimal flap configurations, which are non-symmetric for non-zero yaw angles, are those that minimize the lateral force on the vehicle, while also minimizing the contribution of the flap-induced drag. Based on their results, an adaptive flap system can be designed to improve the static-flap performance. Active flow control with a steady Coanda blowing was investigated in Pfeiffer & King (2012). The authors developed a robust multi-variable closed-loop control strategy to reduce the drag and yaw moment of a three-dimensional bluff body for crosswind yaw angles from 0° to 10° . The controller is synthesized using linear black-box models identified from experimental data. It achieves 22% drag reduction for straight oncoming flow (zero yaw angle), and reduces the yaw moment to zero at a yaw angle as large as 10° . However, in the later case, drag was slightly increased compared to the unforced flow.

Most of the studies directly impact the geometry of the model by the addition of base flaps or curved surfaces. Based on our results in Chapter 3 and Chapter 4, fluidic blowing using pulsed jets similarly improve the aerodynamic performance. However, it affects directly the wake dynamics without changing the model geometry. This fact can be considered as a great advantage over passive devices.

In this work, we apply fluidic forcing to manipulate the wake past a yawed car model subjected to a moderate yaw angle of 5° . According to Fig. 5.2, this yaw angle happens with a high probability. The purpose here is to investigate the control authority of pulsed jets to decrease drag. Although the aerodynamics under steady yaw conditions differ significantly from unsteady crosswind flows, the simplified steady configuration provides insights to more complicated oncoming flow dynamics.

5.2 Experimental setup

The experimental facility and the model are identical to the ones described in Chapter 3. This section only presents the differences with respect to the setup detailed in § 3.2.

A sketch of the setup is shown in Fig. 5.3. Two coordinate systems are distinguished: the aerodynamic coordinates (X_o, Y_o, Z_o) with X_o parallel to the free-stream velocity U_∞ and the body-fixed coordinates (x, y, z) aligned with the length axis of the car model. The origin of the former system lies at point O_o which is located on the raised flow and at the center of the car model, while the latter system has the same origin O as described in the previous chapters for a clear demonstration of the wake region. Crosswind is simulated by turning the model with respect to the upstream velocity by a yaw angle β . At zero incidence, i.e. $\beta = 0^\circ$, X_o aligns with x , similar to the analysis reported in the previous chapters. Here, the yaw angle is fixed at $\beta = 5^\circ$. The experiments were performed at $U_\infty = 25 \text{ m s}^{-1}$, corresponding to a Reynolds number $Re_H \approx 5 \times 10^5$, based on the height of the model.

Measurements of forces and moments

In a yawed configuration, not only the drag but also the side force and yaw moment need to be characterized. For that, we use of a six-component force and moment balance. It enables measurements of the forces and moments acting on the model along the three directions. The measuring system is composed of a 9129AA Kistler multicomponent dynamometer using piezo-electric force sensors and a 5080A charge amplifier. The maximum permitted measuring range is $[-10, 10]$ kN for forces and $[-500, 500]$ N·m for moments. The calibrated range used here is $[0, 60]$ N. Measurement uncertainty due to the hysteresis and nonlinearity is less than 0.3% of the full scale span.

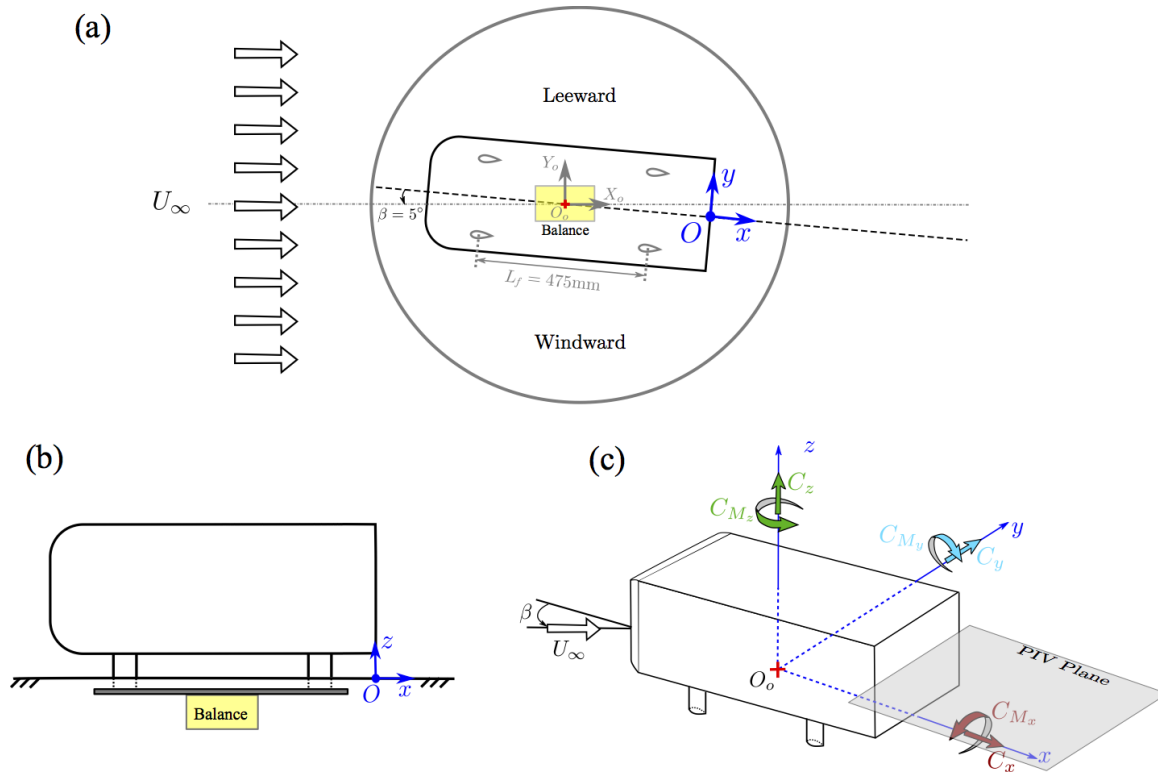


Figure 5.3: Sketch of the yawed model setup. (a) Top view; (b) side view; (c) perspective view.

The balance has been calibrated outside the wind tunnel. More than 150 independent experiments with calibrated loads on the different measurement channels allow us to establish an calibration matrix. The corresponding equation is:

$$\mathbf{S} = \mathbf{G}\mathbf{F}, \quad (5.1)$$

where \mathbf{S} is the signal vector, \mathbf{F} the known load vector and \mathbf{G} the calibration matrix. For a multi-component force transducer, the design ensures that all the loads acting on the model are separated into single component as best as possible. In principle, there is only a linear interaction between the load and the measured signal. \mathbf{G} is a 6×6 matrix with non-zeros values on the diagonal. In reality, there exist systematic errors due to interactions among different components which may cause a few-percent difference in the linear characteristic. Therefore it is often necessary to measure more components in order to separate the errors during calibration to improve the accuracy. In the present study, these interactions are taken into account by including second-order nonlinear terms in the matrix \mathbf{G} which is of size 6×21 . The matrix \mathbf{G} is then used in the analysis software to determine the aerodynamic loads from the measured balance data: $\mathbf{F}_a = (\mathbf{G})^{-1}\mathbf{S}$ (Tropea & Yarin, 2007; Paillé, 2017).

The balance is mounted inside the raised floor and is connected to the model through a metal plate of thickness 15 mm, as shown in Fig. 5.3(b). The metal plate is connected to the model by the use of four profiled supports and is aligned with the model, while the balance is parallel to the wind tunnel axis X_0 , as depicted in Fig. 5.3(a). Thus the balance measures aerodynamic forces in the wind tunnel frame. However, we are interested in the forces in the model frame as the drag to be overcome by the propulsion system is against the car's travel motion. At this end, the measured quantities are projected on the body axes (x, y, z) with the origin O_o of the wind tunnel frame. In the following, the mentioned forces and moments refer to the body-fixed reference (x, y, z) with the origin O_o as presented in Fig. 5.3(c). The data is acquired by a 16-channel *Data Translation DT9857E* data acquisition module at 100 Hz.

A low-pass filter at 10 Hz is used to get the time-averaged forces F_i and moments M_i with $i \in \{x, y, z\}$. Each coefficient of the forces and moments is expressed as follows:

$$\begin{aligned}
 \text{Drag coefficient: } C_x &= F_x/qS \\
 \text{Lateral force coefficient: } C_y &= F_y/qS \\
 \text{Lift coefficient: } C_z &= F_z/qS \\
 \text{Roll moment: } C_{M_x} &= M_x/qSl_m \\
 \text{Pitch moment: } C_{M_y} &= M_y/qSl_m \\
 \text{Yaw moment: } C_{M_z} &= M_z/qSl_m
 \end{aligned} \tag{5.2}$$

where $q = 1/2\rho U_\infty^2$ is the dynamic pressure, $S = HW$ is the frontal area of model and $l_m = 1/2L_f$ is half the distance between two support feet (see Fig. 5.3(a)). To be consistent with the previous chapters, we make $C_x = C_D$ without ambiguity.

Note that there is a drift in the output signal over time, which is a typical characteristic of using piezoelectric sensors. Although the design of the balance has limited this drift, it still affects the accuracy of the measurements when the recording time is long. Hence, we remove this drift from the raw data by estimating a drift rate α using signals in quiescent air recorded over more than 30s. The corrected signal is obtained by subtracting αt from the original recorded data, where t is the relevant recording time. The coefficient α varies from different experiments and it was calculated for each of them to improve the accuracy of the corrected data.

Although the six force components are measured, we focus on the most relevant quantities concerning the crosswind dynamics, i.e. the drag force C_D along x , the side force C_y along y and the yaw moment C_{M_z} along z .

Reservoir pressure regulation

In the previous chapters, the actuation amplitudes are regulated by changing the initial supply pressure P_0^i in the compressed air reservoir located inside the model (see Fig. 3.2(b)). In this chapter, we apply a proportional-integral-derivative (PID) controller to maintain the reservoir pressure at a constant set-point during the actuation for all investigated frequencies. The sensor of the PID controller is a Bourdon Sedem[®] E913 pressure transmitter which measures the instantaneous pressure inside the reservoir. An electro-pneumatic regulator (SMC[®] ITV3030) is used to control the reservoir pressure steplessly according to the output command of the PID controller. In the following, we denote by P_0 the supply pressure in the reservoir.

Velocity measurements

PIV measurements are performed with the same methodology described in § 3.2.3. The measurements are acquired in the lateral plane at mid height $z = 0.67$, as presented in Fig. 5.3(c). The time between a pair of images yielding one velocity field is 50 μ s. The image pairs are recorded at a sampling rate of 3.5 Hz. Velocity vectors are processed with an interrogation window of 32×32 pixels with a 50% overlap, giving a spatial resolution of 2.7 mm corresponding to 0.009 H . The field of view covers a region of approximately $2.5 H \times 1.8 H$. The velocity statistics are computed with 1500 independent velocity fields.

Hot-wire measurements using the StreamlinePro Anemometer System described in § 3.2.3 are performed for the measurement of boundary layer profiles over the model's lateral surface. The hot-wire probe is fixed to a profiled traverse system installed on the roof of the wind tunnel. Boundary layer profiles are measured with respect to the normal direction of the model's surface,

thus the probe is carefully regulated to align with the model axis x and is traversed along y . The precision of the displacement system is $16\ \mu\text{m}$.

Real-time system

The control applied in this chapter uses the same Labview Real-time module presented in § 3.2.4. The main difference is that we increase the sampling rate of the real-time processing to $F_{RT} = 5\ \text{kHz}$ and the acquisition frequency to $2.5\ \text{kHz}$. The increase of F_{RT} is to have more possibilities of periodic frequencies and their corresponding duty cycles (DC). For details, see § 3.2.4. The tested periodic frequencies and duty cycles are the subset of the harmonics derived from $F_{RT} = 5\ \text{kHz}$, as shown in table 5.1. The displayed duty cycles are obtained by changing

N_{sp}	f [Hz]	St_H	DC	N_{sp}	f [Hz]	St_H	DC
—	0	0	100%	50	100	1.2	48%
500	10	0.12	47%	33	151	1.8	45%
357	14	0.17	47%	25	200	2.4	48%
278	18	0.21	47%	20	250	3	45%
250	20	0.24	47%	17	294	2.3	47%
156	32	0.38	47%	15	333	4	47%
125	40	0.48	47%	13	385	4.6	46%
100	50	0.6	47%	12	417	5	42%
74	68	0.8	46%	11	455	5.4	45%
63	80	1	46%	10	500	6	40%

Table 5.1: Tested periodic forcing parameters. N_{sp} is the number of sampling points in one time period of $f \in [0, 500]\text{Hz}$. $f = 0$ denotes the continuous blowing.

the threshold of the Heaviside function from 0 to 0.1, i.e. $b(t) = H(\sin(2\pi ft) - 0.1)$, $b(t)$ being the control law to generate periodic forcing. The value 0.1 is chosen based on the results of Chapter 3 which show that high frequencies with a duty cycle lower than 50% perform better than those having a high duty cycle.

5.3 Unforced flow

In this section, we describe the unforced flow characteristics at yaw angle $\beta = 5^\circ$. The results furnish the baseline to be compared with the forced wakes. First, we compare the boundary layer profiles close to the flow separation over the leeward and windward sides. Then, we illustrate the statistics and dynamics of the base pressure and near wake. We also discuss the mean forces and moments for this yaw configuration.

Boundary layer conditions

The boundary layer at separation sheds vorticity into the flow and conditions the roll-up process of the free shear layers originating from the trailing edges (Morris & Foss, 2003). To identify different boundary layer conditions, the hot-wire anemometry is used to measure the streamwise velocity at two points located at the leeward and windward trailing edge. The hot-wire probe is displaced 1mm downstream of the trailing edge for safe traversing. The coordinates for the two points are respectively $(x, y, z) = (0, 0.6, 0.67)$ and $(0, -0.6, 0.67)$ which are indicated in Fig. 5.4(a). Figure 5.4(b-d) present the profiles of the time-averaged streamwise velocity and the standard deviation. The ordinate Δy corresponds to the wall distance. Figure 5.4(b)

illustrates the dimensional profiles, while in Fig. 5.4(c,d) we normalize Δy by the boundary layer thickness $\delta_{0.99}$ which is $\delta_{0.99}^{\text{lee}} = 18.5\text{ mm}$ for the leeward and $\delta_{0.99}^{\text{wind}} = 14.6\text{ mm}$ for the windward side. Note that the mean velocity \bar{u} is already divided by the upstream velocity U_∞ . The most significant difference between the two boundary conditions lies in the wall vicinity. Instead of a typical turbulent boundary layer profile as observed at the windward side, leeward side presents a layer of thickness 1 mm close to the wall with very low velocities inside. We further give a close view of this layer in Fig. 5.4(c). Intriguingly, there exists a reversal in the sign of the velocity gradient with a minima at $\Delta y/\delta_{0.99}^{\text{lee}} = 0.032$. This profile is reminiscent of the separated boundary layer except that we do not observe a reversed flow here as the hot-wire measurement technique applied in this study is not able to distinguish the flow direction. Based on the observation, we assume that the velocities below $\Delta y/\delta_{0.99}^{\text{lee}} = 0.032$ may be negative due to an adverse pressure gradient and that the leeward boundary layer has separated upstream of the trailing edge. Figure 5.4(d) shows that the maximum fluctuating velocities of both boundary layers are more than 15% of the upstream velocity and are concentrated close to the wall.

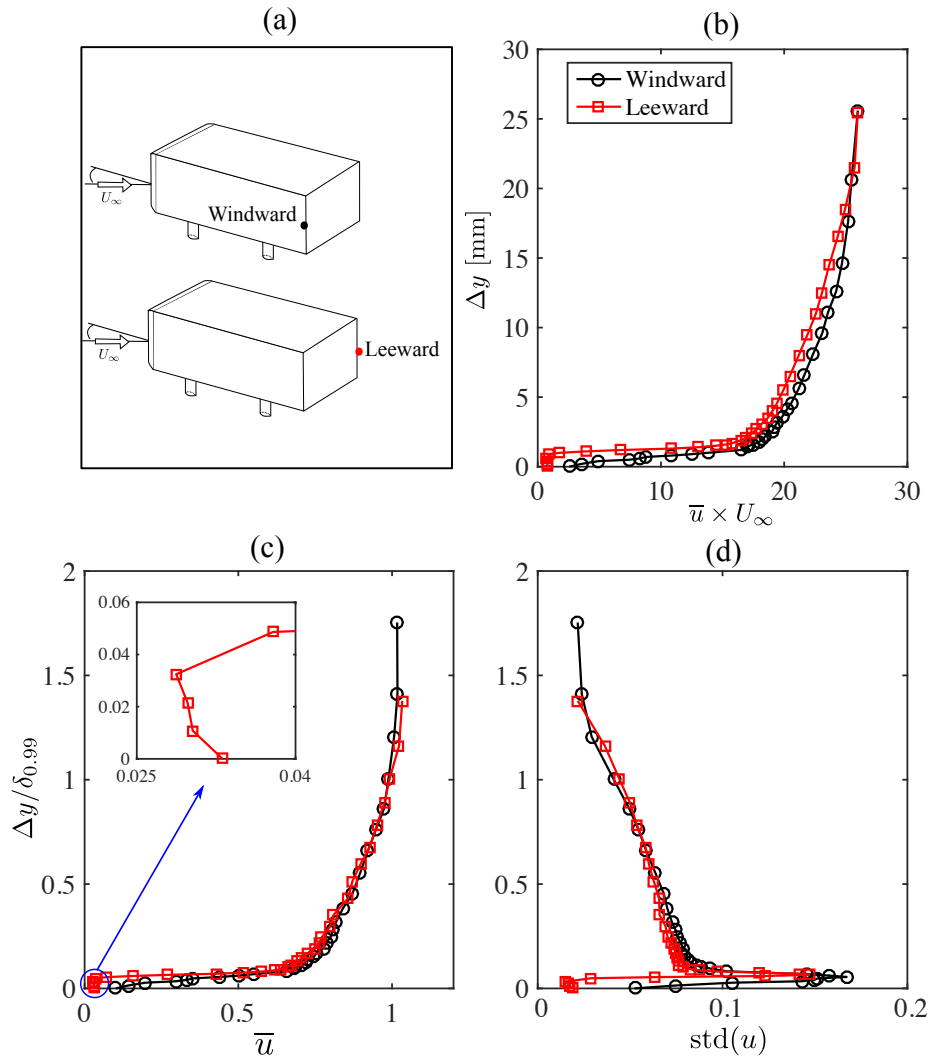


Figure 5.4: Time-averaged streamwise velocity from the hot-wire measurements. (a) Measuring point positions. (b) Dimensional boundary layer velocity profiles. Note that we denote by \bar{u} the non-dimensional velocity. (c) Non-dimensional boundary layer velocity profiles. The inserted figure gives a close view of the leeward profile near the wall. (d) Standard deviation of the velocity.

Near wake and base pressure

Now we turn our attention to the near wake flow. The aim here is to compare the yawed ($\beta = 5^\circ$) and aligned configurations by detailing their wake, base pressure and aerodynamic forces.

To clarify the changes of flow caused by a yaw angle, we compare in Fig. 5.5 the mean velocity field in the mid-height plane $z = 0.67$ and the base pressure for the aligned and yawed model. Note that the results for the aligned model were obtained at $U_\infty = 30 \text{ m s}^{-1}$, but the corresponding wake topology is equivalent to that at $U_\infty = 25 \text{ m s}^{-1}$. In particular, Barros (2015) demonstrated that the mean velocity profiles in the wake are almost superimposed for these two upstream velocities. Thus, we consider that this comparison is sufficient to describe the influence of yaw angle.

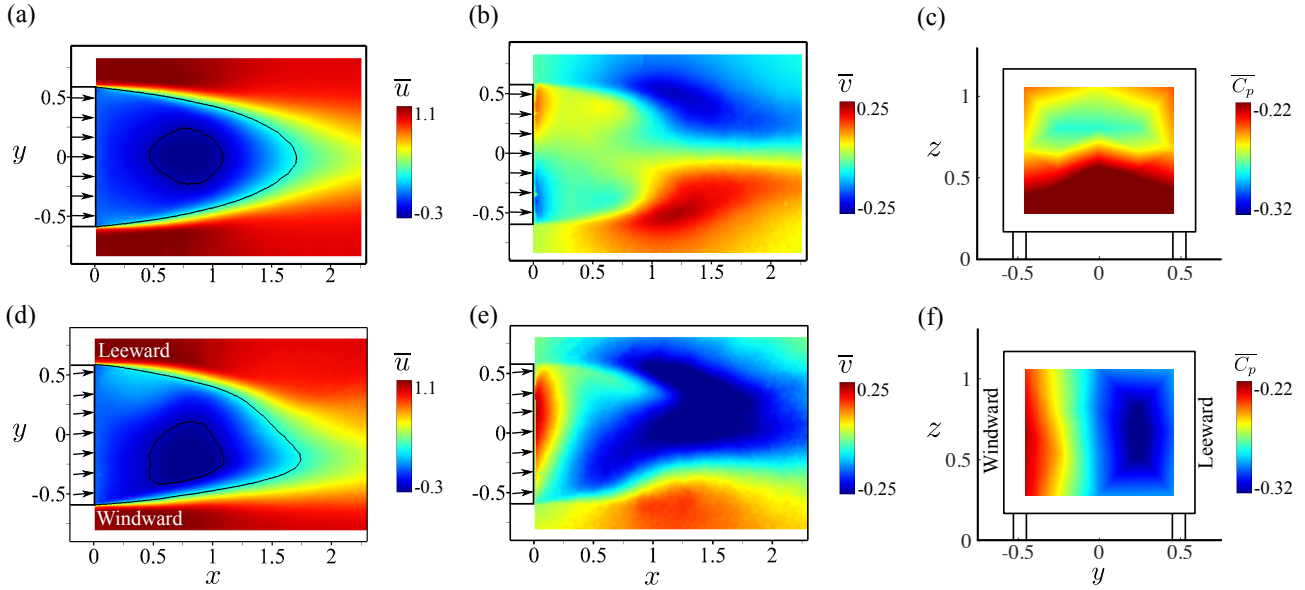


Figure 5.5: Mean wake in the mid-height plane and base pressure for (a-c) the aligned model at $U_\infty = 30 \text{ m s}^{-1}$ and (d-f) the yawed model at $U_\infty = 25 \text{ m s}^{-1}$. From left to right: the color maps of the mean streamwise velocity \bar{u} , the mean spanwise velocity \bar{v} and the base pressure. Black lines in (a) and (d) are iso-contour lines at $\bar{u} = \pm 0.25$. The arrows on the model show the direction of oncoming velocity.

For the aligned model, the distributions of \bar{u} , \bar{v} and \bar{C}_p are all symmetric with respect to $y = 0$. The presence of the yaw angle breaks this symmetry. The iso-contour lines in Fig. 5.5(d) are deviated towards the windward side, and a high curvature is observed at the leeward side near the end of the recirculation region. The distribution of \bar{v} in Fig. 5.5(e) shows that most of the free-stream flow is entrained into the wake region from the leeward side, manifested by the large blue region with negative spanwise velocities. Thus, the mean wake exhibits a large clockwise recirculating structure which is shown later in Fig. 5.12. This asymmetry is expected as the boundary conditions at the windward and leeward side differ from each other leading to different shear layer dynamics and recirculating flows. The observations suggest us that if the entrained flow from the windward side can be increased by the shear layer excitation, it may counteract the opposing leeward flow and symmetrize the wake which has been shown to be beneficial for the drag reduction in Chapter 4. This problem will be the subject of § 5.5. Additionally, the distribution of \bar{C}_p in Fig. 5.5(f) is consistent with the velocity field. A large low-pressure zone located near the leeward edge confirms the existence of the clockwise recirculating flow at the same side. On the other hand, we observe that the topology of the horizontal velocity field at mid-height $z = 0.67$ for the yawed configuration is quite similar to

that of the vertical velocity field at $y = 0$ for the aligned condition (see Fig. 5 in Barros *et al.* 2016b).

The wake dynamics can be further analyzed by the distribution of Reynolds stresses $\overline{u'u'}$, $\overline{v'v'}$ and $\overline{u'v'}$. These quantities are depicted in Fig. 5.6 for the two configurations as in Fig. 5.5. All

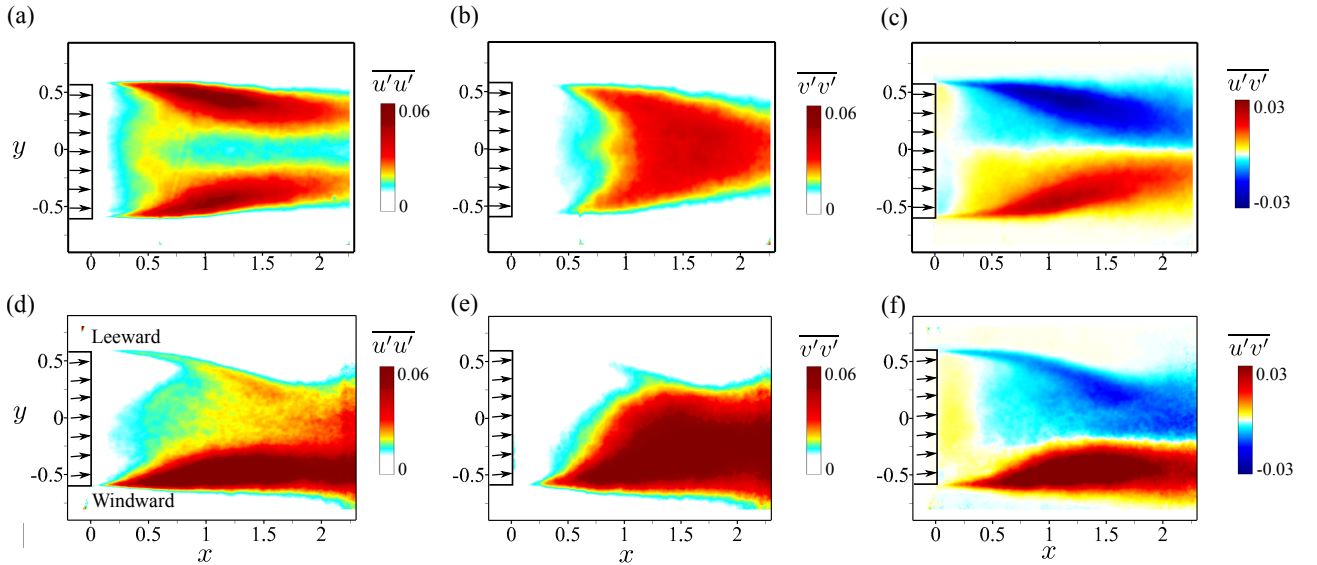


Figure 5.6: Reynolds stresses in the mid-height plane for (a-c) the aligned model at $U_\infty = 30 \text{ m s}^{-1}$ and (d-f) the yawed model at $U_\infty = 25 \text{ m s}^{-1}$. The arrows on the model show the direction of oncoming velocity.

three quantities are concentrated along the shear layers, especially for $\overline{u'u'}$ and $\overline{u'v'}$. The shear layers of the aligned model feature a symmetric distribution, in agreement with the balanced wake shown in Fig. 5.5. For the yawed configuration, the velocity fluctuations along the leeward shear layer are considerably higher than those along the windward shear layer. The turbulent dynamics along the leeward shear layer are expected to be damped by the flow curvature (Borée *et al.*, 2002; Bradshaw, 1973). These distributions of Reynolds stresses are similar to those on the vertical plane $y = 0$ for the aligned model where the fluctuating motions are concentrated in the bottom shear layers with wall proximity. In particular, leeward (windward) shear layer resembles the top (bottom) shear layer of the aligned model. This observation suggests that the presence of side wind induces similar global effects as those created by the wall proximity or by any other asymmetries or controls (Barros *et al.*, 2017).

Mean forces and moments

Table 5.2 compares the base pressure, forces and moments for aligned and yawed configurations. The yaw condition decreases the time-averaged base pressure by 22% and increases the drag by 3%. The important base pressure drop is associated with the appearance of the wake asymmetry demonstrated in Fig. 5.5(d,e). The drag increase is consistent with the results of Pfeiffer & King (2012), but is smaller than the observations of Grandemange *et al.* (2015) and García de la Cruz *et al.* (2017a) with flaps installed at the back surface.

We did not measure C_y and C_{M_z} for the aligned model, but these values are assumed to be near zero as the distribution of velocity and pressure is symmetric with respect to $y = 0$, see Fig. 5.5(a-c). For the yawed configuration, an important side force C_y is obtained which is induced by the asymmetric pressure distribution along the leeward and windward surface. Although the measurements of the pressure along the lateral surfaces are not available in the present study, we can get a hint from the results of Pfeiffer & King (2012) where a similar 3D

Configuration	$\langle \overline{C_p} \rangle$	C_D	C_y	C_{M_z}
Aligned model	-0.231	0.266	–	–
Yaw angle $\beta = 5^\circ$	-0.280	0.274	0.314	-0.23

Table 5.2: Averaged base pressure, forces and yaw moment coefficients for the unforced flow past the aligned and yawed model. Results are obtained at $U_\infty = 25 \text{ m s}^{-1}$.

bluff body was investigated at a crosswind angle $\beta = 10^\circ$. The pressure around the model of their study is shown in Fig. 5.7. It illustrates an overall lower pressure on the leeward side than

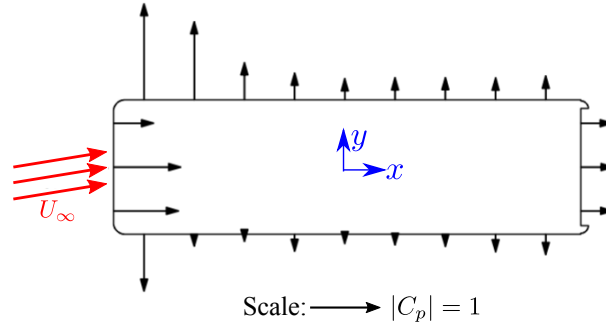


Figure 5.7: Results extracted from Pfeiffer & King (2012). Pressure distribution along a cross-section of the 3D bluff body at yaw angle $\beta = 10^\circ$. The length of the black arrows correspond to the magnitude of the pressure coefficients. Positive (negative) pressure coefficients point inwards (outwards).

the windward side which leads to a positive lateral force. In particular, the lowest pressure locates near the leeward nose of the model which is related to the high flow curvature at this region. According to Grandemange *et al.* (2014), a non-zero lateral force C_y is likely to increase the drag due to the induced drag effect which is linked to the streamwise vorticity in the far wake. However, the issue of induced drag for square-back bluff bodies remains to be clarified with further investigations. On the other hand, the result in Fig. 5.7 points to a different contribution of the side forces from the front and rear parts of the model. The yaw moment is actually generated by this different contribution. In the present study, the yaw moment is negative, indicating that a larger contribution of the side force comes from the front part due to the low pressure near the leeward nose of the model.

5.4 Leeward forcing

In the following, we focus on the actuated flows. In this section, periodic forcing is applied along the leeward edge. The aim is to investigate the effects of leeward forcing on the base pressure, drag and near wake. The results will motivate and provide hints for future studies of closed-loop control.

5.4.1 Global effects of actuation

To quantify the effects of actuation at various frequencies and amplitudes, we define the following parameters:

$$\gamma_p = \frac{\langle \overline{C_p} \rangle_a}{\langle \overline{C_p} \rangle_u}, \quad \gamma_D = \frac{C_{D_a}}{C_{D_u}}, \quad \gamma_y = \frac{C_{y_a}}{C_{y_u}}, \quad \gamma_{M_z} = \frac{C_{M_{z_a}}}{C_{M_{z_u}}}. \quad (5.3)$$

The subscript ‘u’ represents unforced flow and ‘a’ stands for actuated flow. These parameters indicate the changes of base pressure, drag, side force and yaw moment, respectively. The definition of γ_p is the same as the cost function J in Chapter 3: $\gamma_p < 1$ ($\gamma_p > 1$) represents the increase (decrease) of base pressure. For the other three parameters, a value smaller than 1 corresponds to a reduction of the absolute value of the related quantity. The effects of actuation on these parameters are shown in Fig. 5.8. For a clearer plot, the abscissa is shown with a logarithm scale. The applied frequencies and their corresponding duty cycles are listed in table 5.1. The uncertainties of these measured ratios are about 0.3% based on a confidence interval of 95%. For all the investigated frequencies, the leeward actuation increases both γ_p and γ_D . Augmenting the supply pressure P_0 further promotes this increase of γ_p and γ_D for the whole frequency range. The highest value of γ_p and γ_D are both found at $St_H = 0.8$ independent of P_0 . Note that this frequency value is also responsible for the highest increase of drag in the study of Barros *et al.* (2016b) when the forcing is applied along the top leading edge. In addition, the trend of γ_p in Fig. 5.8 agrees well with the curve in Fig. 8 of Barros *et al.* (2016b) which demonstrates this dependence of γ_p on St_H of the top edge without yaw angle. We have mentioned in § 5.3 the similarity of the unforced flow features between the mid-height plane $z = 0.67$ at $\beta = 5^\circ$ and the symmetric plane $y = 0$ at $\beta = 0^\circ$. Here, the variation of γ_p for these two cases further underlines their similarity in the forced flow features.

Leeward actuation increases γ_y for almost all the test cases while decreases γ_{M_z} for the whole range of St_H . Few points around $St_H = 0.8$ are below $\gamma_y = 1$ but their variations are as small as the measurement uncertainty 0.3%. The dependence of γ_y on P_0 is not clear for

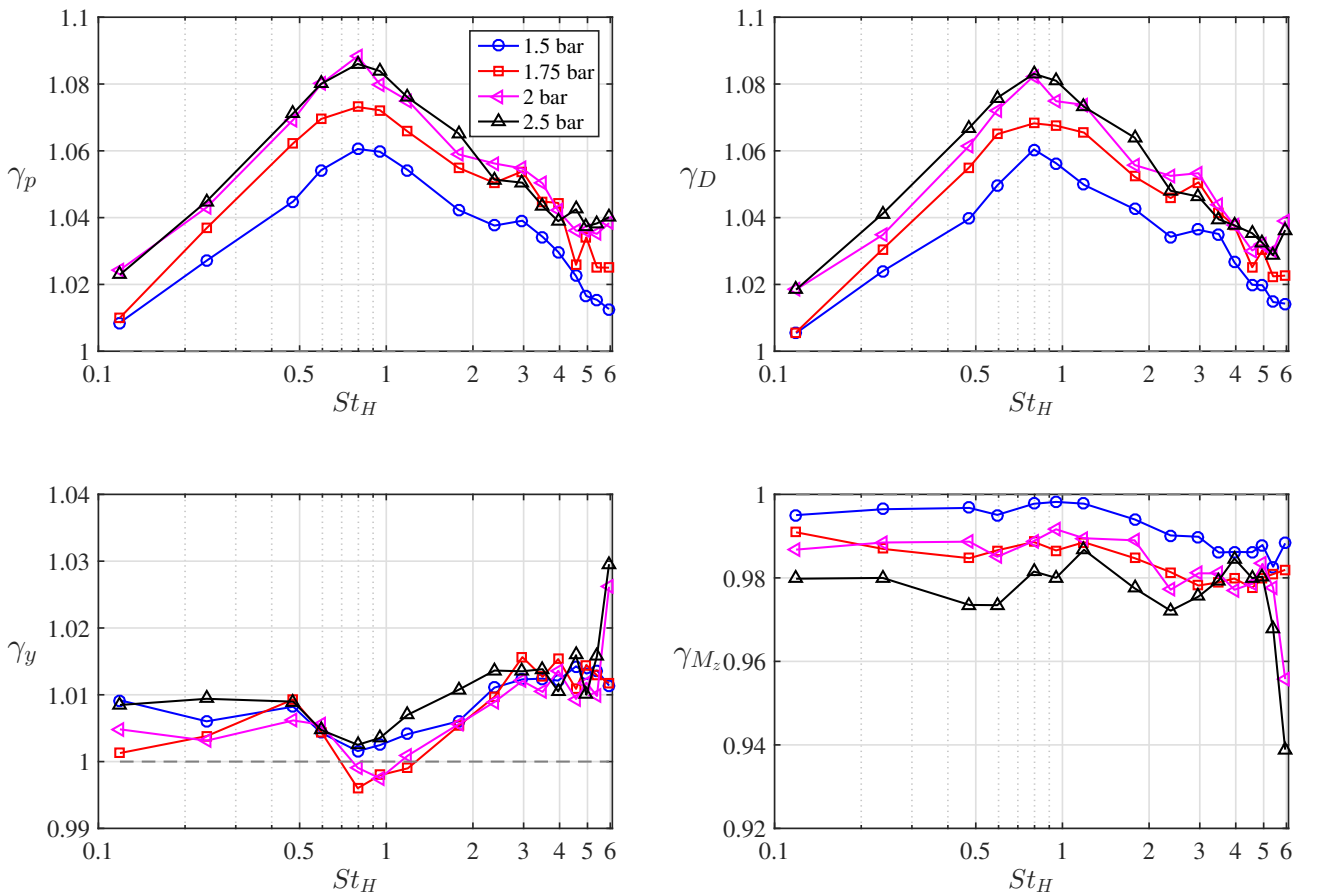


Figure 5.8: Effects of leeward forcing on the ratios of base pressure γ_p , drag γ_D , side force γ_y and yaw moment γ_{M_z} as a function of the non-dimensional frequency St_H and supply pressure P_0 . The unforced value equals to 1 for all four quantities.

$St_H < 5.5$ since the variations with P_0 are less than $\pm 1\%$. At $St_H = 6$, the impact of P_0 is more pronounced and it appears that γ_y increases and γ_{M_z} decreases with increasing P_0 . The highest value of γ_y and the lowest value of γ_{M_z} are both obtained at $St_H = 6$ with $P_0 = 2.5$ bar. In addition, at $St_H = 0.8$ where γ_D has been increased by 9%, the corresponding variations of γ_y and γ_{M_z} remain small (less than 2%), indicating that the forcing effect at this frequency is more important on the drag than on the side force and moment.

Moreover, Fig. 5.8 suggests a positive correlation between γ_p and γ_D , and a negative correlation between γ_y and γ_{M_z} . Their linear relations and correlation coefficients are reported in Fig. 5.9. The decrease of base pressure accounts for 100% of the drag increase, while

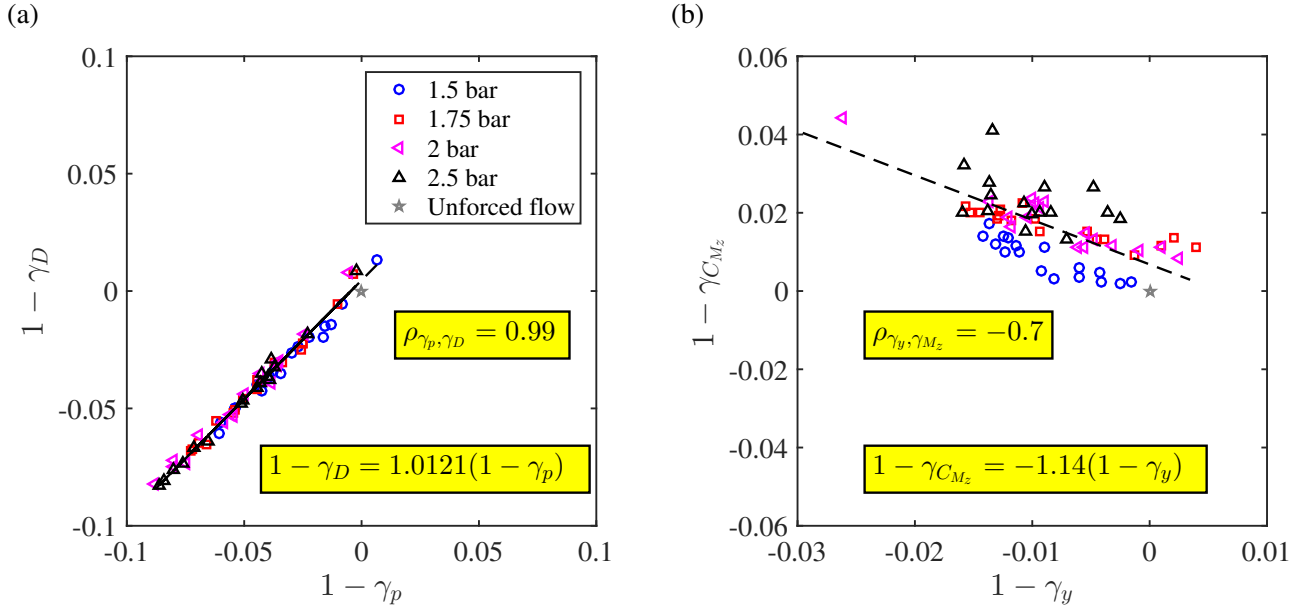


Figure 5.9: Correlation between (a) $1 - \gamma_p$ and $1 - \gamma_D$; (b) $1 - \gamma_y$ and $1 - \gamma_{M_z}$. $\rho_{\gamma_p, \gamma_D}$ and $\rho_{\gamma_y, \gamma_{M_z}}$ are their correlation coefficient, respectively. Note that $1 - \gamma_p = \Delta C_p / \langle \overline{C_p} \rangle_u$.

without yaw, Barros (2015) measured that only 70% of base pressure increase contributes to the drag increase. This suggests that the C_D vs. C_p relation should be reviewed for the yawed configuration. The ratio between the decrease of γ_{M_z} and increase of γ_y is -1.14 . We have mentioned before that the yaw moment is related to the balance of side forces C_y in the front and rear parts of the model. To gain insights on the variation of C_y in the rear part, we show in Fig. 5.10 the profiles of the streamwise velocity \bar{u} measured at $x = -0.08$ prior to the leeward separation. The velocity is accelerated by actuation, implying a decrease of the corresponding pressure. We also verify that the actuation does not affect the velocity over the windward side. This suggests that C_y in the rear part increases. Therefore, a counter-moment is created, which reduces the yaw moment. Similar observations have also been reported in Pfeiffer & King (2012) where side surface pressures were measured by sensors. Fig. 5.10 also presents that the velocity acceleration is more pronounced at $St_H = 6$, revealing a higher side force and a higher counter-moment. Hence this frequency yields the most significant increase of γ_y and reduction of C_{M_z} .

5.4.2 Effects on the base pressure and near wake

To shed more light into the underlying mechanisms responsible for increasing drag, we devote the following paragraphs to analyze the dynamic changes of base pressure and near wake under actuation. We focus here on two configurations with $P_0 = 2.5$ bar: (1) the low-frequency forcing

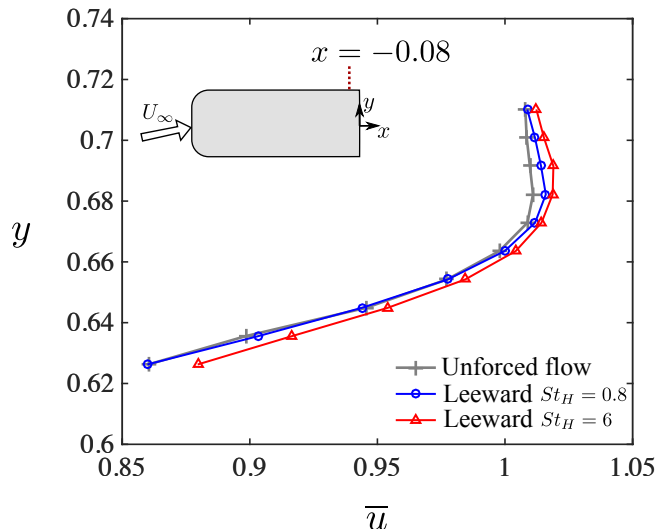


Figure 5.10: Profiles of the time-averaged streamwise velocity \bar{u} over the rear leeward surface at $x = -0.08$ (data extracted from PIV measurements). Note that the side surfaces of the model are located at $y = \pm 0.6$.

at $St_H = 0.8$ with the maximum drag increase (+9%); (2) the high-frequency forcing at $St_H = 6$ with the minimum yaw moment (-6%) and less increase of drag (+4%).

First, we describe the effects of actuation on the base pressure distribution and the temporal variation of the lateral pressure gradient. The data used for this analysis are recorded during 2.5 minutes, corresponding to 12000 convective time units $t_c = H/U_\infty$. Figure 5.11(a) compares the contour maps of the time-averaged base pressure for the unforced and forced flows. It is clear that the base pressure near the forced edge is decreased by actuation at both frequencies (see blue zones on the pressure distribution). Figure 5.11(b) highlights the four pressure values at the model's mid-height line. The actuations reduce the pressure along the whole spanwise direction. This observation is consistent with the findings of the open-loop tests of the bi-modal wake control: the base pressure drops close to the forced edge independently of the applied frequency. We also investigate the statistics of the lateral pressure gradient defined as:

$$\frac{\partial C_p}{\partial y} = \frac{1}{2} \frac{C_{p8} - C_{p5}}{y_8 - y_5} + \frac{1}{2} \frac{C_{p7} - C_{p6}}{y_7 - y_6}. \quad (5.4)$$

This definition was used in Chapter 4 to quantify the lateral wake asymmetry. Figure 5.11(c) shows the PDF of $\partial C_p / \partial y$. The three curves collapse with the most probable gradient at $\partial C_p / \partial y = -0.12$, indicating that the forcing has no impact on the degree of asymmetry. Note that the pressure gradient $\partial C_p / \partial z$ along z is centered around zero for all three cases (not shown here). We further analyze the spectrum of $\partial C_p / \partial y$ (Fig. 5.11(d)) which reflects the lateral wake dynamics such as vortex shedding. Not only distinct peaks at the forcing frequency can be distinguished, a broadband increase in the low frequency range ($St_H < 0.15$) is also discernible. This suggests that the actuation promotes the low-frequency wake motions by exciting the shear layer at a higher frequency.

The changes of base pressure are related to the modifications of the near wake flow. Figure 5.12 shows the time-averaged in-plane streamlines of the velocity field in the mid-height plane for all three configurations. All of them feature a similar streamline topology with a more extended clockwise recirculating motion close to the leeward side. This is in agreement with the distribution of the mid-height line pressure in Fig. 5.11(b) and the coincident PDF

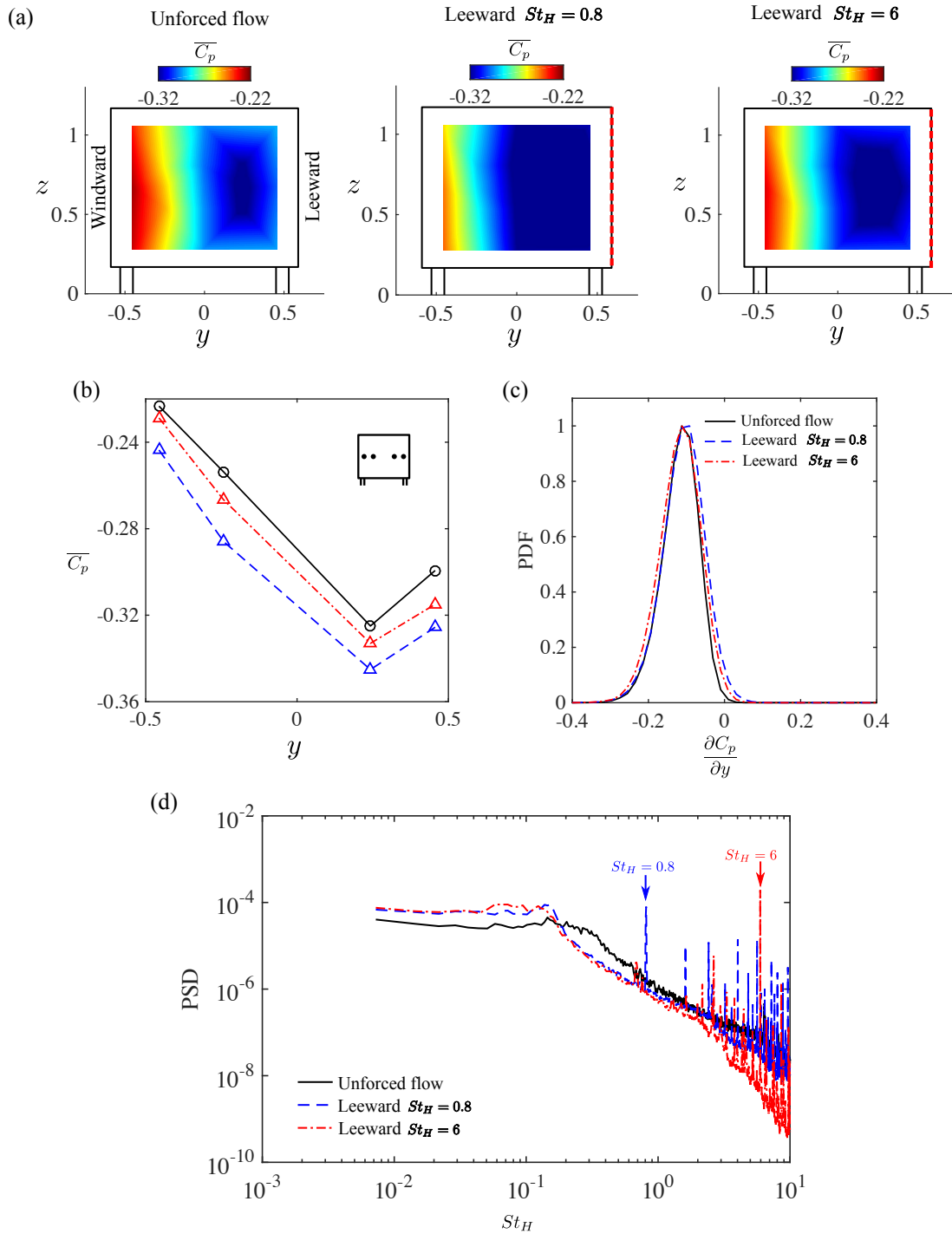


Figure 5.11: Effect of leeward actuation on the base pressure at $St_H = 0.8$ and $St_H = 6$ with $P_0 = 2.5$ bar. (a) Distribution of time-averaged pressure $\overline{C_p}$ for the unforced flow and two forced flows. The forced edge is highlighted by the red dashed line. (b) $\overline{C_p}$ on the mid-height line; (c) PDF of the lateral pressure gradient; (d) PSD (power spectral density) of the lateral pressure gradient.

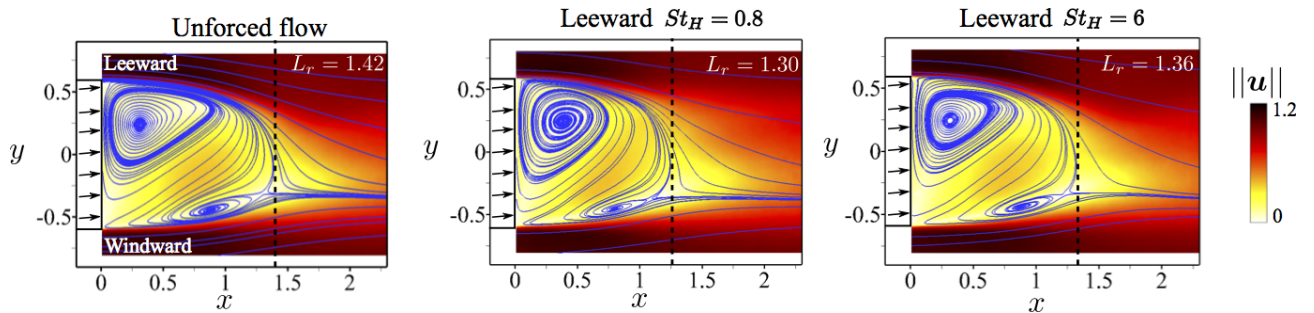


Figure 5.12: Effects of leeward forcing on the near wake in the horizontal mid-height plane $z = 0.67$. Streamlines of the mean velocity field overlapped with the contour maps of the velocity magnitude $\|\mathbf{u}\| = \sqrt{\bar{u}^2 + \bar{v}^2}$.

of $\partial C_p / \partial y$ shown in Fig. 5.11(c). In particular, the location of the lowest pressure value in Fig. 5.11(b) agrees with the location of the center of the leeward recirculating structure. A significant difference can be observed in the bubble length. A decrease of 8% and 4% is measured respectively for the low-frequency ($St_H = 0.8$) and high-frequency forcing ($St_H = 6$). These observations are very similar to those analyzed in § 4.4 where we compare the asymmetric state $\#N_u$ of the unforced bi-modal flow with the forced asymmetric wake, except that here we do not observe a change of the degree of asymmetry.

The effects of actuation on the shear layer dynamics resemble also those in § 4.4. We observe similarly a significant enhancement of the turbulent dynamics along the forced shear layer, as shown in Figure 5.13 for the distributions of $\overline{u'u'}$, $\overline{u'v'}$ and $\overline{v'v'}$ along the forced leeward shear layer of the three cases. In particular, the turbulent fluctuations are most amplified at $St_H = 0.8$, in agreement with the results in Barros *et al.* (2016b). Figure 5.13(d) reports the streamwise evolution of the shear layer thickness δ_w (Eq. (4.3)). The increase of δ_w and its derivative $d\delta_w/dx$ for the forced flow illustrates a thicker shear layer with a higher growth rate. These changes lead to a reduction of the bubble length (see Fig. 5.12) and an increase of the entrained flow inside the recirculation bubble as demonstrated in Fig. 5.14 for the streamwise evolution of the integral of the spanwise velocity kinetic energy \mathcal{V} inside the domain $\Omega_{\bar{u} < 0}$ (Eq. (4.4)). Moreover, the shorter bubble length and the higher increase of the entrained flow at $St_H = 0.8$ is coherent with its higher shear layer thickness δ_w and growth rate $d\delta_w/dx$.

Similar to the scenario described in § 4.4, the enhancement of the shear layer turbulent dynamics is detrimental to the drag reduction. On the one hand, it decreases the pressure along the bubble boundary explicitly by increasing the fluctuation term $\overline{v'_n v'_n}$ in Eq. (4.2). On the other hand, it enhances the entrainment process which reduces the bubble length thus decreasing the radius R_s of the bubble curvature. The reduction of R_s leads also to a pressure decrease along the boundary ∂B of the bubble (see Eq. (4.2)). As $(\delta C_p)_{\partial B} \sim (\delta C_p)_{\text{base}}$ (Barros *et al.*, 2016b), we obtain ultimately a decrease of base pressure and drag increase.

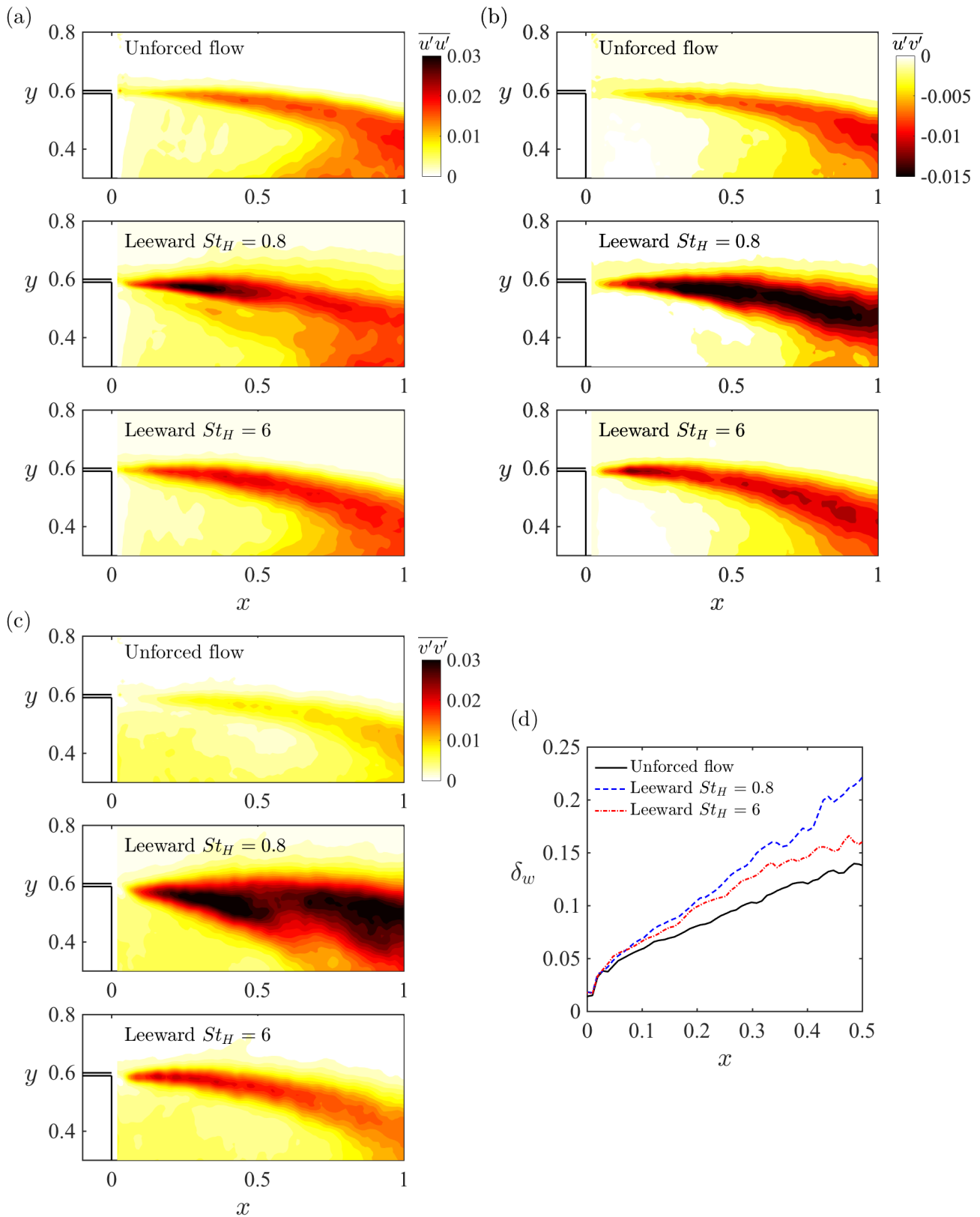


Figure 5.13: Effects of leeward forcing on the shear layer dynamics. Distribution of (a) $\overline{u'u'}$, (b) $\overline{u'v'}$ and (c) $\overline{v'v'}$ for the unforced flow and forced flows with $St_H = 0.8$ and $St_H = 6$. (d) Streamwise evolution of the shear layer thickness δ_w according to Eq. (4.3).

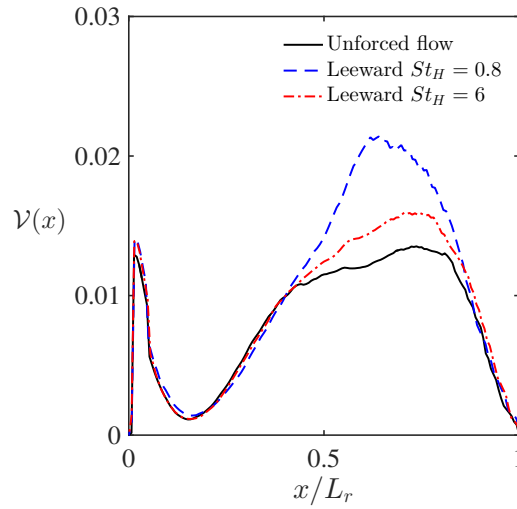


Figure 5.14: Streamwise evolution of \mathcal{V} (Eq. (4.4)) for the unforced flow and leeward forced flows at $St_H = 0.8$ and $St_H = 6$.

5.5 Windward forcing

Having examined the leeward forcing, this section is devoted to investigate the windward forcing. In § 5.5.1 we report the global effects of actuation on the base pressure, drag and yaw moment. The associated changes of the near wake dynamics and the underlying physical mechanisms are discussed in § 5.5.2.

5.5.1 Global effects of actuation

When discussing Fig. 5.8 in the previous section, we noted that the supply pressure P_0 does not affect significantly the behavior of the curve. Here we focus only on the influence of the forcing frequency by looking at the results at a constant pressure supply $P_0 = 2.5$ bar. At this pressure level, the effective jet velocity V_{eff} , calculated as $V_{\text{eff}} = (\overline{V_{\text{jet}}^2})^{\frac{1}{2}}$, is about $0.5U_\infty$ for the considered frequencies. The variations of the base pressure, drag, side force and yaw moment, represented by $\gamma_p, \gamma_D, \gamma_y, \gamma_{M_z}$, respectively, are presented in Fig. 5.15. For the whole range of frequencies, the windward forcing increases the base pressure, reduces drag and side force, and augments the yaw moment, imposing exactly the opposite effects when compared with those of leeward forcing. One can still note the positive correlation between γ_p and γ_D and the negative correlation between γ_y and γ_{M_z} . Their correlation coefficients are $\rho_{\gamma_p, \gamma_D} = 0.84$ and $\rho_{\gamma_y, \gamma_{M_z}} = -0.74$, respectively. Intriguingly, when considering the points at $St_H > 0.8$, we found $\rho_{\gamma_p, \gamma_D} \approx 1$. This finding indicates that the drag reduction at low frequencies ($St_H \leq 0.8$) is not well correlated to the base pressure. To identify the origin of this behavior, we would need pressure measurements along the side of the model which we do not have in the present experimental setup.

It is interesting to note that γ_D presents two minimums located at $St_H = 0.48$ and $St_H = 6$, respectively. They both reduce the drag by about 6%, $St_H = 0.48$ being slightly better. However, they present a significant difference in the side force γ_y and yaw moment γ_{M_z} . Forcing at $St_H = 0.48$ has an insignificant increase of yaw moment (2%), whereas nearly 10% of increase is obtained at $St_H = 6$. Analogous to our analysis of leeward forcing, this modification is related to the change of C_y at the rear windward side. We report the spanwise profiles of \bar{u} at the windward and leeward separation point at $x = 0.01$ in Fig. 5.16. At the forced windward side, the actuation $St_H = 6$ notably accelerates the flow, implying a decrease of pressure close to the rear windward edge. This acceleration effect is quite similar to that induced by an inward-

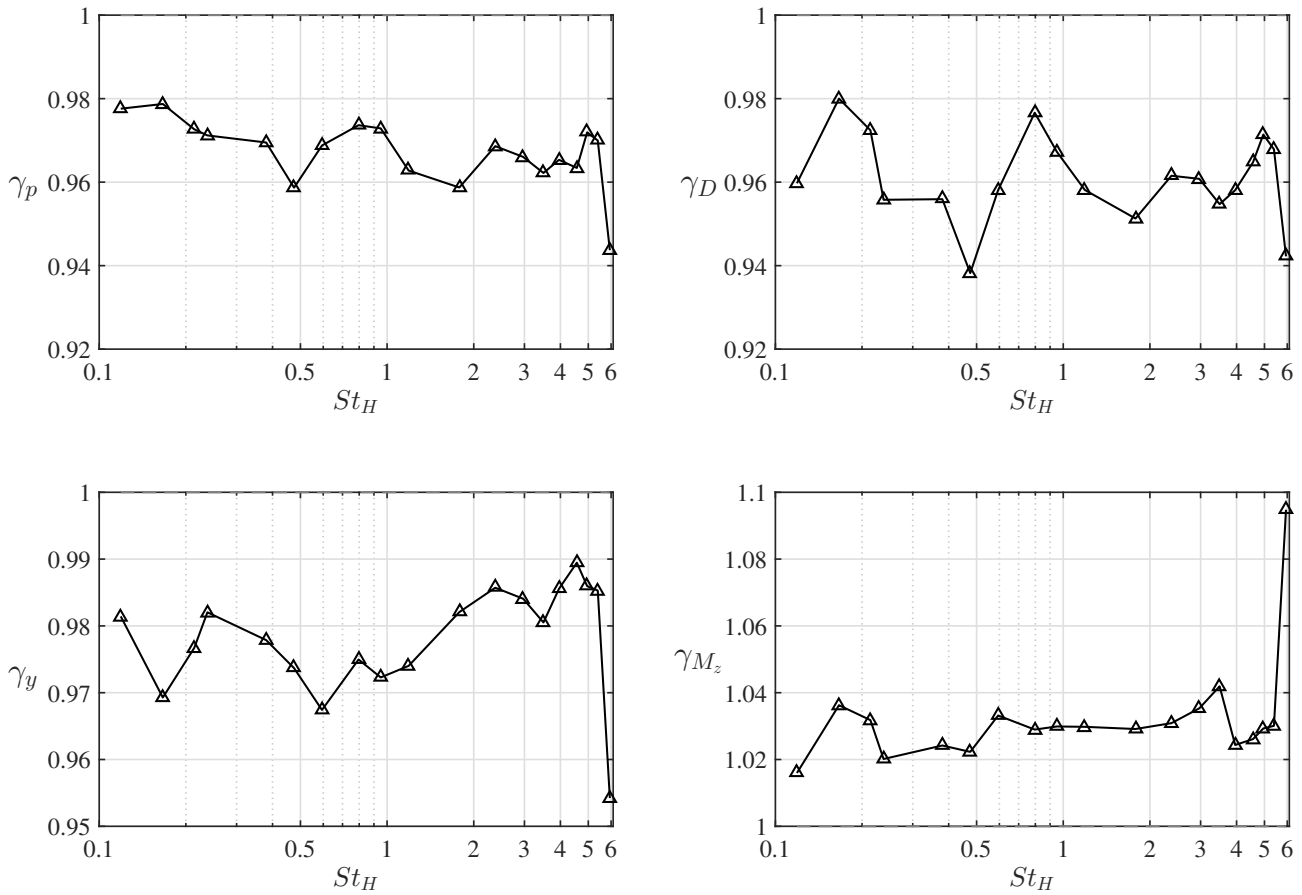


Figure 5.15: Effects of windward forcing on the ratios of base pressure γ_p , drag γ_D , side force γ_y and yaw moment γ_{M_z} as a function of the non-dimensional frequency St_H . The supply pressure is fixed at $P_0 = 2.5$ bar.

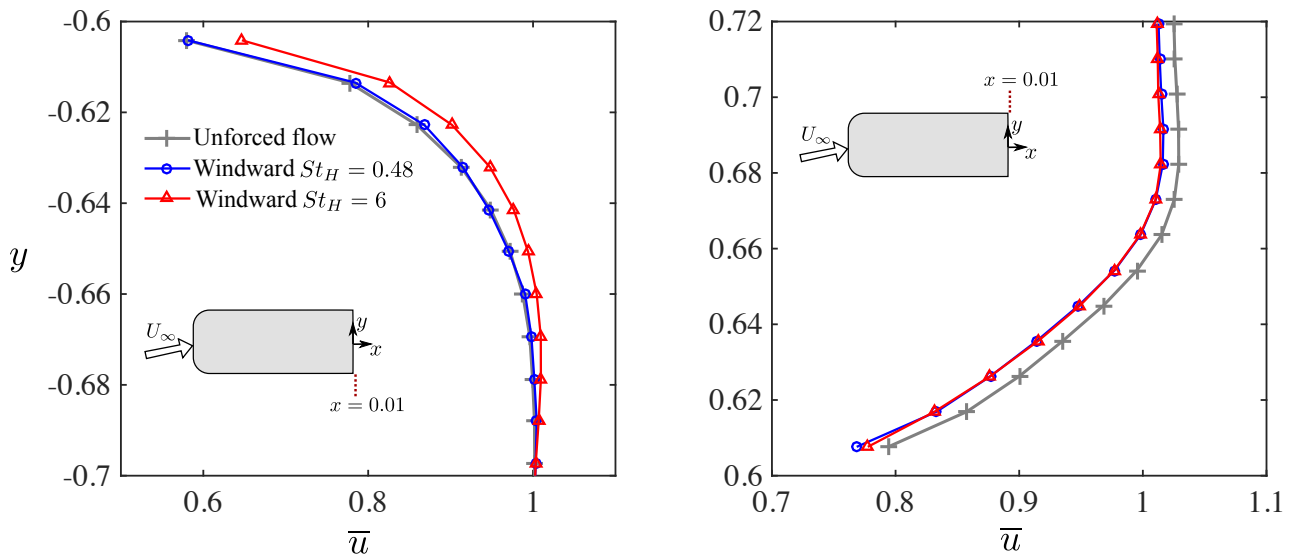


Figure 5.16: Profiles of the time-averaged streamwise velocity \bar{u} at $x = 0.01$ for the windward (left) and leeward (right) side. The inserted figures indicate the position of the investigated line. Note that the side surfaces of the model are located at $y = \pm 0.6$. Data are extracted from PIV measurements.

deviated flap along the windward edge. Hence it is reasonable to compare the actuation at $St_H = 6$ to a virtual *fluidic flap* having the similar effect of a real flap. In contrast, $St_H = 0.48$ shows no evident variation of the velocity.

Although no actuation is applied at the leeward edge, we note a deceleration close to the leeward separation (see Fig. 5.16), indicating an increase of the wall pressure. Moreover, it suggests that there exists a reorganization of the free-stream flow surrounding the model under actuation. The change of wall pressure along the respective side corroborates the decrease of γ_y and increase of γ_{M_z} . In particular, $St_H = 6$ exhibits both an increase of pressure on the leeward side and a decrease of pressure on the windward side, thus resulting in larger changes of γ_y and γ_{M_z} .

We may further estimate the pressure increase related to the flow deceleration in the potential flow at $y = 0.72$ by applying Bernoulli equation on a streamline emerging from the upstream flow. Assuming that the upstream flow has the same pressure and velocity for the three cases, we can write $(\delta\overline{C_p})_{po} = (\overline{p}_a - \overline{p}_u)/0.5\rho U_\infty^2 = \overline{u}_u^2 - \overline{u}_a^2$ where ‘po’, ‘u’ and ‘a’ are the potential, unforced and actuated flow, respectively. Note that \overline{u}_u and \overline{u}_a are normalized by U_∞ . Based on the data in Fig. 5.16, we obtain $(\delta\overline{C_p})_{po} = 0.026$ and 0.029 respectively for $St_H = 0.48$ and 6 . These values will be used later for the comparison of changes in base pressure.

Given the significant difference of the yaw moment for $St_H = 0.48$ and $St_H = 6$, we would expect two contrasting actuation mechanisms. In the following paragraphs, we analyze what these two mechanisms are and how they lead to the similar drag reduction with more details of the base pressure and velocity field data set.

5.5.2 Effects on the base pressure and near wake

We focus now on the analyses of drag reduction achieved by both $St_H = 0.48$ (low frequency) and $St_H = 6$ (high frequency) along the windward edge. Similar to Fig. 5.11, the effects of the windward actuation on the base pressure statistics are resumed in Fig. 5.17. The distribution of the base pressure for the two forced flows shown in Fig. 5.17(a) are quite different. For $St_H = 0.48$, the pressure is more uniform, whereas a clear spanwise pressure gradient can be noticed for $St_H = 6$. This observation can be also confirmed from Fig. 5.17(b) which highlights the pressure values along the mid-height line of the model. The actuation at $St_H = 0.48$ increases the pressure close to the leeward edge and decreases that close to the windward edge, resulting in a balanced distribution. While for $St_H = 6$, a global increase of the pressure is obtained. To gain insights on the relation between the base pressure increase close to the leeward edge and that related to the flow deceleration in the free-stream flow shown in Fig. 5.16, we apply the equation of the time-averaged momentum conservation along the y direction immediately downstream of the trailing edge where the mixing layer assumptions ($\overline{u} \gg \overline{v}$ and $\partial/\partial y \gg \partial/\partial x$) are reasonably valid. The equilibrium between the dominant terms reads:

$$\frac{\partial\overline{C_p}}{\partial y} + 2\frac{\partial\overline{v'v'}}{\partial y} = 0. \quad (5.5)$$

Thus, after integration in the y direction, Eq. (5.5) shows that $\overline{C_p} + 2\overline{v'v'}$ is constant across the mixing layer. So we get $(\overline{C_p})_{po} + 2(\overline{v'v'})_{po} = (\overline{C_p})_b + 2(\overline{v'v'})_b$ where ‘po’ and ‘b’ means the potential flow and the model base respectively. In the potential flow, we have $(\overline{v'v'})_{po} \approx 0$. Hence the relation above can be expressed as

$$(\delta\overline{C_p})_b = (\delta\overline{C_p})_{po} - 2(\delta\overline{v'v'})_b, \quad (5.6)$$

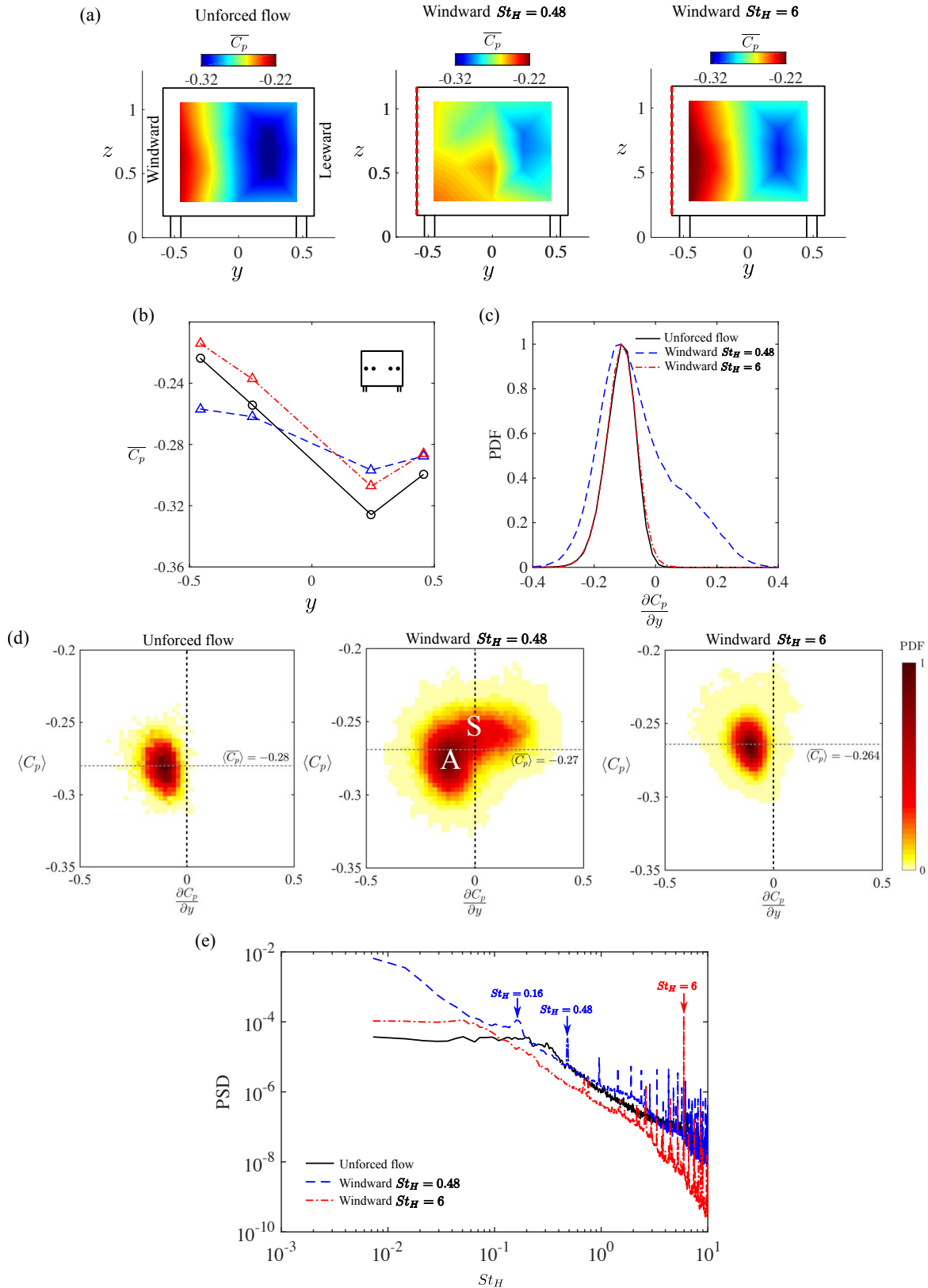


Figure 5.17: Effect of windward actuation on the base pressure. (a) Distribution of the time-averaged pressure $\overline{C_p}$ for the unforced flow and forced flows at $St_H = 0.48$ and $St_H = 6$ with $P_0 = 2.5$ bar. The forced edge is highlighted by the red dashed line. (b) $\overline{C_p}$ on the mid-height line. (c) PDF of the pressure gradient $\partial C_p / \partial y$. (d) Joint PDF of the area-averaged base pressure $\langle C_p \rangle$ versus $\partial C_p / \partial y$. The letters ‘A’ and ‘S’ indicates the asymmetric and symmetric state of the forced wake at $St_H = 0.48$ respectively. (e) PSD of the pressure gradient $\partial C_p / \partial y$.

where $(\delta\overline{C_p}) = \overline{C_{pa}} - \overline{C_{pu}}$. We take $(\delta\overline{C_p})_{po}$ calculated in § 5.5.1 with the potential flow data, $(\delta\overline{C_p})_b$ measured at the pressure sensor closest to the leeward edge and $(\delta\overline{v'v'})_b$ nearest to the pressure sensor from the PIV measurements. The results reported in table 5.3 agrees well with Eq. (5.6). This relation demonstrates that the pressure increase in the free-stream flow (positive $(\delta\overline{C_p})_{po}$) contributes to the base pressure recovery close to the trailing edge, whereas $\delta\overline{(v'v')}_b$ constitutes a detrimental component.

	$(\delta\overline{C_p})_{po}$	$(\delta\overline{v'v'})_b$	$(\delta\overline{C_p})_{po} - 2(\delta\overline{v'v'})_b$	$(\delta\overline{C_p})_b$
$St_H = 0.48$	0.026	0.009	0.008	0.01
$St_H = 6$	0.029	0.006	0.017	0.014

Table 5.3: Comparison of the pressure increase in the outer potential flow and on the base surface near the leeward edge. For details, see text.

We further analyze the temporal variation of the pressure gradient $\partial C_p/\partial y$ and its relation with the temporal variation of the base pressure. Figure 5.17(c) shows the PDF of $\partial C_p/\partial y$, and Fig. 5.17(d) presents the joint PDF of the area-averaged base pressure $\langle C_p \rangle$ versus $\partial C_p/\partial y$. The PDF at $St_H = 0.48$ covers a broad interval showing not only probabilities at negative values but also non negligible percentage at positive values. Correspondingly, the joint PDF features an extended colored zone suggesting a more fluctuating wake. In addition, when $\partial C_p/\partial y$ approaches to zero, a higher base pressure is obtained. This observation reminds us the results of the bi-modal wake as presented in Fig. 4.2 and Fig. 4.4 of Chapter 4 where two peaks of PDF appear respectively at the negative and positive side. The difference here is that we do not observe a distinct peak at positive $\partial C_p/\partial y$. It seems that the forced wake at $St_H = 0.48$ meanders between two different states: one is asymmetric as in the unforced flow and another is statistically symmetric but exhibits a fluctuating spanwise movement. These two states are qualitatively indicated in Fig. 5.17(d) by the letters ‘A’ and ‘S’. The state ‘S’ presents a higher $\langle C_p \rangle$, suggesting that the drag reduction at $St_H = 0.48$ may be related to the presence of this mean symmetric state. The appearance of two states suggests that the actuation affects the organization of the global wake. The PDF of the pressure gradient along z (not shown here) is also broader but centered at zero. In contrast, forcing at $St_H = 6$ does not modify the PDF curve, indicating no change of the asymmetric organization of the near wake. In addition, the PDF of the wall-normal pressure gradient, not shown here for brevity, also collapses with that of the unforced flow. The joint PDF conserves the concentrated distribution at negative values similar to the unforced flow, but presents an overall increase of $\langle C_p \rangle$. In contrast to the case $St_H = 0.48$, the increase of $\langle C_p \rangle$ at $St_H = 6$ seems to be associated with a global effect imposed on the mean unforced wake.

Figure 5.17(e) presents the PSD of $\partial C_p/\partial y$ to demonstrate the changes in the spanwise wake dynamics. At $St_H = 0.48$, a significant increase of energy is observed at very low frequency range ($St_H < 0.1$), in agreement with the appearance of the highly fluctuating spanwise motion reported in Fig. 5.17(d). Moreover, in addition to the peak at the forcing frequency $St_H = 0.48$, one can note another peak emerging at $St_H = 0.16$, which is not observed in the other two cases. This frequency is related to the vortex shedding mode also observed in the wake of the aligned model and in the forced flow of Chapter 4. This finding reveals again that low-frequency dynamics associated with large-scale motions are highly modified by $St_H = 0.48$. At $St_H = 6$, the spectrum shows a prominent peak at the forcing frequency, which is accompanied by an overall attenuation of the energy in the frequency range $St_H \in [0.1, 1]$. The slight increase of energy at $St_H < 0.1$ may be related to the moderate increase of fluctuations shown in Fig. 5.17(d).

We investigate now the relation between the base pressure and near wake changes. Fig-

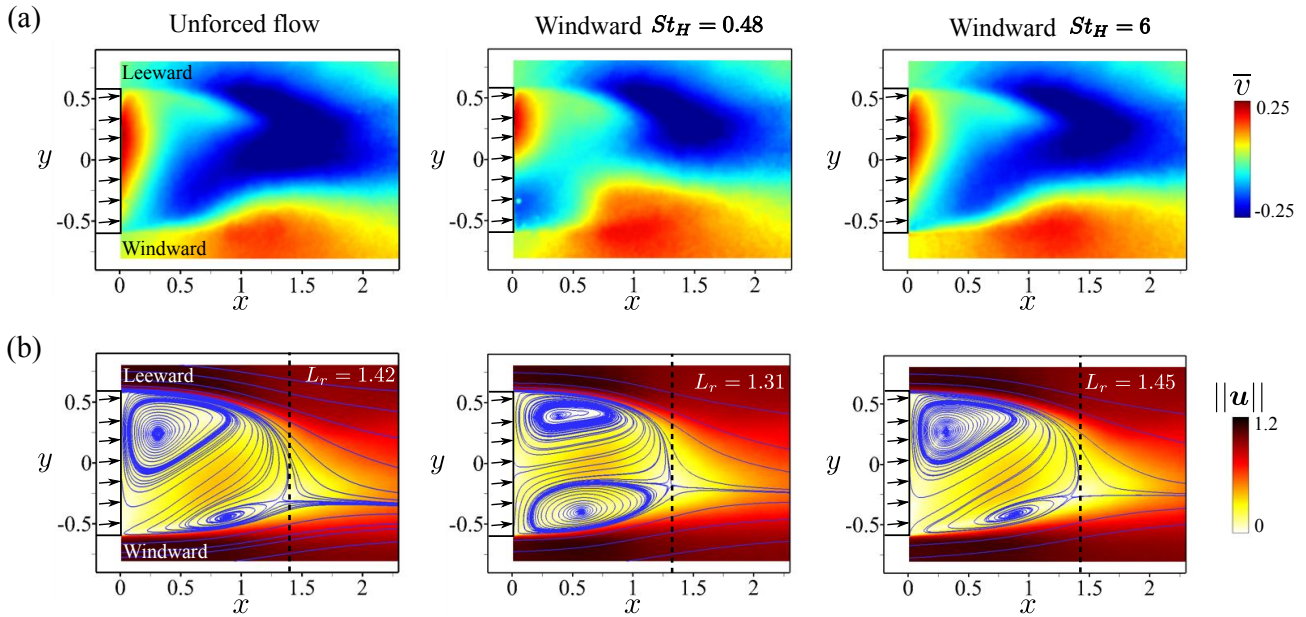


Figure 5.18: Effect of the windward forcing on the near wake. (a) Color maps of the time-averaged spanwise velocity \bar{v} on the mid-height plane $z = 0.67$ for the unforced flow and forced flows at $St_H = 0.48$ and $St_H = 6$. (b) Streamlines of the mean velocity field overlapped with the contour maps of the velocity magnitude $\|\mathbf{u}\| = \sqrt{\bar{u}^2 + \bar{v}^2}$.

Figure 5.18 shows the time-averaged spanwise velocity \bar{v} and the 2D-approximated streamlines. At $St_H = 0.48$, the actuation strongly modifies the recirculating flow by symmetrizing \bar{v} along the opposing shear layers. The flow entrained into the wake from the windward side is enhanced by actuation, resulting in a more balanced wake, as presented by the in-plane streamlines where the two counter-rotating recirculations feature the similar size. However, at $St_H = 6$, the forced flow exhibits the same topology as the unforced flow. In the following paragraphs, we analyze first the case with $St_H = 6$, then with $St_H = 0.48$.

The mean flow topology of the forced wake with $St_H = 6$ agrees well with the pressure distribution on the mid-height line shown in Fig. 5.17(b), the lowest pressure being closest to the center of the leeward recirculation. The frequency $St_H = 6$ corresponds to nearly 30 times that of the natural shedding frequency. The effect of such a high-frequency forcing has been already investigated in Barros *et al.* (2016b) as well as in Chapter 3 with actuation along the four trailing edges. It creates a fluidic *boat-tailing* effect which is characterized by an inward deviation of the shear layer close to the separating edges leading to a thinner wake. This effect is analogous to that of an inward-deviated flap installed at the trailing edge which modifies the shape of the bubble by adding a surface geometry (Grandemange *et al.*, 2015; García de la Cruz *et al.*, 2017a). Here, we would expect the same effect for the windward high-frequency forcing. The analysis of flow accelerations discussed with Fig. 5.16 has shown the analogy between the windward high-frequency and a *fluidic flap*. To further demonstrate this effect, Fig. 5.19(a) shows the iso-contour lines at $\bar{u} \in \{-0.25, 0.25, 0.6\}$. The contours in the forced flow are deviated towards the leeward side, indicating a vectoring effect by actuation. To quantify this deviation, the angle θ of the streamline emerging from the leeward and windward separation point $(x, y) = (0, 0.6)$ and $(x, y) = (0, -0.6)$, respectively, is plotted in Fig. 5.19(b). Along the leeward streamline, no deviation is noticed, while a higher angle is obtained all along the windward streamline. The angle at $x = 0$ increases from 2° (unforced flow) to 7.5° (forced flow). In particular, the initial drop of θ in the forced flow implies a reversal of the sign of streamline curvature immediately downstream of the forced edge, which is characteristic of a local rise in base pressure. This finding corroborates again that forcing at $St_H = 6$ is analogous to a fluidic

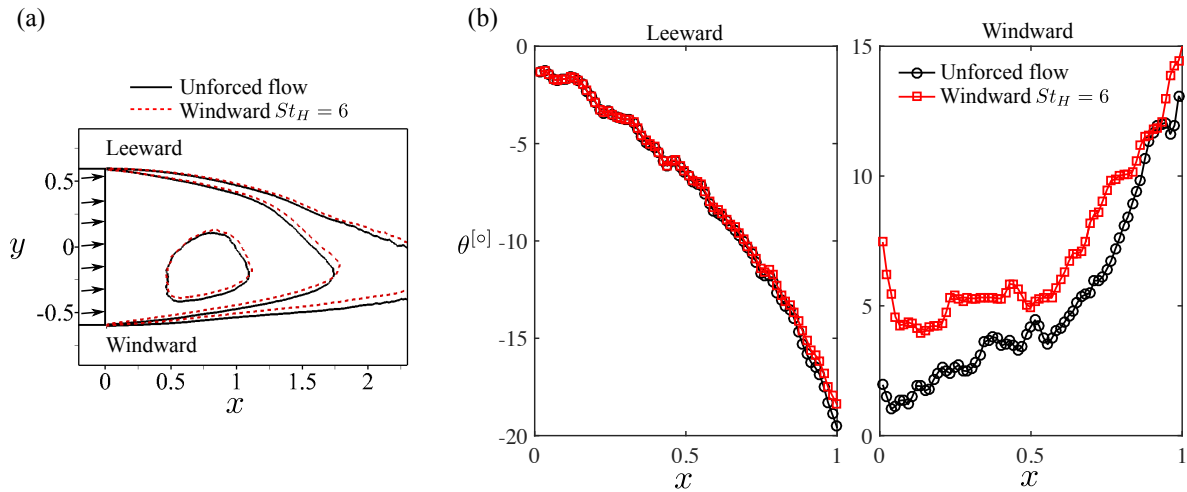


Figure 5.19: Effect of the windward forcing $St_H = 6$ on the wake orientation. (a) Iso-contour lines of time-averaged streamwise velocity $\bar{u} \in \{-0.25, 0.25, 0.6\}$. Black line: unforced flow; red dashed line: high-frequency forced flow. (b) Streamwise evolution of the velocity angle $\theta = \arctan(\bar{v}/\bar{u})$ of the streamline issuing from the leeward $(x, y) = (0, 0.6)$ and windward separation point $(x, y) = (0, -0.6)$.

deviated flap which leads to a global vectorization of the mean wake. The wake vectorization is accompanied with a deceleration of the leeward outer flow as observed in Fig. 5.16. The ultimate base pressure increase across the spanwise direction may be a result of the combined effect of the fluidic flap and the decrease of \bar{u} in the leeward outer flow.

Moreover, we note a slight increase of the wake length of about 2%, as indicated in Fig. 5.18. This is closely related to the reduced shear layer growth and wake entrainment rate resulted from actuation. The related reduction can be quantified by the streamwise evolution of the integral of the turbulent kinetic energy \mathcal{K} and averaged kinetic energy \mathcal{E} inside the domain $\Omega(\bar{u} < 0)$ defined in Eq. (3.8) and (3.9). We replace \bar{w} by \bar{v} in Eq. (3.9) to study the mid-height plane. The results are shown in Fig 5.20. Both quantities are damped by actuation. Reduced turbulent energy has been also reported in the studies of Glezer *et al.* (2005); Dandois *et al.* (2007); Vukasinovic *et al.* (2010); Oxlade *et al.* (2015); Barros *et al.* (2016b) and our results in Chapter 3. It is explained by the high dissipation rate promoted by the small-scale jet structures which inhibits the flow from being entrained into the separating shear layer. Given the analysis above, we conclude that high-frequency forcing has not only a fluidic wake shaping effect like a deviated flap but also a stabilizing effect on the wake fluctuations.

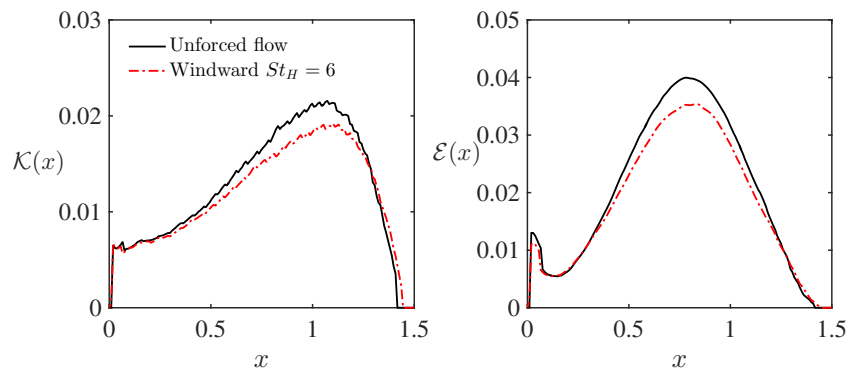


Figure 5.20: Streamwise evolution of \mathcal{K} (Eq.(3.8)) and \mathcal{E} (Eq.(3.9)) for the baseline and windward forcing at $St_H = 6$.

We turn our attention now to the case $St_H = 0.48$. The actuation mechanisms differ from

those analyzed above for $St_H = 6$. A symmetrized mean wake is achieved, indicating that the actuation induces a change of the recirculating flow in the wake. We emphasize that the capability of such low-frequency forcing to force the reorientation of the recirculating flow in the near wake has been already demonstrated in the control of bi-modal wake (Chapter 4) and in the single-edge actuation (Barros *et al.*, 2016b). Besides, once the wake is symmetrized either by the windward forcing or by the control of bi-modality, the anti-symmetric vortex shedding is enhanced, as evidenced in Fig. 5.17(c) and Fig. 4.11(b). This symmetrization similarly changes the curvature of the streamlines surrounding the recirculation region as indicated in Fig. 5.21. The results of $St_H = 6$ are also presented for comparison. The iso-contour lines of \bar{u} show that the wake with $St_H = 0.48$ is thinner and shorter than the unforced and the high-frequency forced flows. The thinning of wake for $St_H = 0.48$ is also measured by the high streamline angles at $x > 0.5$ on the windward side while no important angle change is noticed on the leeward side. However, the angle immediately downstream of the windward trailing edge shows no boat-tailing effect when compared to $St_H = 6$. The initial angle fluctuation may be related to the pulsed-jet structure at $St_H = 0.48$. This fact means that the thinner wake is more likely to be a result from the wake symmetrization than the fluidic boat-tailing effect.

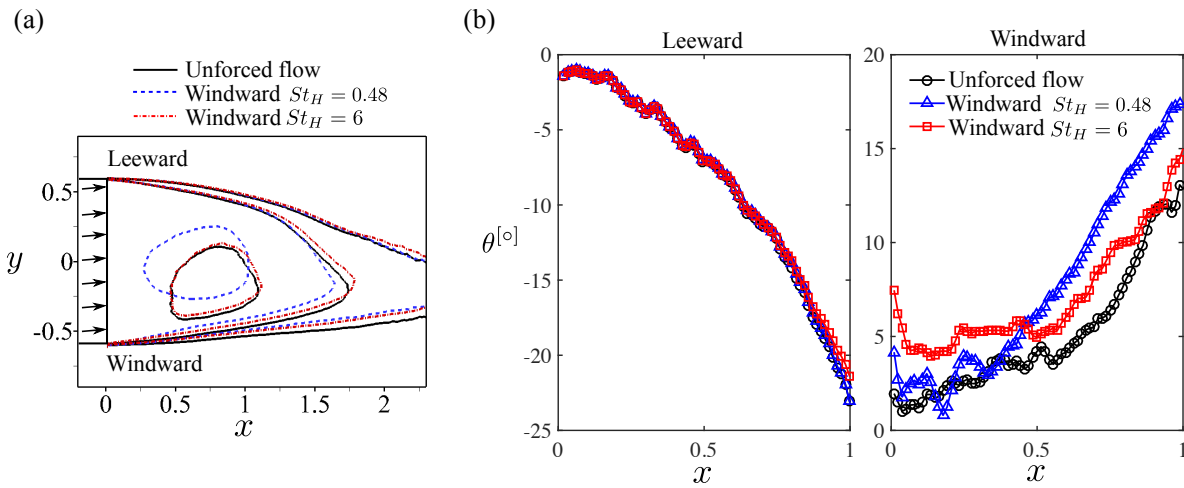


Figure 5.21: Effect of windward forcing $St_H = 0.48$ on the wake topology and streamlines. The results of $St_H = 6$ are repeated for comparison. (a) Iso-contour lines of the time-averaged streamwise velocity $\bar{u} \in \{-0.25, 0.25, 0.6\}$. (b) Streamwise evolution of the velocity angle θ of the streamline issuing from the leeward $(x, y) = (0, 0.6)$ and windward separation point $(x, y) = (0, -0.6)$.

The recirculation bubble length L_r is reduced by 8% for $St_H = 0.48$. According to the discussion in § 5.4.2, this reduction is associated with the shear layer dynamics. Figure 5.22(a) compares the distribution of $\overline{v'v'}$ along both shear layers for the unforced flow and the windward forced flow with $St_H = 0.48$. The resulting streamwise evolution of the maximum $\overline{v'v'}$ is presented in Fig. 5.22(b). The forced flow features an increase of fluctuations along both shear layers for the whole range of the shown streamwise distance. The more significant increase of $\overline{v'v'}$ near the forced windward edge appears to play an essential role for the development of the shear layer further downstream. Along the leeward side, $\overline{v'v'}$ is also increased although no actuation is applied here, indicating the interactions between opposing shear layers. Larger velocity fluctuations suggest a higher mixing of the shear layer. This can be further confirmed from the shear layer thicknesses as shown in Fig. 5.22(c). The thicker shear layer with a higher growth rate is amenable to the bubble shortening observed in Fig. 5.18, the physics being already discussed in the leeward forcing section § 5.4.

Note that in the results presented by Barros (2015), when the wake is forced at all four shear layers with this low frequency, the drag is increased. However in the present study,

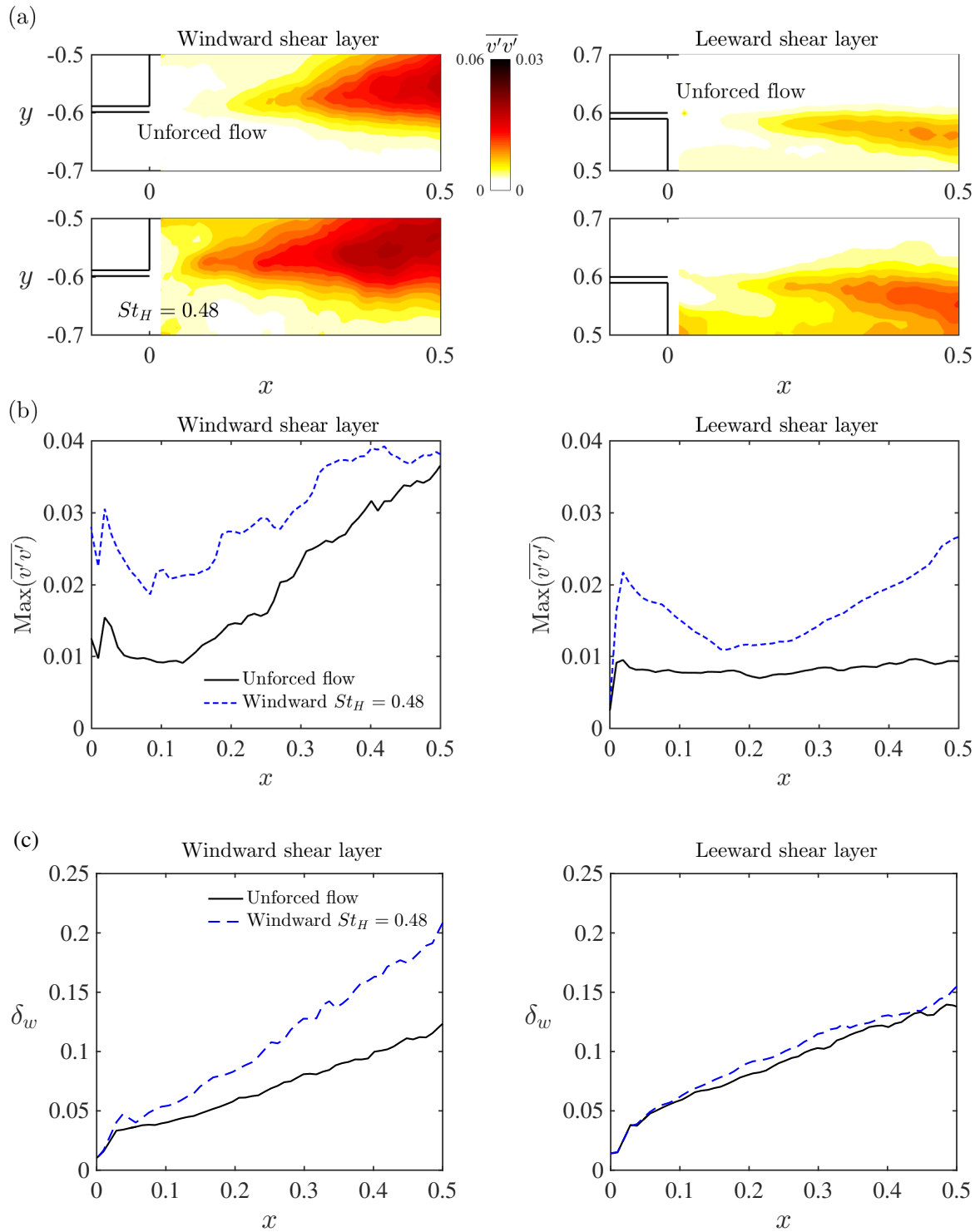


Figure 5.22: Effect of windward forcing at $St_H = 0.48$ on the shear layer properties. (a) Distribution of $\overline{v'v'}$ along the windward (left column) and leeward (right column) shear layers. (b) Streamwise evolution of the maximum $\overline{v'v'}$ along the shear layers. (c) Streamwise evolution of the shear layer thickness δ_w (see Eq. (4.3)).

we achieve an important drag reduction with the single edge low-frequency forcing. The most important difference is the emergence of a symmetric state in our results. The counter-clockwise recirculation at the windward side extends by the effect of the windward shear layer excitation. Concomitantly, the opposing clockwise recirculation shrinks in size, the center of which moves away from the base compared to the unforced flow. Thus, the lowest pressure value on the mid-

height line of the unforced flow is increased (see Fig. 5.17(b)). The wake symmetrization also alters the outer flow yielding a pressure increase in the leeward potential flow (see table 5.3). Hence, the base pressure recovery at $y > 0$ in Fig. 5.17(b) may be ascribed to the modification of the clockwise recirculating flow and the combined pressure increase in the leeward potential flow. On the other hand, the base pressure decreases at $y < 0$ as a consequence of the extension of the windward counter-clockwise recirculation under actuation. The base pressure increase dominates this competition, so we obtain ultimately an area- and time-averaged base pressure recovery.

Additionally, following the studies of 2D bluff body wakes (Roshko, 1955, 1993b), high bluntness having a thick and short bubble would increase the drag. In the case of $St_H = 0.48$, although the bubble is shortened, it is also thinner. It would be difficult to estimate the change of bluntness and its influence on the drag. On the contrary, the longer recirculation region observed at $St_H = 6$ is beneficial for drag reduction.

Summary We explored in this section how the windward forcing at frequencies $St_H = 0.48$ and $St_H = 6$ lead to similar drag reduction by investigating the associated base pressure and wake properties. Two fundamentally different mechanisms are identified. Low-frequency forcing promotes the turbulent vortex roll-up along the windward shear layer and enhances the mixing between the free-stream flow and the inner recirculating flow, thus increases the entrainment of fluid, leading to a symmetrized wake with a shorter and thinner bubble. This wake symmetrization increases the base pressure and decreases the drag. High-frequency forcing operates like a fluidic flap and imposes a fluidic boat-tailing effect which deviates the wake towards the leeward side without changing the organization of the recirculating flows. In addition, it has a stabilizing effect on the wake fluctuations. The resulting bubble region is thinner and longer. In this high-frequency forcing case, the wake shaping is responsible for drag reduction. Note that although similar drag reduction of about 6% is achieved for both cases, the forcing at $St_H = 0.48$ provides an interesting application for car manufacturers as it barely increases the yaw moment which is not the case for $St_H = 6$.

5.6 Windward bi-frequency forcing

In the previous section, It was demonstrated that windward forcing decreases the drag either by wake symmetrization resulting from the shear layer turbulence enhancement or by fluidic boat-tailing. These two effects are obtained respectively at two frequencies with one order of magnitude difference. The results point to the following question: can the boat-tailing effect be superimposed on a symmetrized wake to achieve further drag reduction by using both mechanisms? The goal of this section is to provide hints to this question by analyzing the effects of a bi-frequency forcing on the flow dynamics.

5.6.1 Global effects of bi-frequency actuation

We first present the methodology to generate the bi-frequency actuation. The idea is to superimpose two harmonics at low and high frequency, respectively. The binary actuation command is obtained by multiplying a squarewave at low frequency f_{low} with another one at high frequency f_{high} . The corresponding control law reads:

$$b_{\text{bf}}(t) = b_{LF}(t) \times b_{HF}(t) = H(\sin(2\pi f_{\text{low}}t)) \times H(\sin(2\pi f_{\text{high}}t - 0.1)), \quad (5.7)$$

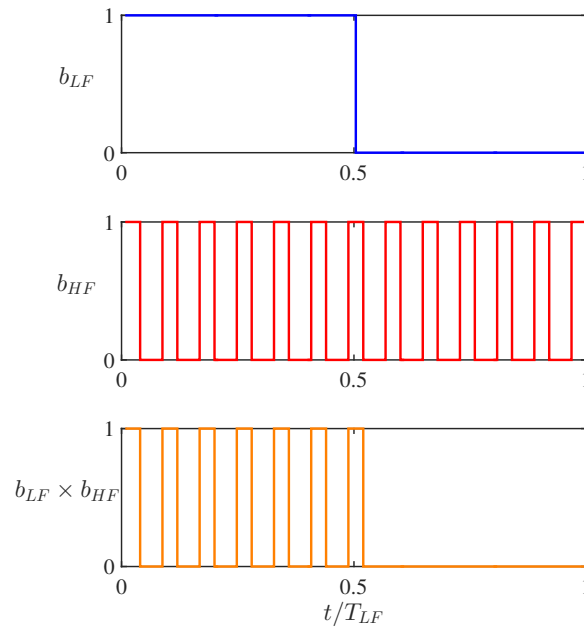


Figure 5.23: Bi-frequency actuation command generated by the multiplication of two periodic square-waves at low and high frequency respectively. T_{LF} corresponds to the period of the low frequency component.

where the subscript ‘bf’ denotes bi-frequency and the threshold 0.1 is the same as that taken in the generation of periodic forcing (see § 5.2). An example is shown in Fig. 5.23 with $St_{H_{low}} = f_{low}H/U_{\infty} = 0.48$ and $St_{H_{high}} = f_{high}H/U_{\infty} = 6$. In this study, we fix the high frequency to $St_{H_{high}} = 6$ since the boat-tailing effect is most effective at this value. A large range of low-frequency forcing can influence the roll-up of vortices in the shear layer thus modifying the recirculating flow in the near wake. The frequency $St_H = 0.48$ has the maximum drag reduction in periodic forcing but may not maintain the same performance when combined with high-frequency forcing. Given such considerations, we perform a parametric study by varying the low frequency in the range $St_{H_{low}} \in [0.12, 3]$ in order to determine the best actuation frequency in terms of drag reduction. The lowest and highest values of $St_{H_{low}}$ correspond to $\frac{1}{50}St_{H_{high}}$ and $\frac{1}{2}St_{H_{high}}$ respectively. This kind of bi-frequency forcing has been investigated numerically by Inoue (1992) on the development of a mixing layer. In his study, the maximum ratio between the high and low frequency ($St_{H_{high}}/St_{H_{low}}$) is only up to 8. Our study covers more ratio possibilities, and the high ratio up to 50 enables us to explore new mechanisms resulting from the combination of frequencies having one order of magnitude difference. In the following, we denote by $St_{H_{bf}} = St_{H_{low}} \otimes St_{H_{high}}$ the combined bi-frequency forcing.

To clarify the differences in the pulsed-jet pattern and actuation energy for periodic and bi-frequency forcing, we exemplify in Fig. 5.24 the phase-averaged jet velocity for the cases $St_H = 0.48$ and $St_{H_{bf}} = 0.48 \otimes 6$. The supply pressure is maintained constant at $P_0 = 2.5$ bar, the same as in § 5.5. The velocity overshoot related to the sudden opening of the solenoid valve is about $1.4U_{\infty}$ for both. This overshoot appears only once for $St_H = 0.48$, on the contrary to its periodic occurrence for the case of $St_{H_{bf}} = 0.48 \otimes 6$. The behavior of high-frequency forcing in the latter case is similar to that of a single high-frequency forcing. Regarding to the actuation energy, the momentum coefficient C_{μ} of $St_{H_{bf}} = 0.48 \otimes 6$ is less than half that of $St_H = 0.48$.

We report the effects of bi-frequency forcing on the pressure and drag in Fig. 5.25(a) with respect to the low frequency $St_{H_{low}}$. For comparison, the curves of periodic forcing as a function of St_H are also shown. It is clear that the bi-frequency forcing behaves quite differently. It

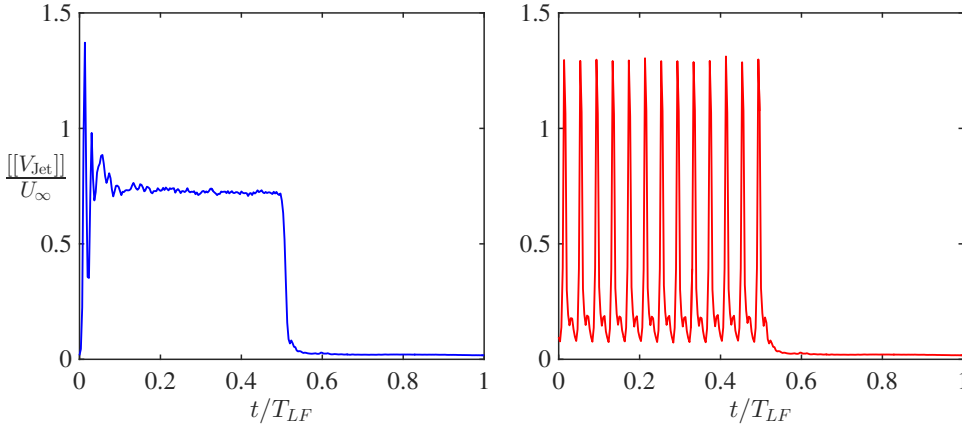


Figure 5.24: Phase-averaged jet velocity $\frac{[V_{jet}]}{U_\infty}$ for $St_H = 0.48$ (left) and $St_{H_{bf}} = 0.48 \otimes 6$ (right). T_{LF} is the period of low frequency $St_H = 0.48$.

leads to a higher base pressure recovery except for $St_{H_{low}} = 0.17$. Regarding the curve of γ_D , a higher drag reduction is achieved for most of the cases. The highest drag reduction of about 7% is obtained at $St_{H_{bf}} = 0.24 \otimes 6$, outperforming the best periodic forcing at $St_H = 0.48$. But $St_{H_{bf}} = 0.48 \otimes 6$ does not perform as well as $St_H = 0.48$. Intriguingly, another local minimum can be identified at $St_{H_{bf}} = 1.8 \otimes 6$, the low frequency of which being one order of magnitude larger than that of the optimal bi-frequency forcing $St_{H_{bf}} = 0.24 \otimes 6$. Moreover, a peak at $St_{H_{bf}} = 0.17 \otimes 6$ is noticeable and is associated with the lowest drag reduction. This peak is also discernible at $St_H = 0.17$ in the drag curve of periodic forcing. A further study on the pressure gradient spectrum reveals that the vortex shedding frequency at $St_H^{vs} = 0.16$ is significantly enhanced for the cases of $St_{H_{bf}} = 0.17 \otimes 6$ and $St_H = 0.17$, presenting a harmonic resonance. This finding is similar to the results obtained by Barros *et al.* (2016a) for the forced wake resonances with an out-of-phase actuation along the lateral edges at the vortex shedding frequency. Their study also showed that this resonance increases the drag for the aligned condition. Our results here demonstrate that the wake resonance can also be achieved by a single edge forcing at the vortex shedding frequency. However, it does not yield drag increase under yawed condition but leads to the least drag reduction. Intriguingly, this resonance is even more amplified when a high-frequency effect is superimposed.

To better understand the curve trend of γ_D under bi-frequency forcing, we display in Fig. 5.25(b) the color map of the time-averaged base pressure $\overline{C_p}$ as a function of the forcing frequency. We compare the results with and without the combination of $St_{H_{high}} = 6$. In the case of periodic forcing, the low pressure regions (blue zones) are all located near the leeward edge as in the unforced flow. In contrast, a reversal distribution is shown in several results of the bi-frequency forcing, indicating a change in the sign of the gradient $\frac{\partial \overline{C_p}}{\partial y}$. To quantify the variation of $\frac{\partial \overline{C_p}}{\partial y}$, Fig. 5.25(c) shows the evolution of $\frac{\partial \overline{C_p}}{\partial y}$ with increasing frequency for both periodic and bi-frequency forcing. The whole frequency range of periodic forcing yields $\frac{\partial \overline{C_p}}{\partial y} < 0$ with the smallest $|\frac{\partial \overline{C_p}}{\partial y}|$ obtained at $St_H = 0.48$. The bi-frequency actuation, however, leads to a positive $\frac{\partial \overline{C_p}}{\partial y}$ in the range $St_{H_{low}} \in [0.24, 1.8]$. $\frac{\partial \overline{C_p}}{\partial y}$ first increases up to a maximum positive value at $St_{H_{bf}} = 0.48 \otimes 6$ followed by a gradual decrease to -0.1 . When crossing the line $\frac{\partial \overline{C_p}}{\partial y} = 0$, a symmetric base pressure distribution is correspondingly observed in Fig. 5.25(b). The bi-frequency forcing $St_{H_{bf}} = 0.48 \otimes 6$ combines $St_H = 0.48$ which induces the highest enhancement of the shear layer turbulence in periodic forcing and $St_H = 6$ which has the most effective fluidic boat-tailing effect. The combined effect reverses the lateral pressure gradient which is linked to an opposing wake asymmetry with respect to the unforced flow. As discussed in the following sections, this means that the turbulence forcing at low

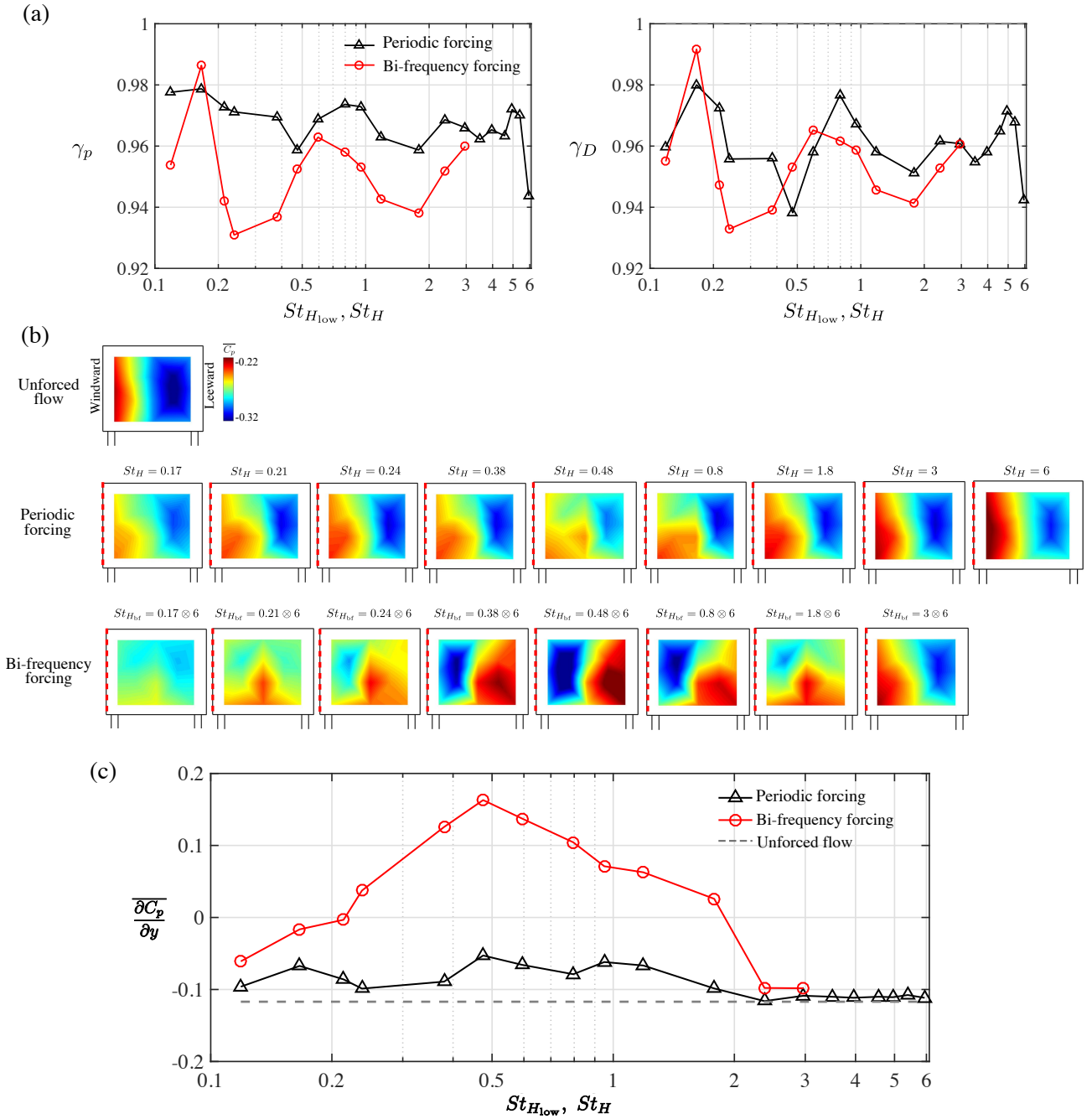


Figure 5.25: Effect of windward bi-frequency forcing on the base pressure. (a) Dependence of the base pressure and drag on the low-frequency component $St_{H_{low}}$ in the bi-frequency actuation (red line). Periodic forcing (black line) as a function of St_H is shown for comparison. (b) Color maps of C_p . The red dashed line indicates the forced edge. (c) Evolution of the time-averaged pressure gradient $\frac{\partial C_p}{\partial y}$ with increasing frequency, St_H for periodic forcing and $St_{H_{low}}$ for bi-frequency forcing. The gray dashed line indicates the value of $\frac{\partial C_p}{\partial y}$ for the unforced flow.

frequencies needs to be tuned in order to achieve the mean wake symmetry for various mean separation angles of the windward shear layer.

Based on the discussion in § 5.5, we would expect a higher drag reduction for the cases with $|\overline{\partial C_p / \partial y}| \approx 0$ as they correspond to a symmetrized wake. On the other hand, less drag reduction is expected for a large positive value of $\overline{\partial C_p / \partial y}$ since a reversed asymmetry is raised by the actuation. To shed further light on the connection between the degree of symmetry and drag reduction, we report in Fig. 5.26 the values of $\overline{\partial C_p / \partial y}$ in the same plot of γ_D for the bi-frequency actuation. One can notice that in the range of $St_{H_{low}} \in [0.24, 1.8]$ where $\overline{\partial C_p / \partial y} > 0$, the curve of γ_D shows the same trend as that of $\overline{\partial C_p / \partial y}$. A higher drag reduction is obtained when $|\overline{\partial C_p / \partial y}| < 0.05 \approx 0$, corroborating the correlation between drag reduction and wake symmetrization. In particular, the two points closest to $\overline{\partial C_p / \partial y} = 0$ ($St_{H_{bf}} = 0.24 \otimes 6$ and $St_{H_{bf}} = 1.8 \otimes 6$ respectively) corresponds exactly to the global and local minimum observed in the curve of γ_D in Fig. 5.25(a). When $St_{H_{low}} > 1.8$, $\overline{\partial C_p / \partial y}$ decreases to negative values and lower drag reduction is obtained.

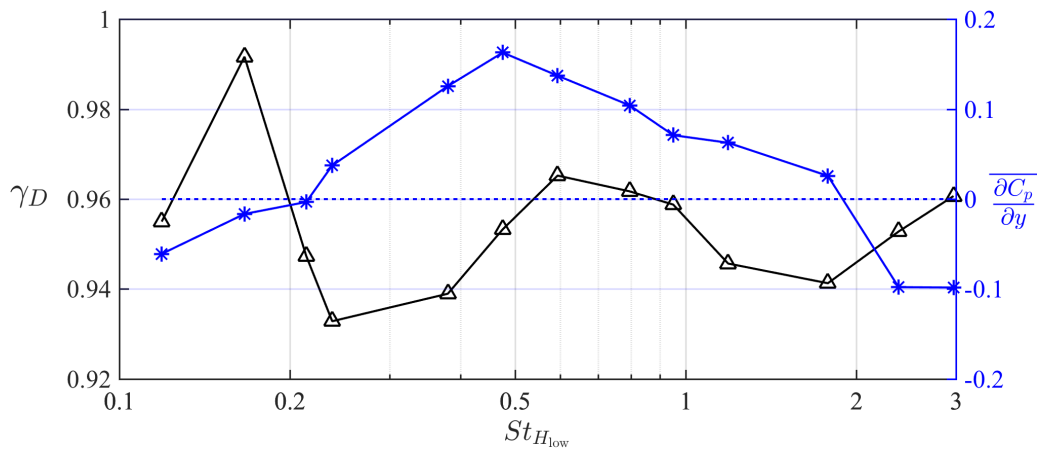


Figure 5.26: Variation of γ_D (\triangle) and $\overline{\partial C_p / \partial y}$ ($*$) as a function of $St_{H_{low}}$ for the windward bi-frequency actuation. The blue dashed line corresponds to the zero pressure gradient.

For $St_{H_{low}} = 0.17$ and 0.21 , we notice a low drag reduction even if $|\overline{\partial C_p / \partial y}| < 0.05$. The reason may lie in the strong amplification of the oscillating vortex shedding when forcing at frequencies near $St_H^{vs} = 0.16$ which has been shown to be detrimental to the drag reduction (Barros *et al.*, 2016a).

Bi-frequency forcing also modifies C_y and C_{M_z} when compared to the periodic forcing.

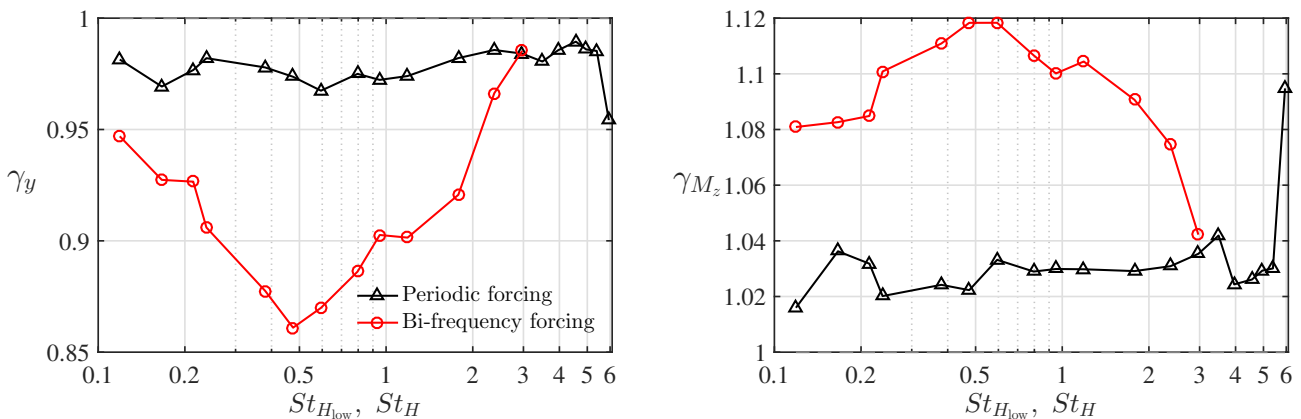


Figure 5.27: Side force and yaw moment as a function of $St_{H_{low}}$ for the windward bi-frequency actuation (red line) and as a function of St_H for the periodic forcing (black line).

Except $St_{H_{bf}} = 3 \otimes 6$, bi-frequency forcing leads to a global higher reduction of C_y and greater increase of C_{M_z} . In particular, the reduction of C_y for the cases where $St_{H_{low}} < 2.4$ is even higher than that of the single high-frequency forcing $St_H = 6$. This observation is not surprising since the combination with $St_{H_{high}} = 6$ introduces a flow acceleration close to the forced trailing edge, thus creating a low pressure zone near the rear windward side which decreases C_y and increases C_{M_z} . Besides, an extremum is obtained at $St_{H_{bf}} = 0.48 \otimes 6$ for both C_y and C_{M_z} , indicating a highest flow acceleration in this case. No evident changes are observed at $St_{H_{bf}} = 3 \otimes 6$ because $St_{H_{bf}} = 3 \approx 18St_H^{vs}$ can not be reasonably considered as low frequency. The resulted combination performs similarly to the single high-frequency forcing at $St_H = 3$.

Based on these observations, we select two configurations to clarify the effects of bi-frequency forcing on the near wake flow: (1) $St_{H_{bf}} = 0.24 \otimes 6$ which results in the highest drag reduction (7%); (2) $St_{H_{bf}} = 0.48 \otimes 6$ in order to compare with the best periodic forcing $St_H = 0.48$. This will be discussed in the following section.

5.6.2 Effects on the base pressure and near wake

In this section, we analyze how the bi-frequency forcing modifies the wake and how they differ from the single low-frequency forcing. The aim is to understand how the low frequency $St_{H_{low}} \in \{0.24, 0.48\}$ and high frequency $St_{H_{high}} = 6$ take effect during the bi-frequency forcing. In the following, we focus on the comparison of four configurations: the unforced flow, the optimal drag periodic forcing $St_H = 0.48$, the optimal drag bi-frequency $St_{H_{bf}} = 0.24 \otimes 6$ and $St_{H_{bf}} = 0.48 \otimes 6$ which yields the highest spanwise pressure gradient.

First, we analyze the statistics of the base pressure from which the spanwise flow movement can be inferred. Figure 5.28(a) shows the PDF of the pressure gradient $\partial C_p / \partial y$ for each configuration. The center of the PDF distribution, i.e. the time-averaged gradient value $\overline{\partial C_p / \partial y}$, moves gradually from the small negative value ($\overline{\partial C_p / \partial y} = -0.053$ at $St_H = 0.48$) to the small positive value ($\overline{\partial C_p / \partial y} = 0.037$ at $St_{H_{bf}} = 0.24 \otimes 6$) and then to the high positive value ($\overline{\partial C_p / \partial y} = 0.16$ at $St_{H_{bf}} = 0.48 \otimes 6$). This evolution appears more clearly in the joint-PDF color maps shown in Fig. 5.28(b). The small value of $\overline{\partial C_p / \partial y}$ at $St_H = 0.48$ indicates that it is effective to symmetrize the wake. On the other hand, the coexistence of the asymmetric and symmetric states suggests that this frequency may not be strong enough to fully symmetrize the wake. For $St_{H_{bf}} = 0.24 \otimes 6$, only one single symmetric state is observed but the PDF of the pressure gradient features a wide band suggesting a more fluctuating spanwise movement. This observation is similar to the results of the feedback control of the bi-modal behavior in Chapter 4 where the wake is symmetrized but presents also high fluctuations. The disappearance of the asymmetric state ‘A’ suggests that $St_{H_{bf}} = 0.24 \otimes 6$ is just enough to achieve an adequate wake symmetrization. The resulting higher degree of symmetry is the reason why the value of $\overline{C_p}$ at $St_{H_{bf}} = 0.24 \otimes 6$ is higher than that at $St_H = 0.48$. Forcing at $St_{H_{bf}} = 0.48 \otimes 6$ appears to be too strong for the symmetrization that the PDF distribution center is reversed to the positive side making the wake again asymmetric. These measurements suggest that by carefully selecting the low frequency component for the bi-frequency forcing, we are able to symmetrize the wake or even reverse the wake asymmetry. Apparently, this can not be achieved by a single-frequency forcing.

Now we look at the time-averaged base pressure distribution. In Fig. 5.28(c), we show the pressure coefficients on the mid-height line of the model as in the previous sections. Focus is placed on the two bi-frequency forcing cases since $St_H = 0.48$ has already been analyzed in § 5.5. The uniform distribution for $St_{H_{bf}} = 0.24 \otimes 6$ and the reversed distribution for $St_{H_{bf}} = 0.48 \otimes 6$ with respect to the unforced case are clearly visible. In the latter case, the lowest pressure is located at the opposing position with respect to that of the unforced flow,

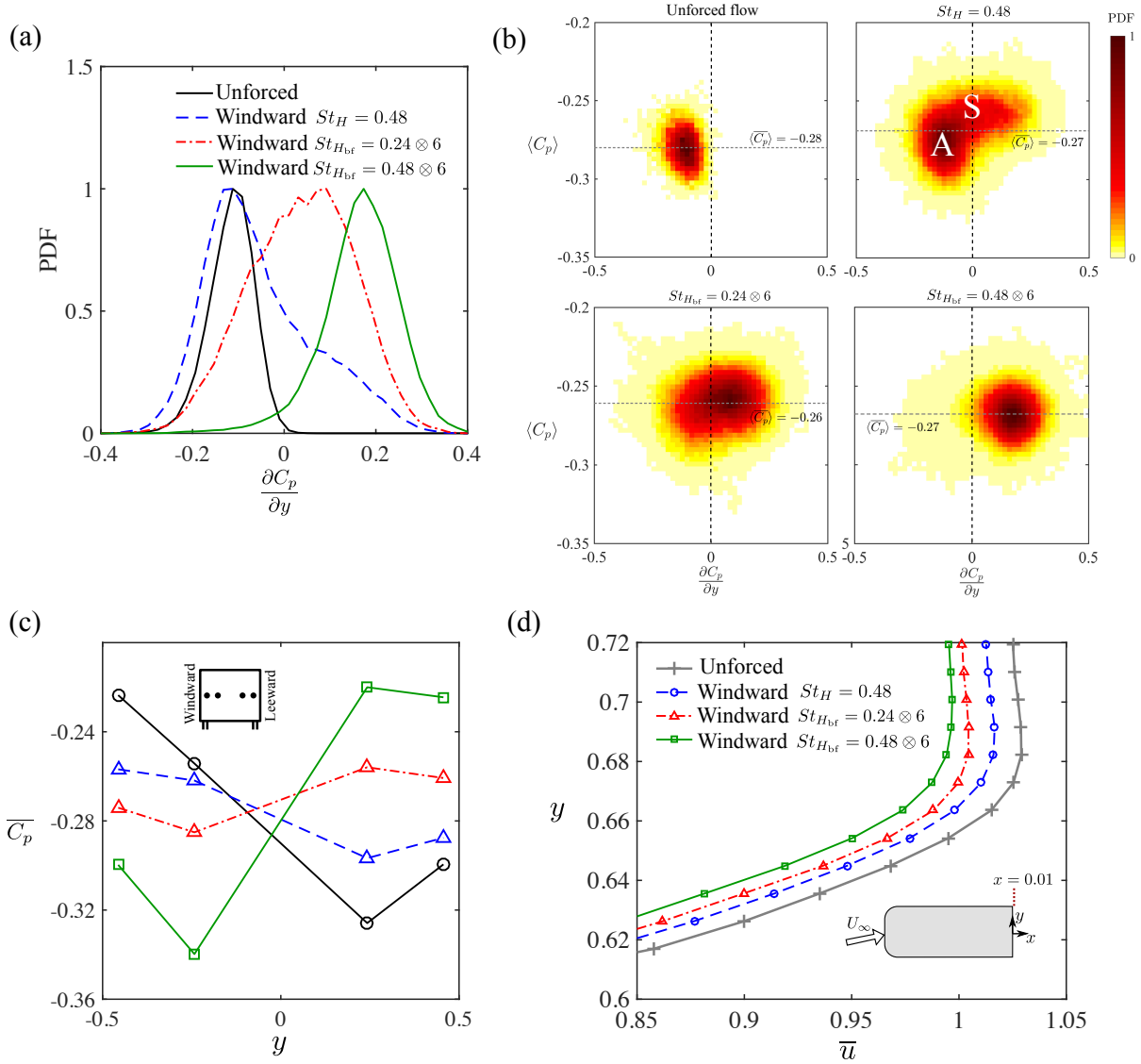


Figure 5.28: Comparison of the windward forcing effects on the base pressure for the unforced flow and the forced flows at $St_H = 0.48$, $St_{H_{bf}} = 0.24 \otimes 6$ and $St_{H_{bf}} = 0.48 \otimes 6$. (a) PDF of the lateral pressure gradient $\partial C_p / \partial y$. (b) Joint PDF of area-averaged base pressure $\langle C_p \rangle$ versus $\partial C_p / \partial y$. (c) Mid-height line distribution of the pressure $\overline{C_p}$. (d) Profile of the time-averaged streamwise velocity \bar{u} along $x = 0.01$ at the leeward side.

suggesting a reflectional change of the corresponding recirculation in the wake. Furthermore, the pressure close to the unforced leeward edge is increased by 15% and 33% for $St_{H_{bf}} = 0.24 \otimes 6$ and $St_{H_{bf}} = 0.48 \otimes 6$, respectively. According to Eq. (5.6), we would expect a pressure increase in the outer flow and this increase may be highest at $St_{H_{bf}} = 0.48 \otimes 6$. This expectation is well confirmed by Fig. 5.28(d). In addition, the data at the corresponding points agree well with Eq. (5.6). This change in the outer flow is closely related to the altered wake features induced by actuation which will be discussed in the following paragraphs.

The 2D streamlines of the unforced and forced wakes are depicted in Fig. 5.29. The wakes under actuation frequencies $St_H = 0.48$ and $St_{H_{bf}} = 0.24 \otimes 6$ exhibit both symmetric recirculations and a shorter bubble length in comparison to the unforced flow. The higher degree of symmetry in the case of $St_{H_{bf}} = 0.24 \otimes 6$ can be identified from the backward flow direction parallel to the x axis in the middle of the recirculation region. Another difference is the position

of the centers of the two counter rotating recirculations. At $St_{H_{bf}} = 0.24 \otimes 6$, the center of the windward recirculation is closer to the base than that of the leeward recirculation, in contrast to the case of $St_H = 0.48$. This distribution agrees with the $\overline{\partial C_p / \partial y}$ values and the distribution of $\overline{C_p}$ on the mid-height line in Fig. 5.28(c). The lowest pressure for these two cases is located at the opposite side, associated with the corresponding center of the recirculation closer to the base. At $St_{H_{bf}} = 0.48 \otimes 6$, the wake is asymmetric with a larger recirculation at the windward side, in opposition to the unforced flow. This asymmetry is consistent with the observations in Fig. 5.28. In addition, the bubble length becomes even shorter than the other two forced configurations.

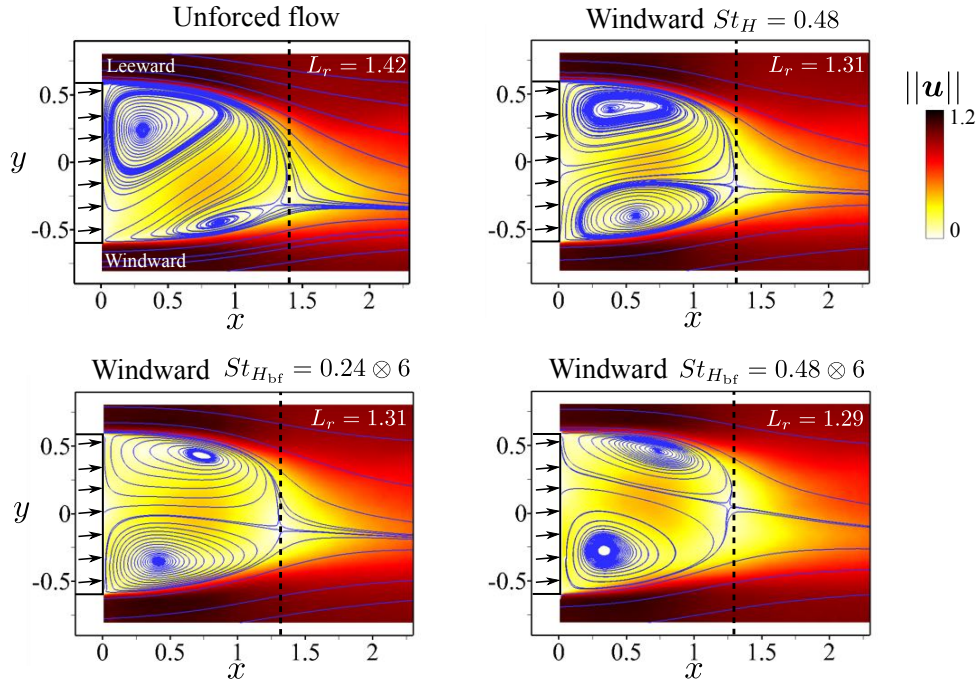


Figure 5.29: Comparison of the mean wake recirculations in the mid-height plane $z = 0.67$ for the unforced flow and forced flows at $St_H = 0.48$, $St_{H_{bf}} = 0.24 \otimes 6$ and $St_{H_{bf}} = 0.48 \otimes 6$. The streamlines are overlapped with the contour maps of the velocity magnitude $\|\mathbf{u}\| = \sqrt{\bar{u}^2 + \bar{v}^2}$.

The modification of the global wake symmetry or reversed asymmetry points to the important role of the low-frequency forcing on the flow. What is the contribution of the high-frequency component in the bi-frequency forcing? Can we still observe the fluidic boat-tailing effect in this case? To answer these questions, we examine in Fig. 5.30(a) the iso-contour lines of \bar{u} for the bi-frequency forcing $St_{H_{bf}} = 0.24 \otimes 6$. It shows that the wake is not only symmetrized by forcing but also deviated towards the leeward side. The deviation downstream of the windward edge is most significant and results in a thinner wake. We further investigate the velocity angle along the streamline emerging from the windward trailing edge in Fig. 5.30(b). The case $St_{H_{bf}} = 0.24 \otimes 6$ is compared with $St_{H_{bf}} = 0.48 \otimes 6$ and $St_H = 6$ to clarify the influence of the high-frequency component $St_{H_{high}} = 6$. The two curves corresponding to $St_{H_{bf}} = 0.24 \otimes 6$ and $St_H = 6$ nearly collapse immediately downstream of the separation ($x < 0.15$). Therefore the boat-tailing effect related to $St_H = 6$ also acts at $St_{H_{bf}} = 0.24 \otimes 6$. In contrast, this is not observed for the single-frequency forcing at $St_H = 0.48$. Moreover, in the near field $x < 0.6$, the velocity angle for $St_{H_{bf}} = 0.24 \otimes 6$ is higher than that for $St_H = 0.48$, suggesting that the former leads to a larger shear layer deviation and a thinner wake. Further downstream at $x > 0.6$, the two curves for $St_{H_{bf}} = 0.24 \otimes 6$ and $0.48 \otimes 6$ collapse. In addition, their angle in this interval is even higher than the single high-frequency forcing $St_H = 6$. These findings confirm the effectiveness of high-frequency boat-tailing in the bi-frequency actuation immedi-

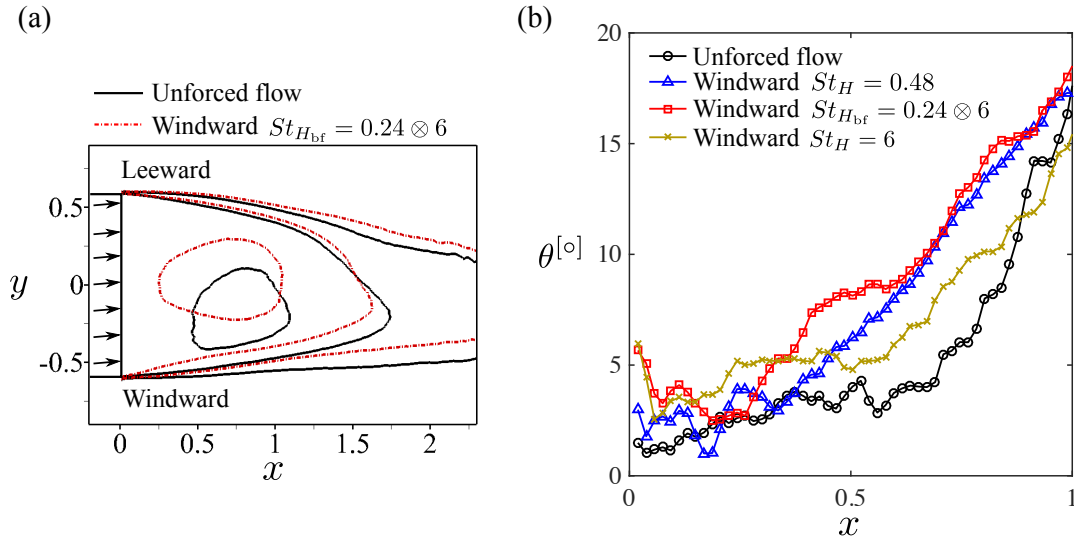


Figure 5.30: Effect of bi-frequency forcing on the wake orientation. (a) Iso-contour lines of the time-averaged streamwise velocity $\bar{u} \in \{-0.25, 0.25, 0.7\}$ for unforced flow and forced flow at $St_{H_{bf}} = 0.24 \otimes 6$ on the mid-height plane $z = 0.67$. (b) Streamwise evolution of the velocity angle θ of the streamline issuing from the windward trailing edge $(x, y) = (0, -0.6)$.

ately downstream of the forced trailing edge. We may consider the bi-frequency forcing as a ‘tuned’ low-frequency forcing by ‘adding’ a fluidic flap. Forcing at $St_{H_{bf}} = 0.24 \otimes 6$ permits to adequately symmetrize the wake and to achieve also a thinner wake by boat-tailing effect. Nevertheless forcing at $St_{H_{bf}} = 0.48 \otimes 6$ seems to be too strong to symmetrize the wake. It yields a reversed asymmetry with respect to the unforced flow and leads to a lower drag reduction compared to $St_{H_{bf}} = 0.24 \otimes 6$.

As discussed in the previous section, we would expect different shear layer thicknesses and growth rates for the three forced cases in Fig. 5.29. Figure 5.31 shows the streamwise evolution of the corresponding windward shear layer thickness. The bi-frequency forcing leads to a thicker shear layer and a higher growth rate than the single-frequency forcing. The thickest shear layer associated with the highest initial growth rate is found for $St_{H_{bf}} = 0.48 \otimes 6$. This agrees with the reversal of wake asymmetry which is related to the enhancement of the entrainment in the windward shear layer. The comparison illustrates that the coupling of low and high frequency enhances further the effect obtained with a single low frequency forcing. In the following section,

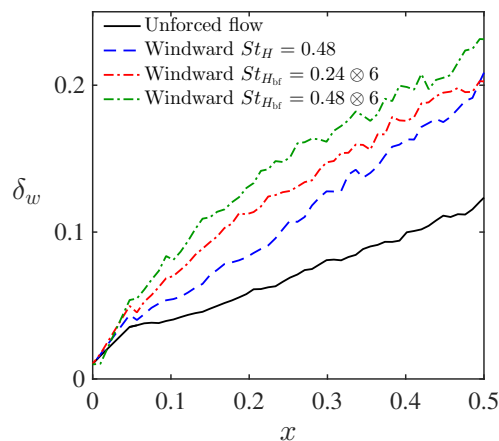


Figure 5.31: Streamwise evolution of the windward shear layer thicknesses.

we will examine the phase-averaged flow field to get a further understanding on the unsteady entrainment mechanisms.

5.6.3 Analysis of the phase-averaged velocity statistics

We compare the two forcing configurations $St_H = 0.48$ and $St_{H_{bf}} = 0.48 \otimes 6$ with the aim to understand why the mean wake is symmetrized and reversed, respectively. According to Hussain & Reynolds (1970), in a flow with highly periodic characteristics, the velocity $u(\mathbf{x}, t)$ can be decomposed into a mean component \bar{u} , a periodic fluctuation \tilde{u} and a chaotic fluctuation u'' :

$$u(\mathbf{x}, t) = \bar{u}(\mathbf{x}) + \tilde{u}(\mathbf{x}, t) + u''(\mathbf{x}, t). \quad (5.8)$$

\tilde{u} is the contribution of the periodic movement and is defined as $\tilde{u} = \llbracket u \rrbracket - \bar{u}$ where $\llbracket u \rrbracket$ is the phase-averaged velocity. u'' is the random velocity fluctuation associated with the turbulent motion. This decomposition enables the determination of the relative contribution of the periodic and random motions to the Reynolds stress. In fact, the time-averaged Reynolds stresses are equal to the sum of the time-averaged correlations due to periodic fluctuations and random motions, for example, $\overline{u'v'} = \overline{(\tilde{u} + u'')(\tilde{v} + v'')} = \overline{\tilde{u}\tilde{v}} + \overline{u''v''}$. In particular, we are interested in the transport of the fluid momentum towards the wake region through the boundary of the recirculation bubble by actuation. To do so, we examine the v_n component in the streamline coordinates ($v_n = v \cos(\theta) - u \sin(\theta)$ where $\theta = \arctan(v/u)$) rather than v in the model reference system. Here we take the mean streamline emerging from the windward trailing edge $(x, y) = (0, -0.06)$ to approximate the boundary of the recirculation bubble. It can be shown that by projecting the fluctuating velocity vector on this line we can get:

$$\overline{u'v'_n} = \overline{\tilde{u}\tilde{v}_n} + \overline{u''v''_n}. \quad (5.9)$$

This equation enables us to identify the corresponding contributions of $\overline{\tilde{u}\tilde{v}_n}$ and $\overline{u''v''_n}$ to $\overline{u'v'_n}$ and to distinguish their differences in periodic and bi-frequency forcing.

First we examine the quantity $\tilde{u}\tilde{v}_n$ for different phases. Note that in the present study no phase-locked PIV measurements are performed. However, the velocity measurement (at a sampling rate of 3.5 Hz) and the actuation command signal (at a sampling rate of 5 kHz) were recorded simultaneously. This enables us to attribute a phase to the acquired pictures. By dividing the period into N_{wd} equal windows (window width $2\pi/N_{wd}$), we are able to distribute the phase-identified velocity fields into the corresponding window. Then we can obtain an approximation of the phase-averaged velocity statistics by averaging the velocity fields in the same window. A similar procedure has been successfully applied by Perrin *et al.* (2007). Here, we set $N_{wd} = 25$. The number of pictures in each phase window is approximately 60.

Figure 5.32(a) and (b) compares the phase-averaged spanwise periodic fluctuation \tilde{v} at phases $t/T \in \{0.16, 0.32, 0.48, 0.64, 0.8, 0.96\}$ for both forced cases. The velocity field of the periodic fluctuations (\tilde{u}, \tilde{v}) is overlaid over the color maps. Figure 5.32(c) shows the evolution of $\tilde{u}\tilde{v}_n$ with increasing phase along the separation streamline of the mean recirculation bubble. At the very beginning of the stroke phase ($t/T = 0$), the pulse-jet creates a pair of counter rotating vortices at the exit of slit, the size of which is too small to be captured in the present measurement. With increasing stroke time, these two vortices grow up and are convected downstream. At $t/T = 0.16$, we can clearly distinguish a positive (red spot) and negative (blue spot) \tilde{v} downstream of the actuation slit for both forced flows. A sketch is given in Fig. 5.32(a) to facilitate the understanding. The positive \tilde{v} is related to the jet-induced counter-clockwise rotating vortex. The constitution of the negative \tilde{v} is twofold. First, it may be related to the jet-induced clockwise rotating vortex. The location of the negative \tilde{v} is downstream of the positive

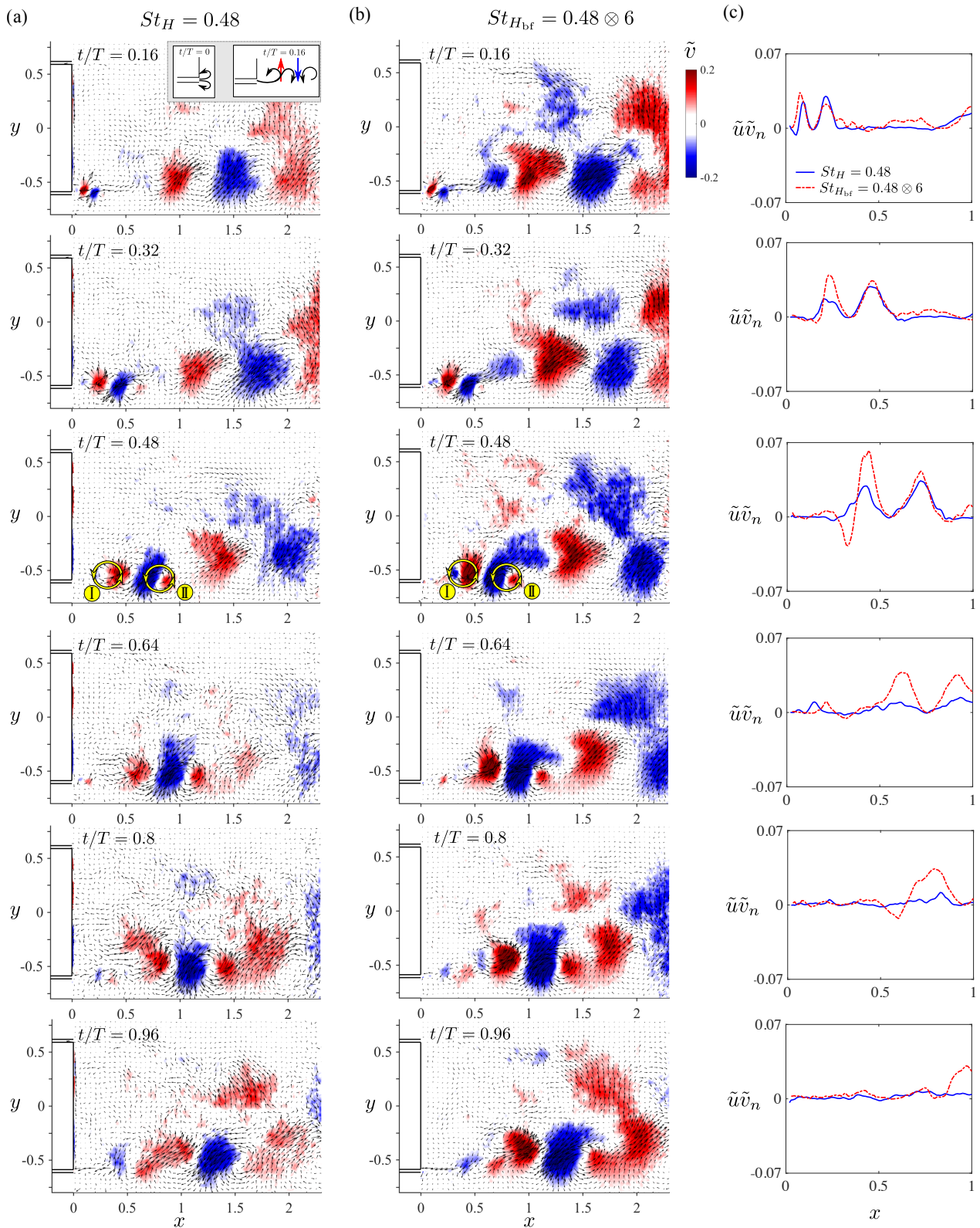


Figure 5.32: Color maps of the phase-averaged spanwise periodic fluctuation \tilde{v} at the single frequency forcing $St_H = 0.48$ (a) and the bi-frequency forcing $St_{H_{bf}} = 0.48 \otimes 6$ (b). From top to bottom, the snapshots correspond to the phases $t/T \in \{0.16, 0.32, 0.48, 0.64, 0.8, 0.96\}$. Periodic fluctuation velocity vectors (\tilde{u}, \tilde{v}) are overlaid over the color maps. The sketch at $t/T = 0.16$ illustrates the evolution of the jet structures from $t/T = 0$ to $t/T = 0.16$. The inserted circles at $t/T = 0.48$ indicate two counter-clockwise rotating structures. (c) Streamwise evolution of the periodic fluctuation $\tilde{u}\tilde{v}_n$ along the separation streamline of the mean recirculation bubble at the corresponding phases of (a) and (b).

\tilde{v} because the clockwise rotating vortex is initially adjacent to the boundary layer and thus is convected with a higher velocity about $V_c \approx 0.5U_\infty$, whereas the counter-clockwise rotating vortex is adjacent to the recirculating flow with a much lower velocity. On the other hand, Barros (2015) has shown that the formation of the jet structure downstream of the trailing edge induces a disruption of the shear layer. If this is true in our case, the disruption would yield the roll-up of a counter-clockwise rotating vortex which induces a negative \tilde{v} downstream of the positive \tilde{v} (see the inserted sketch). A better spatial resolution of the velocity field would be required to identify these two contributions of negative \tilde{v} . The streamwise evolution of $\tilde{u}\tilde{v}_n$ at $t/T = 0.16$ presents two peaks at the corresponding positions of the positive and negative \tilde{v} . The positive sign of the two peaks indicates that at the position of negative \tilde{v} , \tilde{u} is also negative. The peak value and location of both forced cases are quite similar at this phase.

With increasing t/T , the positive and negative \tilde{v} are progressively convected downstream. From $t/T = 0.32$, the bi-frequency forcing $St_{H_{bf}} = 0.48 \otimes 6$ features a higher periodic fluctuation until to the end of the actuation period, manifested both by the darker color in Fig. 5.32(b) and by the peak value of $\tilde{u}\tilde{v}_n$ in Fig. 5.32(c). The highest fluctuation is observed at $t/T = 0.48$ close to the end of the stroke phase. In particular, at $t/T = 0.48$ we can notice clearly an induced outward movement upstream of the significant positive \tilde{v} (dark red spot) and an inward movement downstream of the significant negative \tilde{v} (dark blue spot), forming two counter-clockwise rotating structures which are marked by the circles and labeled by \textcircled{I} and \textcircled{II} respectively in the figure. The generation of the counter-clockwise rotating structure \textcircled{II} supports our above conjecture concerning the disruption of the shear layer.

To show the influence of the high periodic fluctuation on the absolute wake movement, we display in Fig. 5.33 the distribution of the phase-averaged spanwise velocity $\llbracket v \rrbracket$ overlaid with the velocity vector ($\llbracket u \rrbracket, \llbracket v \rrbracket$) at phases $t/T \in \{0.48, 0.8\}$. For $St_H = 0.48$, the strong

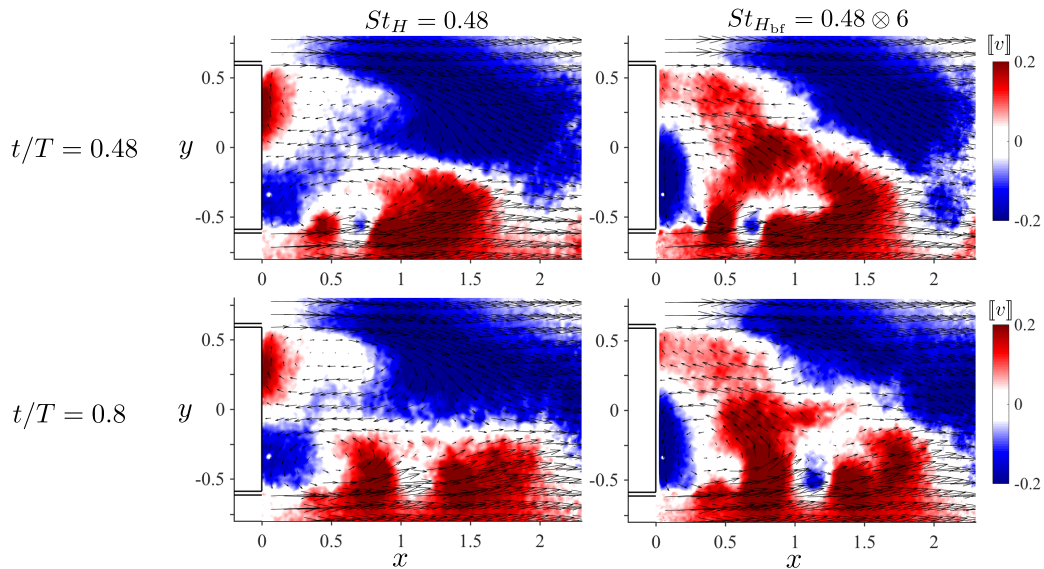


Figure 5.33: Phase-averaged spanwise velocity $\llbracket v \rrbracket$ overlaid with the phase-averaged velocity vectors ($\llbracket u \rrbracket, \llbracket v \rrbracket$). Left column: $St_H = 0.48$; right column: $St_{H_{bf}} = 0.48 \otimes 6$.

periodic movement related to the counter-clockwise structure \textcircled{I} in Fig. 5.32(c) enables the flow to penetrate into the center of the recirculating region thus symmetrizing the mean wake. For $St_{H_{bf}} = 0.48 \otimes 6$, the periodic fluctuation is even higher; the resulting spanwise flow crosses the central line $y = 0$ and affects the leeward side, hence reversing the mean wake asymmetry. From these observations, we infer that the bi-frequency forcing further increases the periodic fluctuation induced by the single low-frequency forcing and promotes the effects of the latter. This also explains why $St_{H_{bf}} = 0.24 \otimes 6$ can symmetrize the wake while $St_H = 0.24$ can not.

From $\tilde{u}\tilde{v}_n$ obtained at all phases, we can calculate the time-averaged periodic fluctuation $\overline{\tilde{u}\tilde{v}_n}$ and identify its contribution to the time-averaged shear stress $\overline{u'v'_n}$. Figure 5.34 shows the streamwise evolution of $\overline{u'v'_n}$, $\overline{\tilde{u}\tilde{v}_n}$ and $\overline{u''v''_n}$ along the separation streamline of the mean recirculation bubble. $\overline{u''v''_n}$ is obtained by $\overline{u''v''_n} = \overline{u'v'_n} - \overline{\tilde{u}\tilde{v}_n}$. The unforced flow is also shown for comparison. Immediately downstream of the actuation slit ($x < 0.2$), $\overline{\tilde{u}\tilde{v}_n}$ increases for both types of actuation compared to the unforced flow. In addition, the bi-frequency forcing $St_{H_{bf}} = 0.48 \otimes 6$ provokes a higher value for all three quantities in this zone. The higher values of $\overline{u''v''_n}$ for the bi-frequency forcing may be related to the high-frequency component at $St_{H_{high}} = 6$. Further downstream, the values of $\overline{u'v'_n}$ for $St_{H_{bf}} = 0.48 \otimes 6$ remain nearly constant and become lower than those for $St_H = 0.48$, although the values of $\overline{\tilde{u}\tilde{v}_n}$ for $St_{H_{bf}} = 0.48 \otimes 6$ are globally higher than those for $St_H = 0.48$. The difference is due to the random motion component $\overline{u''v''_n}$ which starts to drop in the range $x > 0.2$ for $St_{H_{bf}} = 0.48 \otimes 6$ but strongly increases for $St_H = 0.48$. To quantify exactly the contribution of the periodic and random motions to the total stress, we integrate the three quantities along the interval $x \in [0, 0.5]$. For $St_H = 0.48$, the contribution is 31% and 69% for the periodic and random motions, respectively. For $St_{H_{bf}} = 0.48 \otimes 6$, the contribution is 49% and 51%, respectively. The periodic motion contribution is clearly more important for the bi-frequency forcing. Additionally, close to the trailing edge ($x < 0.2$), the random motion component $\overline{u''v''_n}$ of the forced flows is in the same order of magnitude as the unforced flow, indicating that the increase of $\overline{u'v'_n}$ close to the trailing edge under actuation is related to the increase of the periodic motion component $\overline{\tilde{u}\tilde{v}_n}$.

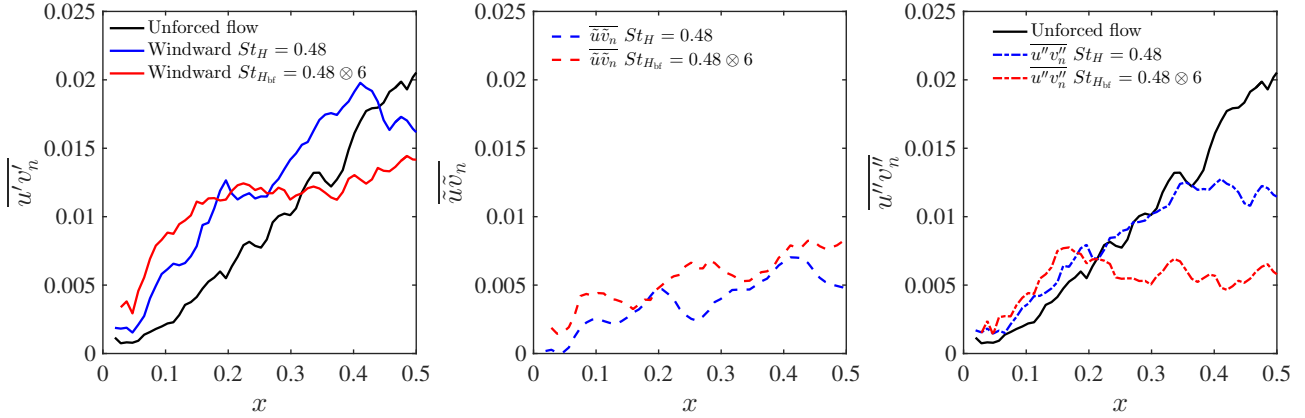


Figure 5.34: Streamwise evolution of the total shear stress $\overline{u'v'_n}$, the periodic motion component $\overline{\tilde{u}\tilde{v}_n}$ and the random motion component $\overline{u''v''_n}$ along the separation streamwise of the recirculation bubble. We remind that $\overline{u'v'_n} = \overline{\tilde{u}\tilde{v}_n} + \overline{u''v''_n}$.

We did not discuss the influence of the jet velocity on the results because no parametric study of the supply pressure was performed. However, we presume that the jet velocity V_{Jet} would highly affect \tilde{v}_n and hence $\tilde{u}\tilde{v}_n$. Small $\tilde{u}\tilde{v}_n$ would be unable to reorient the wake. Similarly, strong $\tilde{u}\tilde{v}_n$ would reverse the wake asymmetry.

The discussions above furnish a global view of what happens when the wake is forced using a bi-frequency actuation. To conclude, from the time-averaged view, $St_{H_{bf}}$ couples the large-scale structure modification achieved at $St_{H_{low}}$ and the boat-tailing effect achieved at $St_{H_{high}} = 6$ by enhancing the shear layer entrainment and simultaneously deviating the shear layer and the global wake. From the phase-averaged view, the periodic fluctuation motion related to the low-frequency jet is further enhanced by the bi-frequency forcing and leads to higher entrainment rates which are capable of altering the organization of recirculating flow in the wake.

5.6.4 On the drag reduction using LGPC

Having performed the systematic bi-frequency forcing tests, we wonder if there exist other combinations of multiple frequencies that can reduce the drag even further? Is the base pressure feedback useful to get better results? One effective way to answer these questions is to apply LGPC for finding the optimal solution by the use of automatic learning.

We apply the generalized non-autonomous control design LGPC-3 $b = K(\mathbf{s}, \mathbf{h})$ as introduced in Chapter 2, where \mathbf{s} is the sensor feedback and \mathbf{h} is a vector of time-periodic functions. Only the windward edge is forced and the lateral pressure gradient is returned, constituting a non-autonomous single-input single-output system with respect to the experimental plant. The control objective is to minimize the drag. Hence, we define the cost function to be minimized as the time-averaged drag under the actuated state normalized by its unforced value:

$$J = \frac{C_{D_a}}{C_{D_u}}. \quad (5.10)$$

This is exactly the definition of γ_D presented in Eq. (5.3). We note that, due to the existence of drift in the balance signal output, J estimated from the real-time data needs to be corrected. This correction can only be performed a posteriori for each generation. In this way, we ensure that the breeding of the next generation is based on the corrected J values.

Given the significant changes in the dynamics of the lateral pressure gradients discussed previously, the feedback of this gradient may provide important information for a closed-loop control. Hence, we define the sensor input vector \mathbf{s} of LGPC-3 as

$$\mathbf{s} = (s_1, s_2) = \left(\frac{\partial C_p}{\partial y}, \widehat{\frac{\partial C_p}{\partial y}} \right). \quad (5.11)$$

s_1 is the real-time lateral pressure gradient which contains broadband dynamics. s_2 is determined by filtering s_1 using a first order low-pass filter. The inclusion of a filtered signal in the sensor feedback is inspired from the open-loop results which showed significant modifications of the low-frequency dynamics. The cutoff frequency at -3dB corresponds to $St_H = 0.36$, thus the passband covers the vortex shedding mode. By low-pass filtering s_1 , we put our interest specially on the low-frequency dynamics. The time-periodic input vector \mathbf{h} comprises 12 harmonic functions $h_i(t) = \sin(2\pi f_i t)$, $i = 1, \dots, 12$ listed in table 5.4. The selected frequencies are a subset of those presented in table 5.1. The variety of frequencies permits LGPC to explore new possibilities of frequency combination.

Controller input	h_1	h_2	h_3	h_4	h_5	h_6	h_7	h_8	h_9	h_{10}	h_{11}	h_{12}
f_i (Hz)	10	18	20	40	68	100	200	294	333	417	455	500
St_{H_i}	0.12	0.21	0.24	0.48	0.8	1.2	2.4	2.3	4	5	5.4	6

Table 5.4: Description of the harmonic functions $h_i(t) = \sin(2\pi f_i t)$ used as inputs of LGPC-3 for windward forcing.

Up to $N = 9$ generations with $M = 50$ individuals in each are evaluated. Each individual is tested for a time period of $T = 10$ s. This value is approximately 840 convective time units $t_c = H/U_\infty$, which is sufficient for a good statistical accuracy. The evolution of J with increasing generation is depicted in Fig. 5.35. When the generation n increases, the values of J decrease gradually, highlighting the learning of increasingly better control laws. After $n = 7$, the performance of the best individual appears to converge.

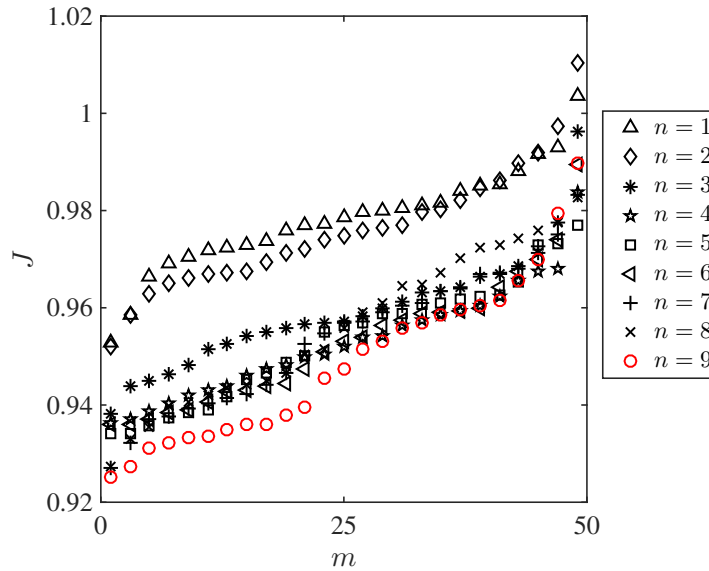


Figure 5.35: Evolution of the cost value J versus the individual m for 9 generations $n = 1, \dots, 9$.

The optimal control law reads:

$$b^\odot = H(-0.931(h_{12} - h_3) - 0.1). \quad (5.12)$$

This law combines two harmonic functions: h_3 at $St_H = 0.24$ and h_{12} at $St_H = 6$. They are exactly the two frequencies whose combination leads to the maximum drag reduction in the bi-frequency forcing (see § 5.6.1). In addition, no sensor feedback is included in b^\odot . The resulting cost $J = 0.925$ is slightly better than $J = 0.933$ obtained for the bi-frequency forcing $St_{H_{bf}} = 0.24 \otimes 6$. A comparison of their actuation command is given in Fig. 5.36 for one period with respect to the low frequency $St_H = 0.24$. Major differences are the time window covered by the high frequency signal and the duty cycle of the high-frequency forcing. The resulting duty cycle of b^\odot is 41.6%, which is larger than the duty cycle value 21% obtained for $St_{H_{bf}} = 0.24 \otimes 6$. The slight difference in the cost value J could be due to this difference of duty cycles.

With the result of LGPC-3, we confirm that the combination of $St_H = 0.24$ and $St_H = 6$

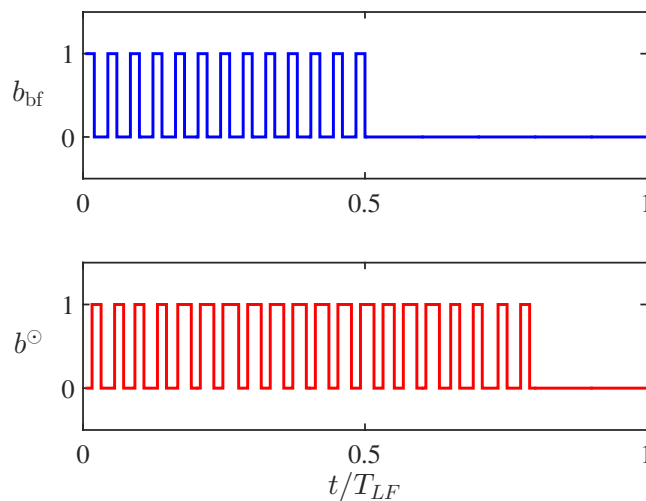


Figure 5.36: Comparison of the actuation command for the bi-frequency forcing $St_{H_{bf}} = 0.24 \otimes 6$ and the optimal LGPC-3 law b^\odot . T_{LF} is the period of the low-frequency $St_{H_{low}} = 0.24$.

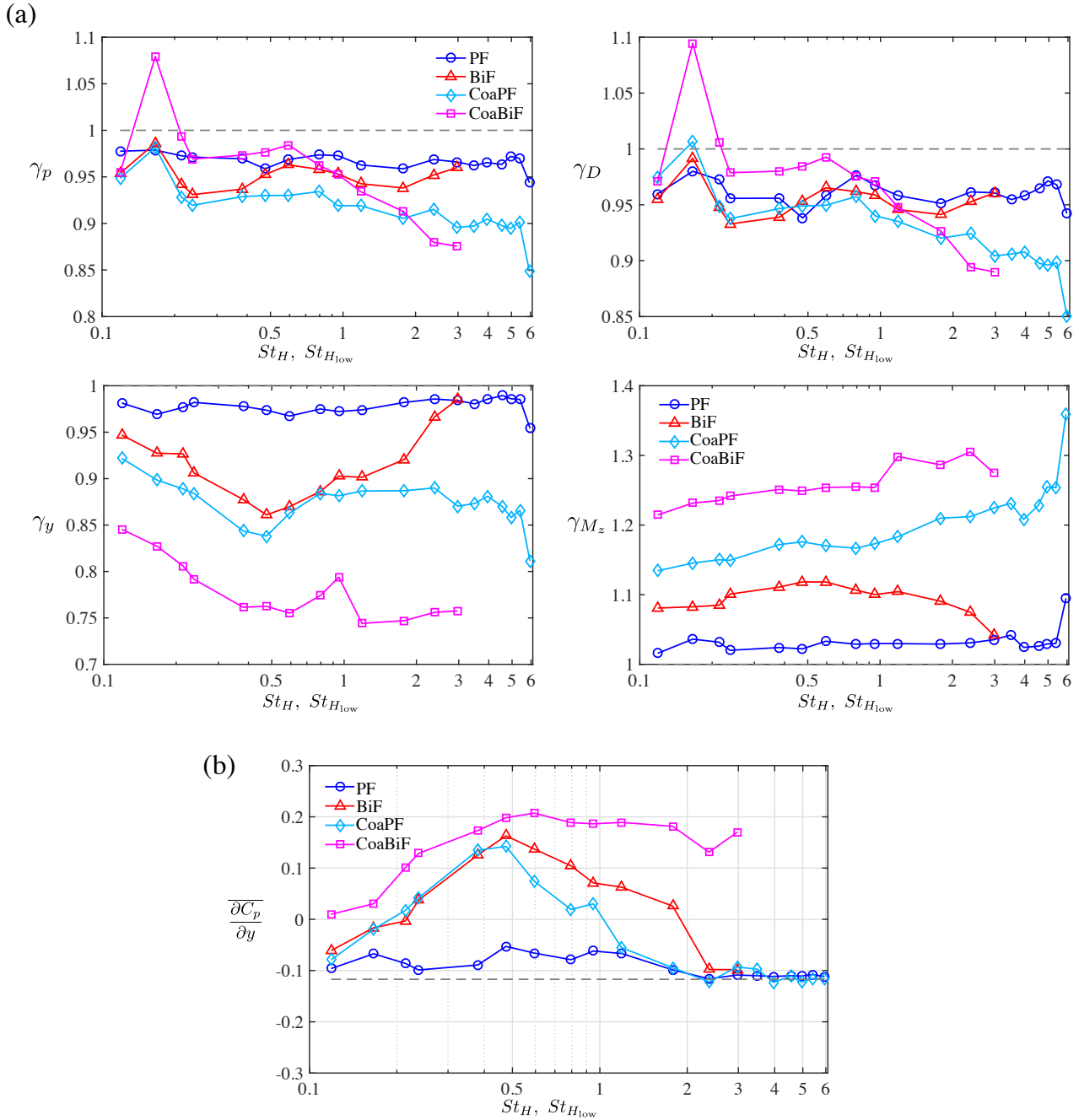
overperforms the other configurations examined in the present study. The influence of the duty cycle on drag reduction appears to be small once the combined frequencies are determined. The underlying mechanisms of the drag reduction are similar to the case of $St_{H_{bf}} = 0.24 \otimes 6$ and are not described here to avoid redundancy. With this finding, LGPC is proven to be effective to find the optimal control with no or little prior knowledge about the control system.

5.7 Unsteady Coanda blowing effect

In this section, we aim to investigate how the unsteady actuation effects discussed previously are affected by the presence of the Coanda surface. For that, Coanda surfaces are added adjacent to each actuation slit as illustrated in Fig. 3.2 of Chapter 3. We focus on the windward forcing due to its benefits for drag reduction. The Coanda effect is known to deviate the shear layer towards the center of the wake. High-frequency forcing also implies this effect. The results of Chapter 3 and Barros *et al.* (2016b) demonstrated that when unsteady blowing is coupled with the Coanda surface, the shear layer deviation is more effective for drag reduction. Furthermore, bi-frequency forcing as introduced in § 5.6 can also act on deviation. In the following, a detailed comparison for periodic forcing (PF), bi-frequency forcing (BiF), Coanda periodic forcing (CoaPF) and Coanda bi-frequency forcing (CoaBiF) is discussed to clarify how the varying shear layer deviation affects the wake and the corresponding drag.

To perform a global and complete comparison, the curves of γ_p , γ_D , γ_y and γ_{M_z} , the lateral pressure gradient $\overline{\partial C_p / \partial y}$ and the corresponding base pressure distribution are displayed in Fig. 5.37(a), (b) and (c), respectively. For the bi-frequency forcing, the abscissa in Fig. 5.37(a) and (b) is the lower frequency $St_{H_{low}}$ in the combination of $St_{H_{bf}} = St_{H_{low}} \otimes St_{H_{high}}$. All forcing configurations are performed at the supply pressure $P_0 = 2.5$ bar. The curves of γ_p and γ_D with the addition of Coanda surface obey a similar behavior, demonstrating that the correlation between the base pressure and drag reduction is not modified by the presence of Coanda effect.

We initially focus on the drag ratio γ_D by comparing BiF with CoaPF. When $St_H \leq 0.48$, the curves of γ_D for BiF and for CoaPF almost collapse. In addition, their pressure gradient $\overline{\partial C_p / \partial y}$ and pressure distribution also match. This shows that BiF couples the low-frequency effect with a boat-tailing effect. Moreover, this boat-tailing effect of $St_{H_{high}} = 6$ is equivalent to the passive Coanda device in the considered low-frequency range. For $St_H > 0.48$, CoaPF leads to a higher drag reduction than BiF. The reasons for such a difference can be inferred from the curve of $\overline{\partial C_p / \partial y}$ and the pressure distribution. CoaPF leads to a lower $\overline{\partial C_p / \partial y}$ than BiF in the interval $0.48 < St_H < 2$. In addition, the frequency where $\overline{\partial C_p / \partial y}$ becomes negative is reduced to $St_H \approx 1$ for CoaPF compared to $St_H \approx 2$ for BiF. This indicates that the shear layer deviation and the enhancement of the turbulence fluctuations obtained with CoaPF is less than those of BiF. For example, when the wake is only symmetrized by CoaPF at $St_H = 0.8$, it is rather reoriented to a reversed asymmetry at $St_{H_{bf}} = 0.8 \otimes 6$ (inferred from the pressure distribution in Fig. 5.37(c)). When the wake comes back to the symmetric state for BiF at $St_{H_{bf}} = 1.8 \otimes 6$, the unsteady Coanda boat-tailing effect at $St_H = 1.8$ seems to be more effective to reduce the drag. Moreover, the performance of CoaPF is more robust than BiF in the interval $St_H \in [0.24, 2.4]$. The best drag reduction is achieved at CoaPF $St_H = 6$, yielding 15% drag reduction which is 2.5 times better than the value achieved with PF at the same frequency without Coanda. This huge drag reduction is related to the enhanced boat-tailing effect resulted from the unsteady Coanda blowing which deviates further the shear layer towards the leeward side and leads to a higher change of the curvature of the streamline immediately downstream of the forced trailing edge. We will quantify in detail the changes of the velocity angle induced by this high-frequency Coanda blowing in a later discussion.



(c)

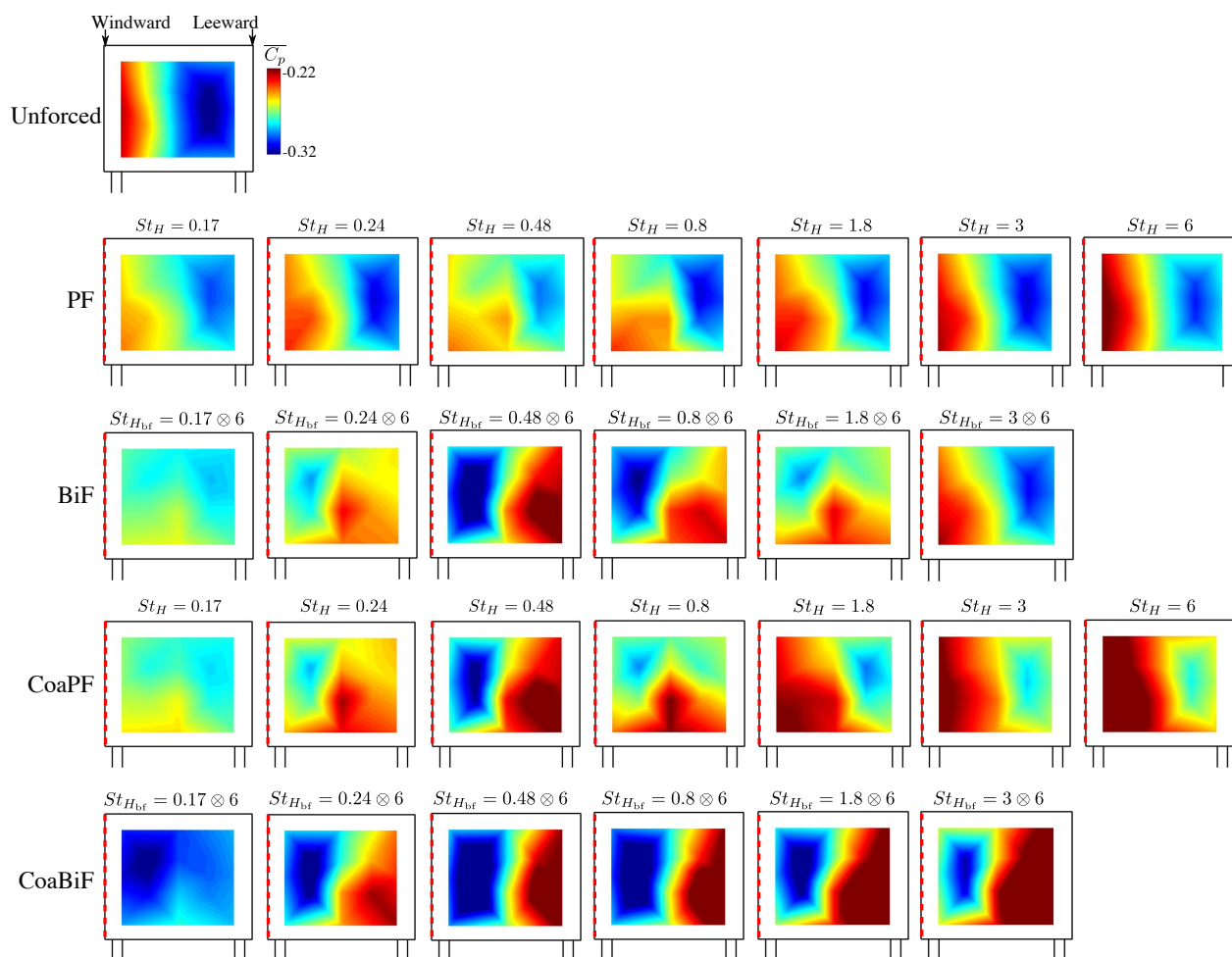


Figure 5.37: Follow-up of the figure in the previous page. (c) Color maps of the base pressure. The forced edge is highlighted by the red dashed line.

Additionally, we note from Fig. 5.37(b) that the mean pressure gradient $\overline{\partial C_p / \partial y}$ is the same for both PF and CoaPF at $St_H = 6$, albeit they feature a significant difference of drag reduction. This corroborates that the boat-tailing effect related to the high-frequency forcing induces no change of the degree of asymmetry of the wake.

When adding the Coanda effect to BiF, the shear layer deviation and turbulence level at low frequencies are further enhanced. This is confirmed by the positive $\overline{\partial C_p / \partial y}$ over the whole span of $St_{H_{low}}$ in Fig. 5.37(b) and the location of low pressure regions (blue zones) in Fig. 5.37(c). The resonance at the vortex shedding mode is more pronounced with CoaBiF, as underlined by the uniform low pressure distribution over the base surface. This resonance increases the drag by 10%. The corresponding curve of γ_D exhibits a larger slope compared with the other three categories. When $St_{H_{low}} < 0.8$, the drag reduction performance is degraded. Given its high value of $\overline{\partial C_p / \partial y}$, we may relate this performance degradation to the high degree of wake asymmetry which is associated with an important pressure drop close to the forced edge. For $St_{H_{low}} > 2$, although $\overline{\partial C_p / \partial y}$ stays on a high level, the drag reduction is about 2% higher with CoaBiF compared to CoaPF. At these frequencies, the shear layer vectorization in CoaBiF starts to damp, the pressure drop near the forced windward edge is attenuated and the pressure close to the unforced leeward edge is increased, leading to slightly higher base pressure and drag reduction.

Now we focus on the impact of unsteady Coanda blowing on the side force and yaw moment, as shown in Fig. 5.37(a). Clearly, the addition of the Coanda surface further decreases the side force and increases the yaw moment. This modification can be ascribed to three reasons: (1) the enhancement of the flow acceleration over the rear windward surface introduced by the Coanda effect, (2) the low pressure along the Coanda surface and (3) the flow deceleration over the rear leeward surface. The resultant effect of the four forcing categories on γ_y and γ_{M_z} can be ordered in the following way: PF < BiF < CoaPF < CoaBiF with the most prominent change for CoaBiF. In particular, we note that despite a 15% drag reduction at CoaPF $St_H = 6$, the corresponding yaw moment is increased almost by 36%. This suggests that, for a small yaw angle as in the present study, a trade-off must be determined between minimizing the drag and meanwhile not triggering the safety issues caused by the large yaw moment. Despite the better performance of the boat-tailing effect for drag reduction, the associated yaw moment is high. On the contrary, for BiF with which we achieve drag reduction by changing the dynamics of the shear layer, although less drag reduction is obtained, the increase of the yaw moment is significantly lower than that induced by the boat-tailing effect. For safety considerations, BiF would be better than CoaPF and CoaBiF.

We have mentioned above that the significant difference of drag reduction between PF and CoaPF at $St_H = 6$ is related to the enhanced flow deviation downstream of the trailing edge. Figure 5.38 confirms this point by showing (a) the streamlines in the mid-height plane, (b) the iso-contour lines of the time-averaged streamwise velocity \bar{u} , (c) the velocity angle along the streamline originating from the windward trailing edge $(x, y) = (0, -0.06)$ and (d) the pressure on the mid-height line of the model. The streamlines show no change of the flow organization inside the recirculation bubble. The bubble length for CoaPF is slightly reduced by 2% compared to that of PF. The increase of flow deviation by the Coanda effect is clear in Fig. 5.38(b) and (c). The contour lines of CoaPF are more deviated towards the leeward side. The velocity angles along the streamline originating from $(x, y) = (0, -0.6)$ are larger for CoaPF than for PF over the whole range of x . The initial angle at $x = 0.05$ for CoaPF is 11° which is twice that of PF. This significant increase of flow deviation leads to a higher base pressure along the whole span of the model mid-height without changing the lateral pressure gradient, as shown in Fig. 5.38(d). For comparison, in the results of García de la Cruz *et al.* (2017a) under a yaw angle of 6° , the optimal windward flap angle is around 15° which is close

to our results. The high deviation results in a thinner and slightly shorter bubble, similar to the result in § 3.4.3 with high-frequency Coanda forcing along the four trailing edges. Moreover, we observe a further damping of the turbulent kinetic energy \mathcal{K} and average kinetic energy \mathcal{E} inside the forced bubble for CoaPF when compared to that for PF, similar to the observation in Fig. 5.20. This damping may also have a contribution to the drag reduction.

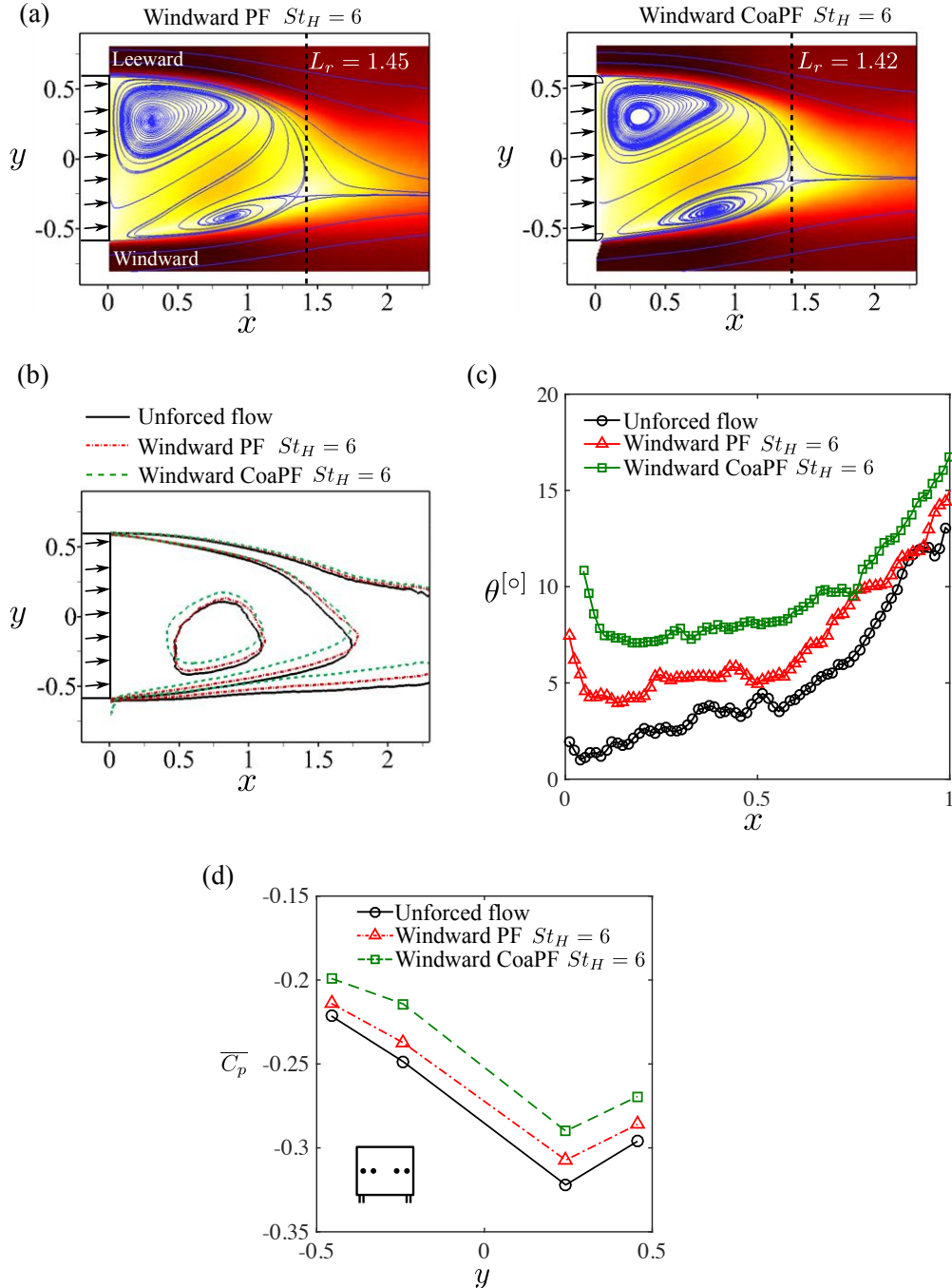


Figure 5.38: Comparison of the effects on the mean wake and base pressure for PF and CoaPF at high-frequency forcing $St_H = 6$. (a) Streamlines of the mean velocity in the mid-height plane $z = 0.67$. (b) Iso-contour lines of the time-averaged streamwise velocity $\bar{u} \in \{-0.25, 0.25, 0.7\}$. (c) Streamwise evolution of the velocity angle θ of the streamline originating from the windward trailing edge $(x, y) = (0, -0.6)$. (d) Time-averaged pressure coefficient \bar{C}_p on the mid-height line of the model.

Figure 5.39 displays how the wake orientation is progressively modified by the PF, BiF, CoaPF and CoaBiF for three representative frequencies at St_H and $St_{H_{low}}$: 0.24, 0.48 and 0.8.

BiF and CoaPF share similar wake topologies for $St_H < 0.5$ and $St_{H_{low}} < 0.5$, corroborating again the equivalent effect of $St_{H_{high}} = 6$ and the Coanda deflection surface. More precisely, at $St_H < 0.5$ and $St_{H_{low}} < 0.5$, the ability of the four forcing categories to reorient the wake obeys the following order: $PF < BiF \approx CoaPF < CoaBiF$. When $St_H > 0.5$ and $St_{H_{low}} > 0.5$, this order becomes $PF < CoaPF < BiF < CoaBiF$.

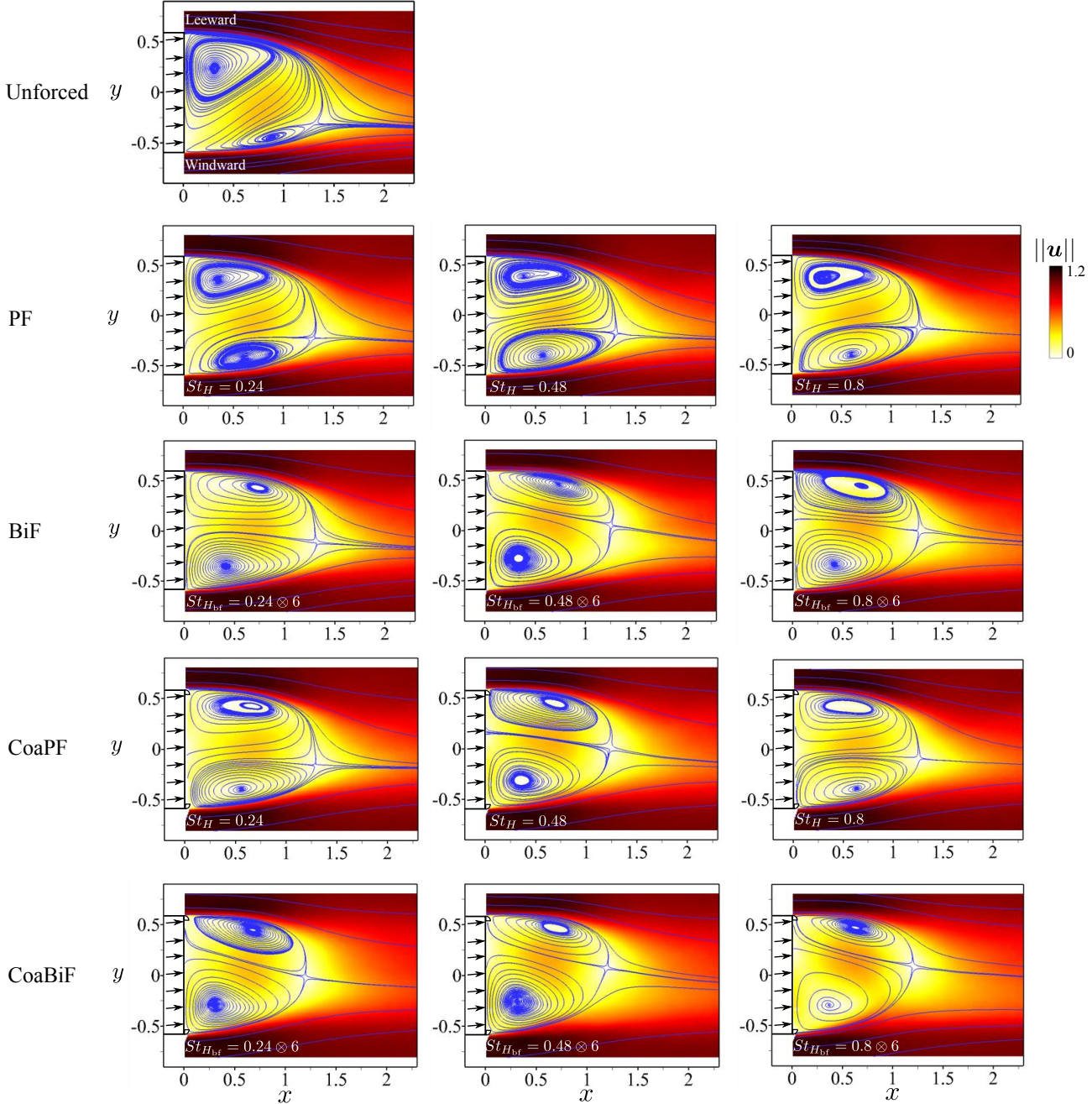


Figure 5.39: Comparison of forcing effects on the wake topology. Left column: $St_H = 0.24$ for PF and CoaPF; $St_{H_{bf}} = 0.24 \otimes 6$ for BiF and CoaBiF. Middle column: similar to the former but with $St_H = 0.48$ and $St_{H_{bf}} = 0.48 \otimes 6$. Right column: similar to the former but with $St_H = 0.8$ and $St_{H_{bf}} = 0.8 \otimes 6$.

In summary, with the comparison of the four forcing categories, we have demonstrated that global wake recirculations can be effectively modified with a variety of actuation patterns along the windward trailing edge. In particular, the new bi-frequency forcing can achieve actuation mechanisms which can not be explored by the single-frequency periodic forcing. The multiple

interaction mechanisms between pulsed jets of different time scales and the windward shear layer play a crucial role in changing the separation angle and thus the wake geometries. The results presented here point to the exciting future directions for closed-loop control under gusty conditions.

Chapter 6

Conclusions and perspectives

6.1 General synthesis

Drag reduction of road vehicles has become a cornerstone challenge due to the increasing government constraints and taxation of CO₂ emissions resulting from the corresponding fuel consumption. In particular, the low pressure in the wake resulted from the flow separation constitutes an important portion of the aerodynamic drag for the bluff form vehicles. In recent years, the rapid development of active flow control smooths the path for achieving drag reduction. Wake manipulation by active devices is one of the most developed fields among various studies.

In the present work, we pursue drag reduction of a square-back car model similar to the Ahmed body studied in Ahmed *et al.* (1984) with a flat base. The wake flow is manipulated by jet actuators at the four trailing edges and is monitored by pressure sensors distributed at the rear side. The investigated turbulent wake is a big challenge for model-based control design due to the difficulties to construct corresponding mathematical models and limited knowledge about the flow in experiments. Our study circumvents this challenge by developing a simple yet effective model-free control strategy: the data-driven linear genetic programming control (LGPC). It optimizes automatically the control laws by mimicking the nature's evolution and learning from trials. The innovation in this work is a very general ansatz for control laws which incorporate multi-frequency forcing, sensor-based feedback including also time-history information feedback and combinations thereof. In this way, any perceivable control logic can be constructed.

We highlight the achievements of LGPC in Part I of Fig. 6.1. The effectiveness of LGPC in discovering and exploiting strongly nonlinear actuation mechanisms is first demonstrated for the stabilization of a forced nonlinearly coupled three-oscillator model (Chapter 2). This model mimicks nonlinear frequency crosstalk features of turbulence control. Three categories of LGPC are developed:

- LGPC-1: $\mathbf{b} = K(\mathbf{h})$, open-loop multi-frequency control;
- LGPC-2: $\mathbf{b} = K(\mathbf{s})$, sensor-based feedback control;
- LGPC-3: $\mathbf{b} = K(\mathbf{s}, \mathbf{h})$, generalized non-autonomous control.

The last category comprises both the sensors \mathbf{s} and the time-periodic functions \mathbf{h} , thus permitting to select between open-loop actuation, sensor-based feedback or combinations thereof depending on which performs better. LGPC-1 explores automatically the optimal amplitude and frequency of the periodic forcing by employing less time than an exhaustive sweep of the actuation parameters. The sensor-based control laws obtained with LGPC-2 and -3 both excite the third oscillator by a hard 'kick' for a quick transient meanwhile sustain the second oscillator at a low fluctuation level. Following the quick transient, the first and second oscillators enter

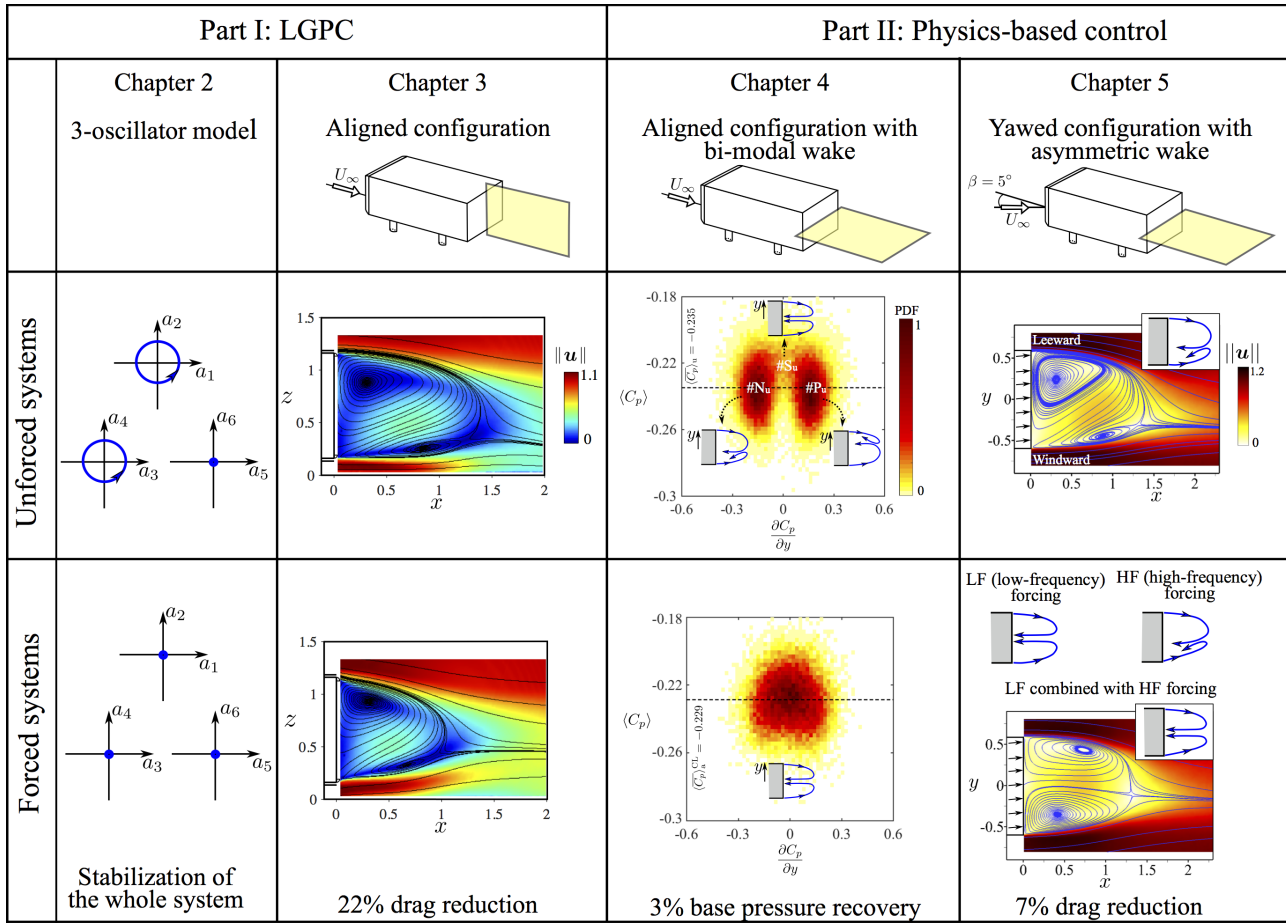


Figure 6.1: Synthesis of the highlighted results for each chapter. Inserted sketches illustrate qualitatively the recirculating flow in the wake.

into a quasi-stable state at nearly vanishing fluctuation levels. Hence, the state feedback hardly needs to actuate and the control command starts to vanish. The whole system is stabilized with only a small investment of the actuation energy at the very beginning of the control. Thus, the sensor-based controllers overperform the optimal periodic forcing as both a lower fluctuation level and a lower actuation energy are obtained. The explored actuation mechanisms demonstrate that the frequency crosstalk can be the only enabling mechanism for stabilization, as typical in turbulence control.

Following the successful demonstration on the dynamical system, LGPC is applied to the drag control experiments of the square-back car model (Chapter 3). The investigated wake is symmetric in the spanwise direction and asymmetric in the wall-normal direction. The four actuation slits are all coupled with Coanda surface deflectors. According to Barros *et al.* (2016b), the optimal periodic forcing on this configuration was found to be at a high frequency and a low duty cycle, yielding 19% drag reduction. In our study, LGPC-1 rapidly identifies a bi-frequency forcing with four actuation slits in unison by testing only 200 individuals in less than 1 hour. This bi-frequency forcing leads to 22% drag reduction, overperforming the past benchmark 19% obtained with the optimized periodic forcing. The estimated actuation power accounts for only 30% of the aerodynamic power saving. In particular, the two frequencies involved in the best control law are again found to be at high frequencies which are $20St_H^{vs}$ and $40St_H^{vs}$ respectively, St_H^{vs} being the vortex shedding frequency. This high-frequency forcing leads to a broadband suppression of energy at very low frequencies for base pressure signals and a global attenuation of the averaged and turbulent kinetic energy in the near wake, resulting in a more stabilized wake. Concomitantly, the mean wake geometry is modified such that the

shear layers are deviated towards the center, resulting in a shorter, narrower, more stream-lined shaped bubble. The drag reduction is ultimately achieved by the combined effect of the wake shaping and stabilization, and can legitimately be called *fluidic boat tailing*. On the other hand, the sensor-based feedback LGPC-2 reproduces high-frequency forcing with a comparable drag reduction to the optimal periodic forcing. This achievement is remarkable considering the experimentally observed time delay of two actuation periods between actuation and sensing. Moreover, LGPC-2 chooses the only sensor which can capture strong enough dynamics in the unforced flow to trigger the feedback cycle and give a good high-frequency signal to noise ratio in the forced flow to create a nearly periodic high-frequency forcing. Hence, LGPC-2 provides not only the optimization of control laws but also a sensor optimization for a general class of control laws. The results of Chapter 2 and 3 highlight the potential of LGPC in discovering and exploiting the most effective nonlinear open- and closed-loop control mechanisms.

In this study, we also particularly address the drag reduction for the square-back car model having a spanwise asymmetric wake. The achievement of this part is synthesized in Part II of Fig. 6.1. In Chapter 4, an intermittent bi-modal wake at zero yaw angle is studied. It consists of two meta-stable asymmetric states which switch between them in a stochastic way, and a low probable unstable symmetric state occurring during the switch of the two asymmetric states. In particular, the base pressure increases once the switch occurs, pointing to the interest of the wake symmetrization control for drag reduction. Single edge periodic forcing tests show that the wake is always blocked into one asymmetric state by actuation and exhibits a low pressure region close to the forced edge. From these flow responses, we infer a physics-based feedback opposition control to symmetrize the wake. When a lower pressure region is detected along one rear side, forcing is applied on the opposite edge to generate an instantaneous and opposing flow reversal. The performance of wake symmetrization depends importantly on the forcing frequency in the feedback-determined actuation phase. The most symmetric distribution is found at $St_H = 0.8$, being the same frequency identified by Barros *et al.* (2016b) which induces the highest shear-layer mixing and entrainment of fluid into the recirculation region. These actuation features enable $St_H = 0.8$ to alter the large-scale recirculating flow and thus to achieve the wake balance. However, only 3% base pressure recovery is obtained with this effective symmetrization. In fact, although the wake symmetrization increases the base pressure, the concomitant actuation effects, namely the enhancement of shear layer mixing and the amplification of vortex shedding, decreases the base pressure. Hence, this control approach needs to be further improved to mitigate the detrimental effect of actuation. A possible way is to determine the minimal energy needed to trigger the mode switching.

Chapter 5 addresses the asymmetric wake at a moderate yaw angle of 5° . From single edge periodic forcing, we observe that the leeward forcing increases drag while the windward forcing leads to drag reduction. Intriguingly, the highest drag reduction (about 6%) in the latter case is achieved at two frequencies having one order of magnitude difference: (1) the low-frequency actuation at $St_H = 0.48$ particularly enhances the forced shear layer turbulence, thus altering the large scale recirculating flow and reducing the drag by wake symmetrization; (2) the high-frequency actuation at $St_H = 6$ acts as a fluidic flap, reducing the drag by a boat-tailing effect. These results of windward periodic forcing inspire us to develop a bi-frequency actuation strategy attempting to further reduce the drag by combining the symmetrization with the fluidic flap effect. However, the combination of $St_H = 0.48$ with $St_H = 6$, i.e. $St_{H_{bf}} = 0.48 \otimes 6$, reverses the wake asymmetry compared to the unforced flow and yields less drag reduction than $St_H = 0.48$. This finding indicates that $St_{H_{bf}} = 0.48 \otimes 6$ is too strong to symmetrize the wake. By varying the low-frequency component in the bi-frequency forcing, we found that the optimal configuration is $St_{H_{bf}} = 0.24 \otimes 6$ which yields 7% drag reduction, outperforming the optimal single-frequency forcing. The resulting wake is simultaneously symmetrized and boat-

tailed. We can properly consider this bi-frequency control as a ‘tuned’ low-frequency forcing by ‘adding’ a fluidic flap. The combined actuation mechanisms can not be explored by any single-frequency periodic forcing. In addition, by applying LGPC-3 on the windward edge with the objective of drag minimization, LGPC-3 identifies automatically the same combination of $St_H = 0.24$ and $St_H = 6$. This result demonstrates again the effectiveness of LGPC to explore the optimal control law with little prior knowledge of the system.

6.2 Perspectives

We can extend the present research to more complex conditions such as the varying oncoming velocity and wind gust. For that we may pursue a robust controller with LGPC by involving the oncoming velocity as an additional sensor or evaluating the cost function at different operating conditions. Moreover, LGPC will be applied on the bi-modal wake to explore potentially new actuation mechanisms other than the opposition control. Larger yaw angle problems will be also addressed. Both the fuel consumption and driving safety shall be considered. To this end, a multi-objective LGPC will be constructed to determine the optimized actuation by driving the four actuation slits independently.

In the very foreseeable future, LGPC and more generally, machine learning control (Duriez *et al.*, 2016), can be expected to solve the control, dynamic modeling and cost function estimation highly effectively and automatically in one or few hours of wind-tunnel testing time. The diagrams for solving these tasks are sketched in Fig. 6.2.

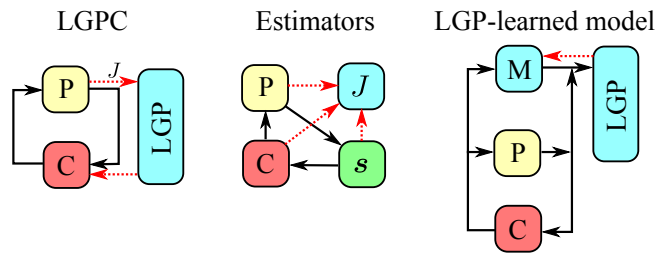


Figure 6.2: LGPC for control, modeling and estimation (figure reproduced from Noack 2017). P: plant; C: control law; M: model; s : sensors; J : cost function. The red dashed arrows highlight the contribution of LGP.

LGPC explores automatically effective control laws from trial data. It is possible that the control optimization exploits the constraints or imperfections of the plant. The optimized solution may have no physical interests if it is related to the defects of actuators or sensors. Hence the characteristics of the actuators and sensors are better to be known a priori so that we can assess their influence on the results. In general, LGPC replaces the conventional paradigm of ‘*from understanding to control*’ by the new paradigm of ‘*from control to understanding*’. It bypasses the challenges of constructing a control-oriented model and goes beyond the model-based approach by identifying powerful nonlinear control laws which may be too complex to be predicted by any model. LGPC has already distilled new and unexpected actuation mechanisms in a number of experiments and simulations via collaborative projects of Pprime and LIMSI. To date, applications of LGPC to other plants include:

- Mixing increase behind a backward-facing step and drag reduction of car models in wind-tunnel experiments (Chovet *et al.* 2017, LAMIH).
- Jet mixing enhancement with multiple minijet actuators (Fan *et al.* 2017; Wu *et al.* 2017, Harbin Institute of Technology).
- Drag reduction of turbulence boundary layer (Harbin Institute of Technology).

- Stabilization of a fluidic pinball in experiments (Raibaudo *et al.* 2017, University of Calgary).
- Stabilization of a fluidic pinball in numerical simulation (Cornejo Maceda 2017, LIMSI). LGPC has outperformed hitherto known control strategies for these plants.

The development of a performance estimator helps to significantly accelerate the learning process and reduce the training time required for LGPC. Kaiser *et al.* (2017) has proposed an estimator which estimates the cost value for newly bred, untested individuals based on the information collected from the tested individuals. The estimation is served by an online visualization of the control laws which display the performance and similarity of control laws in two-dimensional proximity maps (see § 2.2.4 and § 3.5.2). These feature extraction techniques enables the estimator to determine the location of the untested control laws on the map. Based on the proximity to other control laws, we can select control laws which are newly explored or exploited for the next generation to be evaluated. In this way, redundant or similar testings can be avoided and the training time will be significantly reduced.

Dynamic modeling is also strongly modified by the data-driven approaches (Quade *et al.*, 2016; Loiseau *et al.*, 2017). The data-driven regression foundation of LGP may allow to derive simple human-interpretable nonlinear models from the rich actuation response data of control laws. For instance, sparse identification of nonlinear dynamics (SINDy) has been shown to derive nonlinear reduced-order models for cylinder flows from properly prepared data (Loiseau *et al.*, 2017). Combining such an approach with LGPC using the rich data set from actuation to sensing may result in interpretable models distilling new actuation mechanisms that are discovered in the controlled flow. The identified models can then serve as a low-dimensional surrogate of the actual experimental plant in order to facilitate the computation of nonlinear optimal feedback control laws.

The new paths opened by LGPC and more generally, the data-driven approaches, will play a transformative role in future flow control and fluid mechanics in general.

References

- AHMED, S. R., RAMM, G. & FALTIN, G. 1984 Some salient features of the time averaged ground vehicle wake. *Society of Automotive Engineers, SAE Inc* **840300**.
- ALJURE, D. E., LEHMKUHL, O., RODRIGUEZ, I. & OLIVA, A. 2014 Flow and turbulent structures around simplified car models. *Comp. & Fluids* **96**, 122–135.
- BAGHERI, S., BRANDT, L. & HENNINGSON, D.S. 2009 Input–output analysis, model reduction and control of the flat-plate boundary layer. *J. Fluid Mech.* **620**, 263–298.
- BAKER, C.J. 1986 A simplified analysis of various types of wind-induced road vehicle accidents. *J. Wind Eng. Ind. Aerodyn.* **22** (1), 69–85.
- BARROS, D. 2015 Wake and drag manipulation of a bluff body using fluidic forcing. PhD thesis, École Nationale Supérieure de Mécanique et d’Aérotechnique, Poitiers, France.
- BARROS, D., BORÉE, J., NOACK, B. R. & SPOHN, A. 2016a Resonances in the forced turbulent wake past a 3D blunt body. *Phys. Fluids* **28** (6), 065104.
- BARROS, D., BORÉE, J., NOACK, B. R., SPOHN, A. & RUIZ, T. 2016b Bluff body drag manipulation using pulsed jets and Coanda effect. *J. Fluid Mech.* **805**, 422–459.
- BARROS, D., BORÉE, J., O., CADOT., A., SPOHN & NOACK, B. R. 2017 Forcing symmetry exchanges and flow reversals in turbulent wakes. *J. Fluid Mech.* **829**.
- BAYRAKTAR, I., LANDMAN, D. & BAYSAL, O. 2001 Experimental and computational investigation of ahmed body for ground vehicle aerodynamics. *Tech. Rep.*. SAE Technical Paper.
- BEARMAN, P.W. 1965 Investigation of the flow behind a two-dimensional model with a blunt trailing edge and fitted with splitter plates. *J. Fluid Mech.* **21** (02), 241–255.
- BEAUDET, L. 2014 Étude expérimentale et numérique du décrochage dynamique sur une éolienne à axe vertical de forte solidité. PhD thesis, École Nationale Supérieure de Mécanique et d’Aérotechnique, Poitiers, France.
- BEAUDOIN, J-F., CADOT, O., AIDER, J-L & WESFREID, J. 2006 Drag reduction of a bluff body using adaptive control methods. *Phys. Fluids* **18** (8), 085107.
- BECKER, R., GARWON, M., GUTKNECHT, C., BÄRWOLFF, G. & KING, R. 2005 Robust control of separated shear flows in simulation and experiment. *J. Process Control* **15** (6), 691–700.
- BENARD, N., J., PONS P., PERIAUX, J. F., C., BUGEDA, BONNET, J.-P. & MOREAU, E. 2015 Multi-input genetic algorithm for experimental optimization of the reattachment downstream of a backward-facing step with surface plasma actuator. In *46th AIAA Plasma-dynamics and Lasers Conference*, pp. 1–23. AIAA.

- BERGER, E., SCHOLZ, D. & SCHUMM, M. 1990 Coherent vortex structures in the wake of a sphere and a circular disk at rest and under forced vibrations. *J. Fluids Struct.* **4** (3), 231–257.
- BORÉE, J., MAUREL, S. & BAZILE, R. 2002 Disruption of a compressed vortex. *Phys. Fluids* **14** (7), 2543–2556.
- BRACKSTON, R. D., GARCÍA DE LA CRUZ, J. M., WYNN, A., RIGAS, G. & MORRISON, J. F. 2016 Stochastic modelling and feedback control of bistability in a turbulent bluff body wake. *J. Fluid Mech.* **802**, 726–749.
- BRADSHAW, P. 1973 Effects of streamline curvature on turbulent flow. *Tech. Rep.*. Advisory Group for Aerospace Research and Development, Paris, France.
- BRAMEIER, M. & BANZHAF, W. 2007 *Linear Genetic Programming*. Springer Science & Business Media.
- BROWN, G. L. & ROSHKO, A. 1974 On density effects and large structure in turbulent mixing layers. *J. Fluid Mech.* **64** (4), 775–816.
- BRUNTON, S. L. & NOACK, B. R. 2015 Closed-loop turbulence control: Progress and challenges. *Appl. Mech. Rev.* **67** (5), 050801:01–48.
- CADOT, O., EVRARD, A. & PASTUR, L. 2015 Imperfect supercritical bifurcation in a three-dimensional turbulent wake. *Phys. Rev. E* **91** (6), 063005.
- CATTAFESTA, L. & SHELPACK, M. 2011 Actuators for active flow control. *Ann. Rev. Fluid Mech.* **43**, 247–272.
- CHALIGNÉ, S., CASTELAIN, T., MICHARD, M. & JUVÉ, D. 2013 Active control of the flow behind a two-dimensional bluff body in ground proximity. *Comptes Rendus Mécanique* **341** (3), 289–297.
- CHOI, H., JEON, W.-P. & KIM, J. 2008 Control of flow over a bluff body. *Ann. Rev. Fluid Mech.* **40**, 113–139.
- CHOI, H., LEE, J. & PARK, H. 2014 Aerodynamics of heavy vehicles. *Ann. Rev. Fluid Mech.* **46**, 441–468.
- CHOI, H., MOIN, P. & KIM, J. 1994 Active turbulence control for drag reduction in wall-bounded flows. *J. Fluid Mech.* **262**, 75–110.
- CHOVET, C., KEIRSBULCK, L., NOACK, B. R., LIPPERT, M. & FOUCAUT, J.-M. 2017 Machine learning control for experimental shear flows targeting the reduction of a recirculation bubble. In *The 20th World Congress of the International Federation of Automatic Control (IFAC)*, pp. 1–4. Toulouse, France.
- CORNEJO MACEDA, G. Y. 2017 Machine learning control applied to wake stabilization. Master's thesis, LIMSI and ENSAM, Paris, France.
- DAHAN, J. A., MORGANS, A.S. & LARDEAU, S. 2012 Feedback control for form-drag reduction on a bluff body with a blunt trailing edge. *J. Fluid Mech.* **704**, 360–387.
- DANDOIS, J., GARNIER, E. & SAGAUT, P. 2007 Numerical simulation of active separation control by a synthetic jet. *J. Fluid Mech.* **574**, 25–58.

- DEBIEN, A., VON KRBEK, K. A. F. F., MAZELLIER, N., DURIEZ, T., CORDIER, L., NOACK, B. R., ABEL, M. W. & KOURTA, A. 2016 Closed-loop separation control over a sharp-edge ramp using genetic programming. *Exp. Fluids* **57** (40), 1–19.
- D’HOOGHE, A., PALIN, R., REBBECK, L., GARGOLOFF, J. & DUNCAN, B. 2014 Alternative simulation methods for assessing aerodynamic drag in realistic crosswind. *SAE Int. J. Passenger Cars-Mech. Sys.* **7** (2014-01-0599), 617–625.
- DRACOPOULOS, D. C. & KENT, S. 1997 Genetic programming for prediction and control. *Neural Comput. & Appli.* **6**, 214–228.
- DRAZIN, P. G. & REID, W. H. 2004 *Hydrodynamic stability*. Cambridge university press.
- DUELL, E. G. & GEORGE, A. R. 1993 Measurements in the unsteady near wakes of ground vehicle bodies. *Tech. Rep.*. SAE Technical Paper.
- DUELL, E. G. & GEORGE, A. R. 1999 Experimental study of a ground vehicle body unsteady near wake. *Tech. Rep.*. SAE Technical Paper.
- DURIEZ, T., BRUNTON, S. & NOACK, B. R. 2016 *Machine Learning Control — Taming Nonlinear Dynamics and Turbulence. Fluid Mechanics and Its Applications* 116. Springer-Verlag (in print).
- ENGLAR, R. J. 2001 Advanced aerodynamic devices to improve the performance, economics, handling and safety of heavy vehicles. *Tech. Rep.*. SAE Technical Paper 2001-01-2072.
- ENGLAR, R. J. 2004 Pneumatic heavy vehicle aerodynamic drag reduction, safety enhancement, and performance improvement. In *The Aerodynamics of Heavy Vehicles: Trucks, Buses, and Trains*, pp. 277–302. Springer.
- EU, LEGISTATION 2017 Reducing CO2 emissions from passenger cars. https://ec.europa.eu/clima/policies/transport/vehicles/cars_en/.
- EVARD, A., CADOT, O., HERBERT, V., RICOT, D., VIGNERON, R. & DÉLERY, J. 2016 Fluid force and symmetry breaking modes of a 3D bluff body with a base cavity. *J. Fluids and Structures* **61**, 99–114.
- EVSTAFYEVA, O., MORGANS, A. S. & DALLA LONGA, L. 2017 Simulation and feedback control of the Ahmed body flow exhibiting symmetry breaking behaviour. *J. Fluid Mech.* **817**.
- FABRE, D., AUGUSTE, F. & MAGNAUDET, J. 2008 Bifurcations and symmetry breaking in the wake of axisymmetric bodies. *Phys. Fluids* **20** (5), 051702.
- FAN, D., WU, Z., ZHOU, Y., LI, R. & NOACK, B. R. 2017 Optimization of jet mixing using machine learning control. *In preparation* .
- FIEDLER, H. E. 1998 Control of free turbulent shear flows. In *Flow Control*, pp. 335–429. Springer.
- FLEMING, P. J. & PURSHOUSE, R. C. 2002 Evolutionary algorithms in control systems engineering: a survey. *Control Engineering Practice* **10** (11), 1223–1241.
- FOURRIÉ, G., KEIRSBULCK, L., LABRAGA, L. & GILLIÉRON, P. 2011 Bluff-body drag reduction using a deflector. *Exp. Fluids* **50** (2), 385–395.

- GAO, N., LI, Y. Q., BAI, H. L. & WU, C. J. 2016 Effects of synthetic jets on a D-shaped cylinder wake at a subcritical Reynolds number. *Flow Turb. Comb.* **97** (3), 729–742.
- GARCÍA DE LA CRUZ, J. M., BRACKSTON, R.D. & MORRISON, J.F. 2017a Adaptive base-flap under variable cross-wind. In *52nd 3AF International Conference on Applied Aerodynamics*. Lyon, France.
- GARCÍA DE LA CRUZ, J. M., OXLADE, A. R. & MORRISON, J. F. 2017b Passive control of base pressure on an axisymmetric blunt body using a perimetric slit. *Phys. Rev. Fluids* **2** (4), 043905.
- GARWON, M. & KING, R. 2005 A multivariable adaptive control strategy to regulate the separated flow behind a backward-facing step. In *16th IFAC World Congress, Prague, Czech Republic*.
- GAUTIER, N., AIDER, J.-L., DURIEZ, T., NOACK, B. R., SEGOND, M. & ABEL, M. W. 2015 Closed-loop separation control using machine learning. *J. Fluid Mech.* **770**, 424–441.
- GERHARD, J., PASTOOR, M., KING, R., NOACK, B. R., DILLMANN, A., MORZYNSKI, M. & TADMOR, G. 2003 Model-based control of vortex shedding using low-dimensional Galerkin models. *AIAA paper* **4262** (2003), 115–173.
- GEROPP, D. & ODENTHAL, H. J. 2000 Drag reduction of motor vehicles by active flow control using the Coanda effect. *Exp. Fluids* **28** (1), 74–85.
- GERRARD, J. H. 1966 The mechanics of the formation region of vortices behind bluff bodies. *J. Fluid Mech.* **25** (2), 401–413.
- GLEZER, A., AMITAY, M. & HONOHAN, A.M 2005 Aspects of low-and high-frequency actuation for aerodynamic flow control. *AIAA journal* **43** (7), 1501–1511.
- GOHLKE, M., BEAUDOIN, J.-F., AMIELH, M. & ANSELMET, F. 2007 Experimental analysis of flow structures and forces on a 3D-bluff-body in constant cross-wind. *Exp. Fluids* **43** (4), 579–594.
- GRANDEMANGE, M. 2013 Analysis and control of three-dimensional turbulent wakes: from axisymmetric bodies to road vehicles. PhD thesis, ENSTA, ParisTech.
- GRANDEMANGE, M., CADOT, O., COURBOIS, A., HERBERT, V., RICOT, D., RUIZ, T. & VIGNERON, R. 2015 A study of wake effects on the drag of Ahmed’s squareback model at the industrial scale. *J. Wind Engng. Ind. Aerodyn.* **145**, 282–291.
- GRANDEMANGE, M., GOHLKE, M. & CADOT, O. 2012 Reflectional symmetry breaking of the separated flow over three-dimensional bluff bodies. *Phy. Rev. E* **86**, 035302.
- GRANDEMANGE, M., GOHLKE, M. & CADOT, O. 2013a Bi-stability in the turbulent wake past parallelepiped bodies with various aspect ratios and wall effects. *Phys. Fluids* **25** (9), 095103.
- GRANDEMANGE, M., GOHLKE, M. & CADOT, O. 2013b Turbulent wake past a three-dimensional blunt body. Part 1. Global modes and bi-stability. *J. Fluid Mech.* **722**, 51–84.
- GRANDEMANGE, M., GOHLKE, M. & CADOT, O. 2014 Turbulent wake past a three-dimensional blunt body. Part 2. Experimental sensitivity analysis. *J. Fluid Mech.* **752**, 439–461.

- GRANDEMANGE, M., MARY, A., GOHLKE, M. & CADOT, O. 2013c Effect on drag of the flow orientation at the base separation of a simplified blunt road vehicle. *Exp. Fluids* **54** (5), 1529.
- GUILMINEAU, E. 2008 Computational study of flow around a simplified car body. *J. Wind Engng. Ind. Aerodyn.* **96** (6), 1207–1217.
- HAN, T., HAMMOND, D. C. & SAGI, C. J. 1992 Optimization of bluff body for minimum drag in ground proximity. *AIAA journal* **30** (4), 882–889.
- HENNING, L. & KING, R. 2005 Drag reduction by closed-loop control of a separated flow over a bluff body with a blunt trailing edge. In *44th IEEE Conf. on Decision and Control and European Control Conference CDC-ECC'05*, pp. 494–499. IEEE.
- HENNING, L. & KING, R. 2007 Robust multivariable closed-loop control of a turbulent backward-facing step flow. *J. aircraft* **44** (1), 201–208.
- HERRY, B. B., KEIRSBULCK, L., LABRAGA, L. & PAQUET, J.-B. 2011 Flow bistability downstream of three-dimensional double backward facing steps at zero-degree sideslip. *J. Fluids Eng.* **133** (5), 054501.
- HO, C. M. & HUERRE, P. 1984 Perturbed free shear layers. *Ann. Rev. Fluid Mech.* **16** (1), 365–422.
- HOLLAND, J. H. 1962 Outline for a logical theory of adaptive systems. *J. Assoc. Comput. Mach.* **9** (3), 297–314.
- HOWELL, J. 2015 Aerodynamic drag of passenger cars at yaw. *SAE Int. J. Passenger Cars-Mech. Sys.* **8** (2015-01-1559), 306–316.
- HOWELL, J., SIMS-WILLIAMS, D., SPROT, A., HAMLIN, F. & DOMINY, R. 2012 Bluff body drag reduction with ventilated base cavities. *SAE Int. J. Passenger cars. Mech. Sys.* **5** (1), 152–160.
- HUCHO, W. H., ed. 1998 *Aerodynamics of road vehicles*. Society of Automotive Engineers.
- HUERRE, P. & MONKEWITZ, P. A. 1990 Local and global instabilities in spatially developing flows. *Ann. Rev. Fluid Mech.* **22** (1), 473–537.
- HUSSAIN, A. K. M. F. & REYNOLDS, W. C. 1970 The mechanics of an organized wave in turbulent shear flow. *J. Fluid Mech.* **41** (2), 241–258.
- INOUE, O. 1992 Double-frequency forcing on spatially growing mixing layers. *J. Fluid Mech.* **234**, 553–581.
- JOSEPH, P., AMANDOLESE, X., EDOUARD, C. & AIDER, J.-L. 2013 Flow control using MEMS pulsed micro-jets on the Ahmed body. *Exp. Fluids* **54** (1), 1–12.
- KAISER, E., LI, R. & NOACK, B. R. 2017 On the control landscape topology. In *The 20th World Congress of the International Federation of Automatic Control (IFAC)*, pp. 1–5. Toulouse, France.
- KAISER, E., NOACK, B. R., CORDIER, L., SPOHN, A., SEGOND, M., ABEL, M. W., DAVILLER, G., ÖSTH, J., KRAJNOVIĆ, S. & NIVEN, R. K. 2014 Cluster-based reduced-order modelling of a mixing layer. *J. Fluid Mech.* **754**, 365–414.

- KHALIGHI, B., CHEN, K. H. & IACCARINO, G. 2012 Unsteady aerodynamic flow investigation around a simplified square-back road vehicle with drag reduction devices. *J. Fluids Engng.* **134** (6), 061101.
- KHALIGHI, B., ZHANG, S., KOROMILAS, C., BALKANYI, S. R., BERNAL, L. P., IACCARINO, G. & MOIN, P. 2001 Experimental and computational study of unsteady wake flow behind a bluff body with a drag reduction device. *Tech. Rep.*. SAE Technical Paper.
- KOZA, J. 1992 *Genetic programming: on the programming of computers by means of natural selection*, , vol. 1. MIT press.
- KRAJNOVIĆ, S. & DAVIDSON, L. 2005a Flow around a simplified car, Part 1: Large Eddy Simulation. *J. Fluids Engng* **127** (5), 907–918.
- KRAJNOVIĆ, S. & DAVIDSON, L. 2005b Flow around a simplified car, Part 2: Understanding the flow. *J. Fluids Engng* **127** (5), 919–928.
- KRENTEL, D., MUMINOVIC, R., BRUNN, A., NITSCHKE, W. & KING, R. 2010 Application of active flow control on generic 3D car models. In *Active flow control II*, pp. 223–239. Springer.
- LAHAYE, A., LEROY, A. & KOURTA, A. 2014 Aerodynamic characterisation of a square back bluff body flow. *Int. J. Aerod.* **4** (1-2), 43–60.
- LAWSON, N. J., GARRY, K. P. & FAUCOMPRET, N. 2007 An investigation of the flow characteristics in the bootdeck region of a scale model notchback saloon vehicle. *Proceedings of the Institution of Mechanical Engineers, Part D: Journal of Automobile Engineering* **221** (6), 739–754.
- LEWALLE, J. 1995 Tutorial on continuous wavelet analysis of experimental data. *Mechanical Aerospace and Manufacturing Engineering Dept., Syracuse University, World Wide Web: <http://www.mame.syr.edu/faculty/lewallle/tutor/tutor.html>* .
- LI, R., BARROS, D., BORÉE, J., CADOT, O., NOACK, B. R. & CORDIER, L. 2016 Feedback control of bi-modal wake dynamics. *Exp. Fluids* **57**, 1–6.
- LI, R., NOACK, B. R., CORDIER, L., BORÉE, J. & HARAMBAT, F 2017a Drag reduction of a car model by linear genetic programming control. *Exp. Fluids* **58** (103), 1–20.
- LI, R., NOACK, B. R., CORDIER, L., BORÉE, J., KAISER, E. & HARAMBAT, F 2017b Linear genetic programming control for strongly nonlinear dynamics with frequency crosstalk. *Submitted to J. Machine learning research* (see arXiv:1705.00367).
- LIENHART, H. & BECKER, S. 2003 Flow and turbulence structure in the wake of a simplified car model. *Tech. Rep.*. SAE Technical Paper.
- LIEPMANN, H.W. & NOSENCHUCK, D.M. 1982 Active control of laminar-turbulent transition. *J. Fluid Mech.* **118**, 201–204.
- LITTLEWOOD, R.P. & PASSMORE, M.A. 2012 Aerodynamic drag reduction of a simplified squareback vehicle using steady blowing. *Exp. Fluids* **53** (2), 519–529.
- LLOYD, S. 1956 Least squares quantization in PCM. *IEEE Trans. Inform. Theory* **28**, 129–137, originally as an unpublished Bell laboratories Technical Note (1957).

- LOISEAU, J.-C., NOACK, B. R. & BRUNTON, S. L. 2017 Sparse reduced-order modeling: Sensor-based dynamics to full-state estimation. *Submitted J. Fluid Mech.* (see arXiv:1706.03531).
- LUCHTENBURG, D. M., GÜNTER, B., NOACK, B. R., KING, R. & TADMOR, G. 2009 A generalized mean-field model of the natural and actuated flows around a high-lift configuration. *J. Fluid Mech.* **623**, 283–316.
- MARDIA, K. V., KENT, J. T. & BIBBY, J. M. 1979 *Multivariate analysis*. Academic Press.
- MELIGA, P., CHOMAZ, J.-M. & SIPP, D. 2009 Global mode interaction and pattern selection in the wake of a disk: a weakly nonlinear expansion. *J. Fluid Mech.* **633**, 159–189.
- MINGUEZ, M., PASQUETTI, R. & SERRE, E. 2008 High-order large-eddy simulation of flow over the ‘Ahmed body’ car model. *Phys. Fluids* **20** (9), 095101.
- MORRIS, S. C. & FOSS, J. F. 2003 Turbulent boundary layer to single-stream shear layer: the transition region. *J. Fluid Mech.* **494**, 187–221.
- MORRISON, J. F. & QUBAIN, A. 2009 Control of an axisymmetric turbulent wake by a pulsed jet. *Advances in Turbulence XII* pp. 225–228.
- NARAYANAN, S., NOACK, B. R., BANASZUK, A. & Khibnik, A. I. 2002 Active separation control concept: Dynamic forcing of induced separation using harmonically related frequency. United States Patent **6360763**.
- NAYERI, C.N., HAFF, J., GREENBLATT, D., LOEFDAHL, L. & PASCHEREIT, C.O. 2009 Drag reduction on a generic tractor-trailer using active flow control in combination with solid flaps. In *The Aerodynamics of Heavy Vehicles II: Trucks, Buses, and Trains*, pp. 179–191. Springer.
- NOACK, B. R. 2017 Plenary talk: Closed-loop turbulence control—from human to machine learning (and retour). In *4th Symposium on Fluid Structure-Sound Interactions and Control (FSSIC)*. Tokyo, Japan.
- ÖSTH, J., NOACK, B. R., KRAJNOVIĆ, S., BARROS, D. & BORÉE, J. 2014 On the need for a nonlinear subscale turbulence term in POD models as exemplified for a high-Reynolds-number flow over an Ahmed body. *J. Fluid Mech.* **747**, 518–544.
- OXLADE, A.R., MORRISON, J.F., QUBAIN, A. & RIGAS, G. 2015 High-frequency forcing of a turbulent axisymmetric wake. *J. Fluid Mech.* **770**, 305–318.
- PAILLÉ, F. 2017 Calibration de la balance six composantes kistler. ENSMA internal laboratory meeting.
- PAREZANOVIĆ, V., CORDIER, L., SPOHN, A., DURIEZ, T., NOACK, B. R., BONNET, J.-P., SEGOND, M., ABEL, M. & BRUNTON, S. L. 2016 Frequency selection by feedback control in a turbulent shear flow. *J. Fluid Mech.* **797**, 247–283.
- PAREZANOVIĆ, V., LAURENTIE, J. C., FOURMENT, C., DELVILLE, J., BONNET, J. P., SPOHN, A., DURIEZ, T., CORDIER, L., NOACK, B. R., ABEL, M. *et al.* 2015 Mixing layer manipulation experiment: From open-loop forcing to closed-loop machine learning control. *Flow Turb. Comb.* **94** (1), 155–173.

- PARK, H., CHO, J.-H., LEE, J., LEE, D.-H. & KIM, K.-H. 2013 Aerodynamic drag reduction of Ahmed model using synthetic jet array. *Tech. Rep.*. SAE Technical Paper.
- PASTOOR, M., HENNING, L., NOACK, B. R., KING, R. & TADMOR, G. 2008 Feedback shear layer control for bluff body drag reduction. *J. Fluid Mech.* **608**, 161–196.
- PERRIN, R., CID, E., CAZIN, S., SEVRAIN, A., BRAZA, M., MORADEI, F. & HARRAN, G. 2007 Phase-averaged measurements of the turbulence properties in the near wake of a circular cylinder at high Reynolds number by 2C-PIV and 3C-PIV. *Exp. Fluids* **42** (1), 93–109.
- PERRY, A., PAVIA, G. & PASSMORE, M. 2016 Influence of short rear end tapers on the wake of a simplified square-back vehicle: wake topology and rear drag. *Exp. Fluids* **57** (11), 169.
- PFEIFFER, J. & KING, R. 2012 Multivariable closed-loop flow control of drag and yaw moment for a 3D bluff body. In *6th AIAA Flow Control Conference*, pp. 1–14. Atlanta, Georgia, USA.
- PROTAS, B. 2004 Linear feedback stabilization of laminar vortex shedding based on a point vortex model. *Phys. Fluids* **16** (12), 4473–4488.
- QUADE, M., ABEL, M., SHAFI, K., NIVEN, R. K. & NOACK, B. R. 2016 Prediction of dynamical systems by symbolic regression. *Phys. Rev. E* **94** (1), 012214.
- QUBAIN, A. 2009 Active control of a turbulent bluff body wake. PhD thesis, Imperial College London.
- RAIBAUDO, C., ZHONG, P., MARTINUZZI, R. J. & NOACK, B. R. 2017 Closed-loop control of a triangular bluff body using rotating cylinders. In *The 20th World Congress of the International Federation of Automatic Control (IFAC)*, pp. 1–6. Toulouse, France.
- RECHENBERG, I. 1965 Cybernetic solution path of an experimental problem. Roy. Airc. Establ., Libr. Transl. 1122. Hants, U.K.: Farnborough.
- RIGAS, G., OXLADE, A. R., MORGANS, A. S. & MORRISON, J. F. 2014 Low-dimensional dynamics of a turbulent axisymmetric wake. *J. Fluid Mech.* **755**, R5.
- RIGAS, G. S., MORGANS A., BRACKSTON, R. D. & MORRISON, J. F. 2015 Diffusive dynamics and stochastic models of turbulent axisymmetric wakes. *J. Fluid Mech.* **778**.
- ROSHKO, A. 1955 On the wake and drag of bluff bodies. *J. Aeron. Sciences* **22** (2), 124–132.
- ROSHKO, A. 1993a Free shear layers, base pressure and bluff-body drag. *Tech. Rep.*. Tech. Rep. DTIC Document.
- ROSHKO, A. 1993b Perspectives on bluff body aerodynamics. *J. Wind Eng. Ind. Aerodyn.* **49** (1-3), 79–100.
- ROSSITTO, G. 2016 Influence of afterbody rounding on the aerodynamics of a fastback vehicle. PhD thesis, École Nationale Supérieure de Mécanique et d’Aérotechnique, Poitiers, France.
- ROSSITTO, G., SICOT, C., FERRAND, V., BORÉE, J. & HARAMBAT, F. 2017 Aerodynamic performances of rounded fastback vehicle. *Proceedings of the Institution of Mechanical Engineers, Part D: journal of automobile engineering* p. 0954407016681684.
- ROUMÉAS, M., GILLIÉRON, P. & KOURTA, A. 2009 Drag reduction by flow separation control on a car after body. *Int. J. Num. Meth. Fluids* **60** (11), 1222–1240.

- ROUSSOPOULOS, K. 1993 Feedback control of vortex shedding at low Reynolds numbers. *J. Fluid Mech.* **248**, 267–296.
- ROWLEY, C.W., WILLIAMS, D.R., COLONIUS, T., MURRAY, R.M. & MACMYNOWSKI, D.G. 2006 Linear models for control of cavity flow oscillations. *J. Fluid Mech.* **547**, 317–330.
- RUIZ, T., SICOT, C., BRIZZI, L. E., BORÉE, J. & GERVAIS, Y. 2010 Pressure/velocity coupling induced by a near wall wake. *Exp. Fluids* **49** (1), 147–165.
- RUIZ, T., SICOT, C., BRIZZI, L. E., LEMONIER, J., BORÉE, J. & GERVAIS, Y. 2009 Unsteady near wake of a flat disk normal to a wall. *Exp. Fluids* **47** (4-5), 637–653.
- SAMIMY, M., DEBIASI, M., CARABALLO, E., SERRANI, A., YUAN, X., LITTLE, J. & MYATT, J.H. 2007 Feedback control of subsonic cavity flows using reduced-order models. *J. Fluid Mech.* **579**, 315–346.
- SCHMIDT, H.J., WOSZIDLO, R., NAYERI, C.N. & PASCHEREIT, C.O. 2015 Drag reduction on a rectangular bluff body with base flaps and fluidic oscillators. *Exp. Fluids* **56** (7), 1–16.
- SCHOENBERG, I. J. 1935 Remarks to Maurice Fréchet’s article ”Sur la définition axiomatique d’une classe d’espaces distanciés vectoriellement applicable sur l’espace de Hilbert”. *Annals of Mathematics* **38**, 724–732.
- SCHWEFEL, H. P. 1968 Projekt MHD-Staustrahlrohr: Experimentelle Optimierung einer Zweiphasendüse. Teil I. *Tech. Rep.*. AEG Forschungsinstitut, Berlin, Germany.
- SEIFERT, A., DAYAN, I., HORRELL, C., GROSSMANN, J. & SMITH, A. 2016 Heavy trucks fuel savings using the SaOB actuator. In *The Aerodynamics of Heavy Vehicles III*, pp. 377–390. Springer.
- SEIFERT, A., SHTENDEL, T. & DOLGOPYAT, D. 2015 From lab to full scale active flow control drag reduction: How to bridge the gap? *J. Wind Eng. Ind. Aerodyn.* **147**, 262–272.
- SIMS-WILLIAMS, D.B. 2011 Cross winds and transients: reality, simulation and effects. *SAE International Journal of Passenger Cars-Mechanical Systems* **4** (1), 172–183.
- SIPP, D. 2012 Open-loop control of cavity oscillations with harmonic forcings. *J. Fluid Mech.* **708**, 439–468.
- SOUSANIS, J. 2011 World vehicle population tops 1 billion units. <http://wardsauto.com/news-analysis/world-vehicle-population-tops-1-billion-units/>, [Online; accessed 15-August-2011].
- SPERLING, D. & GORDON, D. 2008 Two billion cars: transforming a culture. *TR news* **259**.
- SYCHEV, V. 1982 Asymptotic theory of separation flows. *Fluid Dynamics* **17** (2), 179–188.
- TROPEA, C. & YARIN, A. L. 2007 *Springer handbook of experimental fluid mechanics*, , vol. 1. Springer Science & Business Media.
- VAN DYKE, M. 1982 *An album of fluid motion*. Parabolic Press Stanford.
- VOLPE, R., DEVINANT, P. & KOURTA, A. 2015 Experimental characterization of the unsteady natural wake of the full-scale square back Ahmed body: flow bi-stability and spectral analysis. *Exp. Fluids* **56** (5), 1–22.

- VUKASINOVIC, B., RUSAK, Z. & GLEZER, A. 2010 Dissipative small-scale actuation of a turbulent shear layer. *J. Fluid Mech.* **656**, 51–81.
- WASSEN, E., EICHINGER, S. & THIELE, F. 2010 Simulation of active drag reduction for a square-back vehicle. In *Active Flow Control II*, pp. 241–255. Springer.
- WINKELMANN, A. E. & GONZALEZ, H. A. 1990 Design of a three-component wall-mounted balance. *AIAA 16th Aerodynamic Ground Testing Conference* .
- WU, Z., FAN, D., ZHOU, Y., LI, R. & NOACK, B. R. 2017 Jet mixing enhancement using machine learning control. *In preparation* .
- YI, W. 2007 Drag reduction of a three-dimensional car model using passive control device. PhD thesis, Seoul Natl. Univ.
- YOUNG, G. & HOUSEHOLDER, A. S. 1938 Discussion of a set of points in terms of their mutual distances. *Psychometrika* **3**, 19–22.
- ZHANG, B., ZHOU, Y. & TO, S. 2015 Unsteady flow structures around a high-drag Ahmed body. *J. Fluid Mech.* **777**, 291–326.
- ZHANG, M., CHENG, L. & ZHOU, Y. 2004 Closed-loop-controlled vortex shedding and vibration of a flexibly supported square cylinder under different schemes. *Phys. Fluids* **16** (5), 1439–1448.

Appendix A

Classical multidimensional scaling (CMDS)

Classical multidimensional scaling (CMDS) is employed to visualize the similarity of control laws (see § 2.1.4). CMDS aims to find a low-dimensional representation of points γ_i , $i = 1, \dots, N_K$, such that the average error between the distances between points γ_i and the elements of a given distance matrix \mathbf{D} , here emulating the distances between the time series of different control laws, is minimal. In order to find a unique solution to CMDS, we assume that $\mathbf{\Gamma} = [\gamma_1 \ \gamma_2 \ \dots \ \gamma_{N_K}]$ with $\gamma_1, \dots, \gamma_{N_K} \in \mathbb{R}^r$ is centered, i.e., $\mathbf{\Gamma}$ is a mean-corrected matrix with $\frac{1}{N_K} \sum_{i=1}^{N_K} \gamma_i = [0 \dots 0]^T$. Rather than directly finding $\mathbf{\Gamma}$, we search for the Gram matrix $\mathbf{B} = \mathbf{\Gamma}^T \mathbf{\Gamma}$ that is real, symmetric and positive semi-definite. Since $\mathbf{\Gamma}$ is assumed to be centred, the Gram matrix is the Euclidean inner product, and we have $D_{ij}^2 = \|\gamma_i - \gamma_j\|_2^2 = B_{ii} + B_{jj} - 2B_{ij}$. In the first step of the classical scaling algorithm, the matrix \mathbf{D}_2 of elements $(D_2)_{ij} = -\frac{1}{2}D_{ij}^2$ is constructed. Then, we form the ‘doubly centred’ matrix $\mathbf{B} = \mathbf{C}\mathbf{D}_2\mathbf{C}$, where $\mathbf{C} = \mathbf{I}_{N_K} - N_K^{-1}\mathbf{J}_{N_K}$ with \mathbf{I}_{N_K} the identity matrix of size N_K and \mathbf{J}_{N_K} an $N_K \times N_K$ matrix of ones. The term ‘doubly centred’ refers to the subtraction of the row as well as the column mean. Let the eigendecomposition of \mathbf{B} be $\mathbf{B} = \mathbf{V}\mathbf{\Lambda}\mathbf{V}^T$ where $\mathbf{\Lambda}$ is a diagonal matrix with ordered eigenvalues $\lambda_1 \geq \lambda_2 \geq \dots \geq \lambda_{N_K} \geq 0$ and \mathbf{V} contains the eigenvectors as columns. Then $\mathbf{\Gamma}$ can be recovered from

$$\mathbf{\Gamma} = \mathbf{\Lambda}^{\frac{1}{2}}\mathbf{V}^T. \quad (\text{A.1})$$

Having only the distance matrix, the resulting representation is only defined up to a translation, a rotation, and reflections of the axes. If the distance matrix is computed using the Euclidean distance and all eigenvalues are non-negative, $\mathbf{\Gamma}$ can be recovered. If $r < N_K$, there exist $N_K - r$ zero eigenvalues, in which case a low-dimensional subspace can be found where the presentation of $\mathbf{\Gamma}$ would be exact. For other distance metrics, the distances of the presentation found by CMDS is an approximation to the true distances. Some eigenvalues may be negative and only the positive eigenvalues and their associated eigenvectors are considered to determine an approximative representation of $\mathbf{\Gamma}$. Note that for the Euclidean distance metric, CMDS is closely related to a principal component analysis (PCA) commonly used to find a low-dimensional subspace. While CMDS, and multi-dimensional scaling generally, uses a distance matrix as input, PCA is based on a data matrix. A distance matrix \mathbf{D} can be directly computed for the centred matrix $\mathbf{\Gamma}$. If the Euclidean distance is employed for computing the distances, the result from applying CMDS to \mathbf{D} corresponds to the result from applying PCA to $\mathbf{\Gamma}$. A proof can be found in Mardia *et al.* (1979). The quality of the representation is typically measured by $\sum_{i=1}^r \lambda_i / \sum_{i=1}^{N_K-1} \lambda_i$, and more generally if \mathbf{B} is not positive semi-definite using $\sum_{i=1}^r \lambda_i / \sum_{\lambda > 0} \lambda_i$.

Aerodynamic drag reduction of a square-back car model using linear genetic programming and physics-based control

The thesis aims to develop effective active flow control strategies for aerodynamic drag reduction of road vehicles. We experimentally examine the effects of fluidic actuation on the wake past a simplified square-back car model. The actuation is performed with pulsed jets at trailing edges and the flow is monitored with 16 pressure sensors distributed at the rear side. We address the challenging nonlinear turbulence control---which is often beyond the capabilities of model-oriented approach---by developing a simple yet powerful model-free control strategy: the data-driven linear genetic programming control (LGPC). This method explores and exploits strongly nonlinear dynamics in an unsupervised manner with no or little prior knowledge about the system. The control problem is to find a control logic which optimizes a given cost function by employing linear genetic programming as an easy and simple regression solver in a high-dimensional control search space. In particular, the present work advances and generalizes the previous studies of genetic programming control by comprising multi-frequency forcing, sensor-based feedback including also time-history information feedback and combinations thereof in the control search space. The performance of LGPC is successfully demonstrated on the drag control experiments of the car model where the investigated turbulent wake exhibits a spanwise symmetry and a wall-normal asymmetry. Approximately 33% base pressure recovery associated with 22% drag reduction is achieved in all considered classes of control laws. The consumed actuation energy accounts for only 30% of the aerodynamic power saving. In this research, we also study the turbulent wakes having a lateral asymmetry: an intermittent bi-modal wake at zero yaw and an asymmetric wake at a moderate yaw angle of 5 degree. For the bimodal wake exhibiting a reflectional symmetry-breaking, a physics-based opposition feedback control is inferred from the previous open-loop control tests. The controller successfully suppresses the bi-modality of the wake and renders a symmetrized wake with a concomitant drag reduction. For the asymmetric wake at yaw, we infer from the single-frequency forcing results a bi-frequency control at the windward edge comprising two frequencies having one order of magnitude difference. This bi-frequency actuation combines the favorable effects of fluidic boat-tailing and balance control of the shear layers. Importantly, LGPC is also applied to this yawed situation and converges to the same bi-frequency actuation. The control strategies proposed in the present study open promising new paths for the control of drag reduction in more complex conditions such as the varying oncoming velocity and wind gust.

Key words: Aerodynamic drag, Wake, Flow control, Feedback control

Réduction de la traînée aérodynamique d'un véhicule à culot droit en utilisant un contrôle basé sur la programmation génétique linéaire et sur la physique

Le but de la thèse est de développer des stratégies de contrôle efficaces pour la réduction de la traînée aérodynamique des véhicules terrestres. Nous examinons expérimentalement les effets d'un forçage fluidique sur le sillage d'un modèle de véhicule simplifié à culot droit. Le forçage est effectué par des jets pulsés aux arêtes et 16 capteurs de pression répartis à la surface arrière permettent d'estimer la traînée instantanée. Nous abordons le problème difficile du contrôle de l'écoulement turbulent non linéaire---qui est souvent au-delà des capacités de la modélisation réduite---par le développement d'une stratégie de contrôle sans modèle: le contrôle via la programmation génétique linéaire (LGPC) dirigé par les données. Cette méthode explore et exploite la dynamique fortement non linéaire d'une manière non supervisée avec pas ou peu de connaissances antérieures sur le système. Le problème est de trouver une logique de contrôle qui optimise une fonction de coût donnée. Cette optimisation est réalisée par la programmation génétique linéaire comme un solveur de régression simple dans un espace de recherche de grande dimension. En particulier, cette recherche fait progresser et généralise les études antérieures sur le contrôle via la programmation génétique en incluant le forçage multi-fréquences, le signal des capteurs, l'historique des informations temporelles et leurs combinaisons dans l'espace de recherche de contrôle. La performance de LGPC est démontrée avec succès sur les expériences de contrôle de traînée du modèle de véhicule simplifié où le sillage turbulent présente une symétrie latérale et une asymétrie normale à la paroi. Environ 33% de récupération de pression au culot associée à 22% de réduction de traînée est obtenue dans toutes les classes de lois de contrôle considérées. L'énergie consommée du forçage ne représente que 30% de l'énergie aérodynamique récupérée. Dans ce travail, nous étudions également les sillages turbulents ayant une asymétrie latérale: un sillage intermittent et bi-modal à dérapage nul et un sillage asymétrique avec un angle de dérapage modéré de 5 degrés. Pour le sillage intermittent, un contrôle de réaction en opposition basé sur la physique est déduit à partir des essais précédents de contrôle en boucle ouverte. Le contrôleur supprime avec succès la bi-modalité du sillage et rend le sillage symétrique avec une réduction de traînée concomitante. Pour le sillage asymétrique en dérapage, nous construisons un contrôle bi-fréquence à l'arête au vent à partir des résultats de forçage à fréquence unique. Ce forçage bi-fréquentiel comprend deux fréquences ayant une différence d'un ordre de grandeur. Il combine les effets favorables de la vectorisation du sillage et le contrôle de l'équilibre des couches de cisaillement. Il est important de noter que la stratégie LGPC est également appliquée à cette situation en dérapage et converge vers le même forçage bi-fréquentiel. Les stratégies de contrôle proposées dans cette étude ouvrent de nouveaux chemins prometteurs pour le contrôle de la réduction de la traînée dans des conditions plus complexes de vitesse amont variable ou de rafale.

Mots clés: Traînée aérodynamique, Sillage, Contrôle des écoulements, Contrôle en boucle fermée